



Towards Highly Active and Stable Oxygen Electrocatalysts

Roy, Claudie

Publication date:
2018

Document Version
Publisher's PDF, also known as Version of record

[Link back to DTU Orbit](#)

Citation (APA):
Roy, C. (2018). *Towards Highly Active and Stable Oxygen Electrocatalysts*. Department of Physics, Technical University of Denmark.

General rights

Copyright and moral rights for the publications made accessible in the public portal are retained by the authors and/or other copyright owners and it is a condition of accessing publications that users recognise and abide by the legal requirements associated with these rights.

- Users may download and print one copy of any publication from the public portal for the purpose of private study or research.
- You may not further distribute the material or use it for any profit-making activity or commercial gain
- You may freely distribute the URL identifying the publication in the public portal

If you believe that this document breaches copyright please contact us providing details, and we will remove access to the work immediately and investigate your claim.

Towards Highly Active and Stable Oxygen Electrocatalysts

a PhD dissertation by

Claudie Roy

Supervisor: Professor Ib Chorkendorff

Co-supervisor: Associate Professor Jakob Kibsgaard

Co-supervisor: Senior Lecturer Ifan E.L. Stephens



Section for Surface Physics and Catalysis
Department of Physics
Technical University of Denmark

May 2018

Front Image

Preface

This thesis is submitted in partial fulfillment of the requirements for the Ph.D. degree from the Technical University of Denmark (DTU). The work presented herein was performed at the Section for Surface Physics and Catalysis (SurfCat), which is part of the Department of Physics, between June 2015 and May 2018. The project was performed under the supervision of Professor Ib Chorkendorff, Associate Professor Jakob Kibsgaard, and Senior Lecturer Ifan E.L. Stephens, who very recently moved to Imperial College London.

Several institutions have played a crucial role in this research. SurfCat is funded by a grant (9455) from the VILLUM FONDEN through the VILLUM Center for the Science of Sustainable Fuels and Chemicals. My PhD work was supported by UPCAT under the project no. 2015-1-12315 from energinet.dk. I also acknowledge the Danish Ministry of Higher Education and Science, and Otto Mønstedts Fond for awarding me a visiting researcher grant for my stay at the Massachusetts Institute of Technology (MIT).

I first want to thank my supervisors, for their guidance and providing me with immeasurable opportunities in terms of collaborations, research facilities and professional development. I could not have hope for more inspiring and stimulating work environment.

I would like to express my gratitude to Professor Yang Shao-Horn and her research group for welcoming me in at the Electrochemical Energy Lab at MIT during Fall 2017. I want to thank Reshma Rao, Botao Huang, Sokseiha Muy, Yu Katayama and Prof. Livia Giordano for all their research help during my stay.

My Doctoral journey would not have been the same without the support and companionship of all my friends and colleagues. I want to ex-

plicitly thank Amado Velazquez-Palenzuela, Brian P. Knudsen, Christoffer Mølleskov Pedersen, Ass. Prof. Christian D. Damsgaard, Elisabetta M. Fiordaliso, Béla Sebök, Jakob E. Sørensen, Søren B. Scott, Niklas M. Secher, Anders Bodin, Jacqueline McAnulty, Robert Jensen and Kenneth Nielsen, with whom I have had the privilege of working closely with, and have helped me along the way. I keep great memories of our many hours spent in the lab. Special thanks goes to Sine Olesen, Erlend Bertheussen, Arnau Verdaguer-Casadevall, Martin Bækbo, Jakob Riedel, Ann-Louise Christoffersen, Elisa Paoli, Mariona Bertran and Morlin Møller, for all the fun stuff outside working hours. Erlend, Sine, Martin, Niklas, Anna, Ifan and Jakob, all made highly appreciated efforts in helping me improve and polish this thesis. Special thank to Sine who fed me with a 10 kg lasagna while writing this thesis.

Last but not least, thanks to my family and friends from back home who stuck with me, and supported me over the last years. I cannot say enough to adequately thank you for making this an even more amazing and memorable adventure.

Kongens Lyngby, May 31 2018
Claudie Roy

Abstract

This PhD thesis presents work on the development of electrocatalysts for oxygen evolution and reduction reactions. The oxygen evolution reaction (OER) is a bottleneck in the large-scale development of electrolyzers, which are promising technologies for energy storage in hydrogen bond. Polymer electrolyte membrane (PEM) electrolyzers rely on scarce and expensive materials like RuO_x -based catalysts to achieve high efficiency. However, RuO_x is also unstable under OER conditions. Part of this work was to study the catalytic activity and stability of oriented thin films of RuO_2 with the (111), (001), and (101) orientations, and compare it to RuO_2 (110) single-crystal and commercial particles. The catalytic activity was measured from stability tests performed in 0.05 M H_2SO_4 and coupled with inductively coupled plasma mass spectrometry to measure Ru dissolution.

The second part of this thesis focuses on the better understanding of NiFeO_xH_y catalysts for the OER in alkaline electrolyte. NiFeO_xH_y as OER catalyst has been used in the industry for decades, but several open questions remain regarding the reasons for its very high catalytic activity. Using a model system of mass-selected NiFeO_xH_y nanoparticles, we addressed two main questions i) the impact of size effect and ii) the role of bulk activity on the oxygen evolution.

The reverse reaction, the oxygen reduction reaction (ORR), was also studied. ORR is the limiting reaction in hydrogen fuel cell technologies, which allow for the conversion of hydrogen back to electricity. The third and last part of this work focuses on the synthesis of Pt-rare-earth alloys on a gram scale. We investigated the alkalide and cyanide reduction, and the high thermal synthesis methods.

Resumé

Denne ph.d.-afhandling præsenterer arbejdet med udvikling af elektrokatalysatorer til oxygenudviklings – og oxygenreduktionsreaktionerne. Oxygenudviklingsreaktionen (OER) er en flaskehals for udbredelsen af elektrolysesystemer, som er lovende teknologier til at gemme energi i hydrogenbindinger. Polymer elektrolyt membran (PEM) elektrolyseceller er afhængige af sjældne og dyre katalysatorer f.eks. RuO_x -baseret materialer for at opnå høj effektivitet. RuO_x er dog også ustabil under OER betingelser. En del af arbejdet under denne ph.d. har været at studere den katalytiske aktivitet og stabilitet af orienterede RuO_2 tyndfilm med orienteringerne; (111), (001) og (101) og sammenligne med RuO_2 (110) enkeltkrystal og kommercielle partikler. Den katalytiske aktivitet blev målt gennem stabilitetsforsøg i 0,05 M H_2SO_4 og sammenholdt med induktivt koblet plasma massespektroskopi til måling af Ru opløst i væsken. Anden del af denne afhandling fokuserer på at opnå en bedre forståelse af NiFeO_xH_y katalysatorer til OER i alkalisk elektrolyt. NiFeO_xH_y , som OER katalysator, har været brugt i industrien i årtier, men der er endnu flere åbne spørgsmål omkring grunden til deres høje katalytiske aktivitet. V.h.a. et modelsystem af masse-selektede NiFeO_xH_y nanopartikler, adresserede vi to centrale spørgsmål; i) indvirkningen af størrelseseffekt og ii) hvilken rolle *bulk* aktivitet spiller på oxygenudviklingen. Den modsatte reaktion, oxygenreduktion (ORR), blev også undersøgt. ORR er den begrænsende reaktion i hydrogenbrændselleteknologier, som konverterer hydrogen til elektricitet. Den tredje og sidste del af arbejdet i dette ph.d.-projekt fokuserede på syntesen af Pt-sjældne jordarter-legeringer i gram-mængder. Vi undersøgte alkali og cyanid reduktion og højtemperatur syntesemetoder.

List of Publications

Appended Publications

Paper I

Scalable Synthesis of Carbon-Supported Platinum-Lanthanide and Rare Earth Alloys for Oxygen Reduction

Claudie Roy, Brian Peter Knudsen, Christoffer Mølleskov Pedersen, Amado Andrés Velázquez Palenzuela, Leif Hojslet Christensen, Christian Danvad Damsgaard, Ifan E.L. Stephens, Ib Chorkendorff
ACS Catalysis, 2017, 8 (3), pp 2071-2080

Paper II

Trends in activity and dissolution on RuO₂ under oxygen evolution conditions: particles versus well-defined extended surfaces

Claudie Roy, Reshma R. Rao, Kelsey A. Stoerzinger, Jonathan Hwang, Jan Rossmeisl, Ib Chorkendorff, Yang Shao-Horn, Ifan E.L. Stephens
Submitted

Paper III

Impact of Size and Lattice Oxygen on Water Oxidation on NiFeO_xH_y

Claudie Roy*, Béla Sebök*, Søren Scott*, Elisabetta M. Fiordaliso, Jakob E. Sørensen, Anders Bodin, Daniel B. Trimarco, Christian D. Damsgaard,

Peter C.K. Vesborg, Ole Hansen, Ifan E.L. Stephens, Jakob Kibsgaard, Ib Chorkendorff

Submitted

Other Publications- Not Appended

Paper IV

Acetaldehyde as an Intermediate in the Electroreduction of Carbon Monoxide to Ethanol on Oxide-Derived Copper

Erlend Bertheussen, Arnau Verdaguer-Casadevall, Davide Ravasio, Joseph H Montoya, Daniel B Trimarco, Claudie Roy, Sebastian Meier, Jürgen Wendland, Jens K Nørskov, Ifan EL Stephens, Ib Chorkendorff
Angewandte Chemie International Edition, 55 (4), pp 1450-1454

Acronyms

OECD	Organisation for Economic Co-operation and Development
USA	United States of America
GHG	Greenhouse Gas
W	Watt
OER	Oxygen Evolution Reaction
ORR	Oxygen Reduction Reaction
PEM	Polymer Electrolyte Membrane
PEMFC	Polymer Electrolyte Membrane Fuel Cell
EC	Electrochemical
CN	Coordination Number
CUS	Coordinately Unsaturated Sites
FE	Faradaic Efficiency
NP	Nanoparticle
LDH	Layered Double Hydroxide
XRD	X-ray Diffraction
TOF	Turnover Frequency
EQCM	Electrochemical Quartz Microbalance
FCEV	Fuel Cell Electric Vehicle
HOR	Hydrogen Oxidation Reaction
USDOE	U.S. Department of Energy
UHV	Ultra-High Vacuum
TEM	Transmission Electron Microscopy
SEM	Scanning Electron Microscopy

XPS	X-ray Photoelectron Spectroscopy
LEIS	Low-Energy Ion Scattering
PLD	Pulsed Laser Deposition
EDS	Energy Dispersive Spectroscopy
RDE	Rotating Disk Electrode
HUPD	Hydrogen Underpotential Deposition
V_{RHE}	V versus Reversible Hydrogen Electrode
GI-EXAFS	Grazing-Incident Extended X-ray Absorption Fine Structures
ICP-MS	Inductively Coupled Mass Spectrometry
MS	Mass Spectrometer
RHE	Reversible Hydrogen Electrode
CV	Cyclic Voltammetry
CA	Chronoamperometry
DFT	Density Functional Theory
FCC	Face-Centered-Cubic
ML	Monolayer
Ln	Lanthanide
RE	Rare-Earth

Contents

Preface	i
Abstract	iii
Resume	v
List of publications	vii
Acronyms	ix
1 Introduction	1
1.1 The Need for an Energy Revolution	1
1.2 Electrochemical Energy Conversion	6
1.2.1 Why Hydrogen as Energy Carrier?	6
1.2.2 Overview of Electrolyzer Technologies	8
1.2.3 Polymer Electrolyte Membrane Fuel Cell	11
1.3 Thesis Outline	14
2 Oxygen Electrocatalysis	16
2.1 The basics of (Electro)Catalysis	16
2.1.1 Thermodynamics of Electrode Reactions	16
2.1.2 Role of a Catalyst	17
2.1.3 Catalyst Design	24
2.2 Overview of Promising OER Catalysts	25
2.2.1 Acid OER Catalysts	25
2.2.2 Alkaline OER Catalysts	30

2.2.3	Does More Active Equals Less Stable?	33
2.3	Overview of State-of-the-Art ORR Catalysts	38
3	Experimental Methods	47
3.1	Sample Preparation	47
3.1.1	Mass-selected Nanoparticles	47
3.1.2	Oriented Thin films	49
3.2	Sample Characterization	51
3.2.1	X-ray Diffraction	51
3.2.2	X-Ray Photoelectron Spectroscopy	52
3.2.3	Low-energy Ion Scattering	53
3.2.4	Electron Microscopy	54
3.3	Measuring Catalytic Activity and Stability	56
3.3.1	Inductively Coupled Plasma Mass Spectrometry	61
3.3.2	Electrochemistry-Mass Spectrometry	62
4	Activity and Metal Dissolution Trends of Rutile RuO₂ under Oxygen Evolution Conditions	63
4.1	Experimental Section	64
4.1.1	Sample Preparation	64
4.1.2	Electrochemical Measurements	64
4.2	Results	65
4.3	Discussion	76
4.4	Conclusion	78
5	Investigation of NiFeO_xH_y Nanoparticles for the Oxygen Evolution	79
5.1	Experimental Section	80
5.1.1	Preparation of Mass-Selected Nanoparticles	80
5.1.2	Physical Characterization	82
5.1.3	Electrochemical measurements	83
5.2	Results	84
5.2.1	Physical Characterisation	84
5.2.2	Catalytic Activity and Stability	90
5.3	Participation of bulk NiFeO _x H _y in the OER	95
5.4	Discussion	99
5.5	Conclusion	100
6	Synthesis of Platinum-Rare-earth Alloys for the Oxygen Reduction	101
6.1	Alkalide Reduction	102
6.1.1	Discussion	108

6.1.2	Conclusion	109
6.2	Cyanide Reduction Synthesis	109
6.2.1	Experimental Section	111
6.2.2	Physical Characterization	113
6.2.3	Electrochemical Oxygen Reduction	119
6.2.4	Discussion	119
6.2.5	Conclusion	121
6.3	High Temperature Synthesis	121
6.3.1	Thermodynamics Calculations and Early Work	122
6.3.2	Experimental Section	126
6.3.3	Results	130
6.3.4	Physical Characterization	131
7	Conclusion and Outlook	139
7.1	Conclusion	139
7.2	Outlook	141
	Bibliography	142
	Appendices	167
A	Supplementary Materials Chapter 4	168
B	Supplementary Materials Chapter 5	174
C	Supplementary Materials Chapter 6	187
D	Appended Articles	190

The focus of this thesis is to investigate new catalysts for the electrochemical oxygen evolution and oxygen reduction reactions taking place in electrolyzer and hydrogen fuel cell applications, respectively. An economy based on hydrogen holds the power to mitigate CO₂ emissions and limit global warming. This chapter serves, first, as a motivation to understand why the world needs to transition from fossil fuels to sustainable energy sources. It also introduces the basic concepts related to catalysis, and more specifically to electrocatalysis, that help the reader understand the research work in Chapter 4, 5 and 6. Finally, the research topics covered in this thesis with an outline to my personal contribution are presented.

1.1 The Need for an Energy Revolution

From 1.6 billion in the pre-industrial era, today's population is estimated at 7.6 billion people [1]. This number is expected to rise by 28% between 2015 and 2040, with most of the increase occurring in non-OECD countries [2]. The world's energy consumption has also increased with the population. In addition to global population, the amplitude of the energy change is affected by the economic activity, the lifestyle, the energy efficiency and the land-use patterns technology [3], just to name a few. That helps to explain why, during the twentieth century, the population increased by a factor of 6, but the energy consumption grew by a factor of 80 [2].

Since the Industrial Revolution [4], the global energy supply is based on fossil fuels. Still in 2015, natural gas, coal and oil represented around 86% of the global energy consumption [2]. Two-thirds of the crude oil reserves are located in the Middle East, but most of it is consumed in the USA, Japan and Europe [5]. This creates a clear economic dependency

that can potentially have a strong impact on social, political and economic interactions. The other main issue regarding the use of fossil fuels is the greenhouse gas (GHG) emissions related to CO₂ emissions, which explains why nearly 75% of the CO₂ emissions in the last 20 years come from fossil fuels [4]. Figure 1.1 shows the country-wise distribution of CO₂ emissions in the world. The bigger the circle in a country, the more CO₂ was emitted in that country in 2015. The largest CO₂ emitters related to the burn of fossil fuels are China with ~ 10.4 MtCO₂ and the USA with ~ 5.4 MtCO₂. India, the second most populous country, ranked after the USA due to lower economic development.

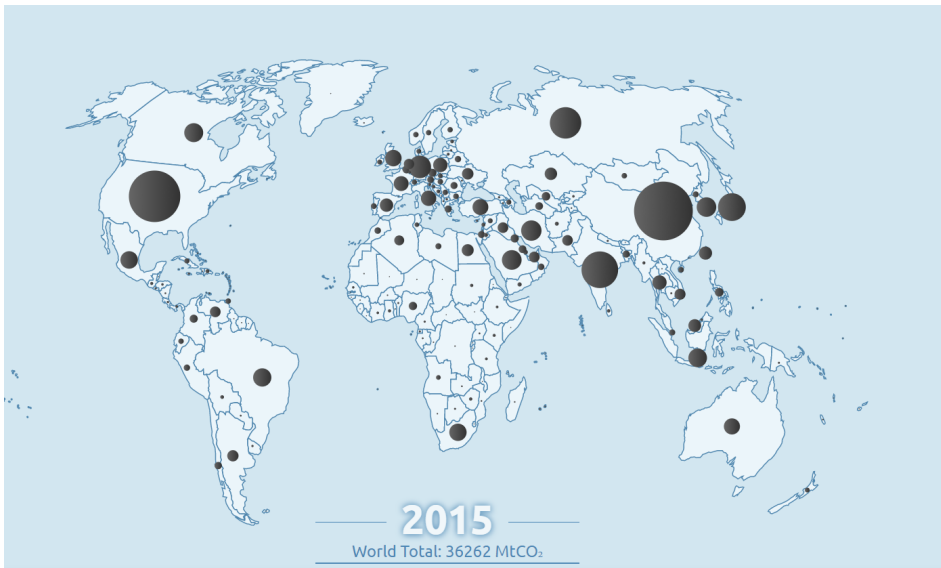


Figure 1.1: World CO₂ emissions related to fossil fuel consumption by country. The size of the dot is proportional to the amount of CO₂ emitted [6]

CO₂ is a GHG together with other compounds such as methane and nitrogen oxide. The introduction of the concept of greenhouse effect goes back to 1810. Joseph Fourier was the first to compare heating of the Earth's atmosphere to the action of glass in a greenhouse through his work on heat transfer [7]. The GHGs are defined as gasses that absorb infrared radiation and release it as heat. On the Earth, a higher GHG concentration leads to less heat escaping the atmosphere, resulting in global warming. Figure 1.2 shows the change in surface temperature between 1910 and 2012 in different areas of the globe. As shown in the map, a temperature increase of $+2.5^{\circ}\text{C}$ has already been observed in some world regions.

Global climate change have long-lasting consequences on nature and human systems. It imperils our lands and water, and it affects the amount

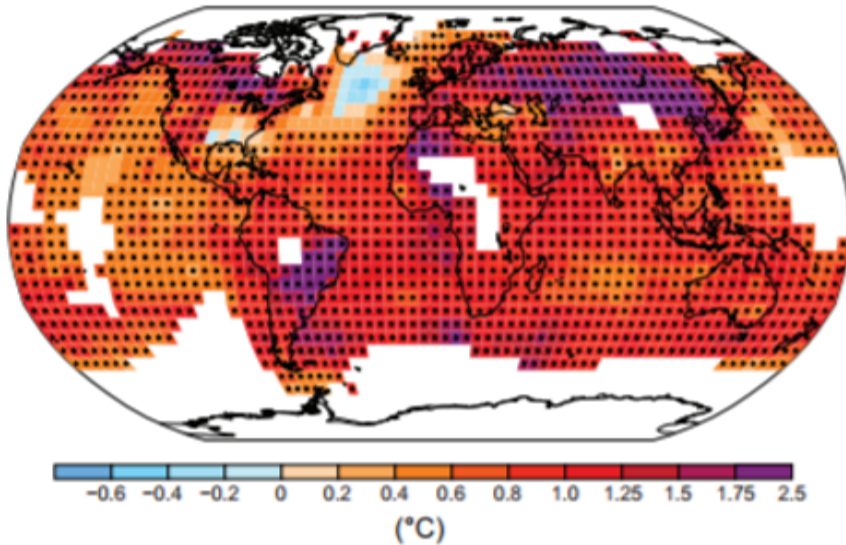


Figure 1.2: Observed changes in surface temperature between 1901-2012 [8]

and pattern of precipitation [8]. Over the years, the increase in atmospheric temperature has led to an even larger increase in water temperature. The rapid ice loss and the thermal expansion of the ocean caused by warmer surface waters are the main causes of sea level rise [3]. It is expected that the sea level rise caused by a global temperature increase of 2°C could compromise food security and could lead to massive population migration from heavily populated coastal communities [9].

Carbon dioxide also reacts with its surroundings. The natural sinks of carbon are plants, by the photosynthesis process, and the ocean, where CO₂ is dissolved to become carbonic acid. Approximately 30% of the atmospheric carbon dioxide goes into water [3], leading to ocean acidification, which has major impacts on the marine ecosystems. For instance, it affects the structure of coral reef and shellfish as carbonate will dissolve at low pH [10]. Some experts claim that climate changes might already be contributing to natural disasters [11].

There is therefore a clear need for substantial and sustained mitigation efforts to limit climate change before it leads to irreversible damages. Mitigation pathways give rise to technological, economic, social and institutional challenges, and no single solution is sufficient on its own [12]. On November 4th 2016, 168 countries ratified the Paris agreement, and set goals regarding GHG emissions, adaptation and finance starting in 2020 [13]. It was agreed for all participating countries to contribute to holding the temperature increase below 2°C above pre-industrial level. This is a daunting

challenge given the lack of progress in mitigating CO₂ emissions so far, and even more so since the withdrawal of the USA in 2017. According to Meinshausen and co-workers [14] burning all proven and recoverable fossil fuels would definitely jeopardize the temperature target. Facing all the evidence regarding climate change, global warming and GHG emissions, the transition to renewable energies is crucial.

As presented in Figure 1.3, oil, coal and natural gas represent around 86% of the total energy consumption. Hydroelectricity and nuclear energy, which are more established and mature technologies, hold 11% of the total energy production. Other renewable energy sources like solar and wind are only responsible for 3%. The development of renewable energy technologies like solar and wind is of great interest as it holds the potential to mitigate carbon emissions. Any future renewable technology needs to be scaled to the terawatt (TW) level in order for it to compete with fossil fuels [15]. Solar energy is, therefore, among the most promising types of renewable energy [15,16]. The sun hits the Earth with 173 kW, out of which 30% is reflected by the Earth's surface, and another portion is used to maintain life. Nevertheless, if we compare this value to the global power consumption of 2015 (17.4 TW), the great potential for the sun to become one of our main energy sources is clear. Experts estimate that wind has the potential to provide us with 25 to 70 TW [15], which makes wind energy another promising candidate.

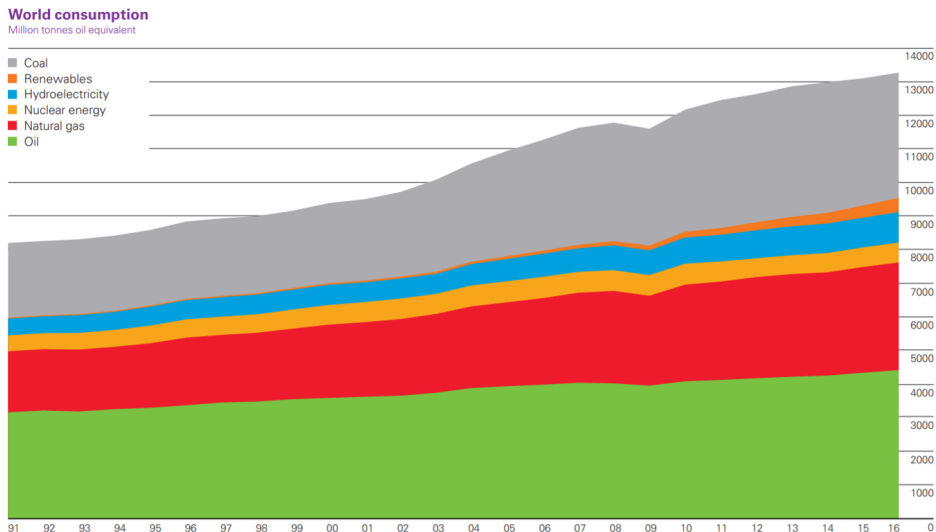


Figure 1.3: World primary energy consumption of coal, renewables, hydroelectricity, nuclear energy, natural gas and oil in million of tonnes oil equivalent [2]

One of the main challenges associated with the use of solar and wind

energy is the fluctuation in energy output that has to match the demand in electricity, that also varies considerably. Figure 1.4 shows an example of the pattern of wind energy production and total energy demand/consumption for a period of 14 days, in September 2016, in Denmark. In this Figure, energy demand changes of around 3.5 GW is observed. The fluctuations in the energy demand are related to the differences of energy required during the day (maximum) and night (minimum). On the other hand, the power generated by wind energy varies greatly over the same period of time, and, most importantly, does not always match the energy demand. To solve this problem, the energy has to be converted and stored with minimized losses, and made available when needed.

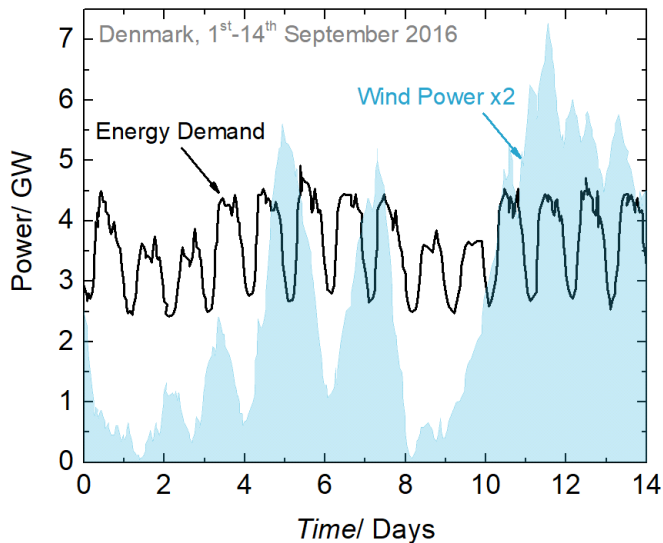


Figure 1.4: Energy demand and wind power production over time for a two week period in September 2018, Denmark. The energy demand represents the energy demand and the blue-shaded area the power production multiply by factor of 2. Data from [17]

Electrical energy storage allows electricity production to be decoupled from the energy demand by a large-scale energy storage that can be used at any time. There are many different energy storage technologies including electrical, mechanical, chemical and thermal [18,19]. Hydrogen fuel cell technology is a chemical energy storage technology that has received increased attention in the last years. Some of the reasons behind this growing interest are the high gravimetric energy density of hydrogen, the fact that

it can be implemented on a wide range of scales, and that the capacity can easily be adapted over time [19]. Most importantly, hydrogen-based energy storage systems can be efficiently coupled to renewable energy technologies.

1.2 Electrochemical Energy Conversion

The conversion of energy coming from renewable sources in chemical bonds represents a big challenge. Hydrogen and electricity are complementary energy carriers as electrical energy can be converted to hydrogen, and vice-versa. This chapter will firstly serve as an introduction to hydrogen production using electrolyzers. Secondly, the reverse process will be addressed, i.e. when hydrogen is used to produce electricity via fuel cell technology. Apart from introducing the basic concepts of these technologies, the focus will primarily be on the limiting reactions, i.e. the oxygen evolution reaction (OER) and oxygen reduction reaction (ORR) for hydrogen production and conversion, respectively. The recent advances of the electrode catalysts with the highest performance will be presented, with emphasis on the types of materials investigated in this thesis.

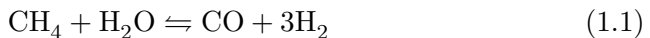
1.2.1 Why Hydrogen as Energy Carrier?

Global warming is shifting the world's energy focus to renewable and zero carbon footprint energy sources. The majority of the world's energy consumption today comes from fossil fuel resources [2]. If the global population wants to turn to carbon-free emission sources, what are the options? Here, I present hydrogen as energy carrier. I introduce briefly why a hydrogen-based economy is an attractive option, and what the challenges related to it are.

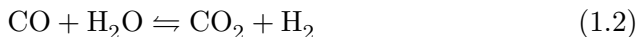
Hydrogen is a very attractive chemical compound with a high gravimetric energy density. The best energy storage systems allow up to 1.3 kWkg^{-1} to be stored compared with 0.2 kWkg^{-1} for Li-ion batteries [5]. To improve hydrogen storage, the challenge is to reduce the large volume that H_2 occupies. The most common way of storing hydrogen is with high-pressure gas cylinders. However, the low hydrogen density, together with high pressure, leads to leakage problems. Hydrogen is not found in nature in a diatomic form, and has to be synthesized. Approximately 50 billion kg H_2 is produced per year globally, which makes it one of the world's most important chemical [20]. It is an extremely important compound in the chemical industry. Hydrogen finds application in the refining industries; it is actively used in petroleum recovery and refining [21]. The other major use of hydrogen is ammonia synthesis for fertilizer production via the Haber-Bosch process [22]. In the eventual development of a hydrogen economy, hydrogen

could also have other really important functions. This clean and non-toxic chemical species also has the potential to be produced in larger scale for application in transportation, other industry related processes and in the heat sector. Indeed, hydrogen offers the possibility of decentralized power production. Storage of energy can help buffer the electricity system, thus helping the integration of variable renewable energy sources by enhancing system security.

As dihydrogen molecule cannot be found in nature, it must be produced from diverse sources. Many hydrogen production technologies exist in different stages of development. Nowadays, approximately 96% of the hydrogen comes from fossil fuels [4,23], where steam reforming and partial oxidation of hydrocarbons are the main production methods. Steam reforming with natural gas is also the cheapest source of hydrogen [24]. Using a Ni-based catalyst, steam reacts with methane to form hydrogen, as described in equation (1.1).



From this, additional hydrogen can be formed via the water-gas shift reaction:



Among the main disadvantages of using steam reforming to produce hydrogen, there is the massive amount of CO/CO₂ emitted. Including all processes, 500 megatonnes CO₂ are emitted annually for hydrogen production [25]. In addition, the process requires a huge amount of energy (heat) to drive the reaction, and large installations. Also, the hydrogen produced from steam reforming is contaminated with CO, which can be problematic for some fuel cell technologies because of catalyst poisoning/deactivation. As one of the main point of interest in developing a hydrogen-based energy system is to reduce the greenhouse gas emissions, steam reforming is not the ideal option. Photolytic processes, another way of producing hydrogen, includes biological and photoelectrochemical production. Currently, production of hydrogen using water only represents 4% of the total production [26]. However, electrolysis of water is very promising on the long run as it could help us reach the atmospheric CO₂ concentration goals. The main advantage of hydrogen production using (photo)electrochemical processes is that it can use renewable energy like wind and solar to oxidize water.

The development of a hydrogen economy requires large-scale and carbon free hydrogen production such as electrolyzer, and technologies that allow re-conversion of H₂ into electricity like fuel cells, on top of distribution

infrastructures [24]. It is a real challenge, as it has to be cost competitive with the existing infrastructure of fossil fuels energy.

1.2.2 Overview of Electrolyzer Technologies

The solutions to our global energy crisis will consist of many different energy storage and conversion technologies. Electricity generation by wind and solar photovoltaics are technologies that are seeing market penetration [20]. However, wind and solar are inherently more variable and uncertain than oil or coal power stations. Although Denmark is already generating 45% of its electricity from wind [27], technical limitations such as grid stability and reliability prevent high penetration rates worldwide. The electrochemical synthesis of hydrogen using intermittent energy sources as buffer to overcome these fluctuations is definitely one promising pathway. The low temperature and fast start-up time of electrolyzers are particularly well suited towards coupling with renewable energies. In this section, both alkaline and polymer electrolyte membrane (PEM) electrolyzers are presented.

During water electrolysis, water is split into its components, hydrogen and oxygen, by applying a current/voltage. This process allows conversion of electricity into chemical energy, and the technology uses up to 100 cells in a parallel circuit to deliver higher rate of hydrogen [26]. The efficiency can be modulated by changing the applied current/voltage. Two types of electrolyzers are introduced: alkaline and PEM electrolyzers. Schematics of the two systems are presented in Figure 1.5. The first one uses alkaline electrolyte while the latter functions under acidic conditions.

Alkaline electrolysis is a mature technology used since the 19th century [29]. The commercial device shows stable performance for up to 15 years with an efficiency ranging from 40 to 80% [26]. Two electrodes are immersed in a caustic potash alkaline electrolyte. The electrolyte is a key component; it provides ionic conductivity and is electronically insulating. As shown in Figure 1.5, left panel, a diaphragm that keeps the gas products apart from each other, separates the cathode and the anode compartments. H_2O is reduced at the cathode and H_2 is produced. OH^- migrates through the diaphragm on the anode side, and is oxidized to O_2 . Alkaline electrolyzers operate at low temperature, between 40-90°C. The typical cathode material is based on nickel nanoparticles supported on carbon. The anode material is usually composed of an alloy of Ni with Co and/or Fe. The maturity, and the cheap and abundant catalysts used are the main advantages of this technology. There are three main downsides to alkaline electrolyzer [28]. Cross-diffusion of H_2 is one of them, since it limits the efficiency, and most importantly represents a safety risk if the concentration of H_2 in O_2 reaches 2 vol.%. To avoid a system shutdown for safety reason, the device has to

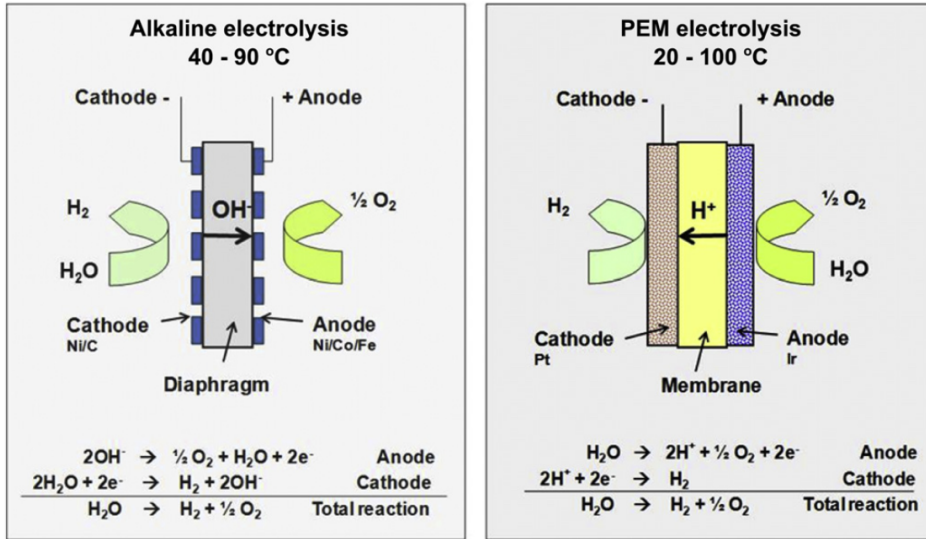


Figure 1.5: Schematic of the operating principle of an alkaline and PEM water electrolysis cell. Taken from [28]

operate at low partial load range. An additional drawback of this technology is the limited current density caused by the high ohmic resistance across the liquid electrolyte and diaphragm. Finally, the device cannot be operated at high pressure, which results in a massive stack design. It should also be noted that while the overpotential for the oxygen evolution reaction is similar in acid and alkaline electrolyte, the hydrogen evolution kinetics are poorer in alkaline [30].

PEM water electrolysis cell was developed to overcome the drawbacks of the alkaline electrolyzers [28,31]. It uses acid electrolyte and a polymer electrolyte that allows very low gas crossover. Typically, the membrane is made of Nafion[®] or fumaprem[®]. The membrane is responsible for providing proton conductivity from the anode to the cathode side. The PEM electrolyzer also has a high operating pressure that enables the design of a compact device [26]. However, due to the strongly oxidizing conditions, only noble metals can be used as electrode materials. Pt is the best catalyst for the hydrogen evolution reaction [32], and requires very low loading [33]. IrO_x- and RuO_x-based catalysts are the most active materials for the oxygen evolution in acid [34,35].

Figure 1.6 compares the voltage efficiency as function of the current densities the alkaline and PEM electrolyzers. For both devices, the hydrogen production efficiency decreases with current density while the hydrogen production rate increases. For a specific cell geometry, this means that there

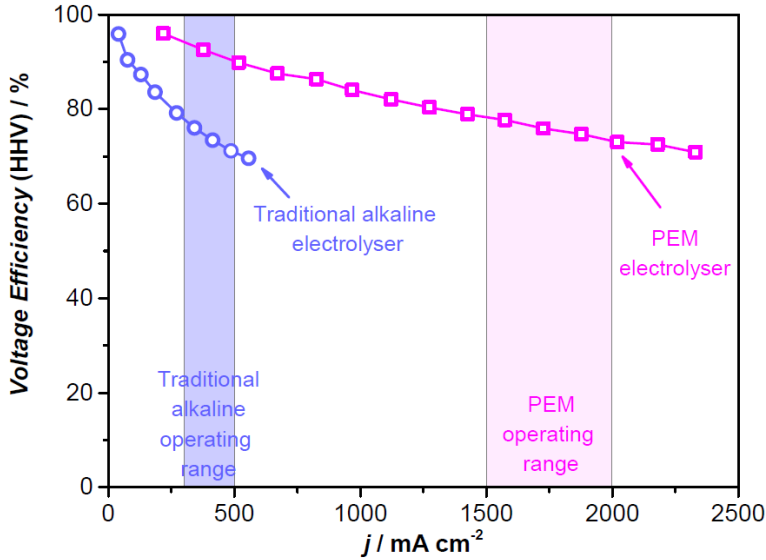


Figure 1.6: Operational ranges of the alkaline (blue) and polymer electrolyte membrane electrolyzers (pink). The voltage efficiency is plotted as a function of the current density and their respective operating range is highlighted. Data for this figure has been adapted from [31].

is a trade-off between the amount of hydrogen one wants to produce and the efficiency of the device. This decrease is associated to mass transport limitation and ohmic resistance. For traditional alkaline electrolyzers, current density between 0.25 and 0.5 A/cm² can be delivered when operating at an efficiency between 70 to 80%. In comparison, for a similar efficiency, PEM water electrolyzers can achieve between 1.5 to 2 A/cm². From this, we can deduce that while alkaline electrolyzers are a mature and low-cost technology, PEM electrolyzers show a greater potential to increase efficiency and reduce capital investments [25] due to the higher current density and broader operational range.

Figure 1.7 shows the overpotential that goes for OER and HER in an alkaline electrolyzers. While high current density for the hydrogen evolution reaction can be achieved at relatively low overpotentials, it has been shown that the majority of the losses in water electrolyzers can be traced back to the oxygen evolution reaction [36,37]. For that reason, and because catalysts dissolve under OER conditions, more effort is needed toward the development of active and stable OER catalysts.

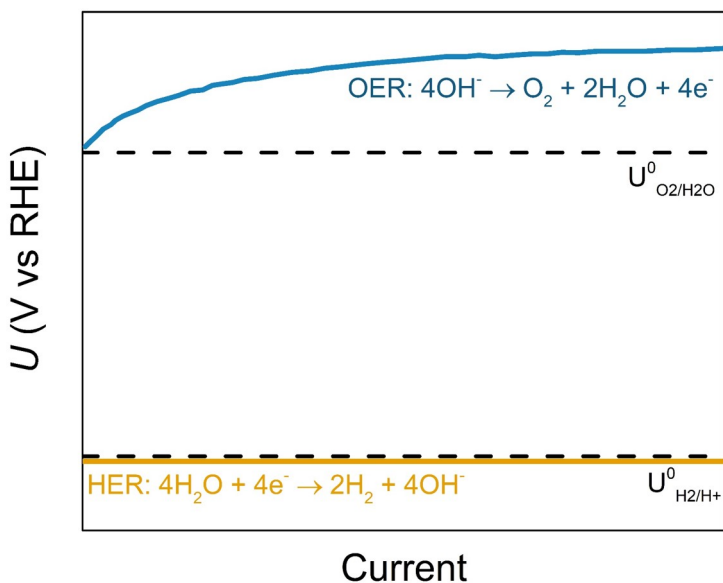


Figure 1.7: Schematic of the overpotentials associated with oxygen evolution and hydrogen evolution reactions taking place in alkaline electrolyzers. Adapted from [37]

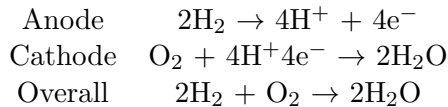
1.2.3 Polymer Electrolyte Membrane Fuel Cell

The requirements of new energy storage technology, for instance through water electrolysis, also involves the development of efficient ways to convert chemical energy into electrical energy. As such, the use of hydrogen as an energy carrier is closely linked to the deployment of electrolyzers and hydrogen fuel cells. Fuel cells are the technology that converts hydrogen, with oxygen from the air, into electricity and forms water as side-product. There are several types of fuel cells currently under development, such as solid oxide, polymer electrolyte membrane, direct methanol, alkaline, phosphoric acid, molten carbonate and reversible fuel cells [38]. Polymer electrolyte membrane fuel cell (PEMFC) is an attractive technology mainly because of its low operating conditions and quick start-up and load following, among others.

Hydrogen fuel cell technology can be integrated to cars where it could mitigate CO₂ emissions related to transportation. Indeed, hydrogen fuel cells can be used to propel fuel cell electric vehicles (FCEVs), a carbon-free technology. FCEVs are electric vehicles using hydrogen stored in pressurized tanks, with a fuel cell for direct conversion into electricity. The first FCEVs were developed in the 1960's [25], but it is only in the last 10 years that the technology has developed to the extent that FCEVs were commer-

cialized for light duty passenger vehicles. Besides light duty passenger cars, hydrogen for application in transport has a promising future in light duty fleet vehicle and heavy-duty trucks, public transportation, non-electrified trains and maritime transport because of the fast recharging time of fuel cell. Hydrogen fuel cells can also be used in other end-use applications related to buildings and industries for heat or electricity production. Indeed, co-generation of power and heat by fuel cells is particularly attractive in the building sector as it can significantly increase the overall energy efficiency [25]. Compared to the 45-50% electric energy efficiency in FCEVs, stationary fuel cells can reach up to 95 % energy efficiency [39], mainly because it can use the heat being generated.

The basic principles of hydrogen fuel cell is simple: The hydrogen and oxygen are recombined, and an electric current is produced. The recombination of the hydrogen and oxygen is an exergonic reaction, but instead of heat energy being liberated, it is electric current that is produced [40]. To understand how an electrical current is produced, we need to look at the two half-cell reactions:



The oxidation and reduction reactions taking place at the anode and cathode, respectively, are illustrated in Figure 1.8, where a schematic of a PEMFC is shown. The reaction at the anode of an acid electrolyte fuel cell consists of ionizing two H_2 molecule into four H^+ , which liberates four electrons. The electrons travel trough an external circuit and will recombine on the cathode side with O_2 and the protons, that diffused through the polymer electrolyte membrane, to form water.

A measured polarization curve from Pt catalysts in PEMFC is shown in red in Figure 1.9. From this, one can observe that the open circuit potential is less than the theoretical value (1). A rapid loss in potential is then observed (2) before the voltage starts falling more slowly and linearly (3). There are few causes of voltage drops including activation loss, ohmic losses and mass transport or concentration losses [40]. At 1.5 A/cm^2 , the potential difference with the thermodynamic potential (green line) is significant. The fuel cell potential is of 0.57 V compared to 1.17 V for the ideal case. The blue curve represents the overpotential of the ORR, and accounts for 70% of the total potential loss. This indicates that most of the losses come from the sluggish kinetic of the ORR, and the design of more active catalysts is key for the increase in efficiency.

The U.S. Department of Energy (USDOE) cited durability and cost as the two main factors limiting the commercialization of hydrogen fuel cells

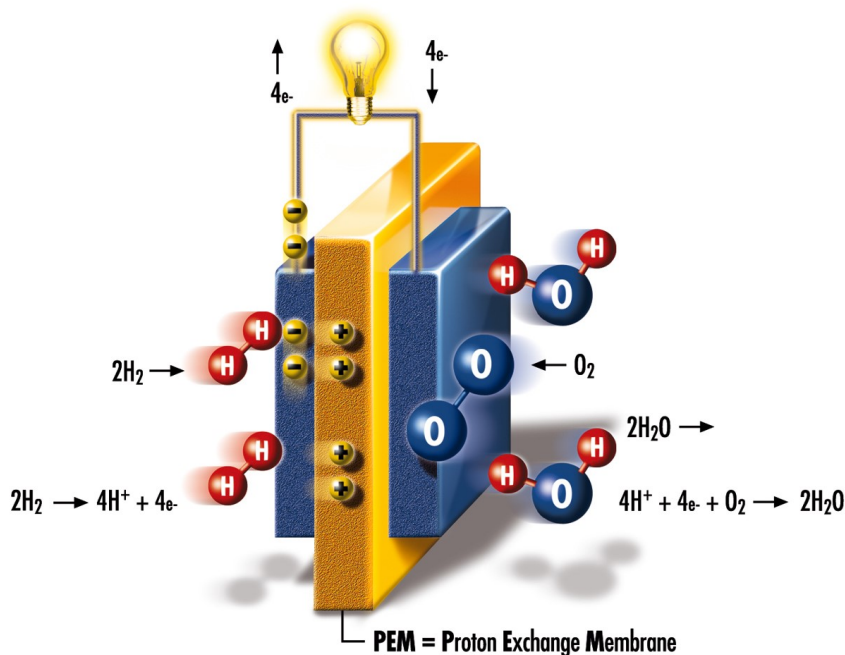


Figure 1.8: Schematic of a polymer electrolyte membrane fuel cell [41]

[4]. Platinum is the best pure metal catalyst for both the hydrogen oxidation reaction and the oxygen reduction reaction taking place at the anode and cathode, respectively. The platinum loading of state-of-the-art fuel cell requires ~ 0.5 mg Pt per cm^2 which results in 50 g Pt per 100 kW vehicle [42]. Using the present technology, and should the 200 tons of Pt produced annually being dedicated only to FCEVs, only four million cars could be manufactured. In comparison, the worldwide automobile production was of 72 millions in 2016 [43]. As platinum is a very scarce and expensive material, the Pt loading really needs to be decreased for the deployment and economic viability of fuel cell vehicles. The anodic reaction, where the hydrogen oxidation reaction takes place, is not the main concern as 0.05 mg Pt per cm^2 of electrode area is necessary, compared to 0.4 mg Pt per cm^2 for the ORR [33]. Similarly to OER, it is highly challenging to find a metal catalyst for ORR that will have stable performance over time due to the acid electrolyte and oxidative potentials under reaction conditions [44–46].

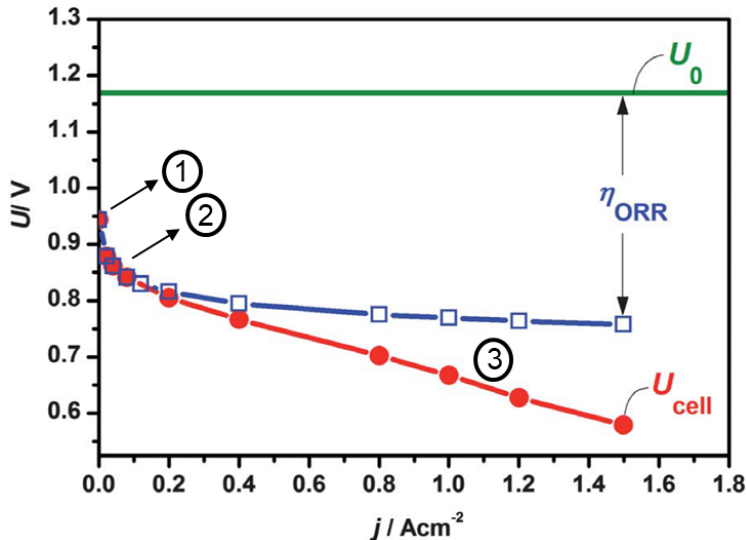


Figure 1.9: Polarisation curve of a state-of-the-art fuel cell. Operated at 80°C, at a total pressure of 150 kPa H₂/O₂. Adapted from [47], [48] and [40]

1.3 Thesis Outline

My PhD work includes the chemical synthesis of Pt-rare-earth alloys for the oxygen reduction, but also in a more general manner the electrochemical testing of new catalysts for the oxygen evolution and reduction reaction. For all studies presented in this thesis, I have collaborated extensively with other researchers. I will depict the whole story but focus will be put on my contribution to the work.

Chapter 2 introduces the relevant parts of the field regarding the oxygen evolution and reduction reaction.

Chapter 3 presents the pertinent experimental methods for a good understanding of the results presented in this thesis.

Chapter 4 explores the electrochemical stability of rutile ruthenium oxide particles and well-defined surfaces for the oxygen evolution in acid electrolyte. The deposition of the RuO₂ oriented thin film electrodes was performed at MIT-EEL by Reshma R. Rao and Jonathan Hwang. I performed the stability measurements and the ICP-MS analysis, and participated to the analysis of the results.

Chapter 5 presents our work on the investigation of NiFeO_xH_y nanoparticles for the oxygen evolution in alkaline electrolyte. The design of the experiments was done by Béla Sebök, former PhD student, and myself. I did all the electrochemical measurements related to this work, except for the isotope labeling experiments, which were performed by Søren Scott, PhD

student. The extensive physical characterization work was performed by Béla Sebök and the electron microscopy part by Elisabetta Maria Fiordaliso, Postdoc at the Center for Electron Nanoscopy at DTU.

Chapter 6 reports the work on the chemical synthesis of Pt_xY alloys on a gram scale. For the alkalide and cyanide reduction synthesis, the work was done in collaboration with a former postdoc at DTU Physics, Amado Andres Velazquez-Palenzuela. The alloys synthesized using thermal annealing was mostly developed by Brian Knudsen and Christoffer Pedersen during their PhD work. My contribution to this work was to follow their protocol and gain information through physical characterization. I was also involved in verifying their hypothesis made using thermodynamic calculations by doing thermal synthesis connected to the mass-spectrometer. Also, I did most of the physical characterization presented in this thesis, as well as the electron microscopy part. Lastly, Amado Velasquez also greatly contributed to this work by doing some of the electrochemical measurements.

Chapter 7 summarizes the main conclusions from my PhD work and provides directions for future research.

Oxygen Electrocatalysis

2.1 The basics of (Electro)Catalysis

This chapter introduces the basic concepts of catalysis applied to oxygen electrochemistry. The notions presented here were chosen with the aim to aid the understanding of Chapter 4, Chapter 5 and Chapter 6.

2.1.1 Thermodynamics of Electrode Reactions

The energy input in electrochemical reactions is the potential difference over two electrodes, ΔU [49]. This difference in potential drives the transfer of protons and electrons, hence influencing the reaction rate. For an electrochemical reaction to take place, electrodes have to be immersed in a highly conductive electrolyte. An electrochemical reaction is divided into two half-reactions, i.e. a reduction and an oxidation reaction, each taking place at their respective electrode. The electrode where the oxidation takes place is called the anode, and the electrode where reduction takes place is called the cathode. As formulated in equation (2.1) [50], the equilibrium potential, U_{cell} , depends on the change in Gibbs free energy, ΔG_f , the number of electrons exchanged in the reaction, n , and the Faraday constant, F :

$$U_{cell} = \frac{\Delta G_f}{nF} \quad (2.1)$$

Let us consider the following generic electrochemical reaction:



The change in Gibbs free energy for a reaction varies with temperature and pressure, and can be represented as function of the standard change in Gibbs free energy, ΔG_f^0 :

$$\Delta G_f = \Delta G_f^0 - RT \ln\left(\frac{a_B^b \cdot a_D^d}{a_M^m}\right) \quad (2.3)$$

Where R is the gas constant, T the temperature, and a , the reactant activity. The reactant activity is defined as function of the pressure, P , and standard pressure, P_0 , as: $a = \frac{P}{P_0}$. The Nernst equation can be obtained by combining equation (2.1) and (2.4), giving:

$$U_{cell} = U_{cell}^0 - RT \ln\left(\frac{a_B^b \cdot a_D^d}{a_M^m}\right) \quad (2.4)$$

The Nernst equation is useful to determine the minimum change in voltage to drive a non-spontaneous electrochemical reaction [49]. Often, if not always, the operating potential deviates from U_{cell}^0 . As presented in equation (2.5), the minimum voltage required to drive a reaction depends on different parameters:

$$U_{cell} = U_{cell}^0 \pm iR \pm \eta_{mt} \pm \eta_a \quad (2.5)$$

That includes, the standard potential, the ohmic drop (iR), the mass transport overpotential (η_{mt}), and the activation overpotential (η_a).

The standard potential is specific to the reaction occurring at the surface. The ohmic losses are the resistance to the flow of electrons through the material of the electrodes, as well as the resistance to the flow of ions through the electrolyte. The mass transport or concentration losses result from the change in the amount of reactant molecules reaching the surface. Finally, the activation overpotential can be reduced through the optimization of the catalyst, since it is a kinetic parameter [40]. The work presented in this thesis mainly concerns the optimization of the activation overpotential by optimizing the catalyst electrode.

2.1.2 Role of a Catalyst

A catalyst is defined as a substance that accelerates a chemical reaction without undergoing any permanent changes itself [51]. A catalyst strictly affects the kinetics, and does not have any impacts on the thermodynamic equilibrium. The analogy in Figure 2.1 illustrates this concept. Let us assume one takes a walk to go from point A to point B. The difference in elevation between point B and A is correlated to the reaction thermodynamics, which cannot change. On the other hand, the pathway to get from A to B, in this case, the reaction kinetics, can be influenced by the catalyst.

The catalyst accelerates a reaction by forming bonds with the reactants. The molecules undergo changes, going through reaction intermediates, before the products detach from the surface. In theory, the same active

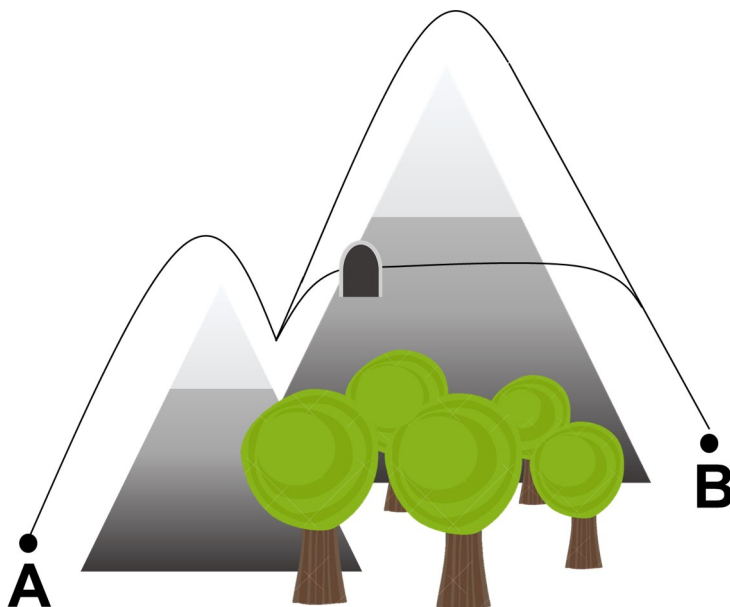


Figure 2.1: Analogy to illustrate the difference between reaction kinetics and thermodynamics

site can undergo this reaction cycle without being affected. The reaction rate depends on the potential energy diagram (Figure 2.2), where the non-catalytic and catalytic reaction are compared. The uncatalyzed reaction can be described by using the Arrhenius equation [51]:

$$k = Ae^{\frac{-E_a}{RT}} \quad (2.6)$$

where E_a is the activation barrier, T the temperature, R the gas constant, and A a constant. The reaction will proceed when there is sufficient energy to overcome the energy barrier. If a reaction is catalyzed, the reactants bond first to the catalyst, through a spontaneous reaction. The reaction proceeds at the surface of the catalyst. The activation energy in that case is smaller than the non-catalyzed activation energy, i.e. ${}^*E_a < E_a$. Once the reaction is completed, the products desorb from the catalyst in an endothermic step.

In thermal catalysis, the reaction is initiated through high pressure and high temperature. In electrochemical reactions, it is by applying voltage/current that the reaction is favored [49]. Using density functional theory calculations (DFT), Rossmeisl, Nørskov and co-workers used a thermodynamic approach to explain the origin of the overpotential for both oxygen

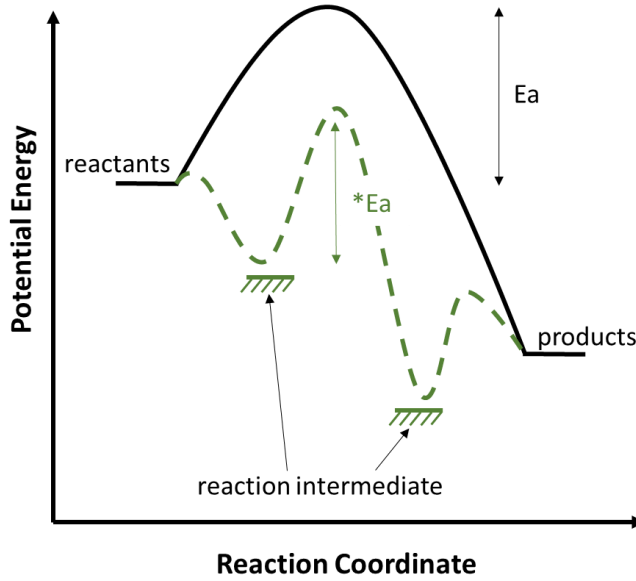
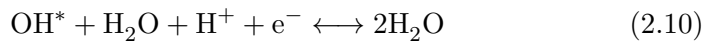
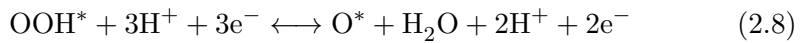
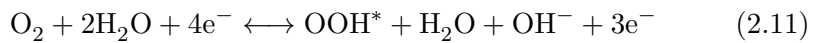


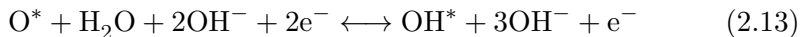
Figure 2.2: Potential energy diagram of an electrochemical reaction, with gaseous reactants and products, and solid catalyst. The uncatalyzed reaction goes over a much considerable energy barrier. Adapter from [51]

reduction [52] and oxygen evolution [53]. For the oxygen reduction reaction (ORR), or inversely, the oxygen evolution reaction (OER), 4 proton-electron transfer steps on single metal sites is assumed. In acidic environment the ORR/OER mechanism is:



Where * denotes surface site. Equivalently, the reaction in alkaline can be written as:





The reaction intermediates (O^* , OH^* , OOH^*) are the same in base and acid electrolyte [54,55]. Each step of the reaction is associated to a specific ΔG . The free-energy diagram for the oxygen evolution on an ideal catalyst is presented in Figure 2.3a. On this ideal surface, the four charge transfer steps are equal resulting in an individual step height of 1.23 eV at room temperature, and a total change in free energy of 4.92 eV, when $U = 0$ V vs RHE. By definition, the overpotential is any deviation from the equal steps.

The free-energy diagram for the ORR on Pt(111) at several electrode potential was calculated [52] (Figure 2.3b). At the equilibrium potential, i.e. $U = 1.23$ V, the barrier for OOH^* formation (ΔG_{OOH^*}) and OH^* reduction (ΔG_{OH^*}) are still uphill in energy. By increasing the overpotential, the driving force the reaction step for each reaction is increase until all the reactions steps become downhill in energy. ΔG_{OH^*} is the potential determining step, which the last step to become downhill in energy. For the ORR on Pt(111), it is at $U = 0.78$ V that all reaction steps are exergonic. Similarly, Rossmeisl and co-workers calculated the free-energy energies of intermediates on RuO_2 for the oxygen evolution at $U = 0, 1.23$ and 1.60 V [53], and the results are presented in Figure 2.3c. According to their findings, it is only at $U = 1.60$ V that they all reaction steps are downhill in energy, and the oxygen is evolved.

According to the free-energy diagram calculated for the ORR on Pt(111) (Figure 2.3b), the ideal catalyst would bind OOH^* more strongly than Pt, but OH^* more weakly. Unfortunately, ΔG_{OOH^*} and ΔG_{OH^*} cannot be varied independently. Because each adsorbate binds the surface via the oxygen atom, it is expected that the too strong binding for O^* also translates for HO^* and HOO^* . The theoretical plot of free energies of adsorption of HOO^* , HO^* and O^* , shows a linear relations, as presented in Figure 2.4. More specifically, the Figure shows that the energy difference between ΔG_{OH^*} and ΔG_{OOH^*} is of ~ 3.2 eV. This difference in energy does not match the one of the ideal case, calculated to be of 2×1.23 eV, which implies that the minimum value for $\Delta G_{\text{OH}^*} + \Delta G_{\text{OOH}^*} \approx 0.8$ eV. As shown in Figure 2.4, for an ideal catalyst, the overpotential is shared equally so that $\Delta G_{\text{OH}^*} = \Delta G_{\text{OOH}^*} \approx 0.4$ eV. Based on these calculation, the best catalyst will have, at least, 0.4 eV in overpotential.

The so called volcano plot is a result of the scaling relation, where the top of the volcano is associated to the ideal catalyst. If the binding is too weak (right side of the volcano), the reactants do not adsorb at the surface of

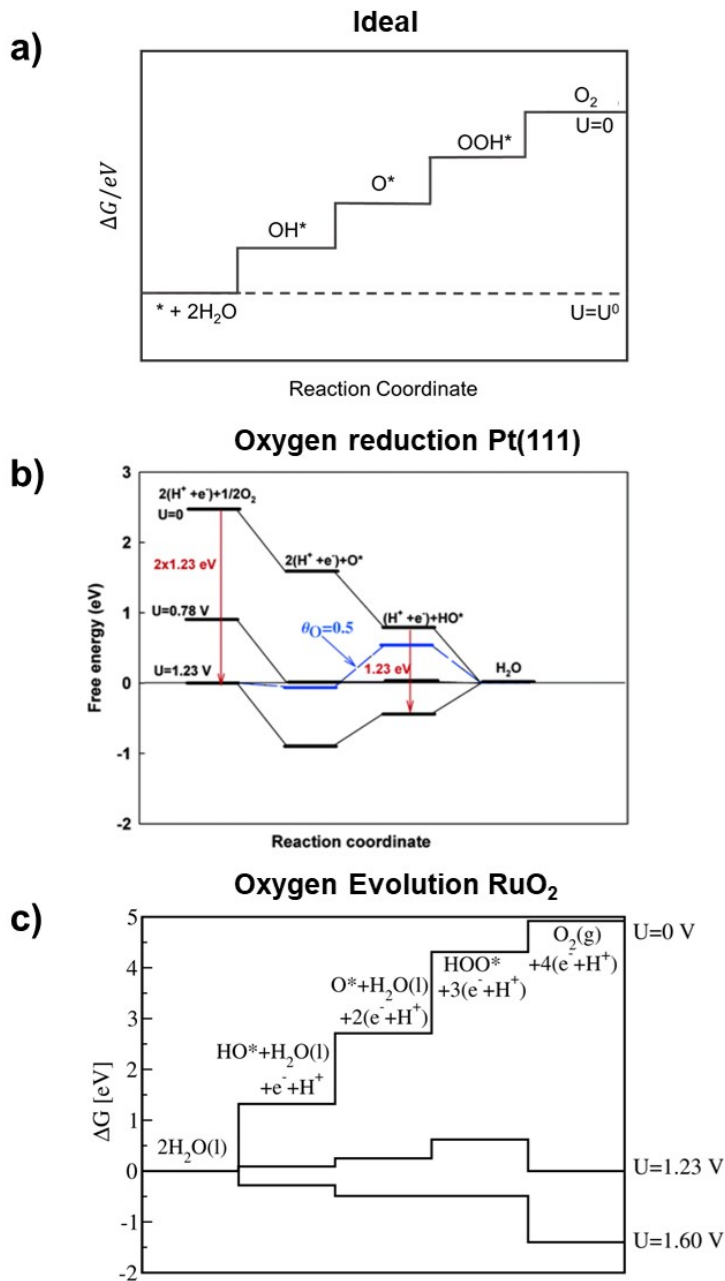


Figure 2.3: Free-energy diagram for a) ideal standard free energy diagram at zero potential ($U=0$ V vs RHE), and at equilibrium potential ($U=E^0$), b) Free-energy diagram for oxygen reduction over Pt(111) for low oxygen coverage are shown at $U=0$, 1.23 and 0.78 V, and c) Free-energy diagram of the OER on O^{*}-covered RuO₂ at $U=0$, 1.23 and 1.60. * represents an active site. a) is adapted from [52,53], b) is taken from [52], and c) is taken from [53].

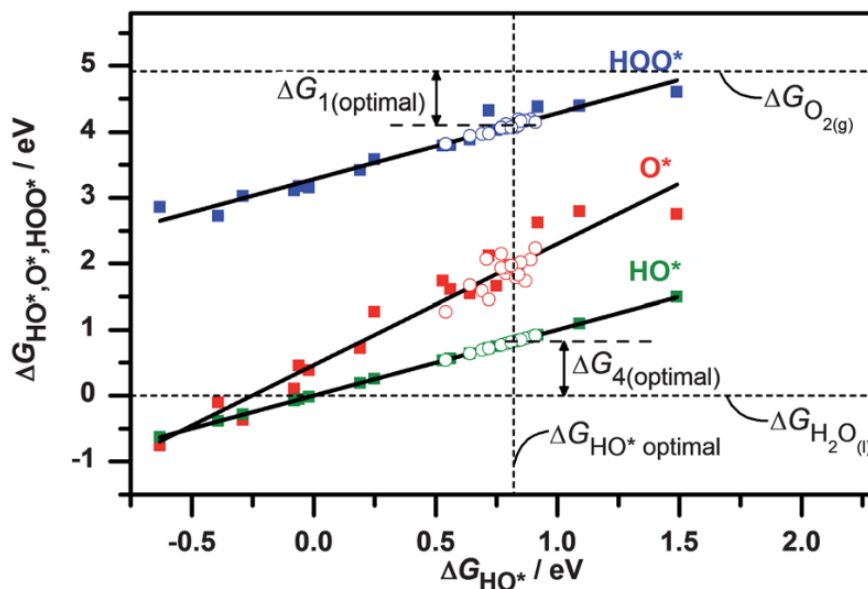


Figure 2.4: Theoretical plot of free energies of adsorption of OOH^* , OH^* and O^* , as a function of ΔF_{OH^*} , for (111), (100) and (211) pure metal surfaces (filled squares), and Pt overlayers on Pt-alloy surfaces (open circles). Figure taken from [53,56]

the catalyst and the reaction does not take place. Conversely, if the binding is too strong (left side of the volcano), the products will not desorb from the catalyst and, therefore, act as a poison. The volcano plots associated to the ORR and OER are presented in Figure 2.5a and b, respectively. The ORR volcano plot plots the theoretical activity measured from DFT calculations as a function of the O binding energy [52]. As presented on this volcano, Pt is the best pure metal catalyst for the ORR. The OER volcano plot for metal oxides in acid and alkaline electrolyte where the overpotential measured for $j=1 \text{ mA/cm}^2$ is plotted as a function of hydroxyl binding energy [57]. The overpotential presented in this OER volcano come from theoretical and experimental data. Figure 2.5b shows that $\text{IrO}_x/\text{SrIrO}_3$ and NiFeO_x have among the lowest overpotential. RuO_x -based catalyst, which is among the most active OER catalysts in acid, was not included in this plot by the author, but should sit very close to the top of the volcano according to previous DFT calculations [53].

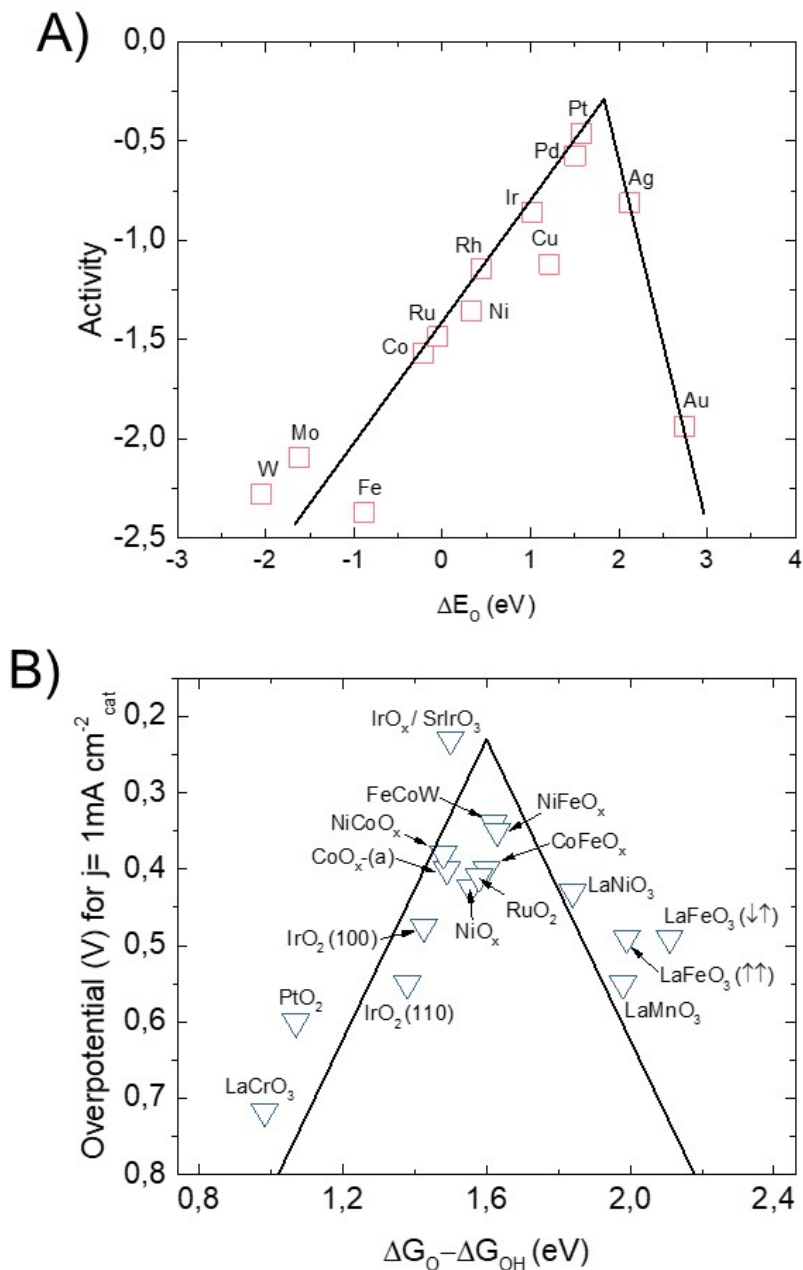


Figure 2.5: a) ORR volcano plot for metals. The ORR activity was calculated from DFT and is plotted as function of the oxygen binding energy. Figure adapted from [52] b) OER volcano plot for metal oxides. The overpotential measured at $j = 1 \text{ mA/cm}^2$, taken from theoretical and experimental data, is plotted as function of the hydroxyl binding energy. Figure adapted from [57].

2.1.3 Catalyst Design

As presented in the previous section, most catalysts bind the reactant intermediates either too strongly or too weakly, hence limiting the reaction rate. The design of more efficient electrocatalysts is a key step in the development of electrochemical devices [51]. There are many approaches that can be used to optimize the binding of the reactants, reactant intermediates and products to the surface of the catalyst. Two main catalytic development strategies can be combined to reach the highest catalytic activity [57]: (i) increasing the total number of active sites, and (ii) increasing the specific catalytic activity of the electrode material.

The first strategy, increasing the total number of active sites, is achieved by increasing the electrochemical surface area of the material, or the loading. The electrochemical surface area can be increased, for example, by using highly porous substrates, like foam, or through the development of high surface-to-bulk ratio catalyst like nanoparticles [51]. However, this approach has a limited impact on the reaction rate as the activity can only increase linearly with the number of active sites. Also, with high material loading, charge and mass transport rapidly become physical limitations.

The other way of increasing the overall catalytic activity is to increase the specific catalytic activity of the electrode material. This strategy is much more appealing as it can lead to orders of magnitude increase in specific activity. To increase the specific catalytic activity, the binding energy of the molecular species to the surface needs to be tuned. An atomic-scale understanding of phenomena in electrochemistry is intimately tied to the electronic structure of the electrode's surface.

The electronic structure of a material can be alter via strain and ligand effects [58,59]. The binding energy of the molecular species to the surface can be tuned via alloying. When a metal is alloyed with another one, its electronic structure is modified by solute metal atoms of a different composition. The internal energy can be modified when the molecule is strained, which in turn also changes the electronic structure [60]. Strain effect can be explained via the d-band model, where a compression/extension in the lattice parameter of a metal will lead the a shift in the d-band centre, resulting in a surface that binds more strongly/weakly the adsorbates [60]. Let us take two example where the ligand and/or strain effects changes the surface's binding energy.

Near-surface alloy (NSA) of Cu/Pt(111) was investigated by Chorkendorff [61], and Stephens [62] and co-workers for the ORR. They showed, using cyclic voltammetry, a lower OH adsorption on NSA Cu/Pt(111), which translated into a weaker binding for *H, *OH and *CO, compare to Pt(111). They ORR electrochemical measurements also show higer activity for the

NSA Cu/Pt(111) than for Pt (111). The weakening effect can be attributed to both ligand and strain effects, as these effects cannot be distinguished.

As second example, let us take the case of a platinum nanoparticle, as shown in Figure 2.6. The (111) and (100) facets, as illustrated, have different coordination numbers (CNs). The (111) surface is a close-packed surface with a CN of 9. In comparison, the (100) is a more open surface with a CN of 8. Terraces, kinks and steps also exhibit different CNs, the most uncoordinated surface being the kink sites. An atom with fewer neighbors results in an upshift of the d-band centre, resulting in a surface which binds more strongly than unstrained Pt.

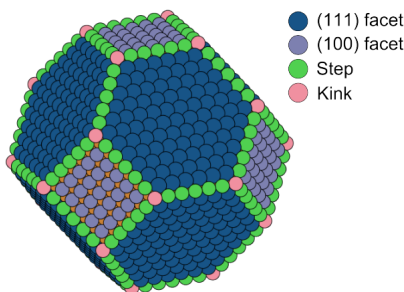


Figure 2.6: Schematic of a nanoparticles where the (111) sites are in blue, (100) sites in purple, steps in green and kinks in pink. Taken from [63]

2.2 Overview of Promising OER Catalysts

This section presents a short overview of the state-of-the-art OER catalysts in acid and alkaline. This overview of the literature is oriented towards the types of materials investigated during this PhD work.

2.2.1 Acid OER Catalysts

Figure 2.7 shows an overview of the most active catalysts in acid electrolyte for the OER. Finding an efficient OER catalyst well-suited for application in PEM electrolyzers is a great challenge, because few catalysts are stable at low pH under experimental conditions. As shown in Figure 2.7, only IrO_x- and RuO_x-based materials show decent activity under these conditions. They are the only materials that can reach $\sim 5 \text{ mA/cm}^2_{\text{oxide}}$ for potentials lower than $2 V_{RHE}$ [30]. As shown in Figure 2.7, the oxidation pretreatment of these materials has a strong impact on their performance. In most cases, Ir and Ru become less active once oxidized. This is observed, for example for the Ru, RuO₂, Ir and IrO₂ thin films reported by Cherevko

and co-workers (Referred as [c] in Figure 2.7) [64]. The most active Ir-based material ever reported is $\text{IrO}_x/\text{SrIrO}_3$ [65]. According to density functional theory (DFT) calculations [65], the high catalytic activity is associated to the formation of IrO_3 or IrO_2 anatase motifs when strontium leaches out. IrO_x is a state-of-the-art OER catalyst in acid electrolyte because of its high catalytic activity and as it corrodes less than RuO_x [64].

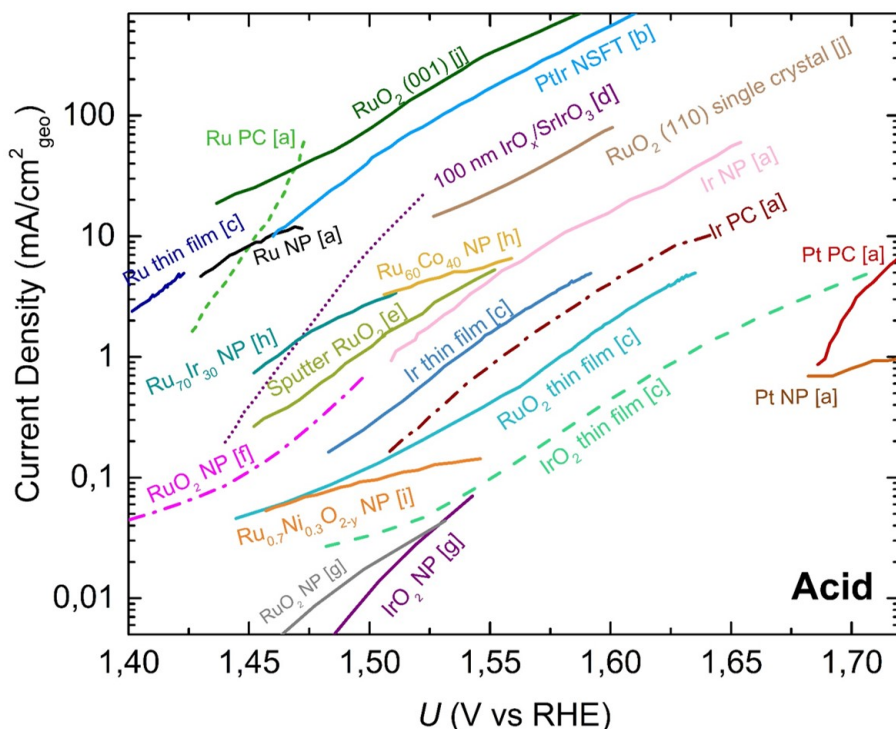


Figure 2.7: Overview of the state-of-the-art for the oxygen evolution reaction: a) In acid media. Data adapted from: [a] for Ru, Ir and Pt polycrystalline (pc) and nanoparticles (NP) [66] [b] for PtIr nanosctruted thin-films (NSTF) [67], [c] for Ru, RuO_2 , Ir and IrO_2 thin films [64], [d] for 100 nm $\text{IrO}_x/\text{SrIrO}_3$ [65], [e] for sputter RuO_2 [68], [f] for RuO_2 NPs [34], [g] for RuO_2 and IrO_2 NP [69], [h] for $\text{Ru}_{70}\text{Ir}_{30}$ and $\text{Ru}_{60}\text{Co}_{40}$ NP [70], [i] for $\text{Ru}_{0.7}\text{Ni}_{0.3}\text{O}_{2-y}$ [71] and [j] for RuO_2 oriented thin film and RuO_2 (110) single crystal (This work).

To the best of our knowledge, metallic Ru is the most active material reported so far [34,36,64]. Stoerzinger and co-workers demonstrated that the ability of a surface to oxidize OH^- groups into O_2 strongly depends on the crystallographic structure of the rutile RuO_2 [35,72,73]. RuO_2 (001) oriented thin film measured in this work shows among the highest catalytic activity in acid. In comparison, we report a lower activity for RuO_2 (110) single crystal, the most thermodynamically stable surface [35].

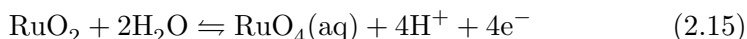
Ir and Ru, both very expensive and scarce materials, can also be mixed with other cheap and abundant elements such as Ni or Co to reach similar performance [70,71]. Another way to decrease the amount of precious metal used is by increasing the surface-to-volume ratio. Stephens, Chorkendorff and co-workers performed a study using a model system, and showed that the diameter of Ru nanoparticle does not strongly affect the catalytic activity [34], which means that the nanoparticles can be optimized to the smallest particle size. Bimetallic Ru-Ir catalysts also present an interesting compromise between higher activity and stability [70,74,75].

Other noble metals such as Au, Pd or Pt could, at first, also seem like interesting candidates because they can resist the harsh environment of PEM electrolyzers. However, they are poor OER catalysts due to the large overpotential required to form an oxide surface layer before the reaction proceeds [55,76]. This is clearly demonstrated by the poor activity of Pt catalysts in polycrystalline and nanoparticulate forms [66].

Because of its exceptional catalytic activity, Ru is often used as benchmark in acid electrolyte. Shao-Horn and co-workers worked intensively on the understanding of the mechanism and active sites responsible for the high activity of rutile RuO₂ catalysts for oxygen evolution [35,72,73,77]. Part of their work consisted of studying preferentially oriented thin films obtained by pulsed laser deposition. They recently investigated a broader range of surface orientations, i.e. RuO₂ (100), (101), (110) and (111). Schematics of these rutile structures are presented in Figure 2.8A-D. In their work, they could correlate the density of active sites, namely coordinatively unsaturated Ru sites (CUS) that are identified in gold color in Figure 2.8A-D, to the increase in OER current measured at 1.53 V_{RHE}, as shown in Figure 2.8E.

They also used these catalysts to investigate the possible participation of lattice oxygen in the oxygen evolution. To do so, they used labelled water, H₂¹⁸O, combined with online electrochemical mass spectrometry. All surfaces tested, i.e. rutile RuO₂ (100), (110), (001), (111) surfaces, and RuO₂ sputter-deposited polycrystalline thin film, showed no evidence of lattice oxygen participation.

Ru-based catalysts are generally more active than Ir-based ones, but also less stable. RuO₂ corrodes according to the following equation:



An overview of the faradaic efficiency (FE) for Ru dissolution during OER, based on OER measurements performed in acid and alkaline electrolyte, is presented in Figure 2.9. The FE to Ru corrosion varies over many orders of magnitude, and is dependant on the pretreatment. The FE

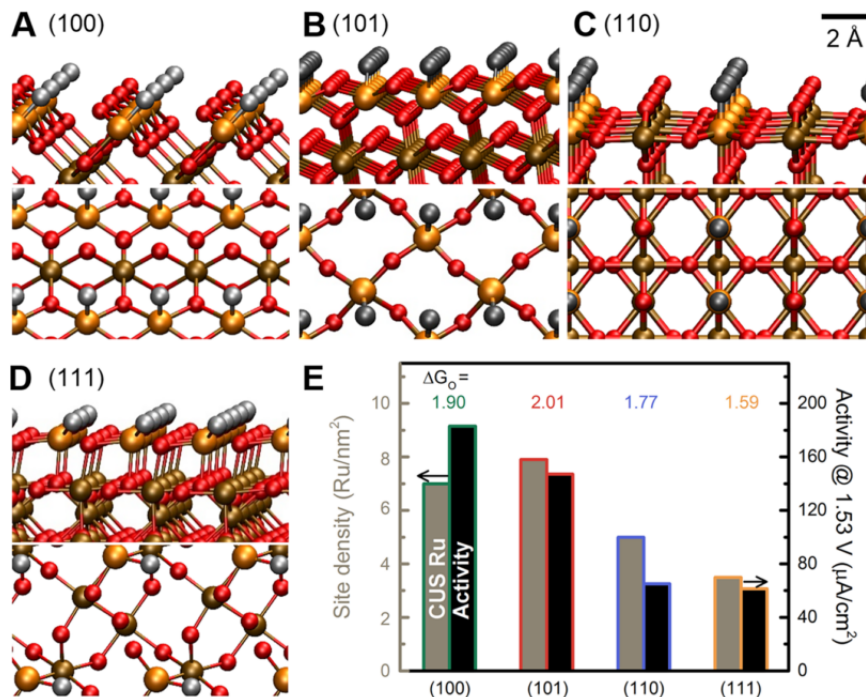


Figure 2.8: RuO₂ oriented surfaces from the side (top image) and from above (bottom image) of the A) (100) B) (101) C) (110) and D) (111). The O atoms are in red, what is define as inactive Ru atoms in brown and the undercoordinated Ru atoms in gold where the O atom on this site is silver. E) Oxygen evolution current measured at 1.53 V_{RHE} (right axis), and the number of undercoordinated Ru per nm² calculated using DFT. The Gibbs free energy per O atoms (ΔG_0 , in eV) is also indicated for each surface. Figure taken from [73].

to Ru dissolution measured for RuO₂ sputter deposited thin films in 0.1 M H₂SO₄ [68] is of 0.01%, while in the case of metallic Ru it reaches FE as high as 15% [34], and 10% for oriented SrRuO₃ in 0.1 M KOH [78]. Figure 2.9 does not show major differences between the FE for Ru corrosion in acid versus alkaline electrolyte. Also, it is not possible to establish any trends between metal dissolution and the current/ potential applied, as the experimental conditions vary significantly for all the studies presented.

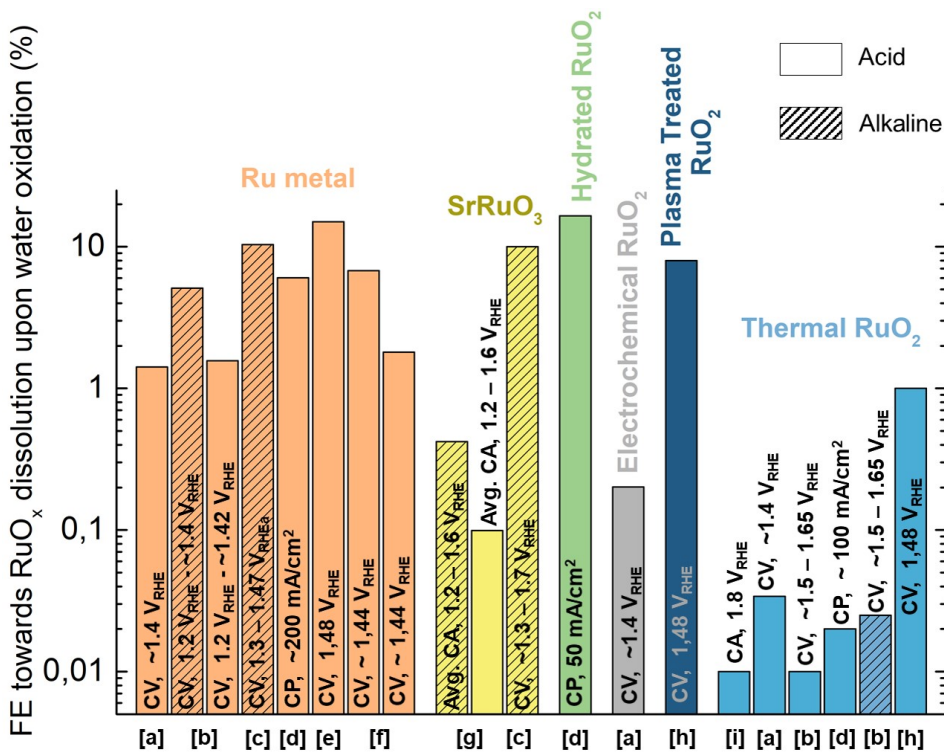


Figure 2.9: Comparison of the faradaic efficiency of dissolution for Ru-based catalysts in acidic and alkaline electrolyte. The faradaic efficiency contributions associated to Ru dissolution during water oxidation, in percentage, were extracted from [a] Hodnik et al. [79] for Ru metal, electrochemically prepared RuO₂ and thermally prepared RuO₂ in 0.1 M HClO₄ [b] Cherevko et al. [64] for Ru metal, and thermally prepared RuO₂ in 0.1 M H₂SO₄ and 0.05 M NaOH. [c] Chang et al. [78] for polycrystalline Ru metal and oriented SrRuO₃ films in 0.1 M KOH. [d] Tamura et al. [80] measured Ru dissolution for Ru metal, hydrous RuO₂ and thermally prepared RuO₂ in 0.5 M H₂SO₄. [e] Paoli et al. [34] for Ru nanoparticles in 0.05 M H₂SO₄. [f] Vukovic et al. [81] electrodeposited Ru electrode. Type A electrode: as prepared electrode, Type B electrode: electrochemical activation of type A in 0.5 M H₂SO₄. [g] Kim et al. [82] SrRuO₃ in 0.1 M KOH. [h] Paoli et al. [83] for Ru dissolution from plasma treated and thermally annealed RuO₂ nanoparticles in 0.05 M H₂SO₄ [i] Frydendal et al. [68] for Ru dissolution from thermally prepared sputter deposited thin films in 0.05 M H₂SO₄.

2.2.2 Alkaline OER Catalysts

In comparison to acid electrolyte, a broader variety of materials can be used in alkaline [30], including transition metal catalysts like Mn, Co, Ni and/or Fe. Figure 2.10 enables the comparison between some of the most active catalysts reported so far. While NiO_x is a poor catalyst for the oxygen evolution [84], bimetallic catalysts made of Ni and Fe show among the highest current density per geometric area. The most active catalysts include NiCeO_x/Au [85], $\text{Ni}_{78}\text{Fe}_{22}$ -Layered double hydroxide (LDH) [86] and $\text{Ni}_{75}\text{Fe}_{15}\text{O}_x\text{H}_y$ NP (this work), as presented. Co-based materials also show a very decent activity [30,87], approaching in some cases the one of NiFeO_xH_y . FeCoW [88], together with $\text{PrBaCo}_2\text{O}_{5+d}$ [89], were also reported as very promising catalysts for this reaction, enabling 10 mA/cm^2 at 300 mV overpotential. In opposition to what was reported in acid electrolyte, scarce and expensive RuO_x - and IrO_x -based materials have relatively low catalytic activity in alkaline electrolyte [35,72], i.e. in some cases comparable or worse than NiO_x , which makes them highly unattractive for their application in alkaline electrolyzers. On top of being active and stable, OER catalysts should be conductive [84]. It was suggested that one way to increase the conductivity of a catalyst is via the use of a more conductive substrate [84,85,90,91]. In Figure 2.10, this is well demonstrated by the activity of NiCeO_x that varies over one order of magnitude when deposited onto a gold substrate versus a glassy carbon one.

The incorporation of Fe into NiO_x , either by intentional addition in the synthesis process or via the Fe impurities contained in the KOH electrolyte [95–98], leads to a drastic activity increase. Figure 2.11a shows NiO_xH_y and NiFeO_xH_y cycled in 0.1 M KOH. NiO_xH_y was cycled in a Fe-free 0.1 M KOH, and the CV is presented in green. An anodic and cathodic peak associated to the oxidation and reduction of Ni^{+2} to $\text{Ni}^{+3/4}$ is observed at around 0.12 and 0.06 V overpotential, respectively. When the same material is cycled in Fe-contaminated 0.1 M KOH electrolyte, a drastic increase in OER activity and a shift in the Ni redox peak are observed (orange curve). Fe does not have any features in the CV, but modifies Ni oxidation states. More specifically, the addition of Fe makes the oxidation of Ni more difficult, shifting the Ni redox feature to higher overpotential. The concentration of Fe leading to the optimal catalytic activity is rather broad. As presented on Figure 2.11b, similar catalytic activity are observed for NiFeO_xH_y where the optimal composition is between 10 and 50% Fe [99–102]. The identification of active sites in NiFeO_xH_y for the oxygen evolution is under debate. One hypothesis is that Fe is the active site [100]. The other hypothesis is that Ni is the active site, and that when Fe is incorporated into the structure, it affects its oxidation state, thus making it active for the reaction [103,104].

2.2. Overview of Promising OER Catalysts

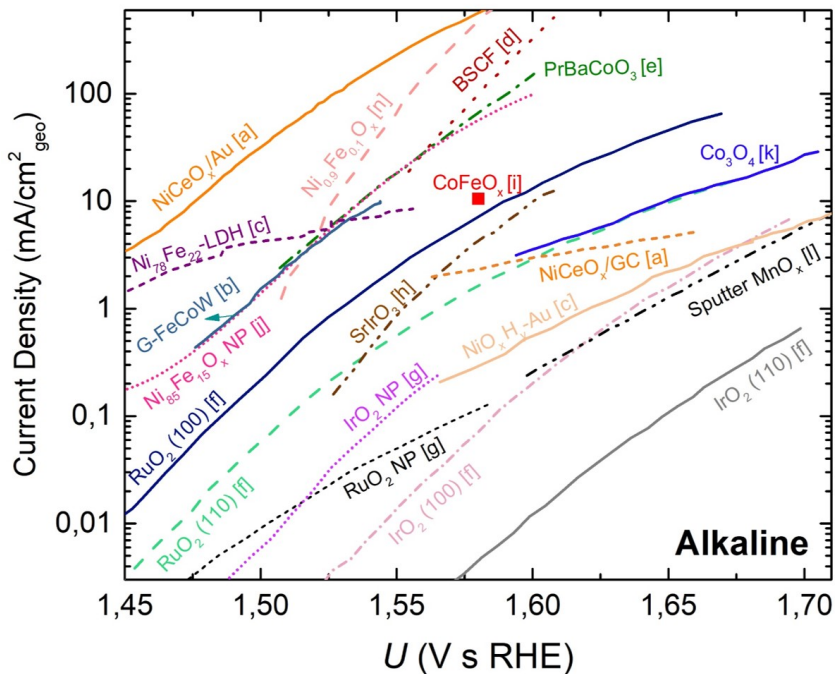


Figure 2.10: Overview of the state of the art for the oxygen evolution reaction in alkaline media. Data adapted from: [a] for NiCeO_x/Au and NiCeO_x/GC [85], [b] for G-FeCoW [88], [c] for $\text{NiO}_x\text{H}_y\text{-Au}$ [84], [d] for BSCF [92], [e] for PrBaCoO_3 [89], [f] for RuO_2 (100), RuO_2 (110), IrO_2 (100), IrO_2 (110) [35], [g] for RuO_2 and IrO_2 NP [69], [h] for SrIrO_3 [93], [i] for CoFeO_x [30], [j] for $\text{Ni}_{85}\text{Fe}_{15}$ (This work), [k] for $\text{Ni}_{78}\text{Fe}_{22}\text{-LDH}$ [86], [l] for sputter MnO_x [68], [m] for Co_3O_4 NP [87] and [n] for $\text{Ni}_{0.9}\text{Fe}_{0.1}\text{O}_x$ [94].

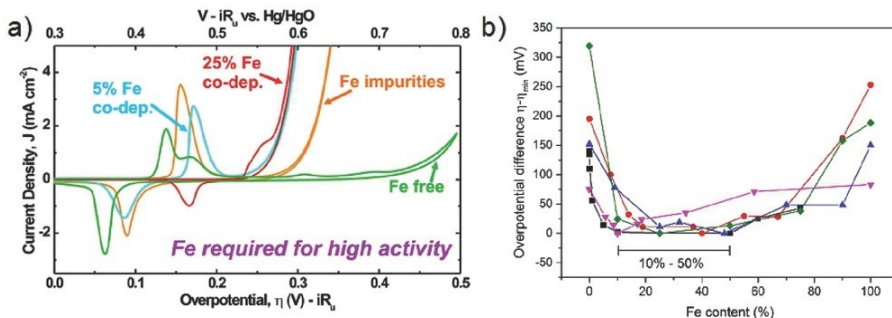


Figure 2.11: a) Effect of Fe on surface redox chemistry of Ni and oxygen evolution activity of $\text{Ni(Fe)O}_x\text{H}_y$ catalyst. The scans were recorded at 10 mV/s in 1.0 M KOH. b) Determination of optimal composition [99], [100], [101], [102] Taken from [105]

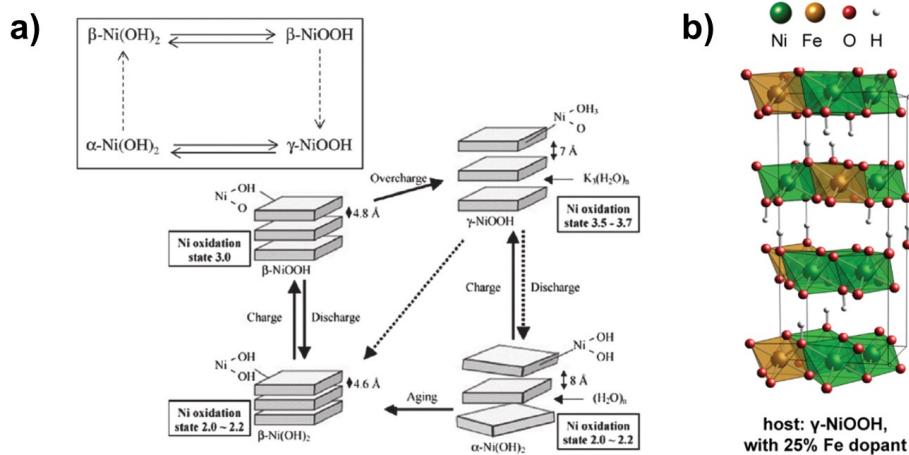


Figure 2.12: a) Bode's diagram where the interlayer distances and average Ni oxidation states are shown for the four phases. Figure taken from [105]. b) Schematic of NiFe layered double hydroxide crystalline structure. Taken from [100]

The NiFeO_xH_y structure can easily be compared to NiO_xH_y . According to the Pourbaix diagram, Ni(OH)_2 is stable in alkaline conditions between pH 9 to 13 [106]. In this structure, Ni has the oxidation state +2. The nature of the catalyst is affected by the electrochemical conditions or, in other words, by the charge/discharge processes, as presented in Figure 2.12a. When Ni(OH)_2 is oxidized and deprotonated, NiO_xH_y is obtained. The oxidation state of Ni can then vary from +2 or +3, if NiOOH is favored [107]. By charging and discharging processes, it is possible to go from $\beta\text{-Ni(OH)}_2$ to $\beta\text{-NiOOH}$. The increase of the potential above the charging of $\beta\text{-Ni(OH)}_2$ to $\beta\text{-NiOOH}$ oxidize the structure to $\gamma\text{-NiOOH}$ [107–109]. The crystallographic structure of the $\beta\text{-Ni(OH)}_2$ is well known but the oxidized phases, β - and $\gamma\text{-NiOOH}$, are under debate. The crystallographic transformations are only valid when the charge/discharge processes take place in Fe-free electrolyte. The intercalation of Fe in Ni(OH)_2 leads to the formation of charged layers that are balanced by anions located in-between the layers [99,100]. For example, H_2O intercalates into the structure and forms hydrogen bond with the OH^- groups in the layers. Figure 2.12b is a schematic of one of the crystallographic structure of $\gamma\text{-NiFeO}_x\text{H}_y$, known as LDH, where Fe substitutes 25% of the initial Ni.

So far, some studies showed that oxygen from the lattice of the oxide material can also contribute to the OER. More specifically, participation of lattice oxygen was previously observed on Au surface oxide [110], IrO_2/Ti [111], Co_3O_4 spinel [112], some Ru-based catalysts [71,113] and perovskite with high metal-oxygen bond valency, including $\text{La}_{0.5}\text{Sr}_{0.5}\text{CoO}_{3-\gamma}$,

$\text{Pr}_{0.5}\text{Ba}_{0.5}\text{CoO}_{3-\gamma}$ and $\text{SrCoO}_{3-\gamma}$ [114]. On the other hand, the participation of lattice oxygen was not observed for oriented thin films of rutile RuO_2 [73], as mentioned above, and perovskites with low metal-oxygen bond valency like LaCoO_3 [114]. For all these studies, isotope labelled water coupled with a sensitive detection method involving mass spectrometry was used.

In the case of NiFeO_xH_y catalyst, the notion of bulk activity implies i) oxidation of water located in-between the nanosheets and ii) oxygen from the lattice that is evolved as O_2 . Bulk activity in NiFeO_xH_y catalyst was supported by recent DFT calculations from Vojvodic and co-workers [115]. These calculations showed similar thermodynamics for the OER intermediates in the bulk of the material and at the surface of the material, i.e. in-between the nanosheets and on the (001) surface orientation. Moreover, Boettcher and co-workers reported a linear increase of the OER current as a function of NiFeO_xH_y loading up to $100 \mu\text{g}/\text{cm}^2$ [116], which could suggest bulk activity. In opposition to this work, Hu and co-workers showed that the apparent turnover frequency decreases with higher loading [117]. As presented here, it can be difficult to distinguish between the surface and bulk activity with high loading and not well-defined experimental conditions. A thorough and reliable answer to this question would require a model system.

2.2.3 Does More Active Equals Less Stable?

Activity is a critical parameter in catalyst development, but achieving stability is also essential. As mentioned previously, stability is a challenge for the OER catalysts considering the very harsh experimental conditions. Long-term testing can be difficult to achieve and, in that case, shorter experimental procedures revealing the stability on the long term are necessary. It is wrong to believe that stability of a catalyst can be evaluated only on the basis of potentiostatic and/or galvanostatic measurements [118]. In such cases, one would assume that a loss of stability would immediately translate into an increase of potential or loss of current, which is not necessarily representative of the phenomena occurring. It was demonstrated that corrosion might occur even though the current/potential is stable [68]. Indeed, it is possible that metal dissolution occurs but as new atoms are then at the surface, the current/potential is not affected. In an effort to overcome this issue, Chorkendorff and co-workers developed an approach where they coupled stability measurements to inductively coupled mass spectrometry (ICP-MS) and electrochemical quartz crystal microbalance (EQCM) [68]. In their work, they sputter deposited MnO_x and RuO_2 on quartz crystal. They performed both potentiostatic and galvanostatic measurements while measuring the amount of metal, Mn or Ru, dissolved in the electrolyte and monitored the mass of the catalysts with the EQCM.

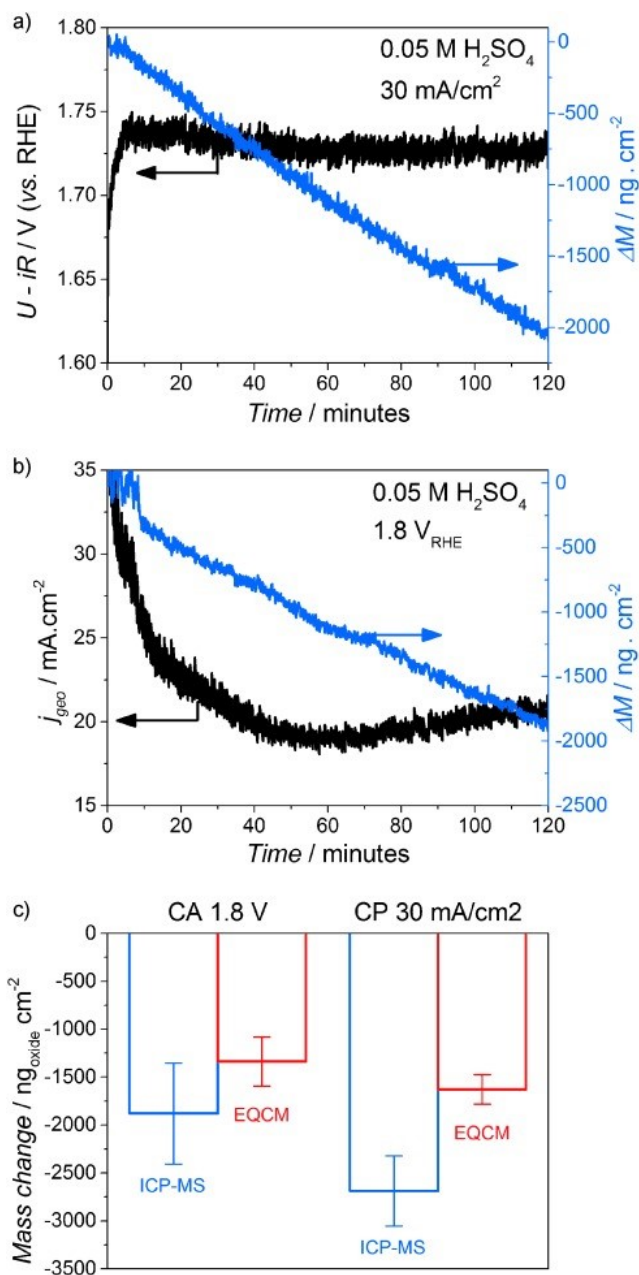


Figure 2.13: Steady-state measurement at a) constant current of 20 mA/cm² and b) constant potential of 1.8 V_{RHE} for 40 nm RuO₂ in 0.05 M H₂SO₄. The black lines refer to the potential/current recorded, and blue lines to the change in mass based on in situ resonance frequency measurements. c) Comparison of the mass loss from the ICP-MS and EQCM measurements adapted for RuO₂ mass. Figure taken from [68]

Figure 2.13 shows the results obtained when doing stability tests at 30 mA/cm² (Figure 2.13a) and 1.8 V_{RHE} (Figure 2.13b) with RuO₂ thin film catalyst in 0.05 M H₂SO₄. The EQCM follows the mass variation during the stability tests by measuring the change in frequency of a quartz crystal resonator. The black lines are associated to the potential (Figure 2.13a) and (Figure 2.13b) current recorded. The blue lines correspond to the mass variation of the RuO₂ catalysts during the measurement. The metal dissolution was also monitored by sampling the electrolyte and measuring the Ru concentrations. In Figure 2.13c, the Ru dissolution rates measured by ICP-MS and EQCM are compared for each measurements.

Figure 2.13a might suggest that RuO₂ is stable under these conditions over 2h. However, the constant mass change registered corresponding to mass loss says otherwise. On the other hand, when looking at the current recorded at 1.8 V_{RHE} (Figure 2.13b), a more evident change is observed. The current rapidly decreases, and then becomes stable at 20 mA/cm². Similarly to what was shown for the chronopotentiometry at 30 mA/cm², a constant mass change/loss occurred. This observation was confirmed with the ICP-MS with which the Ru concentration in the electrolyte was measured (Figure 2.13c). It was suggested, by theoretical studies, that low-coordinated sites, such as steps, kinks and defects, are more likely to corrode than terrace sites [119–121]. Removing a terrace site requires more energy as the terrace site has more bonds than undercoordinated sites.

In the last few years, researchers have also tried to correlate activity with stability [64,78,122–125]. With the aim of establishing a correlation between noble metals and their dissolution profile, Mayrhofer and co-workers performed a comparative study between Ru, Ir and Pt [125]. Using a flow cell/ICP-MS, they focused on the relation between the dissolution of the materials and their activity. The stability of the oxidized metal was evaluated during OER under short-steady-state chronopotentiometries of 600s. Figure 2.14 shows the mass dissolution profile as a function of time and current. The first sweep from reductive to anodic potential leads to oxidation of the surface and, hence, to transient dissolution. A transient dissolution is still observed every time the current is increased, as observed for the first 600s measurement of Ru, Ir and Pt, but the metal dissolution is less than what was observed for the first oxidation. After the transient dissolution, a slow decrease in metal dissolution is observed. As shown in Figure 2.14a, the dissolution rate of Ru at 1.5 mA/cm² is much bigger than the first transient, in contrast to what was observed with Ir and Pt. Also, it is worth noting that at all applied current, Ru has the highest corrosion rate. The reason explaining the very low dissolution of Pt is the formation of a passive surface oxide layer that inhibits further Pt dissolution [125]. The FE associated to the metal dissolution in that work is ranging between 0.0005,

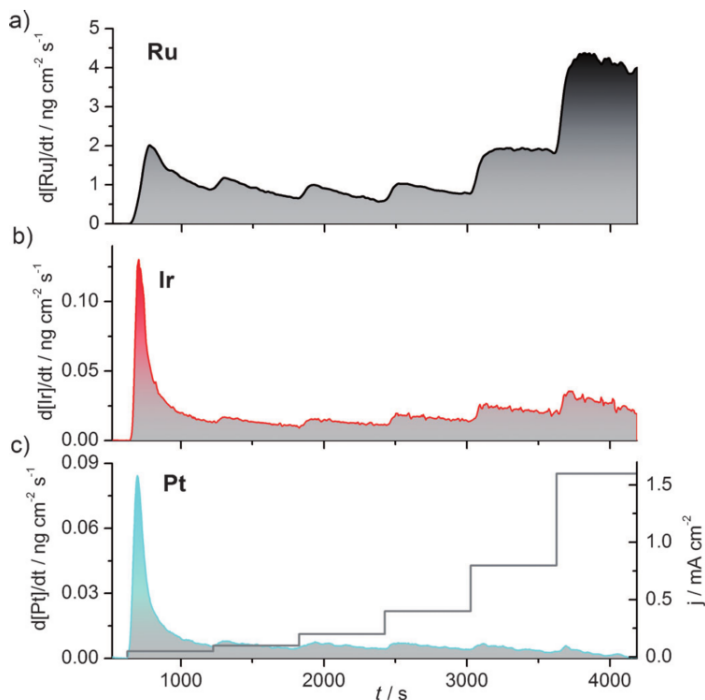


Figure 2.14: Dissolution profile of a) Ru b) Ir and c) Pt under galvanostatic measurements. The current profile (gray line) applied was the same for all metals. Figure taken from [125]

for Pt, to 1%, for Ru.

Iridium is much more stable than ruthenium. Independently of the electrolyte, it was reported that dissolution increases as $\text{IrO}_2 \ll \text{RuO}_2 < \text{Ir} \ll \text{Ru}$ [64]. It was also reported that a combined $\text{IrO}_x/\text{RuO}_x$ system can be a compromise between the excellent catalytic activity of ruthenium oxides and the better stability of iridium oxides [64,74]. Chorkendorff and co-workers reported that submonolayer amount of IrO_x at the surface of RuO_x helps reducing Ru corrosion while reaching decent current density [74]. Strasser and co-workers used a thermodynamic argument to correlate oxygen evolution and metal dissolution [126]. They suggested that O_2 generates catalyst degradation via the discharge of oxide anions. Even though we understand that there is a rationale linking O_2 evolution to dissolution, based on the arguments presented in this work, we do not think that the driving force for RuO_2 dissolution is greater than the one for oxygen evolution.

Figure 2.15 presents the activity-stability relationship reported in acid by a) Markovic and co-workers [75] and b) Mayrhofer and co-workers [125]. The metal dissolution of Os, Ru, Ir, Pt and Au, as presented in Figure

2.2. Overview of Promising OER Catalysts

2.15a, comes from the first sweep from $1.23 V_{RHE}$ to 5 mA/cm^2 , in acid electrolyte. This study reported a decrease in noble metal dissolution for smaller overpotential, where Os is the most unstable and also the most active material. Mayrhofer and co-workers investigated the metal dissolution of similar metals including Rh and Pd on top of Os, Ru, Ir, Pt and Au (Figure 2.15b). In that study, the metal dissolution was measured in situ while cycling from 0 to $1.5 V_{RHE}$. It is very interesting to notice that the trend from that study is really different than the one reported by Markovic and co-workers [75]. In this case, more active catalysts were not directly related to less stable ones. This opens up a very interesting question on the validity of the *universal* claim that Markovic and co-workers [75,78,122,123,127] made: Does a more active catalyst necessarily mean less stable?

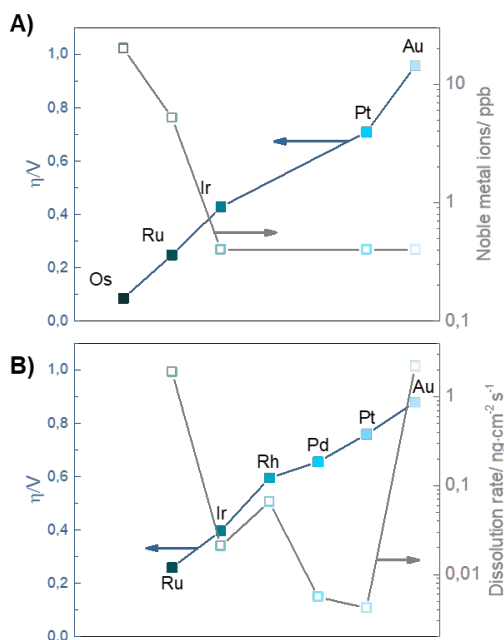


Figure 2.15: Stability and activity relationship for a) Os, Ru, Ir, Pt and Au for the first cyclic voltammetry from $1.23 V_{RHE}$ ($\eta=0$) to 5 mA/cm^2 in acid electrolyte. The metal dissolution is measured from the electrolyte after stability measurement. Data from Markovic and co-workers [75] b) Stability and activity relationship for Ru, Ir, Rh, Pd, Pt and Au measured in-situ while cycling from 0 to $1.5 V_{RHE}$ in acid electrolyte. Data from Mayrhofer and co-workers [125]. Figure adapted from [90].

2.3 Overview of State-of-the-Art ORR Catalysts

The development of new cathode electrodes for the ORR is of paramount importance in the quest to increase hydrogen fuel cell technology on the market. It is reported that Pt loading in PEMFCs should be reduced by a factor of 4 to 10 for large-scale development [42,128]. Over the years, researchers have put a lot of effort in the development of more active ORR catalysts. Pt is the most active pure metal catalyst for the ORR, sitting very close to the top of the volcano plot but still binds $\text{OH}_{ads} \sim 0.1$ eV too strongly for optimal activity. Based on this information, the idea is to develop new ORR catalyst that binds to these intermediate slightly more weakly. The adsorption energy of reaction intermediates to the surface can be optimized by lowering the average energy of the Pt 5d band compare to Fermi level [51]. The Pt 5d band can be modified using strain and ligand effect. The more direct approach for having a great catalyst and low Pt loading is by introducing another metal to the already active Pt catalyst. As highlighted by Chorkendorff and co-workers [56], the ideal ORR catalyst would have only one monolayer of Pt that is, at least, as active as Pt, and have a core made of a cheap and abundant metal, on top of being stable.

When Pt is alloyed with a less noble metal, the corrosive experimental conditions favor the formation of a Pt overlayer while the alloy remains in the core of the material. In the 1990's, Mukerjee and co-workers [129–131] showed that Pt alloyed with transition metal like Ni, Co and Cr have significant increase in activity in PEMFCs, compare to bare Pt. More recently, a broader range of Pt alloys with 3d transition metals were investigated. With the aim of understanding the oxygen reduction better, and eventually being able to predict ORR reactivity, bulk crystalline samples of Pt_3M , $\text{M}=\text{Ti}, \text{V}, \text{Fe}, \text{Co}$ and Ni , were tested [132–134]. From this, Markovic and co-workers were able to demonstrate that these alloys are more active than Pt, and that there is a fundamental relationship between the electrocatalytic activity and the d-band center for the ORR. Pt_3Co showed the highest specific activity measured at $0.9 V_{RHE}$. They also studied the surface reconstruction of these alloys when exposed to different experimental conditions. In their work, all polycrystalline bulk Pt_3M were prepared by conventional metallurgy (i), the samples were annealed (ii) and finally submitted to electrochemical ORR measurements (iii). The LEIS and Auger spectra, and CVs before/after annealing and electrochemistry were recorded, and they found that the near-surface region is dependent on the pre-treatment. Taking Pt_3Fe as example, the LEIS and Auger spectra after annealing compare to the initial one show a change from 75% Pt and 25% Fe to pure platinum due to surface segregation. This Pt overlayer is referred to as Pt-skin and is typically 1-2 nm thick. The influence of ORR EC measurements was

also investigated using Auger spectroscopy on the as-prepared and after EC measurements sample. Auger spectra of the post electrochemically measured Pt_3M bulk sample showed an attenuated Fe signal compare to the one before EC measurements. This indicates that during the ORR measurement in 0.1 M HClO_4 , Fe dissolves and a Pt overlayer is formed. To differentiate between the Pt overlayer created in UHV and electrochemistry, the latter was referred to as Pt-skeleton in opposition to Pt-skin. The Pt-skeleton overlayer was observed to be thicker than that of Pt-skin and also more porous. The differences between PtNi alloy, Pt-Ni/Pt-skeleton and PtNi/Pt-skin for a nanoparticle is presented in Figure 2.16. For both cases, once the Pt overlayer is formed, it act as "protection" for the sub surface alloy from the oxidative ORR conditions [106].

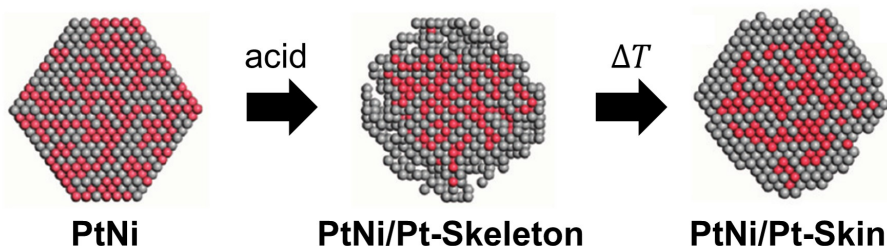


Figure 2.16: Schematics of a PtNi alloy, Pt-Ni/Pt-skeleton and PtNi/Pt-skin nanoparticles. Figure taken from [135].

To better understand how the near surface layer influences the ORR activity, Stamenkovic and co-workers pursued the work with well-defined Pt_3Ni (111), (110) and (100) surfaces [136]. They reported a 90-fold improvement for the Pt_3Ni (111) surface over the commercial Pt/C nanoparticles, which is, to our knowledge, the highest specific activity ever reported. Based on the extremely high activity obtained from this model system, they tried to extend it to the nanoparticulate form. They synthesized Pt_3Ni nanoframe by leaching a Pt_3Ni polyhedra structure [137]. However, translating model to a scalable system like nanoparticles is highly challenging. As expected, even though extremely high, the activity of the Pt_3Ni nanoframe is lower than the one reported for the Pt_3Ni (111) surface. When compared with Pt/C and PtNi/C nanoparticles, it ranks as follows: $\text{Pt/C} < \text{PtNi/C} \ll \text{Pt}_3\text{Ni}$ nanoframes. More specifically, the Pt_3Ni nanoframe shows a 22-fold enhancement in specific activity, and 36-fold improvement in mass activity, when compared to Pt/C nanoparticles. One of the downside of Pt_3Ni nanoframe is the relatively complicated synthesis procedure that cannot be scaled-up easily. It was demonstrated that by scaling up Pt_3Ni nanoframe by a factor of 10, i.e. to obtain a total of 60 mg catalyst, a decrease in ac-

tivity of roughly half was reported. Using the PtNi/C octahedra structure already developed, Huang and co-workers investigated metal-doped PtNi/C [138]. They reported that using Mo as dopant enables better performance and more stable catalyst.

With the aim of integrating Pt₃M catalyst into fuel cell devices, other scientists such as Mayrhofer [139] and Shao-Horn and co-workers [140,141] worked on the development of Pt₃M/C nanoparticles. From PtM_x, where $x > 1$, M=Cu, Ni, Co, came the dealloyed catalysts pioneered by Peter Strasser [142–147]. The dealloyed catalyst refers to a bimetallic alloy where the more reactive component (M in Pt_xM), was preferentially dissolved. For example, dealloyed Pt-Cu [145] and Pt-Ni nanoparticles [148] were reported with uniquely high catalytic activity, i.e. 0.55 and 1.72 A/mg, respectively.

Another category of very active catalysts for the ORR are the hollow Pt-alloy structures. In a very recent review published by Maillard and co-workers [149], they present the recent development made in this field. They explain how the Kirkendall effect or galvanic replacement leads to the formation of hollow Pt-alloy nanoparticles. The Kirkendall effect is described as the interdiffusion of two metals causes by the difference in diffusion rates of the metal atoms [150]. In hollow structure, locally-compressed and -expanded domains co-exist. The structural disorder created by the Kirkendall effect can be simplified by the concept introduced by Calle-Vallejo and co-workers on "generalized" coordination number (\overline{CN}) [151]. \overline{CN} , to which weight is considered to each first-nearest neighbor atoms, allows the comparison in activity of nanoparticles and extended surfaces. Defects, steps or kink sites are more reactive, favoring stronger adsorption of intermediate species and should thus be minimize.

Figure 2.17 presents the state-of-the-art ORR catalyst normalized to the mass of platinum, the most relevant parameter for large scale application of PEMFCs. Interestingly, the most active catalyst reported so far was obtained from leaching of PtNi nanowires and is exclusively constitute of platinum. Although liquid half cells are well-suited for laboratory studies as they required a small amount of material and the parameter of conventional RDE measurements are easy to optimize, Chorkendorff and co-workers [152] showed that it reflects poorly on the performance in a PEMFC. For example, the highly active PtNi/C nanoframe that was reported with a mass activity of 5.7 A/mg_{Pt} at 0.9 V_{RHE} yield to only 0.76 A/mg_{Pt} when tested in a fuel cell. This brings to our attention that our actual way of investigating catalyst activity should be optimized in order to mimic better the real device.

A highly active catalyst is pointless if the surface is unstable. Thus far, the goal of 0.44 A/mg_{Pt} at 0.9 V_{RHE} set by the USDOE [4] was reached, but not the stability requirements. A catalyst would be considered

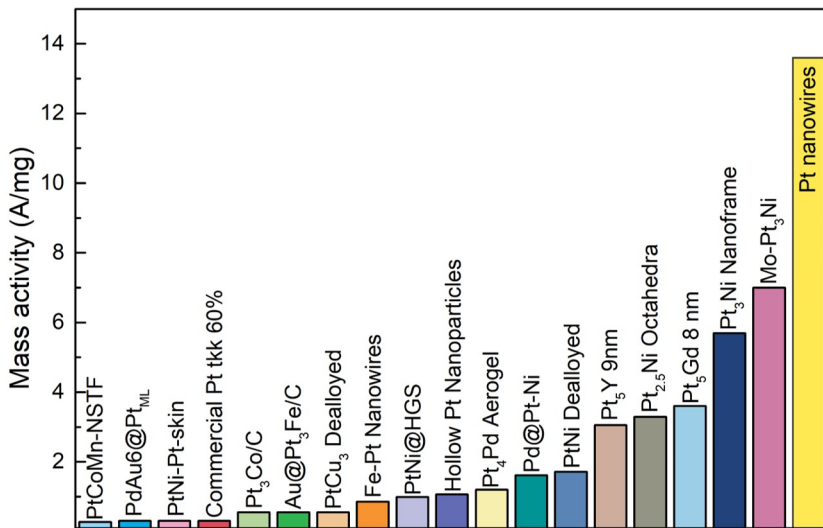


Figure 2.17: Overall ranking of ORR mass activity, normalized by the total mass of metal. Adapted from [153]. All data are taken in O_2 -saturated $HClO_4$ at 1600 rpm at $0.9V_{RHE}$. [154] for PtCoMn-NSTF, [155] for PtAu₆@Pt_{ML}, [135] for PtNi-Pt-skin, [153] for commercial Pt tkk 60%, [156] for Pt₃Co/C, Au@Pt₃Fe/C [157], [145] PtCu₃ dealloyed, [158] for Fe-Pt nanoparticles, [139] for PtNi@HGS, [159] for hollow Pt nanoparticles, [160] for Pt₄Pd Aerogel, [161] for Pd@Pt-Ni, [148] for PtNi Dealloyed, [162] for 9 nm Pt₅Y, [163] Pt_{2.5}Ni Octahedra, [164] for 8 nm Pt₅Gd, [137] for Pt₃Ni nanoframe, [138] for Mo-PtNi, [165] for Pt nanowires

”stable” if after 5000h of operation performance losses of 40% or lower were reached [4]. The generic problem with bimetallic ORR catalysts is the constant leaching of the less noble metal in acid electrolyte with time which results in a more Pt concentrated catalyst. The bimetallic catalyst of Pt alloy with early transition metal shows decent stability in RDE setup under accelerated stability test conditions but as presented, the observation made under such experimental conditions cannot automatically be translated to real operating conditions in PEMFC. Dubau and co-workers tested Pt₃Co/C nanoparticles in PEMFCs and showed direct evidence of bulk Co dissolution. The nanoparticles suffer compositional changes and slowly, the catalyst performance resembled more the one of Pt/C nanoparticles. Figure 2.18 enables the comparison of the nanoparticles composition in Pt and Co. The high-angle annular dark field images of the Pt₃Co nanoparticles over time show a depreciation in Co content to end up with only Pt nanoparticles after the 3422h stability test.

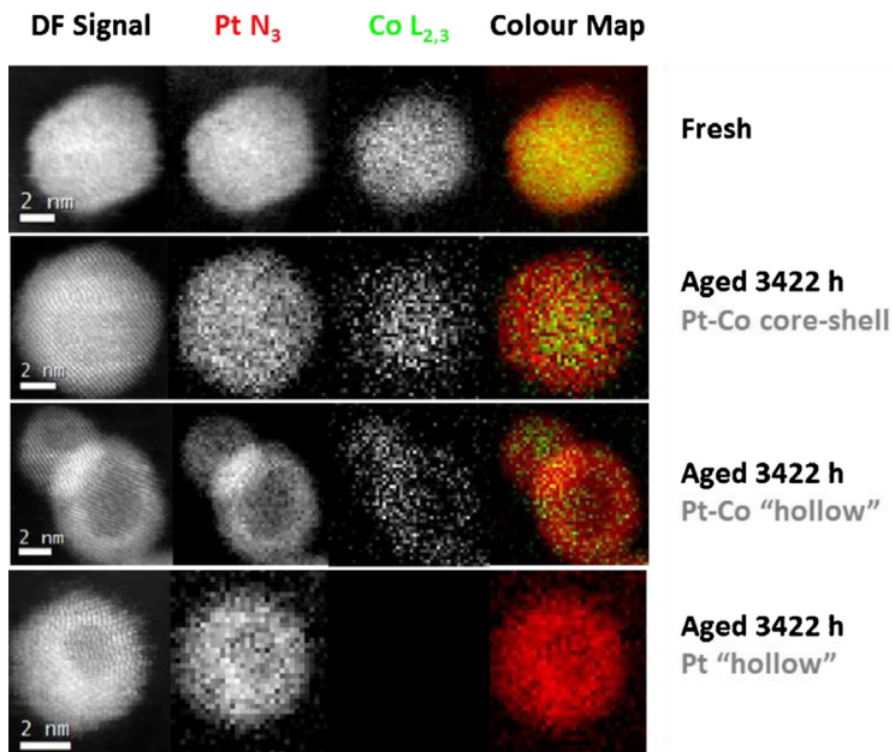


Figure 2.18: High-angle annular dark field images signal of $\text{Pt}_3\text{Co}/\text{C}$ nanoparticles. The elemental maps were constructed using the Pt N_3 (518 eV) and the $\text{Co L}_{2,3}$ (780 eV) edges, respectively. The Pt N_3 signal is shown in red, and the $\text{Co L}_{2,3}$ signal is shown in green. Taken from [166]

In the search of highly active but also more stable Pt-alloy materials for the oxygen reduction, our research group focused on Pt-rare-earth alloys for the oxygen reduction [162,164,167–169]. More specifically, Pt_xY and Pt_xGd have among the highest alloying energy ever reported. The intermetallics of Pt-rare-earth have greater resistance against diffusion over Pt alloyed with transition metals. The reason of their supposedly higher stability is related to the more negative heat of formation [47]. Most recently, Schiøtz and co-workers demonstrated using DFT calculations that there is a correlation between the alloying energy and the diffusion barriers of the less noble component [170]. The overall dissolution process of Pt_3Y and Pt_3Co are compared in Figure 2.19, where an overview of the dealloying energy when the catalysts are tested in PEMFC at 1 V_{RHE} is presented. According to this schematic, the atom of Co or Y that will dissolve has to go through the core alloy and the Pt overlayer. The initial energy barrier to dissolution is proportional to the alloy energy formation, explaining why the dissolution

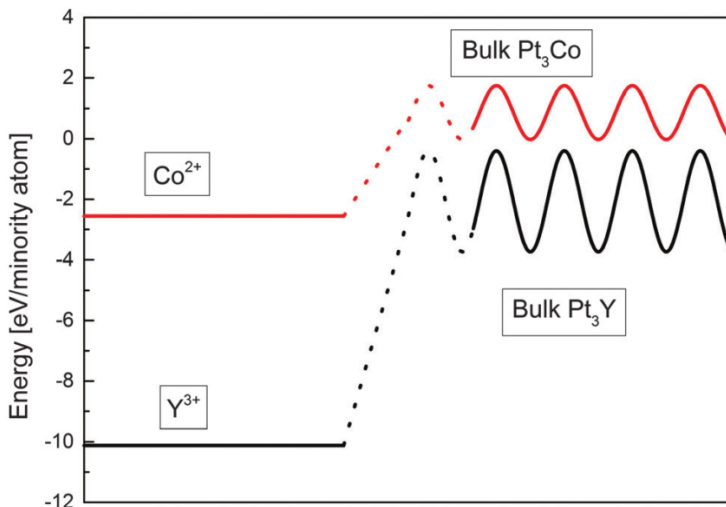


Figure 2.19: Schematic of the energy barrier for dealloying of Pt_3Co and Pt_3Y under operation conditions in polymer electrolyte membrane fuel cell at 1 V vs RHE. Taken from [170]

of Co is easier than Y, according to this study. Once the initial energy barrier is overcome, the dissolution process becomes more favorable. At that point, the energy barrier to dissolution of Y from Pt_3Y is smaller, yet still bigger than Pt_3Co .

After being tested for the ORR, the Pt-rare-earth alloys show the formation of a platinum-skeleton with platinum overlayer being around ~ 1 nm thick. Stephens, Chorkendorff and co-workers [169,171] showed, using polycrystalline surfaces, that the ORR enhancement was attributed to compressive strain imposed onto this Pt overlayer by the alloy in the bulk. To accommodate the larger rare-earth atoms, most of the Pt atoms at the top-most layer are arranged in *kagomé* nets [172]. The Pt-Pt nearest-neighbor in such structure is very short, i.e. $< 2.7 \text{ \AA}$, and bond length of 3 \AA to their neighbor atom. The compressive strain in the Pt overlayer was also shown to be structure sensitive, with the activity for $\text{Pt}_3\text{Y} > \text{Pt}_5\text{Y} \gg \text{Pt}_2\text{Y}$ [168]. The stability of a polycrystalline Pt_xGd film was tested by cycling between 0.6 and 1 V_{RHE} for 1,000 cycles in O_2 -saturated 0.1 M HClO_4 . The loss in activity registered at 0.9 V_{RHE} is of only 15% compared with 75% loss for Ni/Pt(111) under similar experimental conditions [173].

Already showing very promising properties for the ORR in the polycrystalline form [47,56,168], Pt_xY and PtGd_x catalysts were investigated further in the nanoparticulate form. Mass-selected nanoparticles of Pt_xY and PtGd_x were deposited through gas-aggregation technique [162,164].

Nanoparticles with diameter ranging from approx. 4 nm to 9 nm were obtained and tested in O_2 -saturated 0.1 M $HClO_4$ using a RDE setup at 1,600 rpm. Figure 2.20 shows the specific and mass activity reported.

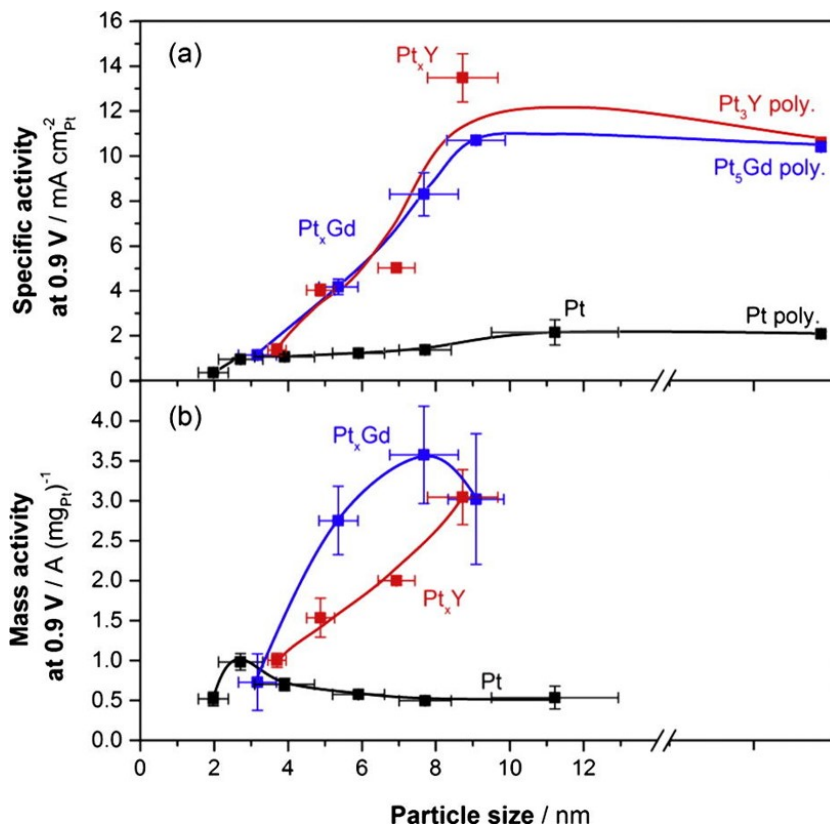


Figure 2.20: a) Surface specific activity and b) mass activity of Pt_xY (red) and Pt_xGd (blue) compared to Pt (black) measured at $0.9 V_{RHE}$, recorded at $50 mV/s$ at 1,600 rpm in O_2 -saturated 0.1 M $HClO_4$. The lines serve as a guide for the eye. Figure taken from [164].

The activity of the Pt_xY (red) and $PtGd_x$ (blue) nanoparticles are also compared with mass-selected Pt nanoparticles (black). The specific activity as a function of nanoparticle diameter (Figure 2.20a) shows an increase in current density from nanoparticles diameter around 4 nm to 8-9 nm. By comparing with Pt nanoparticles, one can observe that there is a critical size, i.e. $< 4-5$ nm, below which no enhancement is observed. The stability of $PtGd_x$ and PtY_x nanoparticles were investigated using the same accelerated stability test as describe above. The comparison of the activity before/after stability test shows a loss in 30-50% in current density at $0.9 V_{RHE}$ for both catalysts [162,164]. The mass activity of the most active Pt_xGd and Pt_xY

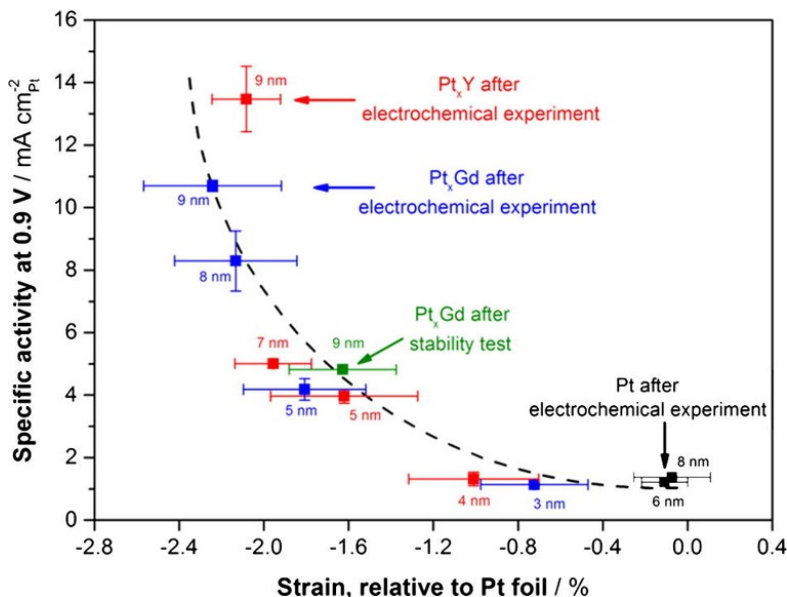


Figure 2.21: Specific activity of Pt_xY (red) and Pt_xGd (blue) measured at 0.9 V_{RHE} in O_2 -saturated 0.1 $MHClO_4$ at 1,600 rpm as function of the strain relative to Pt foil (%), determined by EXAFS after oxygen reduction measurements. The strain after stability test for Pt_xGd is presented in green. Data from Pt nanoparticles (black) after oxygen reduction were added for comparison purposes. The dashed line is a guide to the eye. Data included in this Figure comes from [162,164] and the Figure was taken from [164].

nanoparticle size are compared to the other state-of-the-art ORR catalysts in Figure 2.17, where they rank as the fourth and sixth most active catalyst reported when normalized to the mass of Pt.

To confirm that the increase in activity was due to strain effect, the average nearest Pt-Pt distance of Pt_xY and Pt_xGd nanoparticles was measured with grazing-incident extended X-ray absorption fine structure measurements (GI-EXAFS). The average nearest Pt-Pt distance was compared to polycrystalline Pt one, and strain values in percentage were determined. Figure 2.21 shows that the specific activity scales with the increase in strain.

From these findings, they concluded that the increase in activity compared to bare Pt nanoparticles originates from the fact that a thick Pt overlayer is strained by the core alloy [171], and that the increase in particle size results in the core alloy straining even more the topmost Pt layer. When the nanoparticle size increases, the core alloy contributes even more to strain the Pt overlayer until an optimal is reached. In this case, the optimal is reached around ca. 9 nm for the Pt_xGd as the current density of the polycrystalline film is at that point very similar. The optimal mass activity for

Pt_xGd nanoparticle with diameter around 8-9 nm can be explain by i) the specific activity of the material increasing with particle size and reaching a plateau and ii) the surface to bulk ratio, of the nanoparticles, for which smaller nanoparticle size have more Pt exposed to the electrolyte.

The investigation of mass-selected Pt_xY and Pt_xY nanoparticles for the ORR serves as a model study. The gas-aggregation technique allows the deposition of only few ng per hour which does not make it suitable for large scale development. For that reason, researchers need to come up with a synthesis method that can be scaled up to the gram scale. Many attempted to synthesized Pt-rare-earth nanoparticles [174–178], but without any proof of alloy formation, i.e. no X-ray diffraction spectra showing reflection peaks of intermetallic compound, besides Pt, and no X-ray photoelectron spectroscopy showing the alloy formation through the Y 3d peak, expected at ~ 156.5 eV for metallic Y [162]. So far, only Alivisastos and co-workers [179] proved that they could produce nanoparticles Pt_3Y alloy through a molten reducing agent. Unfortunately, the Pt_3Y catalyst was not tested for the ORR, and the activity cannot be compared to the one reported in the model study [164].

Experimental Methods

The aim of this chapter is to summarize the several techniques that were used in this project to prepare, characterize and evaluate the electrochemical activity and stability of the catalysts.

3.1 Sample Preparation

Physical deposition techniques were used to prepare some of the oxygen evolution catalysts. The next section is a brief summary of the gas aggregation technique and pulsed laser deposition used to obtain NiFeO_xH_y and RuO_2 oriented thin films, respectively.

3.1.1 Mass-selected Nanoparticles

NiFe mass-selected nanoparticles were prepared by Béla Sebök, using a magnetron sputter aggregation source combined with a time-of-flight mass filter (Nano-Beam 2011, Birmingham Instruments Inc.), similar to the one described in [180]. The Nanoparticle Source, as we called it, is ultra-high vacuum (UHV) compatible, with a base pressure of 10^{-10} mbar. A schematic of the Nanoparticle Source is presented in Figure 3.1. It is connected through gate valves to two UHV chambers: the preparation/deposition chamber and the analysis chamber.

The preparation/ deposition chamber was used to sputter or heat the substrate before deposition, if necessary. This chamber is also connected to the analysis chamber where various physical characterization tools including X-ray photoelectron spectroscopy and low-energy ion scattering are available, and allow characterization of the sample without exposing it to air.

The process for depositing mass-selected nanoparticles can be summarized as follows. First, a plasma is formed when a voltage is applied at the

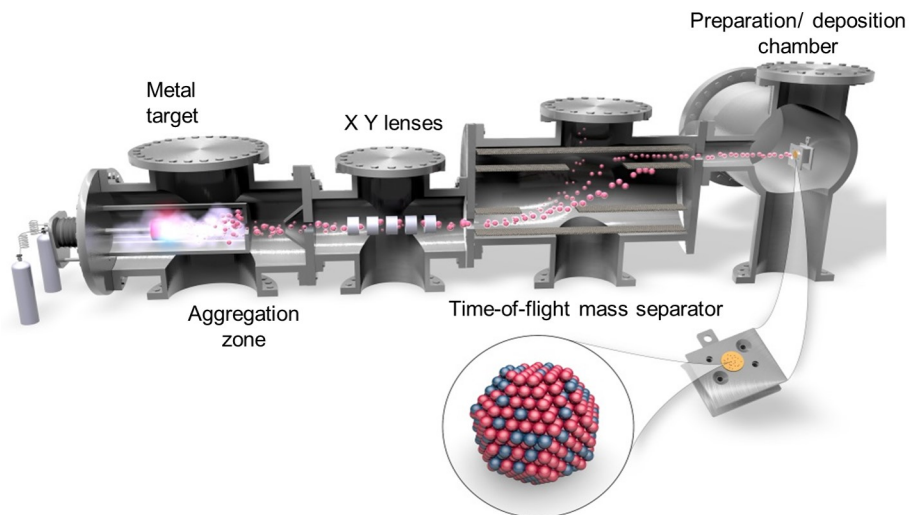


Figure 3.1: Schematic representation of the nanoparticle source used for the synthesis and characterization of the mass-selected nanoparticles in UHV conditions. Courtesy of Jakob Kibsgaard

75 at% Ni/ 25 at% Fe target (99.95%, Kurt J. Lesker Ltd., UK), and Ar^+ is used to sputter the target. The density of the plasma can be tuned by changing the voltage. The compartment identified as the aggregation zone is where collisions of the atoms occur. To favor collisions, and the formation of bigger clusters/ nanoparticles, the compartment is cooled down with liquid nitrogen, and He gas is added, so a pressure between 0.1-1 mbar is reached. The magnetron head can also be moved to adjust the length of the aggregation zone, leading to an increase in residence time and, therefore, an increase in the total number of collisions. The particles are pushed away from the aggregation zone by the noble gas and enter a skimmer. At that point, the pressure is much lower due to differential pumping. The low pressure prevents further growth of the nanoparticles. The negatively charged particles, from their collision with Ar^+ , allow a separation based on their mass-to-charge ratio (m/z), using the lateral time-of-flight mass separator. In a time-of-flight mass separator, high voltage pulses are applied. This induces a lateral displacement of the nanoparticles that depends on m/z , and allows nanoparticles separation. The mass filter was set to be used with negatively charged particles, and to have a mass resolution of approximately $m/\Delta m=20$. A representative deposition current as function of mass is presented in Figure 3.2.

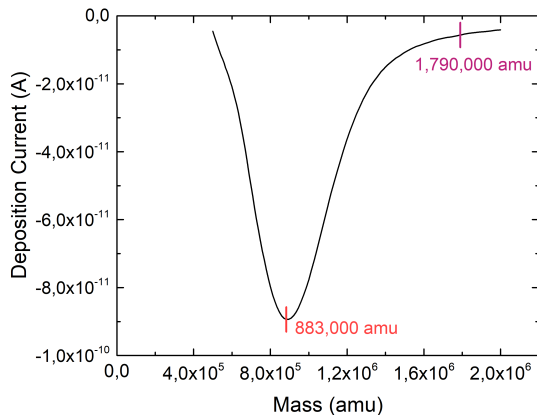


Figure 3.2: Deposition current as function of mass for NiFe nanoparticles. Courtesy of Niklas Mørch Secher

3.1.2 Oriented Thin films

Pulsed laser deposition (PLD) is a physical vapor deposition technique carried out in a vacuum system. The theory on the topic presented in this paragraph is taken from [181]. A simplified version of the PLD process is presented in Figure 3.3. It is a relatively simple method frequently used for thin film growth. In PLD process, a pulsed laser is focused onto a rotating target of the material to be deposited. For the creation of a plasma, the laser energy needs to be above the ablation threshold. Since this process is not in equilibrium, a stoichiometric transfer will take place independently of the vapor pressure of the elements composing the target. The plasma created by the laser pulses is forward-directed, and the deposition takes place on the substrate located in front of it. The energy of the deposited cation species, when they reach the substrate, depends on the fluence of the laser, the pressure in the vacuum chamber and the distance that the species have to travel, i.e. the target-substrate distance. A background gas can be used to reduce the kinetic energy of the ablated species. The background gas can be introduced in the chamber to favor the formation of multication thin film materials such as oxides when using oxygen gas, for example. Finally, the substrate is located on a holder that allows rotation, for an homogeneous deposition, and heating, to influence the growth mode.

PLD enables shot-to-shot control, which is ideal for submonolayer control. One PLD shot can correspond to 0.001 to 1 Å per pulse. The growth kinetics during PLD can be put into 3 distinct categories depending on the energy of the free energies of the film surface (γ_F), substrate surface (γ_S),

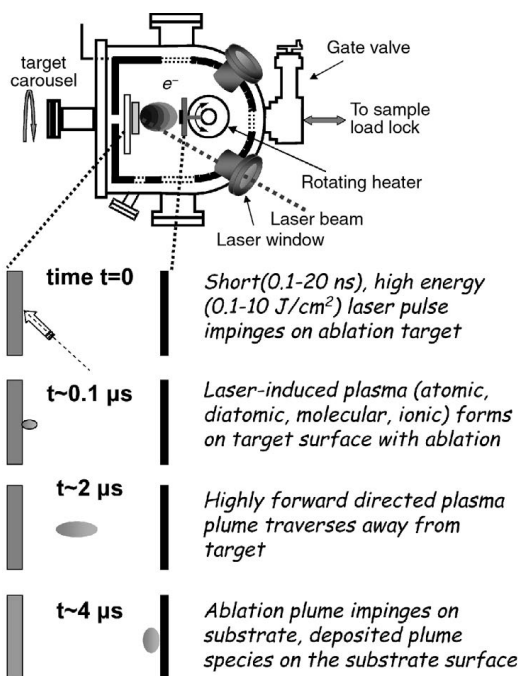


Figure 3.3: Schematic of a pulsed laser deposition chamber including the deposition process. Taken from [181]

and the interface between the film and the surface (γ_I). For the layer-by-layer mode, required for epitaxial growth, the total surface energy of the substrate, i.e. $\gamma_F + \gamma_I$, needs to be lower than the surface energy of the bare substrate (γ_F). For epitaxial growth, choosing the right substrate is essential. Similar lattice parameters of the substrate and the film are required. The bonding of the deposited species for the surface plays a determining role in the growth process that will take place. In this work, oriented thin films of RuO_2 were deposited on single crystal (001)-oriented SrTiO_3 or MgO substrates (from CrysTec and MTI), or (101) or (111) TiO_2 from a polycrystalline RuO_2 ceramic target. The SrTiO_3 substrates were first immersed in NH_4F -buffered HF. They were then annealed at 950°C in O_2 for 1h to obtain an atomically flat surface. The oriented MgO and TiO_2 substrates were annealed in air at 950°C for 2 hours for surface quality recovery. RuO_2 thin film deposition was performed using a KrF excimer laser ($\gamma = 248 \text{ nm}$) to obtain $\sim 25 \text{ nm}$ thick films. The O_2 pressure during the deposition was 50 mTorr and the freshly deposited thin films were cooled to room temperature under 200 Torr O_2 .

3.2 Sample Characterization

Throughout the study reported in this PhD work, X-ray diffraction, X-ray photoelectron spectroscopy, low-energy ion scattering and electron microscopy were used to investigate the various catalysts. In this section I described briefly every technic to enable a better understanding of the results later on.

3.2.1 X-ray Diffraction

X-ray diffraction (XRD) is a bulk physical characterization technique that provides essential information on the nature and structure of crystalline materials. When a sample is bombarded with X-rays, as shown in Figure 3.4, the scattered monochromatic X-rays that are in phase give constructive interferences. The radiation is in phase if the path length between scattering planes is equal to an integer number of wavelengths.

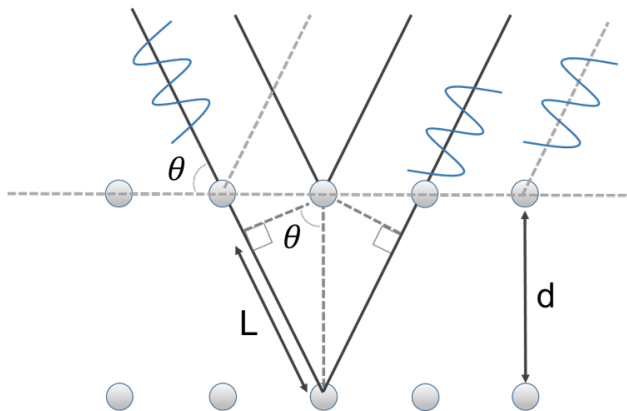


Figure 3.4: Representation of the interaction between X-rays and a crystal lattice that can lead to constructive interference. Adapted from [51]

With Bragg's law, it is possible to derive the lattice spacing from the diffraction of the X-rays by the crystal planes:

$$n\lambda = 2d \sin \theta; \quad n = 1, 2, \dots \quad (3.1)$$

Where λ is the wavelength of the X-rays, d is the distance between two lattice planes, θ is the angle between the incoming X-rays and the normal to the reflecting lattice planes and n is an integer named the order of reflection. The constructive interference lead to peaks that can be associated with the crystallographic structure of a specific material. In a standard XRD configuration, the incident beam and the detector are maintained at the same angle. In that case, a diffractogram as function of 2θ is obtained.

In situ XRD was used in this work to study alloy formation and crystallinity when exposed to experimental conditions, i.e. change in temperature and atmosphere. A schematic of the cell used for in situ XRD measurements is presented in Figure 3.5. The gas tight cell is connected to an external gas system allowing to perform XRD measurements under Ar, He, O₂ and/or H₂ atmosphere. The cell has multiple heating elements that can reach up to 800 °C. Two X-ray transparent windows made of beryllium allow transmission of the incident and diffracted beams. The sample is mounted on a stage made of a ceramic material.

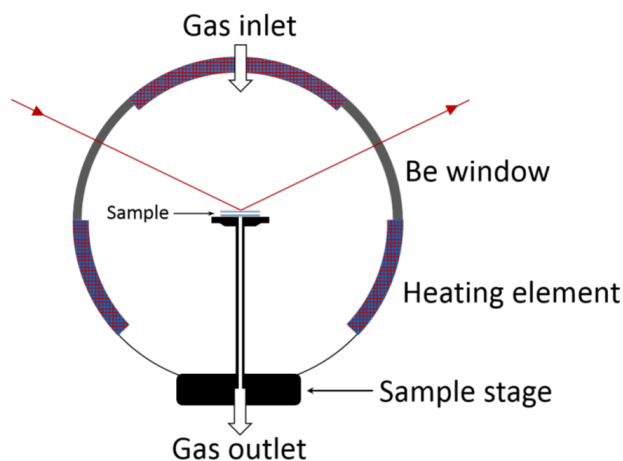


Figure 3.5: Schematic representation of the in situ X-ray diffraction cell. Taken from [182]

3.2.2 X-Ray Photoelectron Spectroscopy

X-ray photoelectron spectroscopy is a highly used technique in surface science to identify the atomic elements contained in a material and their oxidation states [51]. X-rays are produced and directed to the sample. The interaction of the X-rays, $h\nu$, with the material will excite electrons from the core levels of the material, as illustrated in Figure 3.6.

The mean free path of the photoelectrons is low, resulting in a high degree of surface sensitivity for this technique. During XPS measurements, only the topmost layers are probed. The electrons ejected are then detected as function of their kinetic energy (E_{kin}). As shown by equation (3.2), the binding energy of the emitted electrons, E_b , and the contribution coming from the oxidation state of the element, E_{chem} , can be determined. Finally, ϕ is the work function of the analyzer and $h\nu$ the incident energy.

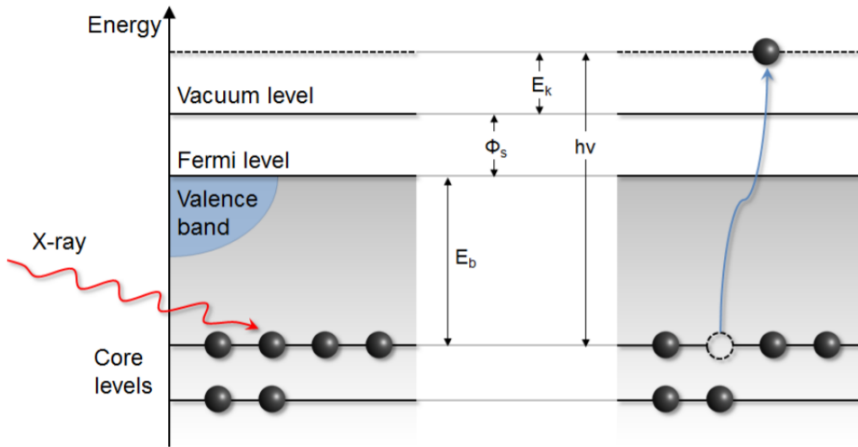


Figure 3.6: Schematic of the photoelectric effect in X-ray photoelectron spectroscopy. On this representation, an electron from the core level is excited by an incident X-ray beam. Figure taken from [183].

$$E_{kin} = h\nu - E_b + E_{chem} - \phi \quad (3.2)$$

An hemispherical electron energy analyzer was used to measure the energy distribution. The intensity of electrons emitted, $N(E)$, from the excitation process as function of the binding energy, obtained from the kinetic energy, is plotted. For the XPS measurements of the NiFeO_xH_y catalyst, unmonochromatized $\text{MgK}\alpha$ radiation from a SPECS XR50 dual filament X-ray gun was used. A Theta-Probe instrument (Thermo Scientific) equipped with a monochromated $\text{AlK}\alpha$ source was used for the $\text{Pt}_x\text{Y/C}$ measurements.

3.2.3 Low-energy Ion Scattering

Low-energy ion scattering (LEIS) relies on ion scattering off the outermost atomic layer of a surface to give information on the elemental composition [184]. In LEIS, noble gas atoms like Ar or He are ionized using an ion gun. Ar^+ or He^+ are then accelerated with a kinetic energy ranging from 1 to 10 keV towards the surface of the sample to analyze. When Ar^+ or He^+ ions interact with the surface, some of the ion gas will be backscattered, and their kinetic energy, E_f , can be detected. The value of E_f is determined according to the laws of conservation of energy and momentum [185].

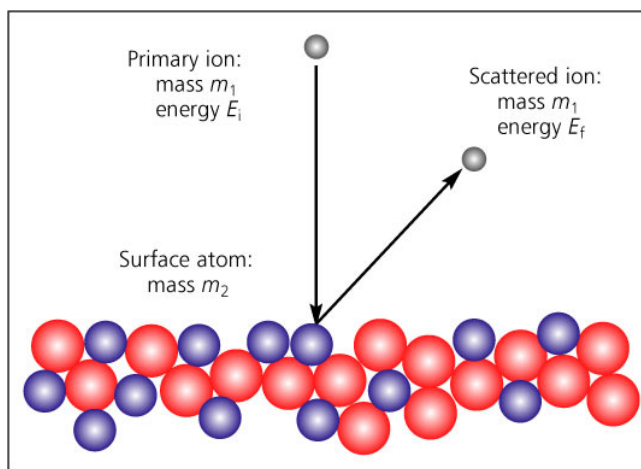


Figure 3.7: Schematic of the low-energy ion scattering principle. Noble gas ions of 1-10 keV (E_i) and mass m_1 hit atoms at the surface of the sample of mass m_2 . The backscattered ions have an energy of E_f that depends on m_1 and m_2 and will be detected. Figure taken from [185]

3.2.4 Electron Microscopy

There is an interrelation between the micro-structure and the chemical, physical and/or mechanical properties of a material. For that reason, electron microscopy, which can be used to get information on the morphology (size, shape, spatial distribution), the structure and the composition, can be very insightful. This section introduces the electron microscopy-based techniques used to characterize the NiFeO_xH_y , Pt/C and $\text{Pt}_x\text{Y/C}$ nanoparticles. More specifically, scanning electron microscopy, transmission electron microscopy and energy dispersive X-ray spectroscopy were used in this work.

The micro-structural characterization is achieved by allowing a probe (light or high energy electron beam) to interact with the specimen. In comparison to visible light, high-energy electrons have a shorter de Broglie wavelength, enabling a significant increase in resolution. This is the reason why significantly higher magnification can be achieved with electron microscopy. Figure 3.8 shows the signals generated from the interaction of the high-energy beam with a solid sample. Depending on the electron microscopy used, the transmitted beam, secondary electrons or scattered X-rays will be investigated.

Backscattered electrons (BEs) originate from the primary beam, and can have energies ranging from zero to the incident energy beam. The secondary electrons are generated by the interaction of the probe with the sample, ejecting electrons from the near surface region. The penetration

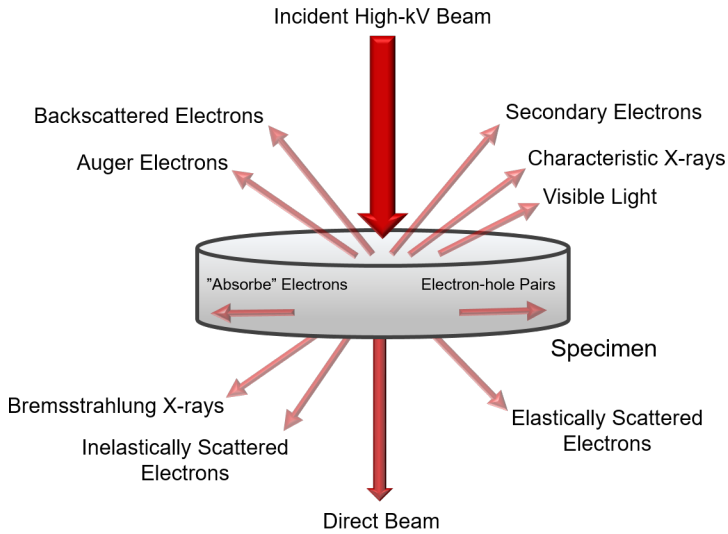


Figure 3.8: Schematic drawing of an high-energy electron beam incident on a solid sample, showing the signals generated that can be used to help characterize the microstructure. Adapted from [186]

depth of the primary electrons depends on the interaction volume, or, in other terms, on the nature of the sample and the acceleration voltage. BEs are electrons that undergo elastic scattering on the atoms at the surface. In that case, the intensity scales with the atomic number. Finally, if the sample is thin enough, like in the case of TEM analysis, the incident beam will be transmitted through the sample.

Transmission Electron Microscopy

Similar to an optical microscope with visible light, the transmission electron microscope uses a collimated beam of electrons transmitted through a thin sample (<100 nm). The images obtained using TEM are a 2D projection of the 3D structure of a sample. A TEM consists of an electron source, electromagnetic lenses, aperture, the sample chamber and detectors, all mounted into a vertical column. The parallel electron beam is created from thermionic or field emission gun. The accelerated electrons will then interact with the sample. The particle-wave duality of the electrons causes the wavefronts to interact with the sample lattice. The resolution of the projection is limited by the wavelength of the probe [186]. To achieve atomic resolution, the electrons from the probe are accelerated with acceleration voltage between 80-300 kV. The high-resolution TEM images of the NiFeO_xH_y nanoparticles acquired in this work were recorded at 80 kV

electron energy, using a FEI Titan E-Cell 80-300 ST TEM with a monochromated electron source and post objective aberration correction. The other TEM images were acquired in bright-field TEM mode in an FEI Tecnai T20 G2 equipped with a thermionic electron source, using 200 keV acceleration voltage.

Scanning Electron Microscopy

Scanning electron microscopy (SEM) relies on the measurement of the secondary or backscattered electrons. In scanning electron microscopy, the surface is scanned by a beam of electrons to gain information on the topography and composition. The electron beam is scanned in a raster pattern. The detected signal is then coupled to the position to create 2D images. In SEM, the secondary and backscattered electrons generated by an electron beam accelerated to 0.5-30 kV located on the same side as the probe are collected. The resolution of the SEM in this work goes up to 0.5-1 nm. The SEM images presented in this work were acquired at 5 kV using an FEI Helios EBS3 microscope equipped with a field emission gun and a through-the-lens detector for high resolution imaging.

Energy Dispersive X-ray Spectroscopy

The incident beam for both TEM and SEM, creates excited states that will generate X-ray emissions. The specific energies of the X-rays can be used to identify the elements in the sample. EDX line scans were recorded using an Oxford silicon drift detector.

3.3 Measuring Catalytic Activity and Stability

The electrochemical activity of NiFeO_xH_y nanoparticles and thin films, RuO_x thin films and particles, and Pt-alloy catalysts were measured. The electrochemical experiments were performed with a VMP2 multi-channel potentiostat (Bio-Logic Instruments) computer controlled using EC-Lab software. The main electrochemical techniques used in this work were cyclic voltammetry (CV) and chronoamperometry (CA). For all electrochemical measurements, a three-electrode setup was used. However, depending on the sample and reaction investigated, specific experimental conditions were used. A schematic of the electrochemical setup used for the measurements of $\text{Pt}_x\text{Y}/\text{C}$ nanoparticles as oxygen reduction catalyst is presented in Figure 3.9. The reference electrode was connected to the cell through a Luggin capillary to prevent contamination from the $\text{Hg}/\text{Hg}_2\text{SO}_4$ reference electrode. The temperature of the cell was controlled via a heated

3.3. Measuring Catalytic Activity and Stability

water jacket at 23°C. A rotating disk electrode setup was used for the ORR measurements and a Pt wired was used as counter electrode. An extra electrode, referred as "dummy" electrode, composed of the same material as the counter-electrode, was used for potential control when inserting the working electrode in the electrolyte.

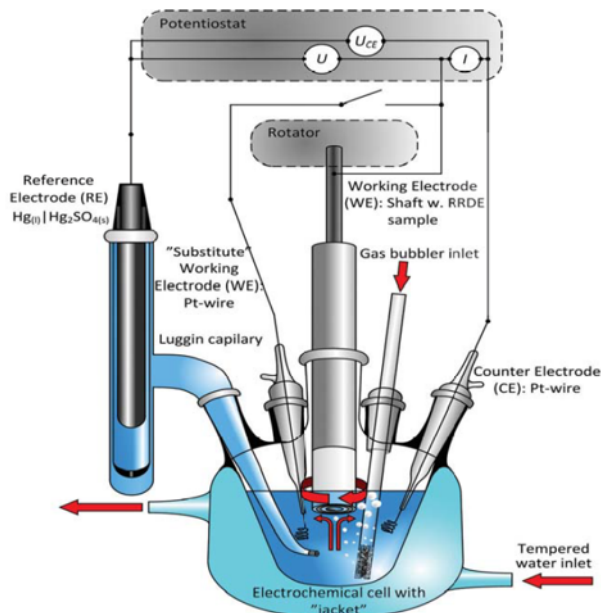


Figure 3.9: Schematic of a three-electrode electrochemical cell. Taken from [187]

The activity and stability measurement of NiFeO_xH_y nanoparticles in N_2 -saturated 1 M KOH (Semiconductor grade, pellets, 99.9%) was performed in a teflon cell to avoid Si contamination from glass corrosion. Except when otherwise stated, a rotating disk electrode setup was used. A Hg/HgO was used as reference electrode and a carbon rod as counter electrode.

To measure accurately the ruthenium dissolution of RuO_2 samples in N_2 -saturated 0.05 M H_2SO_4 , the working electrode compartment was separated from the counter-electrode compartment by a Nafion membrane. The working and counter-electrode compartments were separated to prevent re-deposition of dissolved Ru at the counter electrode. A Hg/ Hg_2SO_4 reference electrode, and a gold mesh as counter electrode were used.

All teflon and glassware were cleaned with aqua regia solution (nitric acid and hydrochloric acid ratio 1:3) and piranha solution (sulfuric acid and hydrogen peroxide 3:1) for 12 hours each, afterwards the glassware was rinsed 3 times with ultrapure water (Milli-Q water, $18.2 \text{ M}\Omega \cdot \text{cm}$).

All the potential values reported in this thesis are corrected for the ohmic losses, and calibrated to the reversible hydrogen electrode (V_{RHE}) in the same electrolyte saturated with 1 bar H_2 over a clean Pt mesh before each experiments. The ohmic resistance was measured by using impedance spectroscopy. The ohmic resistance was determined from the fitted high-frequency intercept measured using electrochemical impedance spectroscopy. The ohmic drop compensation was done by online Ohmic drop correction where 85% correction was applied for CA measurements. The ohmic drop compensation of CVs was done manually where 100% correction was applied.

Electrochemical Characterization of Pt-based Catalysts

This section focuses on the electrochemical characterization of Pt-alloy catalysts for the oxygen reduction. The CV of Pt has a clear signature in perchloric acid electrolyte. This signal is modified in the case of Pt-alloy formation, but the main features remain. Figure 3.10a shows a CV of Pt_xY alloy nanoparticles obtained from thermal annealing (see Chapter 6). The hydrogen underpotential deposition region (HUPD) is labeled in blue. At the measured potentials, hydrogen is adsorbed during the cathodic cycle and desorbed during the anodic one. The energy for the adsorption and desorption of H^+ is highly specific to the nature, and the orientation of the sites, which explain the large features observed. This process is reversible and, therefore, show very similar, if not identical, signals on the positive and negative current axis. At more negative potential than the H_{UPD} region, hydrogen evolution takes place. At more anodic potential, the platinum is oxidized. The reduction of the Pt-oxide takes place around $0.8 V_{RHE}$ (green part of the CV).

The determination of the electrochemical surface area with platinum can be done using the H_{UPD} peak area assuming that there is one hydrogen atom adsorbed per Pt site. However, when characterizing Pt-alloys, it was shown with PtNi, PtCo and other alloy catalysts [133], that the adsorption of hydrogen is affected by the electronic effect of the less noble metal. For that reason, when working with Pt-alloy catalyst, it was suggested that measuring the ECSA with the CO stripping method is more reliable, as it is not influence as easily by electronic effects. The CO stripping method can be summarize as follows. CO molecules adsorb strongly to the surface of platinum, so when applying a potential lower than $0.4 V_{RHE}$, CO will adsorb at the surface of platinum over other anions present in solution. Once CO is adsorbed at the surface of platinum, the solution is purged with an inert gas, in this case Ar, to remove the leftover CO. Once all the CO molecules dissolved in the electrolyte are removed, the potential is increases

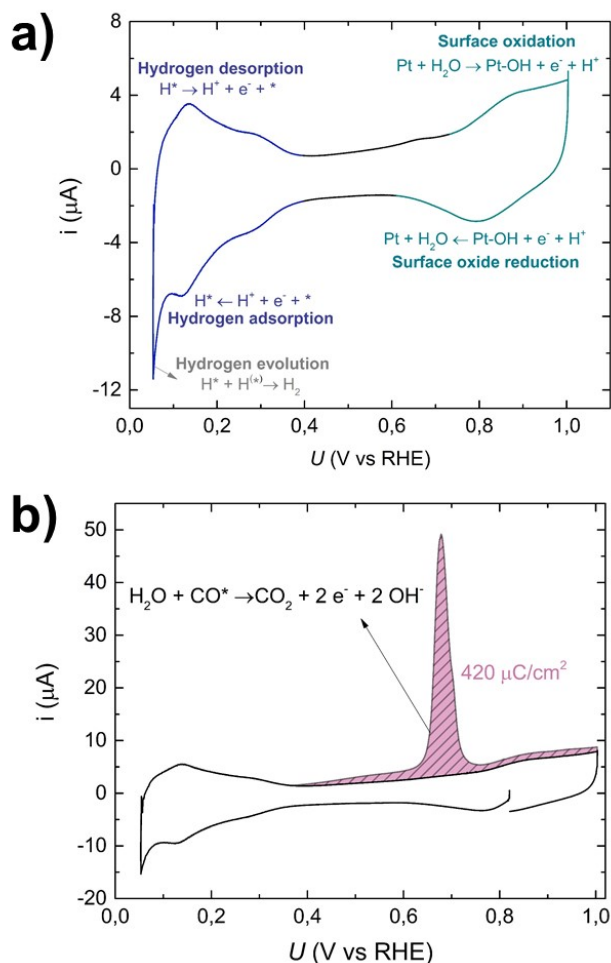


Figure 3.10: a) Cyclic voltammetry of Pt_xY nanoparticles and b) CO stripping measurement in Ar-saturated N_2 0.1 M HClO_4 at 10 mV/s

slowly to more anodic values, and the CO is oxidized to CO_2 . As shown in Figure 3.10b, a sharp peak is obtained when CO oxidizes. Steric repulsion between CO molecules limits the number of molecules that can adsorb to the surface, which explain why the CO-to-Pt ratio is lower than one. However, because this number is not well established and, for sake of simplicity, a 1:1 CO:Pt ratio was used. For a two electron process, and for CO:Pt ratio of 1:1, a charge of $420 \mu\text{C}/\text{cm}^2$ was used [188] and chosen for consistency with previous work from our group [162,164]. CO poisoning experiments were done by bubbling CO gas while holding the potential at 0.1 V_{RHE} at 1600 rpm. The CO was then removed from the electrolyte by purging with Ar,

after what the CO was oxidized by going to anodic potentials.

We assume that the coverage of CO is not affected by surface structure and alloying even though it was shown that both CO and H adsorption are affected by these factors [61,189,190]. For that reason, the ECSA determined using the CO stripping method is most likely lower than the true value.

As mentioned above, a rotating disk electrode (RDE) setup was used to mitigate the mass transport limitation associated to measuring the activity in a stagnant electrolyte. The current measured when using a RDE setup can be explained according to the equation:

$$j_d = 0.62 \cdot n \cdot F \cdot S \cdot D^{(2/3)} \cdot C^{(-1/6)} \cdot \omega^{(-1/6)} \quad (3.3)$$

where n is the number of electrons transferred, F the Faraday constant, S the area of the electrode, D the diffusion coefficient of the reactant in the electrolyte, ν the viscosity of the electrolyte, C the reactant concentration and ω the rotation speed of the electrode. As presented, for a specific electrochemical reaction, the current measured for a transport limited process will increase with rotation speed. Figure 3.11 presents a typical CV recorded with a platinum-based catalyst.

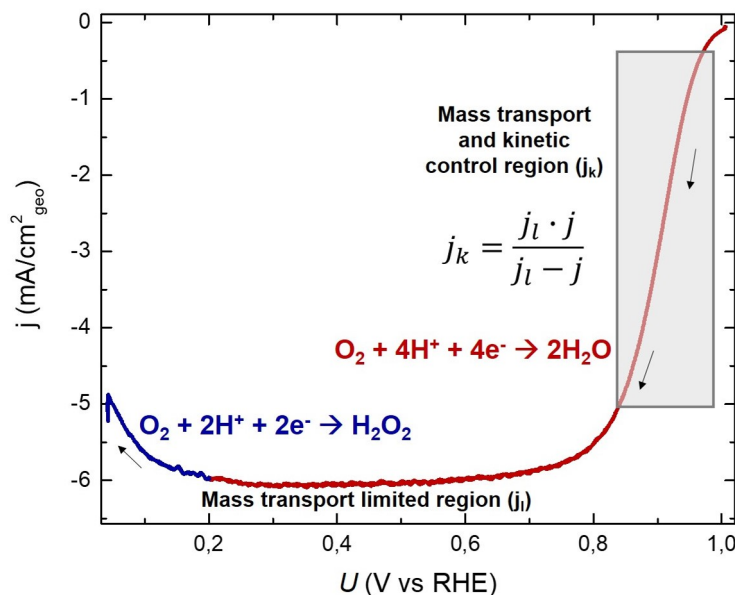


Figure 3.11: Oxygen reduction current on Pt_xY nanoparticles obtained from high temperature synthesis for 360 min. The cyclic voltammetry was recorded in 0.1 M HClO_4 at 50 mV/s at 1600 rpm. The transport and kinetic control region are highlighted. The current in red is associated to the O_2 reduction to H_2O and the blue current to H_2O_2 . The current is normalised by the geometric surface area.

3.3. Measuring Catalytic Activity and Stability

The activity was evaluated at $0.9 V_{RHE}$, where the current is mass transport and kinetically limited. To account only for the kinetic current (j_k), equation was used:

$$j_k = \frac{j_l \cdot j}{j_l - j} \quad (3.4)$$

Where j_l is the limiting current at $0.4 V_{RHE}$ and j the raw current.

3.3.1 Inductively Coupled Plasma Mass Spectrometry

Inductively coupled plasma-mass spectrometry (ICP-MS) is an elemental analysis technique capable of detecting metals and several non-metal elements for concentration as low as part per quadrillion. It has many advantages, such as being a multielemental method, including isotopic analysis, and having a high sample throughput. The ICP-MS was used for Ru detection, for which the concentration can go as low as 0.1 ppb [90].

The ICP-MS employs plasma as ionization source and a mass spectrometer as detector. Figure 3.12 shows a schematic representation of the ICP-MS. The liquid sample is transformed into aerosol droplets using a nebulizer, and introduced into an Ar plasma. The Ar plasma dries the aerosol, dissociates the molecules, if any, and creates singly charge ions. The ions reach the MS, where they are separated based on their mass-to-charge ratio using a quadrupole. The quadrupole which works with radio frequency (RF) and four rods to filter the ions. The system used in this work is from Thermo Fisher Scientific (model iCAP-QC ICP-MS). To quantify the amount of product detected, a calibration curve from 0.1 ppb to 100 ppb made from 1000 ppm metal solution was measured prior to every analysis.

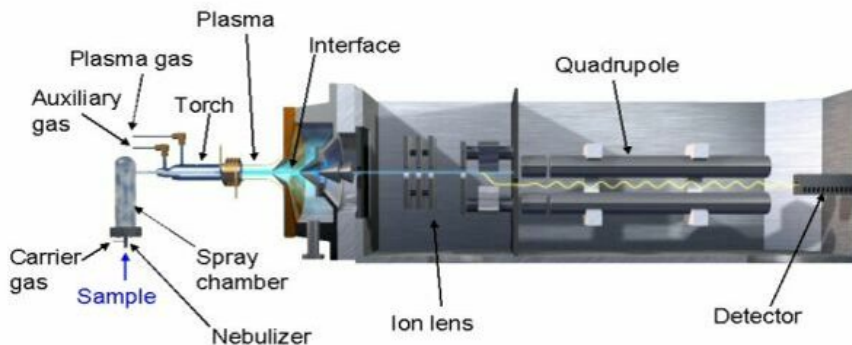


Figure 3.12: Schematic representation of an inductively coupled plasma mass spectrometry using a quadrupole mass spectrometer

3.3.2 Electrochemistry-Mass Spectrometry

Electrochemistry-mass spectrometry (EC-MS) enables real-time detection of electrochemical desorption phenomena. The system is able to catch reactant molecules desorbing from the surface of a flat electrode. These molecules will then be passed to a MS for quantitative analysis. One of the main challenges in such experiments is that electrochemical processes run in wet environments, while the products detection using MS requires high vacuum. The EC-MS consists of a microfabricated membrane coated with a fluorinated polymer and a capillary as described in [191]. The distance between the working electrode and the membrane is called the working distance, and is $100\ \mu\text{m}$. The working compartment consists of $2\ \mu\text{L}$ of electrolyte. The dissolved gasses, once in touch with the membrane, evaporate and are delivered to the MS through capillary using He as carrier gas. The time response of the EC-MS is below 1s. Also, this technique is highly sensitive to certain products: those with relatively fast diffusion and high volatility. It can detect up to 0.05 monolayer of H_2 desorbing from a Pt surface with a signal-to-noise ratio around 20 [191], for example. In this thesis, the EC-MS setup was used specifically for isotope labelling experiments with NiFeO_xH_y nanoparticles. Figure 3.13a shows a schematic of the EC-MS setup, and Figure 3.13b is a photograph of the stagnant thin-layer cell-electrode-membrane chip-interface block assembly.

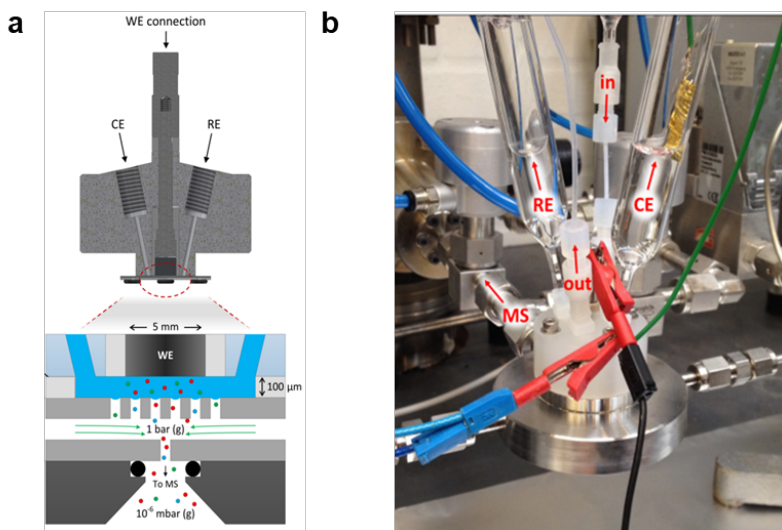


Figure 3.13: a) Cross section of the cell-electrode assembly and membrane chip showing two of the four liquid channels of the cell. b) photograph of the stagnant thin-layer cell – electrode – membrane chip – interface block assembly. Figure adapted from [191]

Activity and Metal Dissolution Trends of Rutile RuO₂ under Oxygen Evolution Conditions

Ru-based catalysts are among the most active for the oxygen evolution reaction (OER) in acid electrolyte, but are also known to corrode under oxygen evolution conditions [34,64,122]. In this work, we investigated well-defined catalysts of rutile RuO₂ with the (111), (101) and (001) orientations developed recently [35,72,73], RuO₂ (110) single crystal [192] and commercial rutile RuO₂ particles for the OER in 0.05 M H₂SO₄. First, we compared the oxygen evolution current of different RuO₂ surface facets with particles. Second, we quantified the amount of Ru dissolved during the oxygen evolution, using inductively coupled mass spectrometry (ICP-MS), and tried to identify if corrosion is structure sensitive. Last, we compared the activity and stability of the RuO₂ catalysts to see if the *universal* stability-activity argued by Markovic and co-workers [78,122,123] applies to RuO₂ surfaces.

The rutile RuO₂ oriented thin films used in this work were deposited by Reshma R. Rao and Jonathan Hwang from the Electrochemical Energy Lab at the Massachusetts Institute of Technology. The physical characterization, including X-ray diffraction and Brunauer–Emmett–Teller measurements, of the RuO₂ particles, was performed by Binghong Han. I performed the electrochemical activity and stability measurements of the samples and the inductively coupled plasma mass spectrometry measurements, and contributed to the analysis of the results.

4.1 Experimental Section

4.1.1 Sample Preparation

Rutile RuO₂ thin films with (100), (001), (101), and (111) orientation were grown by pulsed laser deposition, as reported previously [35,73]. The (100) film was grown on a (001)-oriented SrTiO₃ substrate and the (001), (101) and (111) films were grown on (001), (101) and (111) oriented TiO₂ substrates. Representative X-ray diffraction spectra and atomic force microscopy images, taken from [193], are presented in Appendix A (Figure A.1). For the (110) orientation, a single crystal electrode was used, which was prepared by oxidative evaporation/redeposition of RuO₂ powders as described in reference [192,194]. The nanoparticles were purchased commercially (Sigma-Aldrich, 99.9% trace metal base). Physical characterization of the particles using X-ray diffraction and transmission electron microscopy, performed by Binghong Han, are presented in Figure A.2.

4.1.2 Electrochemical Measurements

At first, the corrosion of RuO₂ nanoparticles was investigated by stability testing ranging from 1.4 to 1.7 V_{RHE}. According to the Pourbaix diagram, the reversible potential for RuO₄ formation is 1.39 V_{RHE} [106], and dissolution can be expected for potentials more positive than this value. Metal dissolution on the oriented thin films was measured for potentiostatic measurements performed at potentials ranging from 1.6 to 1.7 V_{RHE}. Specifically for the oriented thin films, we have experienced that tests at potentials higher than 1.7 V_{RHE}, caused delamination and yielded a poor reproducibility of the OER current. Also, the (100) surface was tested, but high instability of the thin films throughout the measurement prevented us from measuring an accurate corrosion rate. For this reason, only the initial activity of the (100) surface could be measured. The instability could be a result of the design of the samples itself. Finally, the capacitance was measured using CV at 100 mV/s before and after the stability measurements.

The electrolyte was sampled three times per stability test: 1) before and ii) after the insertion of the electrode and iii) after the stability measurement. The concentration of Ru was detected using ICP-MS, and quantified using a calibration curve (see Figure A.3). The amount of Ru measured for the two-hour test was then normalized to the real surface area of the electrode.

4.2 Results

We first evaluated the activity of rutile RuO_2 particles for the OER by cycling up to $1.7 V_{RHE}$ in $0.05 \text{ M H}_2\text{SO}_4$. The average activity of the as-prepared samples is presented in Figure 4.1a, by the blue curve. Then, the impact of the stability measurement on the activity at various anodic potentials was evaluated using a two-hour potentiostatic measurement. More specifically, stability tests were performed at 1.4 , 1.5 , 1.6 and $1.7 V_{RHE}$, as shown in Figure 4.1b. The activity using CV was re-measured post-stability measurements, and the recorded current is presented in Figure 4.1a.

One interesting observation coming from the polarization curves in Figure 4.1a are the two slopes observed: one from 1.45 to $\sim 1.6 V_{RHE}$, and the other one from ~ 1.6 to $1.7 V_{RHE}$. To more easily compare the variation in current after each stability measurement, the initial activity values, represented by the bars in blue in Figure 4.1c, are plotted at $1.55 V_{RHE}$ (dashed) and $1.7 V_{RHE}$ (filled), and compared to the post-stability test current for the same potentials. It is observed that the activity decreases, and that this loss in activity is more significant at more anodic potentials. Indeed, the current at $1.55 V_{RHE}$ after 2 hours at $1.7 V_{RHE}$ is $2.1 \text{ mA/cm}^2_{\text{RuO}_2}$, while the current associated to the stability test at $1.4 V_{RHE}$ is $54.9 \text{ mA/cm}^2_{\text{RuO}_2}$, i.e. closer to the initial current density of $75.7 \text{ mA/cm}^2_{\text{RuO}_2}$. Representative CVs of each sample are available in Figure A.4 and A.5. The amount of Ru dissolved for the two-hour measurements as a function of the potential is presented in Figure 4.1d. It is observed that the amount of Ru dissolved increases with the applied potential, and appears to follow an exponential trend.

The study of well-defined crystallographic structure is essential for a more fundamental understanding of surface processes. For that reason, the catalytic activity of well-defined surfaces, namely RuO_2 thin films with (001), (101) and (111) preferential orientation and RuO_2 (110) single crystal, was measured. Schematics of the rutile RuO_2 structures are presented in Figure 4.2a. A Ru atom can form up to 6 bonds in a rutile structure. The coordinately unsaturated Ru sites (Ru CUS) were identified as the active sites for the oxygen evolution on rutile RuO_2 [53,54]. It was also demonstrated that the activity of RuO_2 scales with the number of CUS Ru-O bond [73]. Each Ru_{CUS} is linked to five Ru-O bonds at the surface of a (110) and (101), and provides one surface site for the reaction. On the other hand, the Ru_{CUS} of the (001) and (111) surface makes four Ru-O bonds, and has two empty sites for the reaction. As such, the density of CUS Ru-O bonds varies with the crystallographic structure, and decreases as follow: (001) < (101) < (111) < (110). The activity recorded at $1.6 V_{RHE}$ taken from the first CV is plotted as a function of the number of

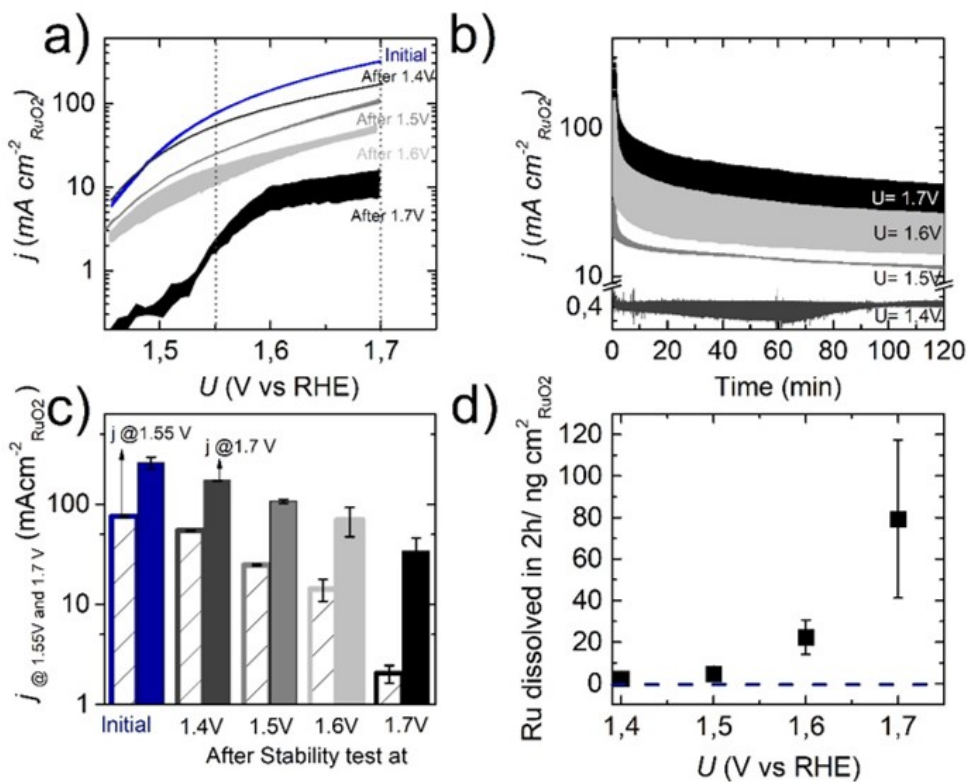


Figure 4.1: a) Tafel plots of RuO₂ particles measurements in 0.05 M H₂SO₄, measured by cyclic voltammetry at 10 mV/s based on 3 independent samples (averaged forward and back and ohmic drop corrected). b) Current densities at 1.55 V_{RHE} and 1.7 V_{RHE} from the polarization curves presented in a). c) Potentiostatic measurements at 1.4, 1.5, 1.6 and 1.7 V_{RHE}. d) Ru dissolution measured using inductively coupled plasma mass spectrometry (ICP-MS) after the two-hour stability test and normalized to the RuO₂ area. The electrolyte was sampled before and after the constant potential measurement. The dotted line is a guide to the eye for zero Ru dissolution.

4.2. Results

CUS Ru-O bonds per nm^2 of unit cell determined for each facet. Figure 4.2b shows a correlation between the density of CUS Ru-O bonds and the activity measured. The observed trend, i.e. increase of current density with CUS Ru-O bonds, corroborates what was reported in 1 M KOH by Shao-Horn and co-workers [35,72,73]. This similarity suggests that the active sites in acid and alkaline electrolyte are the same.

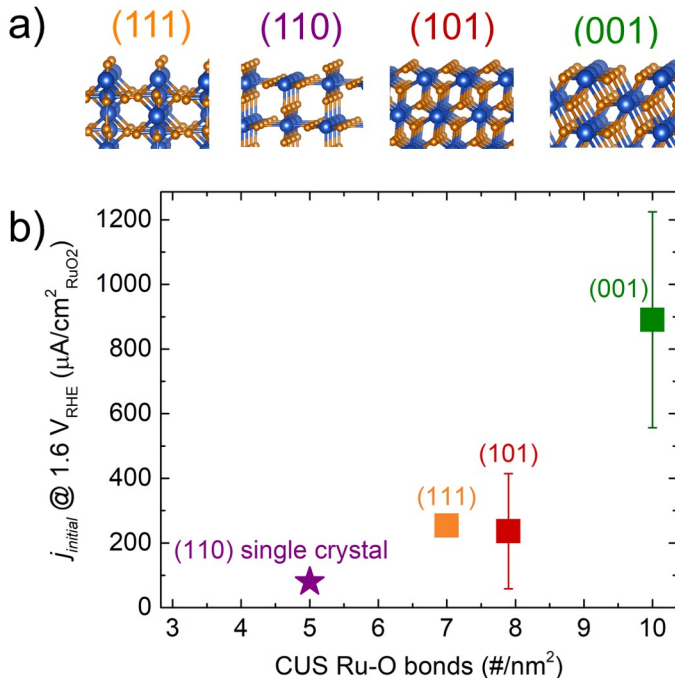


Figure 4.2: a) Schematics of the (111), (110), (101) and (001) facets, and b) Average current density at $1.6 V_{\text{RHE}}$ measured during the first cyclic voltammetry at 10 mV/s in $0.05 \text{ M H}_2\text{SO}_4$ as function of site density of Ru_{CUS} .

Similarly to the experiments performed with the RuO_2 particles, corrosion measurements on preferentially oriented thin films were performed at 1.6 and $1.7 V_{\text{RHE}}$, and the Ru dissolution was monitored using ICP-MS. Figure 4.3a and b present the current generated from (001), (101) and (111) RuO_2 surfaces at 1.6 and $1.7 V_{\text{RHE}}$, respectively. At $1.6 V_{\text{RHE}}$, the potentiostatic measurements show a smooth decay in activity over the two-hour measurement time. At $1.7 V_{\text{RHE}}$, more drastic fluctuations in the current are observed for the (001) and (101) films over the 2 hours. For both potentials, the activity ranks as follows: $(001) > (101) > (111) \approx \text{particles}$.

Figure 4.3c compares the amount of Ru dissolved during the two-hour measurements at 1.6 and $1.7 V_{\text{RHE}}$. The current and amount of Ru dis-

solved for the RuO₂ particles, first presented in Figure 4.1, were added to Figure 4.3 for comparison with the oriented thin films. The highest amount of Ru dissolution for both potentials was measured for the (001) facet, followed by the (101) and (111) facet. RuO₂ particles have the smallest dissolution rate. The amount of Ru dissolved is higher at 1.7 V_{RHE} compared to 1.6 V_{RHE}, and the amount of Ru is dependant on the surface structure. The capacitance of the oriented thin films was measured before and after the chronoamperometric measurements at 1.6 and 1.7 V_{RHE}, and are presented in Figure 4.4 a and b, respectively.

The CVs recorded after the CAs at 1.6 V_{RHE} (darker colors) for the three different preferentially oriented surfaces resemble the initial ones (lighter colors), except for a slight increase in the capacitance value for the surface (red curves). A substantial difference is, however, observed when comparing the CVs recorded before and after the CA at 1.7 V_{RHE} (Figure 4.4b). The biggest change in capacitance value is observed for the (001) surface, with a 2.3-fold increase, followed by the RuO₂ (111) sample, with a capacitance increase of 1.3 times. The capacitance recorded for the RuO₂ (101) remains similar before and after stability test at 1.7 V_{RHE}.

To evaluate the activity and stability of the samples for longer operating time, the oriented thin films used for the stability measurement at 1.6 V_{RHE} were submitted to a second stability test using the same experimental conditions. Figure 4.5a and c shows the OER currents measured for the first and second stability tests at 1.6 V_{RHE}, respectively. The insets show the amount of Ru dissolved during the two-hour experiments. As mentioned above, during the first stability test, the current of the (001), (101) and (111) oriented thin film of RuO₂ decreases over time and converge to a more similar value. The (110) single crystal shows a different current-profile than the other samples. Its current increases during the first ~40 minutes before reaching a steady state. The current recorded for the (110) single crystal is higher after 2h at 1.6 V_{RHE} than it was at the beginning of the measurement. The Ru dissolution for the first stability test ranks as follow: (001) > (101) > (111) > (110) ≈ particles.

Interesting observations can be made when comparing the second stability test to the first one. First, the initial current of all RuO₂ surface facets are higher than what was observed at the end of the two-hour measurement for the first stability test (Figure A.8). Except for the (110) single crystal, the activity measured at 1.6 V_{RHE} is similar in between the two stability test measurements. On the other hand, the amount of Ru dissolved is smaller for the second stability test (Figure 4.5d) than it was for the first one. Except for RuO₂ (101), it seems that the corrosion of Ru reached similar values for all samples. Overall we observed that while the drop in activity is not significant when comparing the stability measurements 1 and

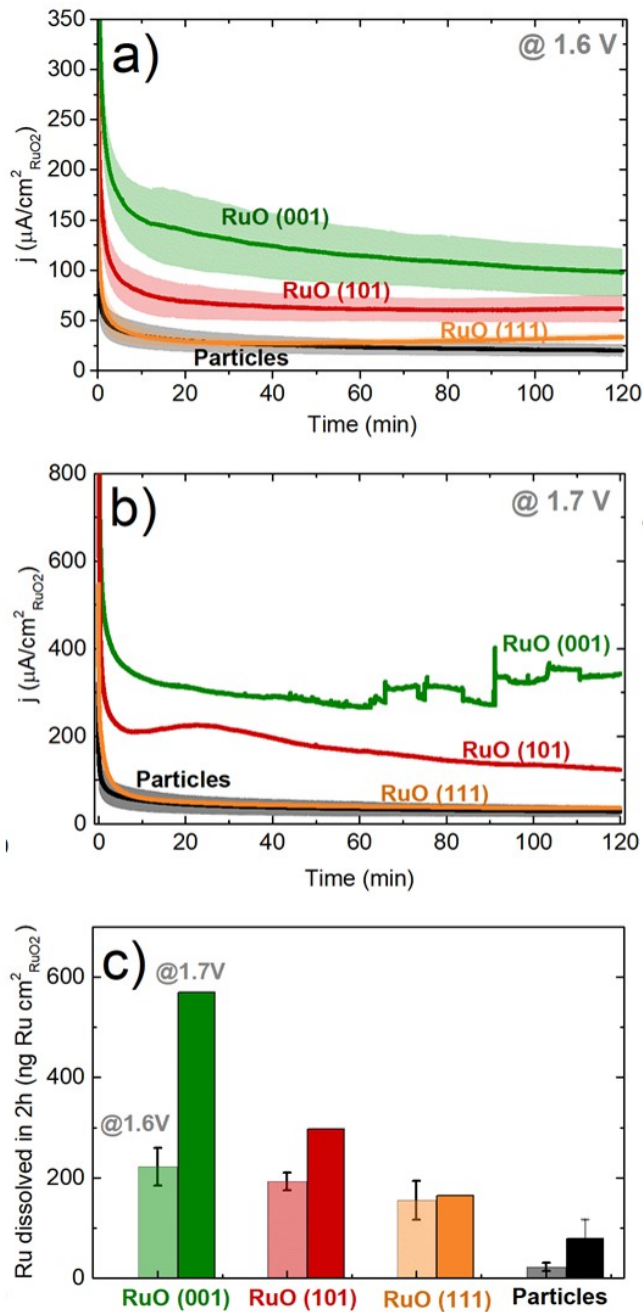


Figure 4.3: Potentiostatic measurements at a) 1.6 V and b) 1.7 V in 0.05 M H_2SO_4 and c) the respective amount of Ru dissolved during these electrochemical testing for the (111), (101) and (001) surfaces.

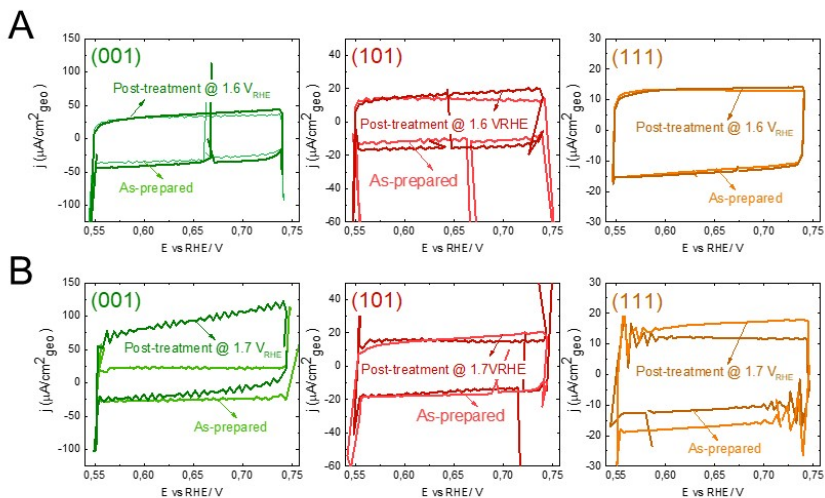


Figure 4.4: Capacitance measurements at 100 mV/s of the (001) (green), (101) (red) and (111) (orange) rutile RuO₂ surfaces before and after potentiostatic measurements at a) 1.6 V_{RHE} and b) 1.7 V_{RHE} in 0.05 M H₂SO₄

2, a drastic difference is observed when comparing the amount of metal that dissolved from the electrode.

To investigate the possible relationship between the activity and stability towards oxygen evolution of rutile RuO₂ powder and well-defined surfaces, including the (110) single crystal, the amount of Ru dissolved for the first and second stability test is plotted as function of the average current density measured over the two-hour stability test, as shown in Figure 4.6. The squares represents the oriented thin films, the stars the (110) single crystal, and the triangles the commercial RuO₂ particles.

For the first stability measurement, it is observed that the average current density of the (001), (101) and (111) surface is proportional to the amount of Ru dissolved, with (001) as the most active but also the least stable. The (110) single crystal and the RuO₂ particles, have very similar catalytic activity around 45 μA/cm². Interestingly, the Ru dissolution of the single crystal and particles are slightly different. Notably, the (110) single crystal has a lower dissolution rate. It is also worth noting that while the average current density of the (110) single crystal is lower than the (111) facet, its Ru dissolution is higher. Contrary to the results obtained for stability test 1, no trend is observed when comparing the results obtained from stability test 2; no relationship can be established between stability and activity.

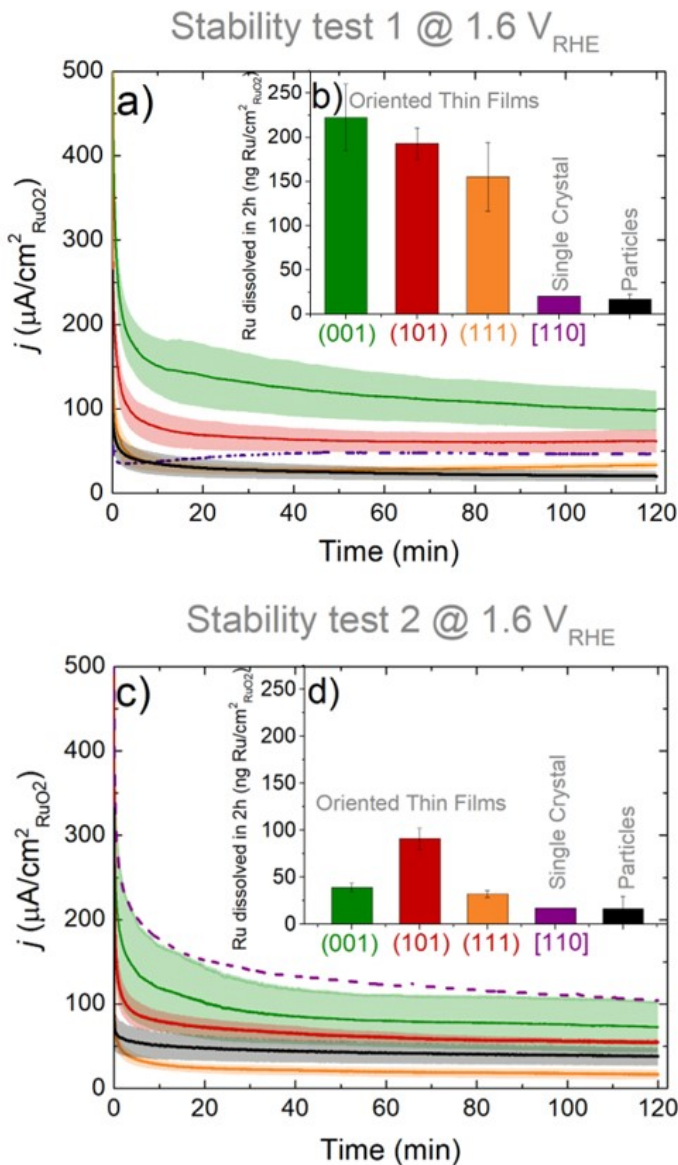


Figure 4.5: Two-hour potentiostatic measurements at 1.6 V_{RHE} in 0.05 M H₂SO₄. a) First stability and b) Second stability test for the (111), (101), (110) and (001) surfaces. The purple dashed line is associated to the (110) single crystal. The insets (B, D) show the corrosion rate of Ru of each oriented thin films measured for their respective stability test.

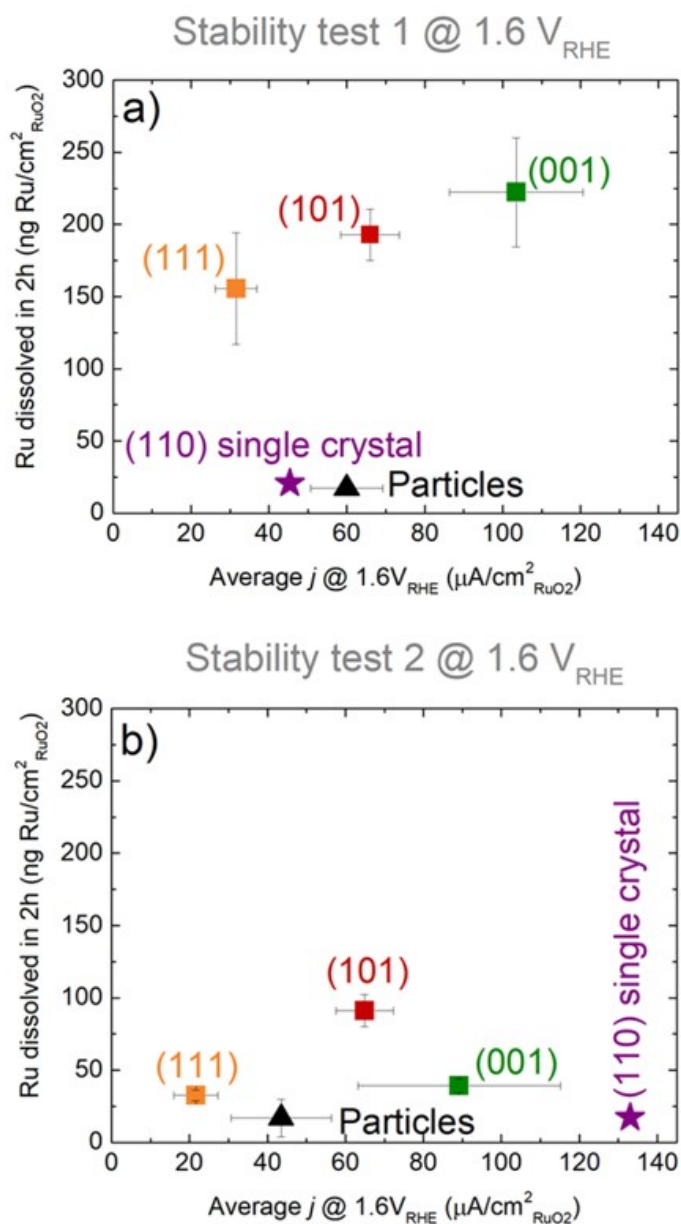


Figure 4.6: Evaluation of the activity-stability relationship through the analysis of the average current at 1.6 V_{RHE} obtained from the stability tests as function of the amount of Ru dissolved for a) the first and b) second stability test, respectively. The squares represent the (001), (101), (111) oriented thin films, the star the (110) single crystal and triangles the commercial RuO_2 particles.

From the amount of Ru dissolved during the first stability test at 1.6 V_{RHE} , and assuming RuO_4 as dissolution product [81], the faradaic efficiency of dissolution upon OER was calculated. Figure 4.7 shows that the faradaic efficiency to dissolution varies from 0.02% for the RuO_2 particles up to 0.11 to 0.26% for the oriented thin films.

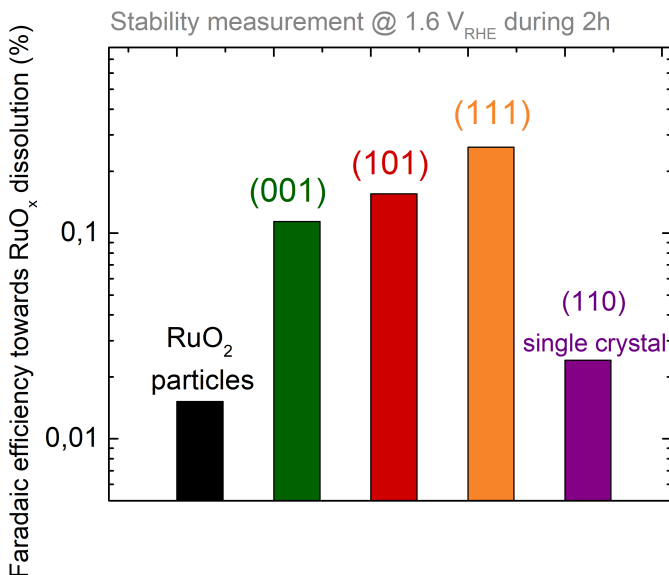


Figure 4.7: Comparison of the Faradaic efficiency of dissolution for well-defined surfaces and particles of RuO_2 catalysts in 0.05 M H_2SO_4 electrolyte. The Ru dissolution was measured from two-hour stability measurement at 1.6 V_{RHE} .

The activity of all rutile RuO_2 surfaces were measured using CV for the as-prepared samples, after 2h, and 4h at 1.6 V_{RHE} . Figure 4.8 shows the average current forward and back at 10 mV/s. To avoid corrosion, and thereby modifying the surface before the stability measurement, only one CV was performed in each case. As observed in Figure 4.8a, the activity of the as-prepared samples ranks as followed: (100) \approx (001) $>$ (111) \approx particles $>$ (110) single crystal. A reasonably narrow scatter is observed, except in the case of the (101) surface facet. The (101) thin film was extremely unstable under experimental conditions at 1.6 V_{RHE} , and delaminated shortly after the start of the first stability test. For that reason, only the initial CV can be presented.

The CVs of the oriented thin films and particles after the two-hour measurement at 1.6 V_{RHE} show a slightly different trend. According to Figure 4.8b, (001) surface remains slightly more active than the (101). The

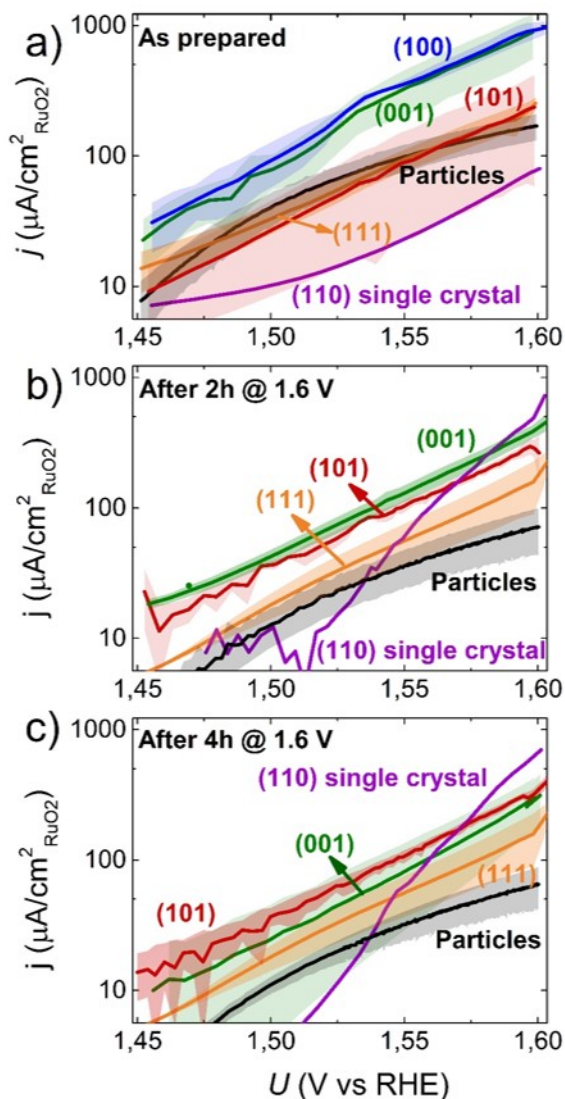


Figure 4.8: Tafel plot of OER activity in 0.05 M H₂SO₄ of (100), (001), (101) and (111) oriented thin films, (110) single crystal and particles, measured by cyclic voltammetry at 10 mV/s (taking mean value of forward and backward cycle and ohmic drop corrected) of the as-prepared oriented thin films (a), after 2h at 1.6V_{RHE} (b) and 4h at 1.6 V_{RHE} (c).

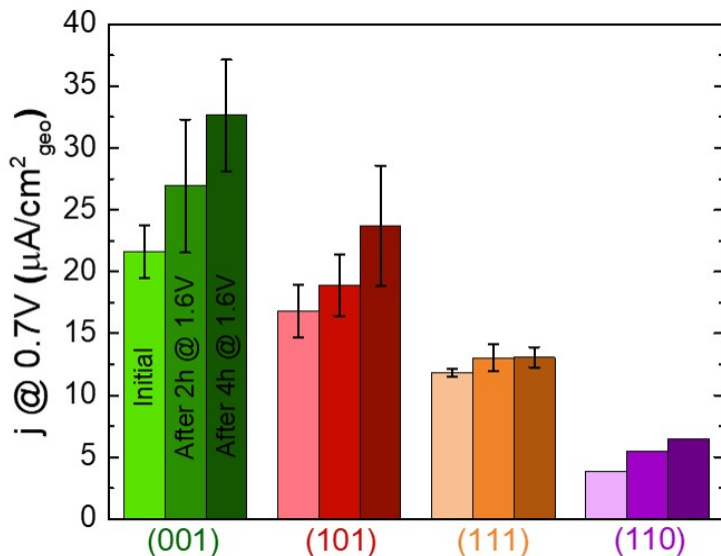


Figure 4.9: Average capacitance values for the (001), (101) and (111) oriented thin film and the (110) single crystal taken from a cyclic voltammeteries at 100 mV/s in 0.05 M H₂SO₄. The current at 0.7 V_{RHE} for the the as-prepared samples, and after stability test at 1.6 V_{RHE} for 2h and 4h are presented.

superior activity of the (101) compared with the (111) oriented thin films is also clearer at this point. The RuO₂ particles are the least active according to our activity measurement. The single crystal became more active over time with a different slope. Indeed, it has a current density of around 728 μA/cm²_{RuO₂} at 1.6 V_{RHE} compared to 74 μA/cm²_{RuO₂} for the as-prepared sample. Except for the (110) single crystal, all other catalysts suffered a loss in activity. Finally, the activity after 4 hours of electrolysis at 1.6 V_{RHE} is presented in Figure 4.8)c. A similar trend after 2h and 4h at 1.6 V_{RHE} is observed.

Capacitance measurements, that relate to the electrochemical surface area and, therefore, the roughness of the samples, were recorded at 100 mV/s. The capacitance of the as-prepared oriented thin films, and after 2 and 4h at 1.6 V_{RHE} are presented in Figure A.6-A.7. The current at 0.7 V_{RHE} taken from these CVs are reported in Figure 4.9. As observed in Figure 4.4, when comparing the capacitance after stability test at 1.6 and 1.7 V_{RHE}, there is an increase in current for longer stability test that translates into higher surface roughness. The surface that exhibits the highest stability over time according to the capacitance measurement is the RuO₂ (111).

4.3 Discussion

The Ru dissolution during oxygen evolution observed from well-defined surfaces (Figure 4.3 and 4.5) and particles of RuO₂ (Figure 4.1) corroborates what was previously reported in the literature, i.e that OER is accompanied by metal dissolution [64,78,81,122]. The amount of dissolved Ru increases with anodic potential (Figure 4.1 and 4.4). On average, the current corresponding to Ru dissolution for the well-defined surfaces and particles is < 0.26% of the total OER current. From the stability measurements performed in this work, we thus assumed that all the current density is going to O₂ evolution. This low faradaic efficiency to dissolution is comparable to what was reported for other thermally annealed RuO₂ catalysts for similar experimental conditions, like the sputter deposited film [68] and RuO₂ mass-selected nanoparticles [83]. From the amount of dissolved Ru measured, we were able to approximate the number of monolayers (ML) that it represents. We calculated that the amount of dissolved Ru at 1.6 V_{RHE} corresponds to ca. 1.5 to 2.5 ML, depending on the surface orientation. At 1.7 V_{RHE}, we expect that the surface reconstruction is more pronounced as between 2 to 3.5 ML are dissolved. The dissolution of Ru explains why we observed an increase in surface roughness through the capacitance measurements (Figure 4.4 and 4.9). However, even though Ru dissolution is affecting the surface termination and morphology, it only represents ~4% of the oriented thin films.

In this work, it is also noted that stability measurements result in a loss of catalytic activity over time. This decrease in current density implies that the freshly exposed surfaces, as a result of Ru dissolution, have different RuO₂ terminations than the as-prepared ones. The loss in activity during the stability tests can also be related to bubble formation. The static measurement does not allow the removal of the O₂ gas as well as a rotating disk electrode setup would. Therefore, some of the active sites at the surface of the electrode can be blocked, which translates into a lower current. The formation of bubbles blocking active sites is evident when comparing the current from the first stability test at 1.6 V_{RHE} after 2h to the initial current of the second stability test at 1.6 V_{RHE} as bubbles were removed in-between (Figure A.8).

As shown in Figure 4.3, the current profile for the stability measurement at 1.7 V_{RHE} is different from the one at 1.6 V_{RHE}. It seems that there is a threshold where the (001) and (101) surfaces become highly unstable. We hypothesize that this could be explained by the reach of surface intermediates with more oxidized Ru state [77], and therefore more prone to dissolution or delamination.

Using the measured Ru dissolution and current densities recorded at constant potential measurements, we investigated if a relationship between the activity and stability of the well-defined surfaces and particles of RuO₂ could be established. The activity from the potentiostatic measurements at 1.6 V_{RHE} for the first 2h (Figure 4.5) decreases in the order (001) > (101) > (111), and the same trend is observed for metal dissolution. These observations show that the corrosion rates are intrinsically dependant of the surface atoms, as different facets have different dissolution rates. For the second stability test, no such trend between the current and the Ru dissolution is observed. While it is clear from these results that OER is accompanied by metal dissolution, the rate at which the Ru is dissolved varies, and is highly dependant on the structure, and possibly the surface defects as previously reported [90,120]. Our results suggest that the activity and the stability are decoupled as the Ru dissolution does not match the change in current density. From the first stability test, the (001) surface is the most active and has the highest dissolution rate/ lowest stability. When this sample is submitted to a second stability test, the lower corrosion rate suggests that the samples contained fewer unstable sites, but the activity remained similar to the initial one. The relationship between activity and stability established using the measured well-defined surfaces of RuO₂ contradicts what was already reported in the literature for other Ru-based catalysts tested in acid [64,68,73,122] and alkaline electrolyte [64,79], which show that there is a correlation between metal dissolution and the activity during the oxygen evolution.

We suspect that density of undercoordinated sites such as kinks, steps and edges, plays a crucial role in the overall stability of surface atoms [64, 119–121,195]. We suggest that the density of surface defects for the oriented thin films scales like: (001) > (101) > (111) > (110). It is also reasonable to assume that the (110) has few defects, as it is a single crystal, compared to oriented thin films. In a similar manner, the RuO₂ particles and (110) single crystal have similar initial activity, but different initial corrosion rates. Our results suggest that RuO₂ corrosion is much more pronounced during the first stability test due to a higher amount of defects at the surface and as the uncoordinated sites dissolve over time, the surface reaches a more stable state. Indeed, except for the (101) surface, all surfaces exhibit a similar dissolution rate during the second stability test.

4.4 Conclusion

The aim of this work was to investigate the possible relationship between activity and stability obtained from RuO₂ particles, preferentially oriented RuO₂ surfaces and a RuO₂ single crystal. Our results show that as observed in alkaline [73], the current density of rutile RuO₂ surfaces scales with the density of CUS Ru-O bonds.

We performed potentiostatic measurements of RuO₂ electrodes coupled to the analysis of the Ru dissolution in the electrolyte using ICP-MS. From our results, we note that the surface structure has a direct impact on the activity and the stability of the electrode. However, we identified different sites responsible for each process, i.e. CUS Ru-O bond as active sites and surface defects as the most unstable sites, explaining why we do not see any evident links between activity and stability. We believe that the more general anti correlation suggested is not enough to explain all the phenomena observed. The results show that catalysts undergo drastic changes due to surface reconstruction, making their investigation very challenging. We think that in situ methods and more sensitive techniques enabling investigation at lower potentials are of high interest for future research on the topic [77,196,197].

Investigation of NiFeO_xH_y Nanoparticles for the Oxygen Evolution

As presented in chapter 1.2, it is well-established that NiFeO_xH_y is among the best metal catalysts for the oxygen evolution reaction (OER) in alkaline electrolyte [105]. Despite the many studies on NiFeO_xH_y catalysts, several questions remain regarding the origin of its high activity. In this work, we used a model system of NiFeO_xH_y nanoparticles deposited through the gas-aggregation technique, described in Section 3.1.1, to investigate (i) the impact of nanoparticle size, (ii) the influence of interparticle distances, and (iii) the participation of lattice oxygen and intercalated water in the OER. We measured the catalytic activity in 1.0 M KOH electrolyte using the RDE setup at 1,600 rpm, and complemented these experiments with X-ray photoelectron spectroscopy, high-resolution transmission electron microscopy and scanning electron microscopy.

The powerful physical method we used to synthesize the NiFeO_xH_y catalyst allows us to vary the surface coverage while having perfect control over the mass, and consequently the size, of the nanoparticles. Thus, using 6.7 nm NiFeO_xH_y particles, we studied the influence of particle proximity on the oxygen evolution. The interparticle interactions were studied earlier using Pt clusters [198] and Cu nanoparticles [199] for the oxygen and carbon dioxide reduction reaction, respectively. In both cases, a positive effect, i.e. an increase in activity and/or selectivity, was registered with decreasing edge-to-edge interparticle distances.

We investigated the bulk activity of NiFeO_xH_y nanoparticles and electrodeposited thin films. Participation of bulk catalyst in the overall activity refers to oxygen coming either from the oxyhydroxide compound or the intercalated water in-between the nanosheets of Ni and Fe [100]. To answer the open question regarding bulk activity, we performed isotope labeling ex-

periments using the electrochemistry-mass spectrometry (EC-MS). In this isotopic study, we prepared NiFeO_xH_y using ¹⁶O or ¹⁸O oxygen isotopes, and monitored the signals related to O₂ evolution, m/z of 32 (¹⁶O¹⁶O), m/z of 34 (¹⁸O¹⁶O) and m/z of 36 (¹⁸O¹⁸O), in an electrolyte having a different isotope. Finally, we used low-energy ion scattering (LEIS) to support the observations made using the EC-MS and isotopic measurements.

In this work, the deposition of the NiFe nanoparticles and most of the physical characterization was performed by Béla Sebők. Elisabetta Maria Fiordaliso from the Center of Electron Nanoscopy, DTU performed the identital location scanning electron microscopy and the high-resolution transmission electron microscopy, and Søren Scott performed the EC-MS measurement. I co-planned the experiments, performed all the electrochemical measurements, and participated in the analysis of the result.

5.1 Experimental Section

5.1.1 Preparation of Mass-Selected Nanoparticles

NiFeO_xH_y nanoparticles were prepared using a magnetron sputtering gas-aggregation nanoparticle source (Birmingham Instruments Inc.), equipped with a lateral time-of-flight mass filter, as described in chapter 3.1.1, and other mass-selected studies reported previously by our group [33,34,162]. Deposition of mass-selected particles using this physical technique includes many advantages over chemical synthesis methods. First, the deposited particles are well-defined and monodispersed in mass. Also, the loading and the electrode coverage can easily be modified. Finally, no unwanted side products from chemical synthesis or surfactants are introduced. The nanoparticles were obtained from a Ni₇₅Fe₂₅ target and deposited onto Au disks. We deposited samples with particles having four distinctive masses: from 120,000 to 2,000,000 atomic mass unit (amu) using negatively charged particles leaving the nanoparticle source. The loading was measured from the deposition current caused by the charged particles.

Calculation of Mass Loading from Deposition Current

Each particle that lands on the substrate carries a charge, which we assume as 1e⁻ per particle. As the particles are mass filtered, the loading can easily be determined. Perfectly spherical nanoparticles and bulk density of 75% Ni and 25% Fe were assumed.

Another way to measure the loading is by using the projected surface area. The main upside of this approach is that similar electrochemical surface areas are obtained, regardless of particles sizes. In this notation, we

take the cross-section of the spherical particles, and calculate the surface this cross-section is covering assuming no overlap. The projected surface area used in this study was of 15% coverage for all different masses.

Determination of the Turn Over Frequency

The turnover frequency (TOF) is a convenient metric to evaluate the intrinsic activity of a catalyst. For OER, the TOF represents the number of O₂ molecules evolved per active site per second. To calculate TOF, we used the following formula:

$$TOF(s^{-1}) = \frac{r_{O_2}}{\#_{Active-sites}} \quad (5.1)$$

Where ($\#_{Active-sites}$) represents the number of active sites. The rate of O₂ produced (r_{O_2} , [s⁻¹]), was calculated from the raw current from OER at 1.6 V_{RHE} (i , [A]), using the Avogadro number (N_A , [6.022 x 10²³ O₂ molecules per mol]), the number of electron transferred (z) and the Faraday constant (F , [C/mol]):

$$r_{O_2} = i \cdot \frac{N_A}{z \cdot F} \quad (5.2)$$

The calculation of the number of active sites, assumed as Ni and Fe atoms in this case, was done using three different approaches. First, we only considered the metal atoms at the surface of the nanoparticles (TOF_{surface}). Secondly, we calculated TOF_{bulk} by normalizing to all the Ni and Fe atoms in the nanoparticles. Finally, we used the Ni²⁺/Ni^{3+/4+} redox feature from the cyclic voltammetry (CV) assuming 1 e⁻ transferred per Ni atoms, and corrected this value so it also included Fe atoms, to determine TOF_{redox}.

To determine the total number of active sites/ metal atoms used to calculate TOF_{surface} and TOF_{bulk}, the number of deposited particles was calculated. The total number of particles, $N_{particles}$, was calculated from the deposition current ($I_{deposition}$, [A]), the time of deposition ($t_{deposition}$, [s]) and the electric charge (C , [6.242 x 10⁻¹⁸ electrons/C]), as shown here:

$$N_{particles} = I_{deposition} \cdot t_{deposition} \cdot C \quad (5.3)$$

$N_{particles}$ was then multiplied by the average number of atoms in each nanoparticle, to give the total number of atoms deposited ($N_{metal-atom}^{particles}$). $N_{metal-atom}^{particles}$ represents all the Ni and Fe atoms deposited, and was, therefore, used to calculate TOF_{bulk}. The number of metal atoms per particle, as described in equation (5.4), was calculated using the mass of the particles deposited ($m_{particle}$, [kg]) times the Avogadro constant (N_A , [6.022 x

10²³mol⁻¹)), and divided by the average molar mass of Ni_xFe_{1-x} ($M_{Ni_xFe_{1-x}}$, [kg/mol]) from which the concentration was determined using XPS.

$$N_{metal-atom}^{particles} = \frac{N_A \cdot m_{particle}}{M_{Ni_xFe_{1-x}}} \quad (5.4)$$

The number of surface atoms used for the determination of TOF_{surface} was calculated using the surface area per particle ($A_{particle}$), the total number of particles ($N_{particles}$) and the surface density of metal atoms (ρ_{NiFe}):

$$N_{surface-metal-atom}^{total} = N_{particles} \cdot \rho_{NiFe} \cdot A_{particles} \quad (5.5)$$

Determination of the Interparticle Distance

The gas-aggregation method used to prepared the nanoparticles allows great precision over the number of particles deposited. By controlling the loading, number of nanoparticles per area, the average interparticle distance can be varied. We deposited nanoparticles with a mass of 950k amu, corresponding to a diameter of 6.7 nm, with coverage of 5%, 10%, 12.5% and 15% onto lacey carbon covered Cu TEM grids. The TEM images were recorded using the same experimental conditions as what was described for the size distribution. ImageJ, an image processing program, was then used to extract the centroid point coordinates of the 2D projections. Calculation of the average edge-to-edge distances were done using a home-made algorithm developed by Béla Sebök, and the average results based on multiple images were used for each loading.

5.1.2 Physical Characterization

The NiFeO_xH_y nanoparticles were characterized using XPS and LEIS i) as-deposited, without breaking the vacuum, and ii) after OER. Before loading the samples in the UHV chamber for the post OER measurements, the samples were rinsed thoroughly with ultrapure water (Milli-Q water, 18.2 MΩ cm) to remove the thick layer of KOH formed from the electrochemical measurements. For all XPS measurements, a SPECS XR50 instrument (Thermo Scientific) with a base pressure of 5×10^{-10} mbar was used. The source was a MgKα, and a survey scan and detailed scans of Au 4f, O 1s, Ni 2p_{3/2} and Fe 2p_{3/2} were recorded. All the spectra were corrected according to the Au 4f_{7/2} peak, which we assumed to correspond to metallic Au at a binding energy of 84.0 eV. All intensities were normalized using the Au 4f peak area, and a Shirley background was used for all spectra. The LEIS measurements were performed using 1 keV He⁺ ions. The intensity of the

LEIS spectra presented in this study are normalized based on the Au peak at 925 eV.

Scanning electron microscopy (SEM) images were acquired at 5 kV using an FEI Helios EBS3 microscope equipped with a field emission gun and a through-the-lens detector for high resolution imaging. High-resolution transmission electron microscopy (HRTEM) images were recorded using a FEI Titan E-Cell 80-300 ST TEM with a monochromated electron source and post objective aberration correction at 80 kV electron energy.

5.1.3 Electrochemical measurements

The mass-selected nanoparticles were compared to NiFeO_xH_y thin films. NiFeO_xH_y thin films were obtained via electrodeposition based on the procedure reported by Boettcher and co-workers [95]. Using a three-electrode setup, a current of -0.2 mA/cm^2 was applied for 5 min in an electrolyte of 0.1 M $\text{Ni}(\text{NO}_3)_2 \cdot 6\text{H}_2\text{O}$ and 5 mM FeCl_2 , using gold disks as substrates. The composition determined by XPS indicates a mix of 32% Fe and 68% Ni at the surface (See Figure B.2).

Electrochemical characterization of the deposited nanoparticles was performed using a RDE setup at 1,600 rpm in a Teflon cell in N_2 -saturated 1.0 M KOH. A Hg/HgO and carbon rod were used as reference electrode and counter-electrode, respectively. The ohmic drop measured using electrochemical impedance spectroscopy over a range of 10-200,000 Hz at a AC amplitude of 10 mV typically ranged from 4 to 18 Ω . The 1.0 M KOH electrolyte was prepared from ultrapure water (Milli-Q, 18 M Ω cm) with KOH (Semiconductor grade, pellets, 99.9%). First, the catalytic activity was measured by recording 5 cyclic voltammograms (CVs) at 10 mV/s up to 1.6 V_{RHE} (Figure B.6). This was followed by a two-hour potentiostatic measurement at 1.6 V_{RHE} (Figure B.8). Finally, the activity was again measured using CVs (Figure B.7). The activity of the different samples for the oxygen evolution reaction presented in this work was taken from the last CV. For each experiment, three independent samples were tested, and the activity was averaged. The same procedure, but with a longer stability measurement, was also performed. For these measurements, the nanoparticles were deposited onto a Au sheet and a static measurement was performed at 1.6 V_{RHE} over 1,000h.

5.2 Results

5.2.1 Physical Characterisation

Samples with four distinctive masses, i.e. from 120,000 to 2,000,000 atomic mass unit (amu), were used in this study. Determining the particle size distribution of each sample type was possible by imaging the nanoparticles, previously deposited onto a lacey carbon grid, with transmission electron microscopy (TEM). Figure 5.1a shows the TEM images of the four different sizes, with rounded shape obtained. The particle size distribution for each of the sample type was made based on the TEM images recorded (see Figure B.3). Figure 5.1b presents the histogram with the nanoparticle diameters distribution measured, which are 3.9 ± 0.5 , 5.4 ± 0.5 , 6.7 ± 0.6 , and 8.4 ± 0.5 nm. A small population of double the intended size obtained for the 6.7 nm and 8.4 nm particles corresponds to double charge double mass nanoparticles.

LEIS was performed on the as-prepared and after OER measurements nanoparticles, and the result is presented in Figure 5.2. The as-deposited spectrum (green curve) shows only two main peaks: Ni/Fe at 772 eV and Au at 925 eV. Ni and Fe cannot be differentiated due to their similar atomic masses. A shoulder from ca. 100 to 450 eV is associated to adventitious carbon. The LEIS spectrum of the as-deposited nanoparticles confirms the cleanliness of the sample. After OER (blue curve), O (~ 450 eV) and K (662 eV), most probably from residual KOH electrolyte, electrochemical oxidation and air exposure, are observed as extra features.

For a detailed understanding of the catalyst composition and oxidation state, the nanoparticles were probed using XPS. Typical survey spectra of the as-prepared 5.4 nm nanoparticles and after OER measurement are presented in Figure 5.3a. The as-deposited sample confirms what was observed by LEIS. Firstly, only Ni, Fe and Au are observed as metal species. The survey also shows a small contribution coming from C. The spectrum of the after OER nanoparticles shows extra peaks associated to C, O and K atoms.

Detailed scans of the Ni 2p and Fe 2p regions (Figure 5.3b) show metallic Ni and Fe for the as-deposited nanoparticles. The analysis of the XPS detailed scans of the nanoparticles after OER reveals the formation of oxide and hydroxide. More specifically, Ni(OH)₂ (855.8 eV) and a small amount of NiO (853.7 eV), and Fe₂O₃ (710.8 eV) and FeOOH (711.6 eV) were identified from the Ni and Fe 2p peaks, respectively [200–202]. The peak at higher binding energy in the Ni 2p region, i.e. around 862 eV, is associated to energy loss features. We drew the same conclusions for the smallest, 3.9 nm, and biggest, 8.4 nm nanoparticles (See Figure B.5).

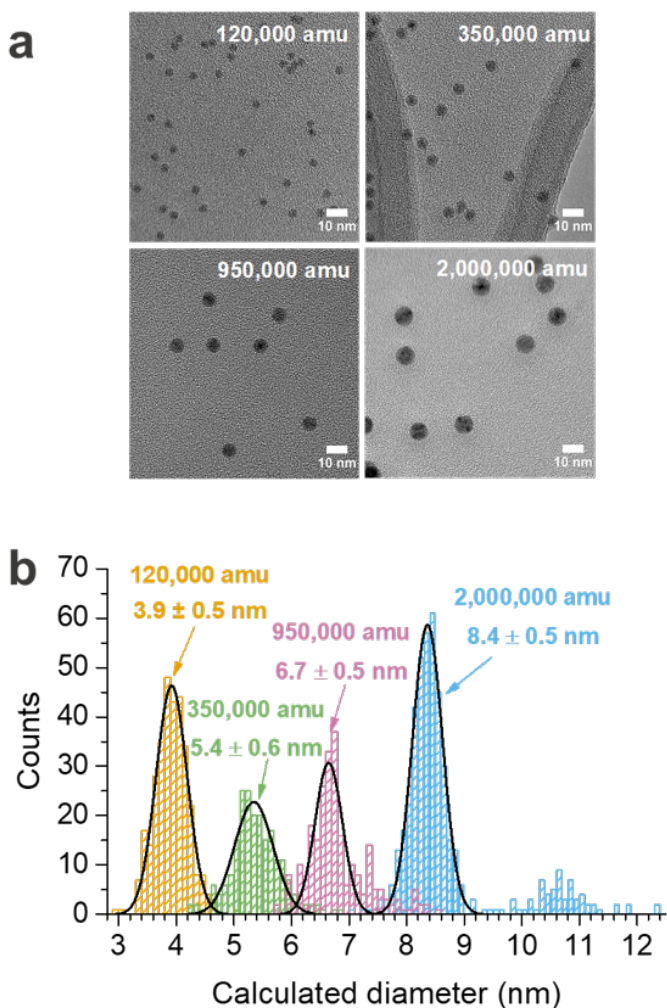


Figure 5.1: a) Transmission electron microscopy images of 120,00 to 2,000,000 amu NiFe particles. b) Respective size distribution calculated using the measured diameters of the particles. The small population around 10.5 nm is double mass double charge nanoparticles

The XPS spectra were used to determine the composition of the as-prepared and after OER nanoparticles (Figure 5.4a). For all nanoparticle sizes, the Ni:Fe stoichiometric ratio is lower on the as-prepared nanoparticles (approx. 75% Ni and 25% Fe), and increases after OER to reach a composition of approx. 85% Ni and 15% Fe. We hypothesize that the change in composition is either due to Ni segregation to the surface, or Fe leaching to the electrolyte during, the oxygen evolution. To make sure that

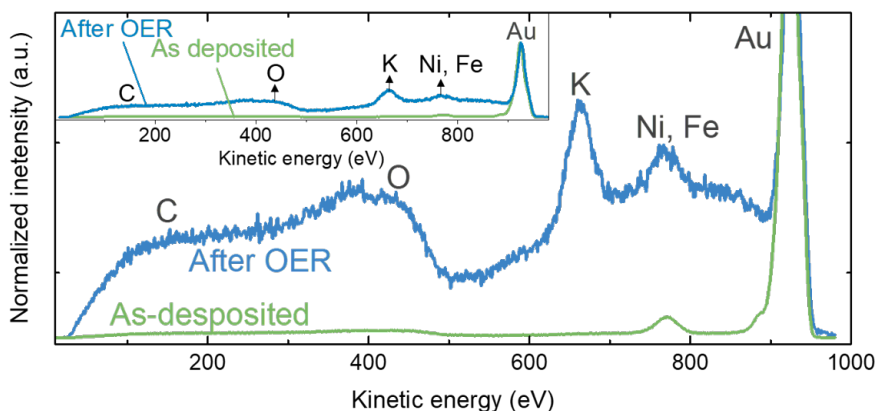


Figure 5.2: Low energy ion scattering (LEIS) spectra of the as-deposited (green curve) and after oxygen evolution reaction (blue curve) NiFeO_xH_y catalyst. The LEIS spectra were normalized to the height of the Au peak.

the small variations in Ni:Fe ratio observed for the different particle size did not drastically affect the recorded activity, we plotted $\text{TOF}_{\text{surface}}$, TOF_{bulk} and $\text{TOF}_{\text{redox}}$ as function of the Fe content (Figure 5.4b) and no clear trend is observed. This indicates that despite the small variation in Fe content, it does not impact the TOFs measured. This observation is in accordance with what was previously reported in the literature [105].

Stability is a main concern for nanoparticle catalysts as they tend to coalesce under experimental conditions [203,204]. In addition, the oxidative conditions under which oxygen evolution operates often lead to metal dissolution [205,206]. In this study, the stability was first assessed by coupling two-hour chronoamperometry at $1.6 V_{\text{RHE}}$ to identical location scanning electron microscopy (SEM). Identical location SEM allowed us to evaluate if the nanoparticles sintered and/or dissolved in an extensive manner. The images from the as-prepared sample and after OER are presented in Figure 5.5. To ease the comparison of the images, particles were selected, and their position is underlined using purple and yellow arrows. By comparing the position of the nanoparticles before (Figure 5.5a) and after OER (Figure 5.5b), we concluded that no major transformations occurred.

High-resolution transmission electron microscope (HRTEM) images was used to gain insights into the morphology and composition at the atomic level of the as-deposited and after OER NiFeO_xH_y nanoparticles. To do so, NiFe nanoparticles were deposited onto a graphene covered Au grid. Images of the as-deposited sample were first recorded. Figure 5.6a shows a detail image of one of the nanoparticles with an inset, where non-uniform orientation of lattice fringes are identified. More specifically, a Ni_3Fe crys-

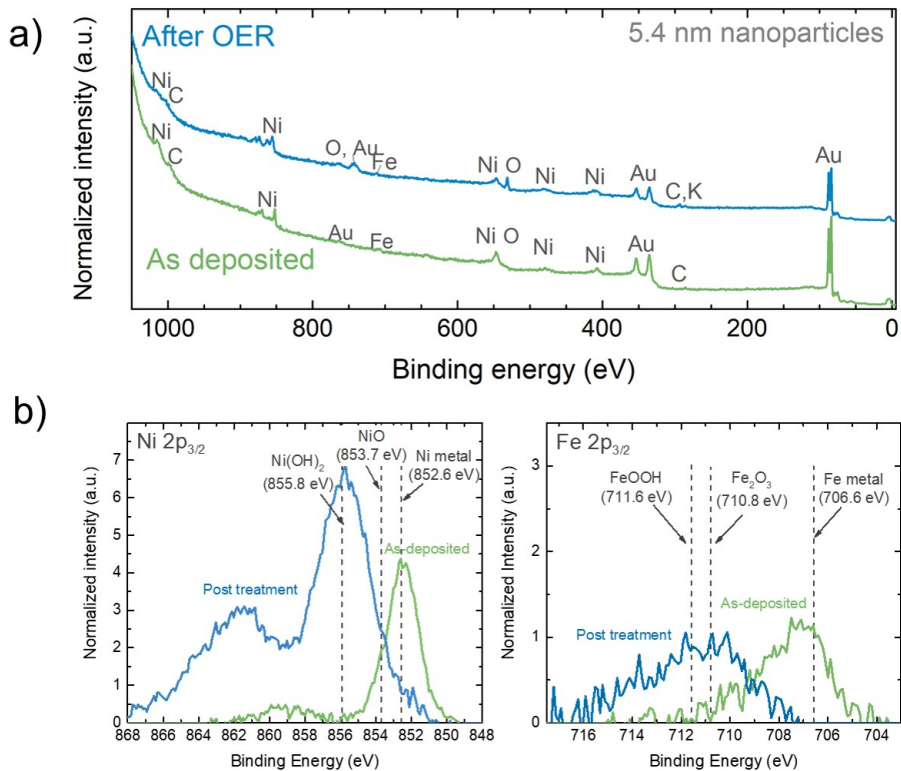


Figure 5.3: a) X-ray photoelectron spectroscopy survey spectra of the as-prepared (green spectrum) and after OER (blue spectrum) 5.4 nm in diameter NiFeO_xH_y nanoparticles. Intensities were normalized using Au 4f peak and b) Spectra of the Ni $2p_{3/2}$ and Fe $2p_{3/2}$ core-level regions. The binding energies showed were taken from [200–202]

talline structure was identified [207]. On Figure 5.6b, nanoparticles that are rounded and homogeneously distributed in size, are shown. The sample was then transferred into a rotating disk electrode (RDE) where two CVs up to $1.5 V_{RHE}$ were recorded. The sample was rinsed thoroughly and transferred back to the HRTEM. Identical location images were then recorded. The milder operating conditions compare to the one described in subsection 5.1.3 were chosen to avoid the corrosion of graphene at too anodic potentials. We observe no change from Figure 5.5b to c, and therefore concluded that the polycrystallinity and the shape of the particles are conserved after OER. It is possible that, even though the sample was rinsed thoroughly, electrolyte leftover causes the reduced sharpness observed on Figure 5.6c. The blurring of the images could also be related to broken graphene coming from the substrate and overlapping with the nanoparticles.

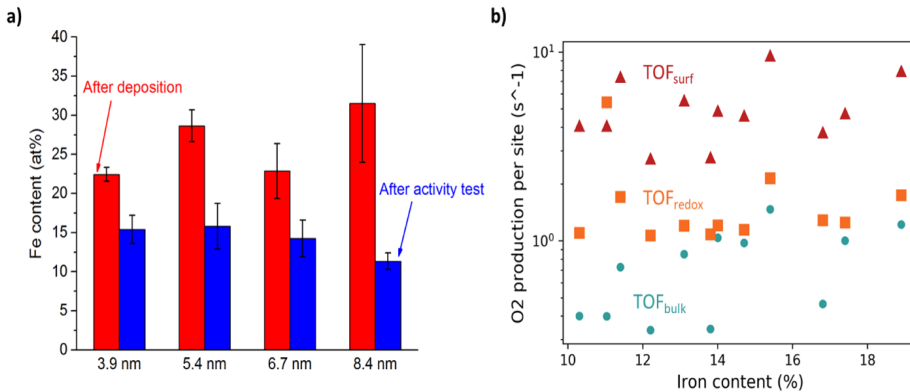


Figure 5.4: a) Fe contents of the as-prepared (red bars) and after OER (blue bars) 3.9 nm, 5.4 nm, 6.7 nm and 8.4 nm in diameter NiFeO_xH_y nanoparticles. The determination of the Fe contents was based on the Ni $2p_{3/2}$ and Fe $2p_{3/2}$ X-ray photoelectron spectroscopy peaks. Error bars depict the standard deviation of the 3 samples of each size. b) $\text{TOF}_{\text{surface}}$ (red triangle), TOF_{bulk} (blue circles) and $\text{TOF}_{\text{redox}}$ (orange squares) as function of the Fe content in % for all NiFeO_xH_y nanoparticles.

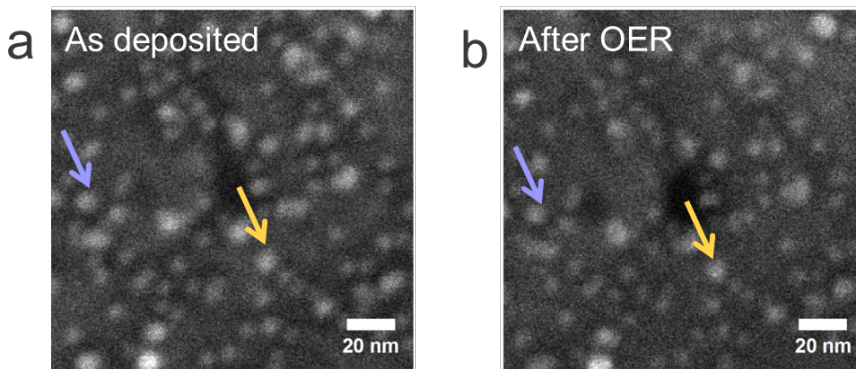


Figure 5.5: Identical location scanning electron microscopy images of the as prepared nanoparticles (a) and after oxygen evolution reaction (b). The arrows are to ease the comparison of the location of the particles.

Energy-dispersive x-ray spectroscopy (EDX) with focused beam was also performed on the same samples that were used for the HRTEM analysis. Ni and Fe elements were mapped in the particle using cross sectional line scans. Because of the intense electron beam, and its impact on the particles, different particles were compared before and after OER. The line scan of the as-deposited particle (Figure 5.7a) shows uniform distribution of Ni

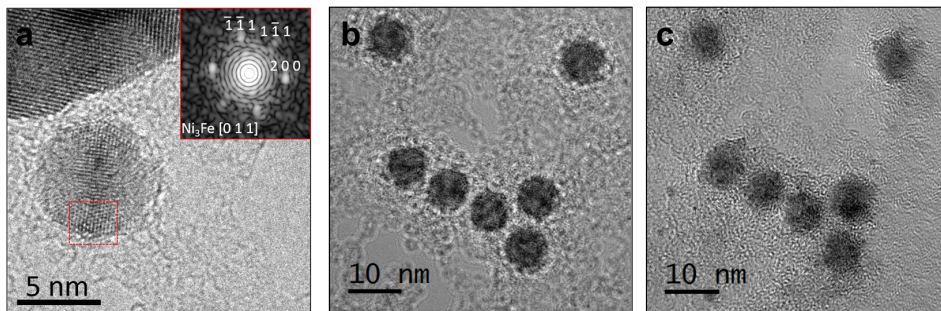


Figure 5.6: High-resolution transmission electron microscopy investigation of 6.7 nm NiFeO_xH_y nanoparticles deposited on graphene coated Au TEM grid (a) HRTEM image of a nanoparticle with Fourier transform of the highlighted area showing Ni_3Fe phase. (b) and (c) show identical location HRTEM images of nanoparticles before (b) and after two CVs up to $1.5 V_{RHE}$ in 1 M KOH at 10mV/s (c).

and Fe across the nanoparticle. Additionally, the expected ratio measured by XPS is conserved, i.e. higher atomic% of Ni compared to Fe. After OER (Figure 5.7b), a decrease in the Fe:Ni ratio is observed, but the distribution remains uniform. Firstly, this confirms the loss of Fe observed by XPS on the nanoparticles after OER. Moreover, it indicates that the higher Ni:Fe atomic ratio measured by XPS is caused by Fe leaching out of the nanoparticles, and not Ni segregation to the surface of the nanoparticles. The atomic % of O increases after OER measurements, which could correspond to the nanoparticles being oxidized. However, in the way the experiment was done, the uncertainty on the atomic% of oxygen is too high to draw any conclusions.

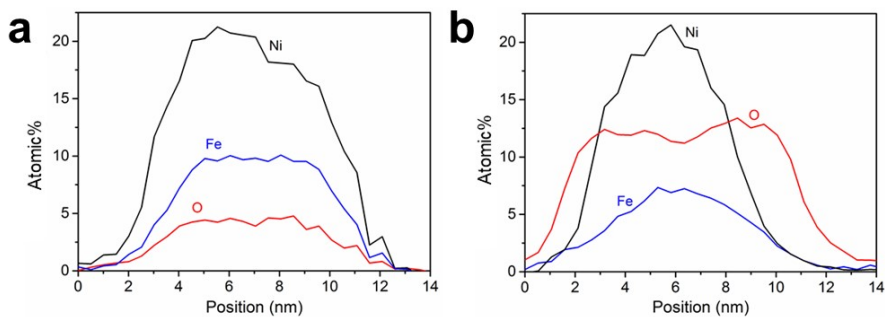


Figure 5.7: Energy dispersive x-ray spectroscopy (EDX) line scans across 6.7 nm NiFe nanoparticles a) after deposition and b) after electrochemical testing.

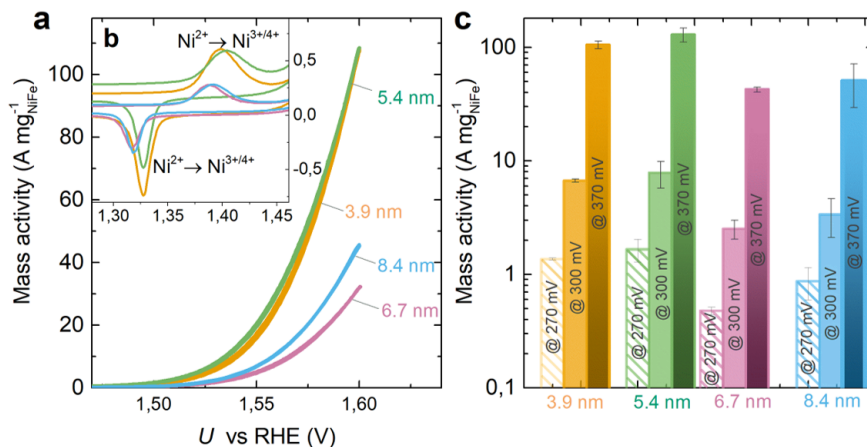


Figure 5.8: (a) Representative cyclic voltammetry (CV) at 10 mV/s, iR-corrected, recorded after chronoamperometric measurement at 1.6 V_{RHE} for 2 hours, and (b) inset of the CVs showing Ni redox peaks. (c) average mass activities at $\eta = 270, 300$ and 370 mV of well-defined NiFe nanoparticles on Au disks in N_2 -saturated 1 M KOH. The average mass activity and standard deviation come from three independent samples. The metal mass was determined from the deposition current.

5.2.2 Catalytic Activity and Stability

The catalytic activity of NiFeO_xH_y nanoparticles was measured in 1 M KOH and the different nanoparticle sizes were compared. Figure 5.8a shows representative CVs recorded for each size after 2h at 1.6 V_{RHE} normalized to the mass measured from the deposition current. From this, we can observe that the 3.9 nm and 5.4 nm nanoparticles have similar and the highest mass activities among the samples measured in this study. The inset highlights what is typically attributed to $\text{Ni}^{2+}/\text{Ni}^{3+/4+}$ redox peak for all samples. The position of the $\text{Ni}^{2+}/\text{Ni}^{3+/4+}$ redox peak is at similar potentials for all particle sizes, which confirms the comparable content in Fe for all samples.

The average activities measured at 270, 300 and 370 mV overpotential after the two-hour potentiostatic measurements taken from the average polarization curves (Figure B.4) are presented in Figure 5.8c. No obvious change in trend is observed when comparing the mass activity at different overpotentials for the four sample sizes. This can indicate that oxygen evolution is not limited by mass transport at these potentials. One could expect that if considerable oxygen evolution was coming from subsurface activity, i.e. intercalated water and/or lattice oxygen, the current would be limited by mass transport due to slower diffusion in the bulk versus the surface at high overpotentials.

To determine the intrinsic activity of the NiFeO_xH_y mass-selected nanoparticles, TOF_{redox} , $\text{TOF}_{surface}$ and TOF_{bulk} values were calculated from the current density measured at 1.6 V_{RHE} taken from the CVs after the two-hour stability test. Figure 5.9 shows the TOFs as function of particle diameter. The values reported for $\text{TOF}_{surface}$ are the highest, independently of particle size, while the values of TOF_{bulk} are among the lowest. TOF_{bulk} shows higher TOFs for smaller particle size. $\text{TOF}_{surface}$ and TOF_{redox} do not show any distinct trend as function of particle diameter. In Figure B.10, we showed that the $\text{Ni}^{2+}/\text{Ni}^{3+/4+}$ reduction peak scales better with the surface area estimated from the deposition current of the nanoparticles than the catalyst loading. This observation is in agreement with the literature stating that Ni redox peak is associated to a surface process [208]. However, according to the TOF values reported, the evaluation of the number of active sites using the $\text{Ni}^{2+}/\text{Ni}^{3+/4+}$ redox feature is higher than the number of surface atoms estimated. We hypothesize that this can either come from a more porous surface than what we estimated, or because the $\text{Ni}^{2+}/\text{Ni}^{3+/4+}$ redox feature corresponds to more than the first monolayer (ML) of Ni in contact with the electrolyte. The catalytic activity of a NiFeO_xH_y thin film was also measured and compared to the nanoparticles. Because the thin film has a ill-defined surface and because we did not use a quartz crystal microbalance to measure accurately the mass deposited, only TOF_{redox} could be calculated. TOF_{redox} obtained for the thin film measurement is slightly lower than for the nanoparticles but has still a comparable activity value.

The maximum and minimum values reported for 5.4 nm NiFeO_xH_y , i.e. $\text{TOF}_{surface}$ and TOF_{bulk} respectively, were compared to state-of-the-art non-noble metal catalysts for the OER in alkaline media, as shown in Figure 5.9b. The reaction rate of the 5.4 nm NiFeO_xH_y particles sample at 300 mV overpotential are among the highest reported for non-noble metal catalysts in alkaline electrolyte; $6.2 \pm 1.6 \text{ s}^{-1}$ for $\text{TOF}_{surface}$ and $1.2 \pm 0.3 \text{ s}^{-1}$ for TOF_{bulk} .

The surface coverage of the 6.7 nm NiFeO_xH_y nanoparticles was varied to study the effect of interparticle distance on the oxygen evolution. The surface coverage values studied as part of the experiment were 5%, 10%, 12.5% and 15%. A representative bright field TEM image along with the average edge-to-edge distance for each loading, written the top corner, is shown in Figure 5.10a. An average surface coverage distance of 8.8 nm, 2.8 nm, 2.2 nm and 1.7 nm interparticle distances were obtained for the surface coverage of 5%, 10%, 12.5% and 15%, respectively.

The current density normalized by mass loading taken at 300 and 370 mV overpotential from CV at 10 mV/s is presented as a function of the average interparticle distances (Figure 5.10b). For both overpotentials the

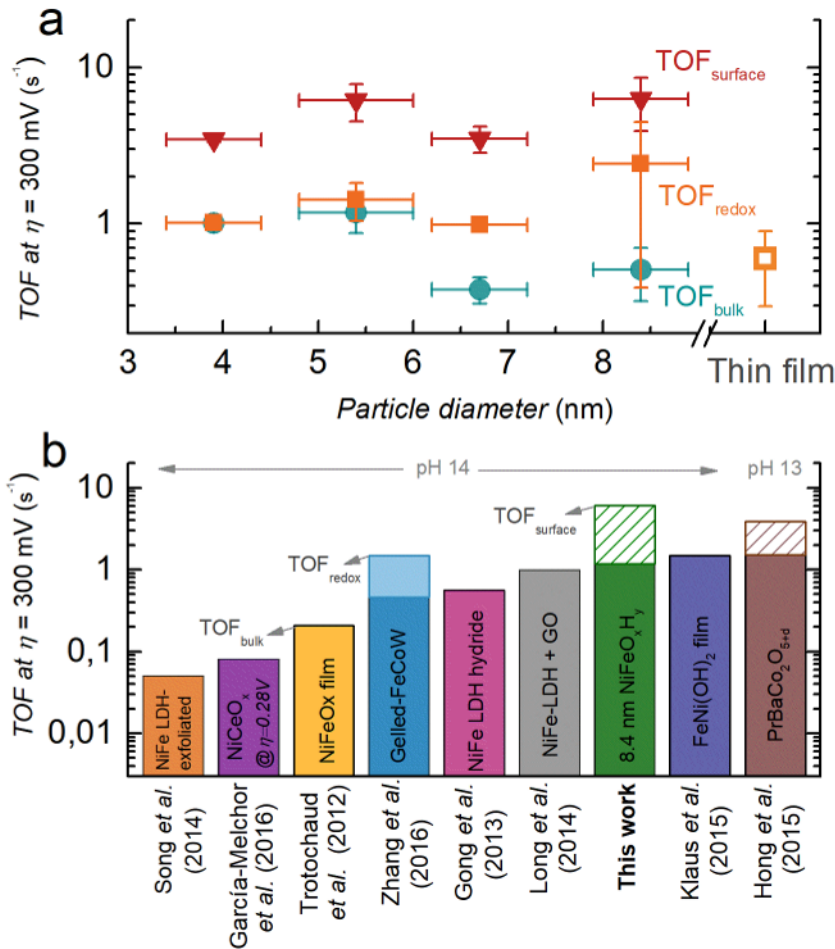


Figure 5.9: Turnover frequency calculated from the total metal mass (TOF_{bulk}), estimated surface atoms ($\text{TOF}_{\text{surface}}$), and the $\text{Ni}^{2+}/\text{Ni}^{3+}/4+$ peak ($\text{TOF}_{\text{redox}}$) of the NiFe nanoparticles at $\eta=300 \text{ mV}$ measured in N_2 -saturated 1.0 M KOH at 10 mV/s as function of particle size. The Ni redox peak was used to measure the TOF of the NiFe thin film. (b) TOF of state-of-the-art non-noble OER catalysts in alkaline. From [209] for NiFe LDH-Exfoliated; from [85] for NiCeO_x ; from [94] for NiFeO_x film; from [88] for Gelled-FeCoW; from [210] for NiFe LDH hydride; from [211] for NiFe-LDH + GO; from [98] for FeNi(OH)_2 film and from [37] for $\text{PrBaCo}_2\text{O}_{5+d}$. When possible bulk and surface/redox TOFs were estimated. The maximum TOF value of Gelled-FeCoW was calculated using the Co redox peak, the BET area for the $\text{PrBaCo}_2\text{O}_{5+d}$ and the Ni redox peak for the $5 \text{ nm NiFeO}_x\text{H}_y$ nanoparticles from this work.

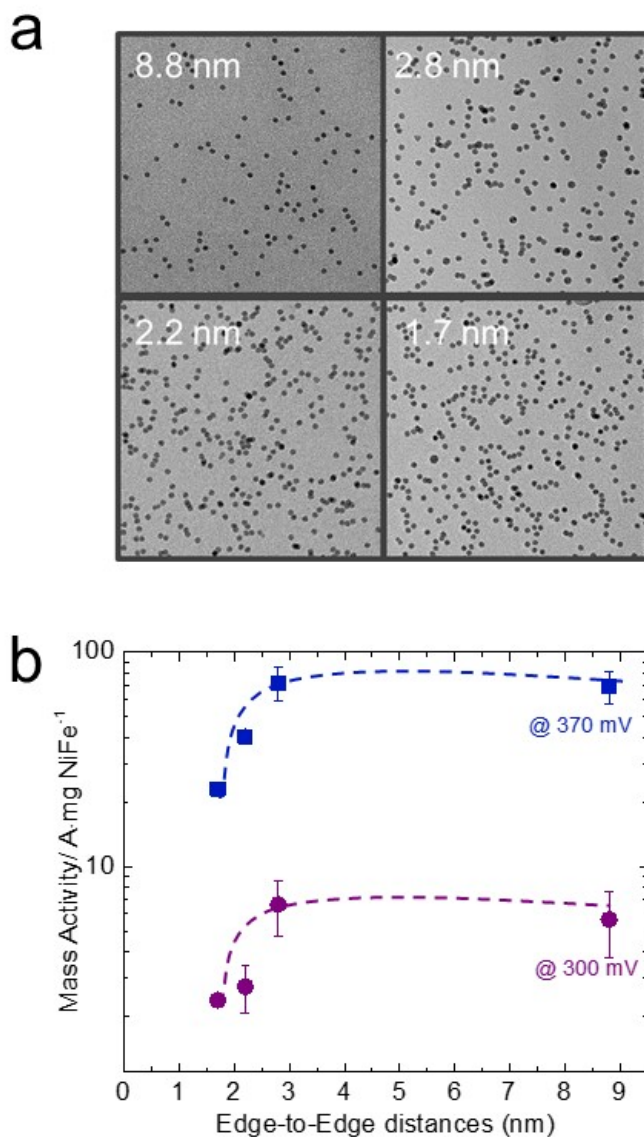


Figure 5.10: a) Representative transmission electron microscopy images of the surface coverage of 5%, 10%, 12.5% and 15% leading to interparticle distances of 8.8 nm, 2.8 nm, 2.2 nm and 1.7 nm where the activity reaches a plateau, respectively. b) Mass activity taken at 300 and 370 mV overpotential activity of 6.7 nm NiFeO_xH_y nanoparticles as a function of the estimated interparticle distances. The dotted lines are a guide to the eye

current density increases from 1.7 to 2.8 mA/cm² at 1.7 nm interparticle distance, where the activity reaches a plateau. The results reported in Figure 5.10 suggest a negative impact for shorter distances, in contrast to other similar studies [198,199]. It is unlikely that the decrease in activity is related to bubble formation at the surface, as a RDE setup and a low catalyst loading (<500 ng/cm²) was used. Using simple calculations, we also investigated the pH effect according to the different loadings, and observed no major pH variations between the lowest and highest metal loading (See Appendix B).

To further probe the stability, longer stability measurement at 1.6 V_{RHE} was performed. A RDE setup could not be used over 1,000 hours and, instead, the stability measurement was performed using a static electrode. Approx. 100 ng of catalyst was deposited onto a gold sheet and tested for OER in 1 M KOH. Figure 5.11 shows the mass activity obtained for 1,000 hours. We observed a relatively stable current for that period of time. The glitches observed are related to the noise from the surrounding. Unfortunately, because the measurement was on a thousand-hour scale, the Ni and Fe dissolution were not measured. However, because the catalyst loading deposited is of 100 ng, we expect that metal corrosion would immediately translate into a drop in current.

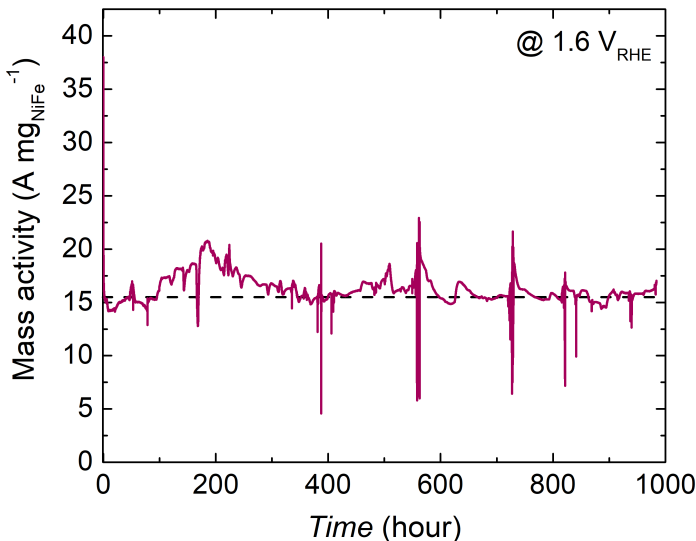


Figure 5.11: Stability measurement recorded at 1.6 V_{RHE} in 1 M KOH using a static electrode for the 6.7 nm in size NiFeO_xH_y nanoparticles. The mass loading of the NiFe was of ~ 100 ng. The dashed line is a guide to the eye.

5.3 Participation of bulk NiFeO_xH_y in the OER

Whether TOF_{bulk} or TOF_{surface} represents the true intrinsic activity depends on whether the bulk or only the surface oxygen contributes to the oxygen evolution, which we investigated with isotope labeling experiments. We used three complimentary isotope labeling procedures, all on samples with 6.7 nm particles, referred to below as procedure a, b, and c, and illustrated schematically in Figure 5.12. Naturally when exposed to air, metallic NiFe nanoparticles oxidize partly to become NiFeO_x. The most abundant isotope of oxygen is ¹⁶O with 99.757% natural abundance. For that reason, the NiFeO_x will mainly contain ¹⁶O. One of the components of the EC-MS setup is sensitive to alkaline electrolyte. Therefore, for practical reasons, we had to perform the electrochemical measurements in 0.1 M KOH (pH=13) instead of 1 M KOH (pH=14).

In procedure *a*, the nanoparticles are first oxidized in 0.1 M KOH made from ¹⁶O-water and OER was performed in ¹⁸O-based electrolyte. The first step consists of cycling the nanoparticles in 0.1 M KOH for 20 cycles between 0.5-1.5 V_{RHE} to obtain NiFeO_xH_y with ¹⁶O. The oxidized nanoparticles were then rinsed thoroughly and transferred at open-circuit voltage to a stagnant thin-layer cell where oxygen evolution was performed in 0.1 M KOH made of ¹⁸O water. It is worth mentioning that the purity of the ¹⁸O water used to prepare the electrolyte is only of 97% , and will thus have to be considered in the data analysis. On the other hand, the high natural abundance of ¹⁶O in water ensures a preparation of NiFeO_xH_y containing 99.8% of ¹⁶O.

In procedure *b*, we performed the opposite procedure as in *a*: oxidizing in ¹⁸O-based 0.1 M KOH and did OER in ¹⁶O-based electrolyte. The same protocol as the one described for procedure *a* was used, but ¹⁸O water was used instead of ¹⁶O water to oxidize the nanoparticles, and then the OER was performed in ¹⁶O electrolyte.

To complement procedure *b* and investigate the difference between oxide and hydroxide, if any, the NiFe nanoparticles were oxidized in ¹⁸O₂ atmosphere. Procedure *c* differs slightly from *a* and *b* by the way the oxide was prepared. NiFe nanoparticles were deposited and annealed at 447°C in the same vacuum chamber where O₂ gas was introduced. This allows for greater sensitivity towards lattice exchange in EC-MS when performing OER in ¹⁶O water. On the other hand, it adds some uncertainty to the initial isotopic composition of the catalyst as the NiFe¹⁸O_x is exposed to ambient air where ¹⁶O₂ is predominant.

The first cycle up to 1.55 V_{RHE} and back to 0.5 V_{RHE} coming from procedure *a* is shown in Figure 5.13a. The potential and current are plotted in the bottom panel, and calibrated m/z=34 (¹⁶O¹⁸O) mass spectrometer

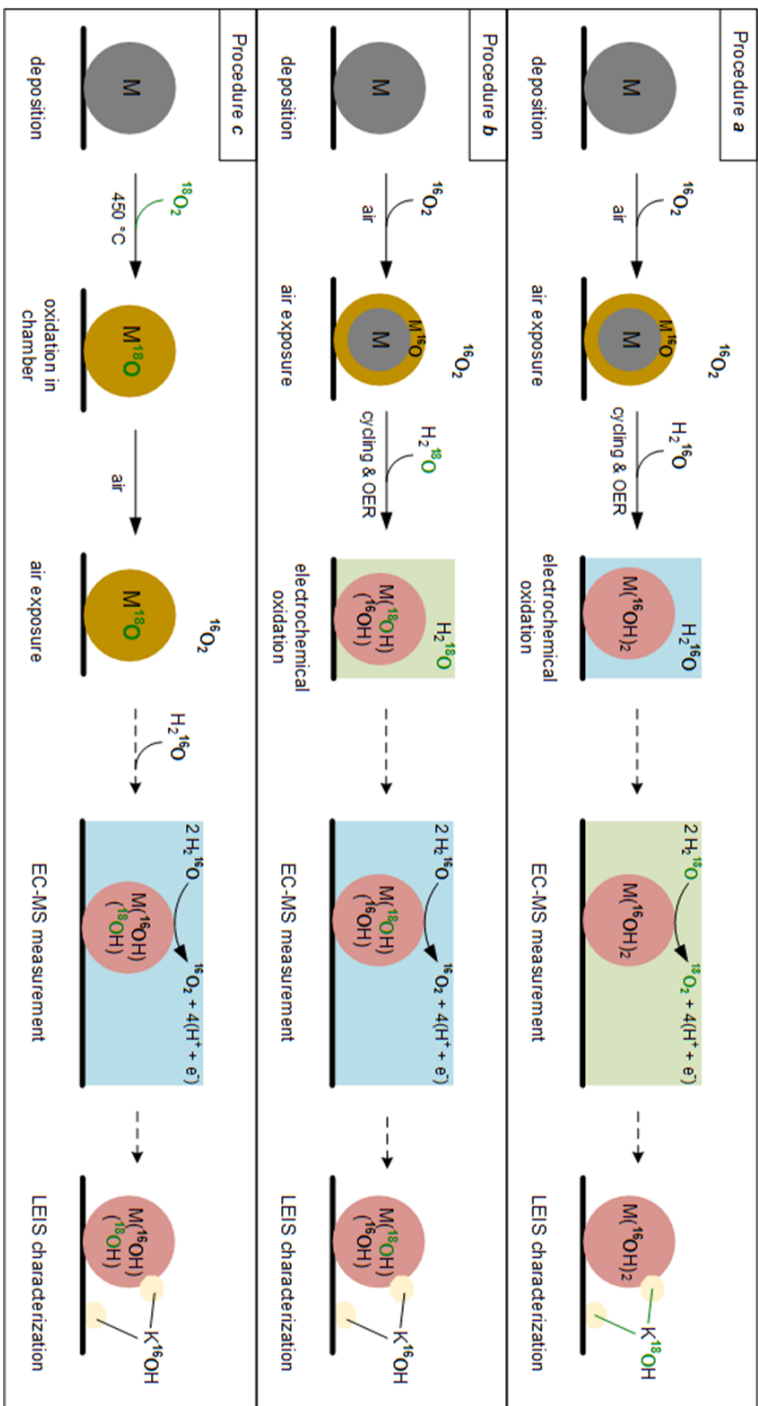


Figure 5.12: Schematic of the three isotope labeling experiments performed in this work. Procedure a) The nanoparticles are oxidized in H₂¹⁶O containing electrolyte and the OER was performed in H₂¹⁸O. Procedure b) The nanoparticles are oxidized in H₂¹⁸O containing electrolyte and the OER was performed in H₂¹⁶O. Procedure c) The nanoparticles are oxidized in ¹⁸O₂ atmosphere and the OER was performed in H₂¹⁶O.

signal is plotted (red trace) in the top panel against a shared time axis. As mentioned above, the electrolyte made of ^{18}O water has only a purity of 97%, and thus, we had to verify if the contribution from ^{16}O came from the lattice oxygen or the electrolyte. The green curve was obtained by multiplying the $m/z=36$ signal ($^{18}\text{O}_2$) by the steady-state $^{16}\text{O}^{18}\text{O}/^{18}\text{O}_2$ measured prior to this experiment (see Figure B.11). This curve represents the $^{16}\text{O}^{18}\text{O}$ signal expected from oxidation of the electrolyte containing ^{16}O impurities. As presented, the measured and expected $^{16}\text{O}^{18}\text{O}$ coincide, indicating that all of the $m/z=34$ signal corresponds to electrolyte oxidation. The same data analysis was done for procedure *b* (Figure 5.13c) and procedure *c* (Figure 5.13e), but in this case with $m/z=32$ ($^{16}\text{O}_2$) as the dominant signal. However, in these cases the sensitivity towards isotope exchange is higher due to the high natural abundance of ^{16}O . The raw data and full cycles for each procedure is available in Figure B.12. We also performed the isotope labeling experiment according to procedure *a* on a NiFeO_xH_y thin film, and still no lattice oxygen or intercalated water oxidation was detected (Figure B.13). Finally, to prove that the EC-MS setup is sensitive enough, we performed isotope labeling experiment using $\text{IrO}_2/\text{TiO}_2$ where we saw ≈ 1 ML exchange (Figure B.14)

As evidence of the sensitivity of the technique in detecting O_2 , $m/z=34$ more precisely for procedure *a*, a simulated signal if 1% of the total ^{16}O contained in the catalyst, equivalent to approximately 10% of a ML, was released in 5s (pink curve), 15s (cyan curve) and 45s (blue curve). The rate of 0.2% ML per second when 10% of a ML is released in 45s, is significantly above the detection limit of the EC-MS. In comparison, the oxygen production rate measured in this experiment is 19% ML per second. This shows that if only 1% of the OER activity were due to lattice oxygen evolution or intercalated water oxidation, the EC-MS would be sensitive enough to detect it. Similar simulations were done for procedure *b* and *c*, and similar conclusions were reached.

Following the isotope labeling experiment coupled to EC-MS, LEIS was performed on the NiFeO_xH_y nanoparticles to make sure that the oxygen isotope was incorporated into the structure. Figure 5.13b, d and f show the LEIS spectra of the as-prepared and after OER following procedure *a*, *b* and *c*, respectively. To remove the layer of KOH, the sample coming from procedure *a* was rinsed with ^{18}O water and samples coming from procedure *b* and *c* were rinsed with ^{16}O water before being transferred to the UHV system. Let us take NiFeO_xH_y nanoparticles coming from procedure *c* (Figure 5.13f) as it allows us to compare the already oxidized sample with the one after OER. The LEIS spectrum of the as-deposited NiFe nanoparticles (grey curve) shows a main peak associated to Ni and Fe and another smaller contribution associated to ^{18}O coming from the in situ oxidation

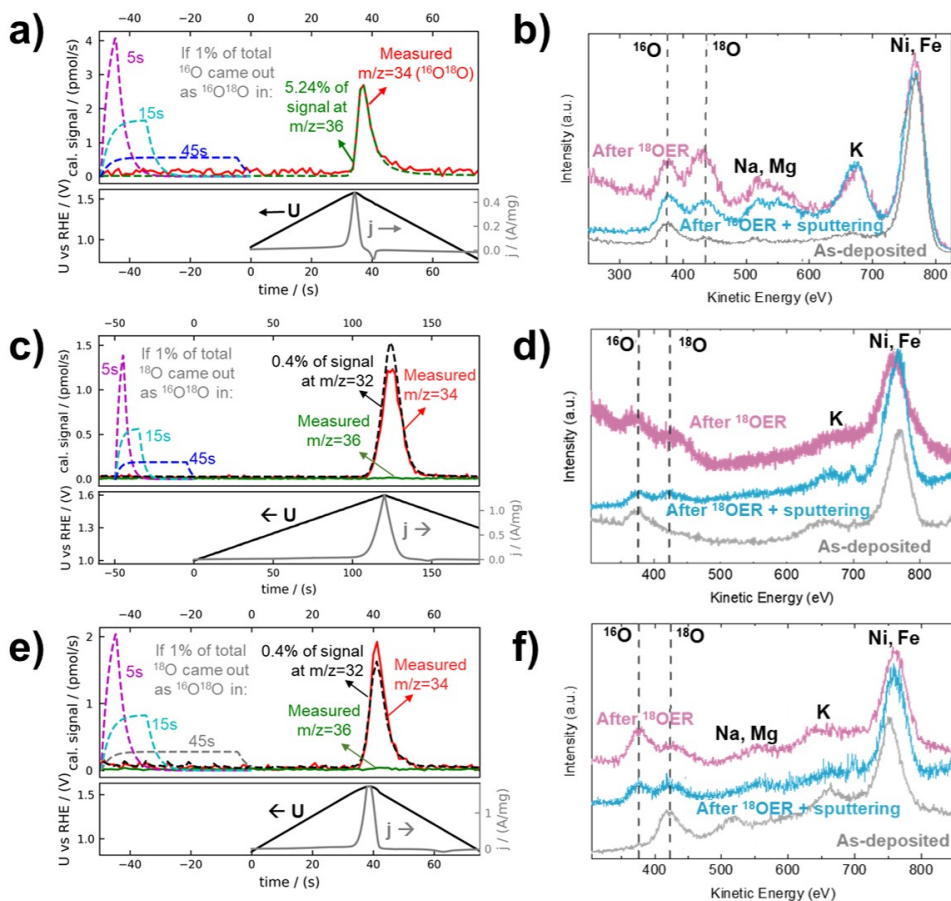


Figure 5.13: EC-MS and LEIS results from isotope labeling experiment using procedure *a* (a-b), *b* (c-d) and *c* (e-f). a) First electrochemical potential cycle in ^{18}O electrolyte after sample preparation with ^{16}O . The bottom panel shows the potential (black, left axis) and current (gray, right axis). The top panel shows calibrated mass spectrometer signal of $^{16}\text{O}^{18}\text{O}$ ($m/z=34$) (red) detected during oxygen evolution in 0.1 M KOH made with ^{18}O water (top panel). The $^{16}\text{O}^{18}\text{O}$ signal expected without lattice exchange due to the composition of the electrolyte, which is a constant fraction of the $^{18}\text{O}_2$ ($m/z=36$) signal, is co-plotted (dashed green). The top panel also shows simulations of the $m/z=34$ signal if 1% of the total ^{16}O contained by the oxidized catalyst came out as $^{18}\text{O}^{16}\text{O}$ in 5s (magenta), 15s (cyan) or 45s (blue). b) The low-energy ion scattering spectra of the sample as deposited (grey), after OER (purple) and after OER and sputtering (blue). For the results from procedure *b* and *c* presented in c,d,e and f, the same interpretation of the data can be done but by interchanging ^{16}O with ^{18}O , and vice-versa.

in $^{18}\text{O}_2$ atmosphere. The LEIS spectrum of the NiFeO_xH_y nanoparticles after OER (purple curve) shows extra contribution from ^{16}O , impurities of Na and Mg coming from the ^{18}O water and residual K. The sample was then sputtered with Ar for 30 min and a LEIS spectrum was again recorded (blue curve). The spectrum after OER after sputtering shows an increase in $^{18}\text{O}/^{16}\text{O}$ suggesting that residual ^{16}O is sputtered away revealing the ^{18}O of the material. Similar observations were made when analysing Figure 5.13b and d.

5.4 Discussion

The results obtained from identical location SEM (Figure 5.5) and the stable current recorded for 1,000 hours (Figure 5.11) indicates that the NiFeO_xH_y are stable against dissolution under reaction conditions. The study of size effect on the OER activity shows higher activity for smaller particle size, when the normalization is done using the loading measured from deposition current, i.e. for the mass activity (Figure 5.8) and TOF_{bulk} (Figure 5.9) measured. As shown in Figure 5.4, the small changes in Fe content cannot explain the variation in activity. No trend could be identified from $\text{TOF}_{surface}$ and TOF_{redox} which are related to the intrinsic activity normalized to surface area of the nanoparticles. In this work, we also focused on identifying if the lattice oxygen and/or intercalated water in-between the nanosheets participate in the oxygen evolution. All the evidence gathered in this work suggests that the OER on NiFeO_xH_y is a surface process. First, we compared the activity of different particle size at 270, 300 and 370 mV overpotential (Figure 5.8) and did not see any obvious difference in trend with particle size. We could argue that if the bulk was contributing significantly to the reaction, we could expect the diffusion of species in the NiFeO_xH_y would limit the current recorded for high overpotential. Second, we observed no dependency on size when normalizing to surface and redox peak. when the current was normalized to surface area ($\text{TOF}_{surface}$ and TOF_{redox}) but saw a size dependency for TOF_{bulk} favoring smaller particles (Figure 5.9). Finally, using in operando isotope labeling experiments coupled to EC-MS following three different approaches show that the oxygen and intercalated water remain in the NiFeO_xH_y under OER conditions, and that the evolved O_2 comes from the oxidation of the water from the electrolyte (Figure 5.13). The LEIS also confirmed that the initial isotopic oxygen was still in the NiFeO_xH_y after OER measurements.

As presented earlier, the participation of lattice oxygen depends on the material investigated: Co_3O_4 [112], $\text{IrO}_2/\text{TiO}_2$ [111], and some perovskites [114]. It was also presented that involvement of lattice oxygen depends

on the structure of a material. Indeed, the phenomenon was observed for amorphous RuO₂-based material but not rutile RuO₂ oriented thin films. For that reason, because we did not observe participation of lattice oxygen or oxidation of intercalated water, we do not rule out that it could be possible on a material synthesized in a different manner. Moreover, it is also possible that bulk activity is only seen at higher overpotentials, which cannot be studied using the EC-MS setup due to bubble formation. Finally, based on these observations, we can conclude that the best measure of intrinsic activity is TOF_{surface}, where the oxygen evolved is normalized by the surface of the particles.

5.5 Conclusion

In conclusion, we used well-characterized mass-selected nanoparticles of Ni and Fe as a model system to investigate their fundamental properties for the oxygen evolution reaction. We confirmed the stability of the NiFeO_xH_y using identical location scanning electron microscopy and a stability measurement that showed a stable current over 1,000h at 1.6 V_{RHE}. We used low-energy ion scattering and the unique capabilities of the microchip-based electrochemistry-mass spectrometry setup to show that oxygen in the catalyst is retained under reaction conditions. The isotope labeling experiments were done using three different approaches on the mass-selected nanoparticles, and was also tested on a NiFeO_xH_y electrodeposited thin film. Our results showed that only the surface was contributing to O₂ evolution; we can thus confirm that the most appropriate value to evaluate the intrinsic activity of this system is TOF_{surface} for which we obtained $6.2 \pm 1.6 \text{ s}^{-1}$ at an overpotential of 300 mV. Finally, the 6.2 s^{-1} for TOF_{surface} serves as a lower limit for the development of new OER catalysts in alkaline electrolyte.

Synthesis of Platinum-Rare-earth Alloys for the Oxygen Reduction

As discussed in Chapter 2, alloys of platinum and rare-earth are promising catalysts for the oxygen reduction. Their weaker binding energy for the reaction intermediates compared to Pt allows for excellent catalytic properties. This class of material is also less prone to dissolution because of the very negative enthalpy of formation [167]. Previous studies using mass-selected nanoparticles of Pt_xY [162] and Pt_xGd [164] raised the interest of this class of alloys for future commercial application even more. However, technological limitations of the gas-aggregation technique used for the preparation, i.e. the slow deposition rate, limits the deposition to nanogram scale, and impedes the electrochemical testing of Pt_xY and Pt_xGd in membrane electrode assemblies. Therefore, a synthesis technique that can be scaled-up to the gram scale needs to be established.

The synthesis of Pt-rare-earth alloys include many challenges. Rare-earth elements have high affinity for oxygen and will form oxides when expose to oxygen contaminants. The oxygen-metal bond is between 700-800 kJ/mol [212], which implies that rare-earth oxides should be avoided as their reduction is difficult. The other obstacle is the notable difference in reduction potential between Pt/Pt_2^+ , with +1.18 V, to those of the rare-earth, for example of -2.37 V for Y/Y_3^+ [213]. This illustrates how chemically different Pt and rare-earths are. Taking all the above into consideration, three different types of chemical synthesis methods were investigated with the aim to obtain intermetallics of platinum and rare-earths in nanoparticulate form. The first synthesis method investigated was the alkali reduction method [214,215]. The second synthesis investigated was the cyanide reduction technique with which the synthesis of Pt_xCe and Pt_xPr alloys was previously reported in micrometer particulate form [212]. I worked in close collaboration

with Amado Velazquez-Palenzuela, former Postdoc at SurfCat, on these two topics. Finally, the last synthesis method investigated was the continuation of the thermal synthesis method, initiated by Brian Knudsen and co-workers in his PhD work [216]. The high temperature synthesis work is supported by thermodynamics calculation made by Christoffer Mølleskov Pedersen in his PhD work [217]. Amado Velazquez-Palenzuela also contributed to the electrochemical characterization of the Pt_xY/C nanoparticles.

6.1 Alkalide Reduction

An alkalide is a chemical compound in which alkali metals hold a negative charge such as Na^- , K^- , Rb^- and Cs^- . In the alkalide reduction method, an alkali metal is mixed with a non-reducible organic complexant. This step allows the alkali anion and cation to form a sandwich structure with the complexant. Once complexed, the alkali anions have a strong reducing power of ~ 3 eV, that enables the production of nanoparticles made of rare-earth metals [215]. A representation of the sandwich structure is illustrated below, where 15-crown-5 ether was used as complexant, and KNa as alloy.

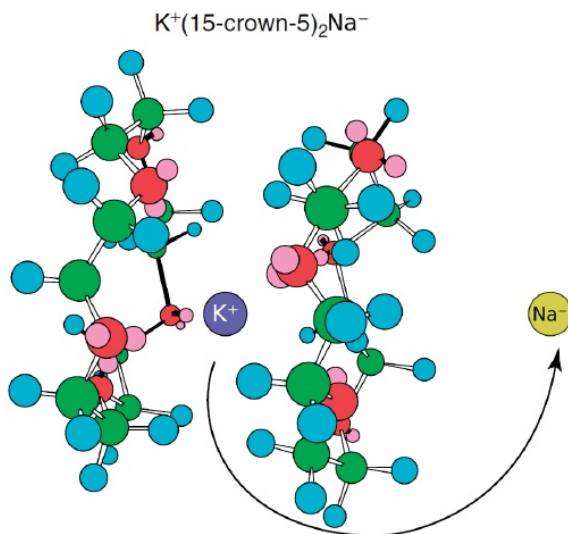


Figure 6.1: Schematic of the $K^+(15\text{-crown-}5)_2Na^-$ sandwich structure formed from mixing 15-crown-5 ether with KNa alloy. Taken from [215,216]

Recently, Wagner and co-workers reported an alkalide reduction method with which they synthesized air- and water-stable gold-coated gadolinium nanocrystals [214]. They used KNa alloy and 15-crown-5 ether to form the sandwich structure presented in Figure 6.1, which they obtained from mix-

ing in tetrahydrofuran (THF). Subsequently, they used this sandwich structure to reduce GdCl_3 . Lastly, they added AuBr_3 to the mixture to form the Au shell. They documented their findings using high resolution transmission electron microscopy (HRTEM), X-ray diffraction (XRD) and energy dispersive X-ray spectroscopy (EDX).

Figure 6.2a shows the well-distributed, and homogeneous in size, core-shell Gd-Au nanocrystals. From the analysis of the nanoparticles with HRTEM, Gd in the core and Au as shell were identified (Figure 6.2b). Bulk elemental analysis of the particle obtained by X-ray fluorescence revealed a composition of 41.6 atomic% Gd and 58.4 atomic% Au.

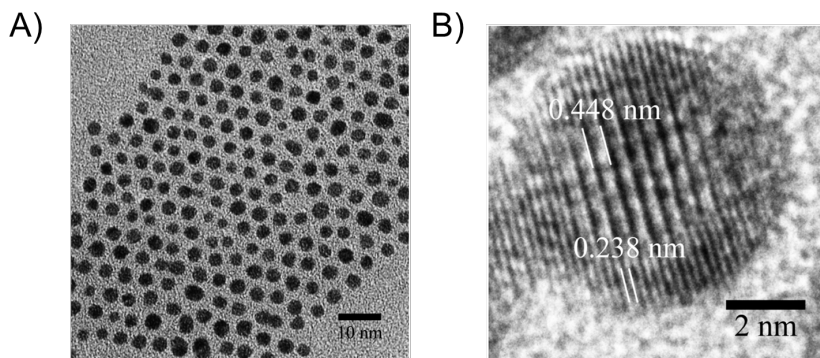


Figure 6.2: A) TEM image of core-shell Gd-Au nanoparticles B) HR-TEM of a nanoparticle with a 4.2 nm Gd core coated with 1.2 nm Au shell. Lattice fringes from the (111) planes of the Au shell and (010) planes of the Gd core as indicated in the figure. Taken from [214]

The composition was further investigated using EDX (Figure 6.3). The composition determined using EDX was 37.6 atomic% of Gd and 62.4 atomic% Au. However, it is worth noting that a peak of similar intensity as Gd, which is attributed to Si, is observed at ca. 1.90 eV.

Finally, the XRD pattern in Figure 6.4 shows contributions from both Au (circles) and Gd (squares). A detailed scan over 14h was recorded from 4° to 30° , and is presented in the inset. This scan shows two extra peaks associated with Gd (010) and Gd (011) at ca. 19.7° and ca. 27.0° , respectively.

In summary, Wagner and co-workers reported a method to obtain spherical and homogeneous core-shell Gd-Au nanocrystals. They used HRTEM, TEM, EDX and XRD to characterize their newly synthesized materials. From their results, questions can be raised regarding the purity of their process as extra unidentified elements can be observed with EDX.

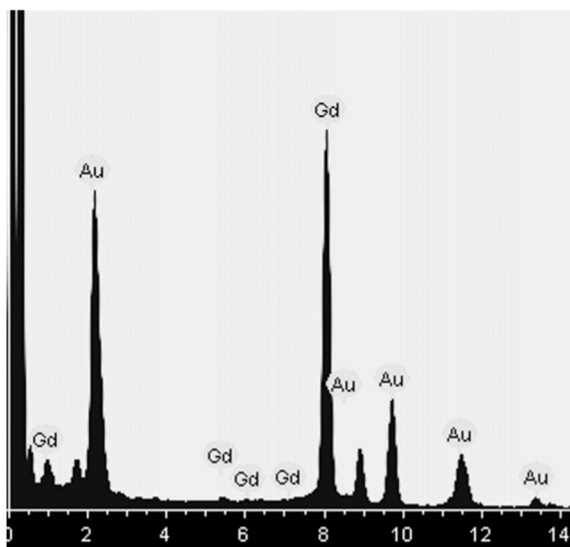


Figure 6.3: EDS spectra of core-shell Gd-Au nanocrystals. Taken from [214]

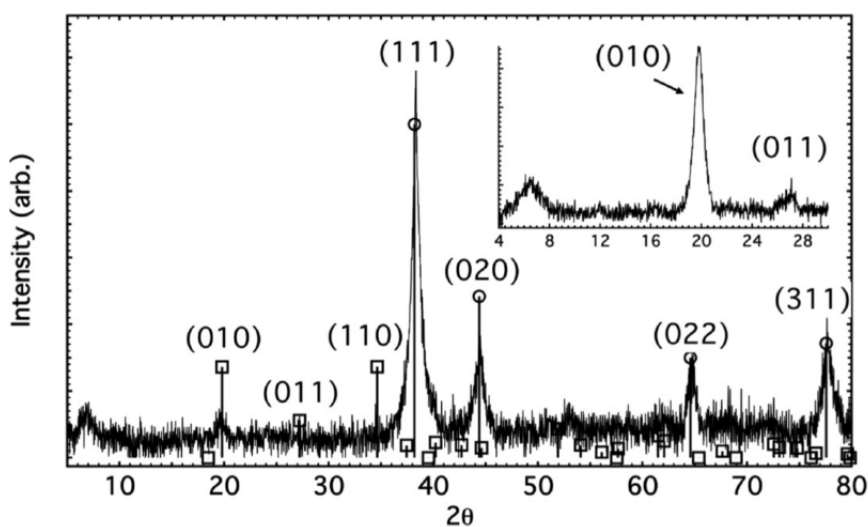


Figure 6.4: X-ray diffraction pattern of the Gd@Au nanocrystals. Peaks from Au (circles) and Gd (squares) are labelled. The inset shows a detail scan recorded during 14h from 4 to 30° where Gd(010) and Gd(011) are identified. Taken from [214]

Results

With the aim of replacing Au by Pt, and producing Pt-coated Gd nanoparticles, we first tried to reproduce the results presented above by closely

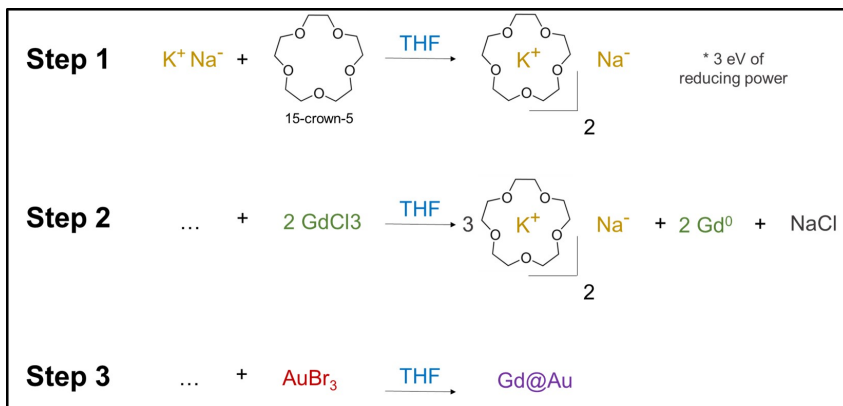


Figure 6.5: Synthesis of core-shell Gd-Au nanocrystals summarized in 3 steps

following their experimental procedure. A schematic of the three steps of this alkalide reduction method is presented in Figure 6.5.

The synthesis was done at room temperature in a Ar-purged glovebox to prevent oxygen contaminations. The concentration of O_2 and H_2O was monitored, and kept below 1 ppm. Also, as reported by Wagner and co-workers, the first attempts of the synthesis were done in a glass beaker. Prior to the synthesis, we dried the THF with Na, distilled it over molecular sieves, and transferred the THF to the glovebox (Omni-Lab system, Vacuum Atmospheres, <0.5 ppm O_2) where the synthesis took place. Step 1 consisted of adding the KNa alloy (44 wt.% Na 56 wt.% K, Sigma aldrich) to the THF. 5-crown-5 ether (98 %, Sigma aldrich) was then added to form the sandwich structure $\text{K}^+(\text{15-crown-5})\text{Na}^-$. For Step 2, GdCl_3 was dissolved in ~ 20 mL of THF and added to the rapidly stirred $\text{K}^+(\text{15-crown-5})\text{Na}^-$ prepared in Step 1. At that point, metallic Gd nanoparticles should be formed. The last step, Step 3, was to slowly add AuBr_3 (99.9 %, trace metal basis, Sigma aldrich) to form the Au shell. Once the synthesis was finished, we recovered the nanoparticles via centrifugation. In addition to what was reported by Wagner and co-workers, we water- and acid-washed (0.1 M HClO_4) the catalyst three times to remove the unreacted species, and dissolved the Gd_2O_3 potentially at the surface of the nanoparticles.

To verify the dispersion and composition of our newly synthesized material, we performed HRTEM and EDX line scans. For the HRTEM analysis, the particles were dispersed in a mixture of ethanol and water with a ratio of 1:1. Figure 6.6 shows the TEM images of the material obtained from the synthesis. The alkalide reduction synthesis lead to non-spherical nanoparticles with a very broad size distribution. Based on the images recorded, the diameters of the particles range between 4.5 to 78.1 nm with average size

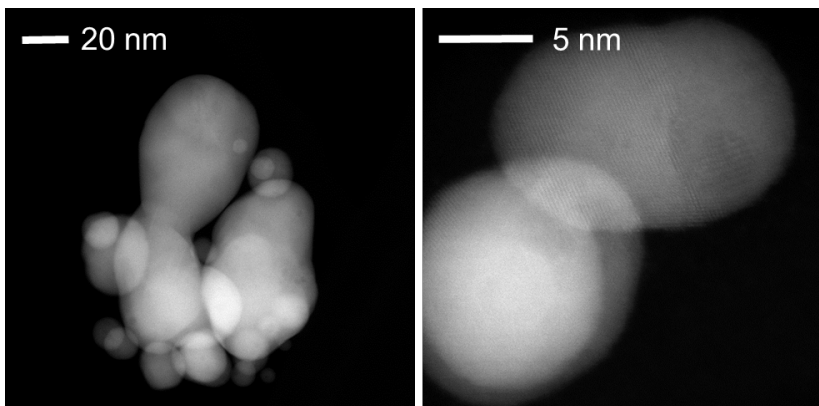


Figure 6.6: High-resolution transmission electron microscopy images of the catalyst obtained from the alkalide reduction at two magnifications. Courtesy of Brian Knudsen

at 21.6 ± 16.5 nm. Also the EDX line scans performed on many different particles only showed Au.

The composition and the chemical state of the elements were analyzed with XPS, where Figure 6.7a shows a survey spectrum of our catalyst. Among the elements detected, we can see clear contributions from Au, O and C, as expected. A more discrete signal associated with Gd is also observed. Surprisingly, Na and Cl were also detected.

For a more accurate analysis, detailed scans of Au 4f and Gd 4d peaks were recorded. The acid- and water-washed catalyst was compared to one annealed at 500°C in an oxygen atmosphere. By doing so, the elements having higher affinity for the oxygen migrated from the core to the surface of the nanoparticles. The Au 4f scans of the washed and annealed samples both show a metallic state with peak position at 84.1 eV. The Gd 4d scans are presented in Figure 6.7c. To help analyzing the Gd spectrum, the results obtained from the alkalide synthesis are compared with what was reported for the Pt_xGd nanoparticles obtained from mass filtered aggregation technique (green-yellow curve) [164]. The Gd 4d spectra of the as-prepared Pt_xGd shows a metallic state with a peak at 141.8 eV. When exposed to air, the gadolinium of the Pt_xGd oxidized, and a shift to higher binding energy is observed (142.4 eV). While both the washed and annealed samples seem to contain gadolinium oxide, a huge contribution at 155.1 eV associated with Si 2s of SiO_2 is observed for the material annealed at 500°C . The Si contamination was confirmed by the observation of a peak at 102.7 eV, which is associated with Si $2p_{3/2}$.

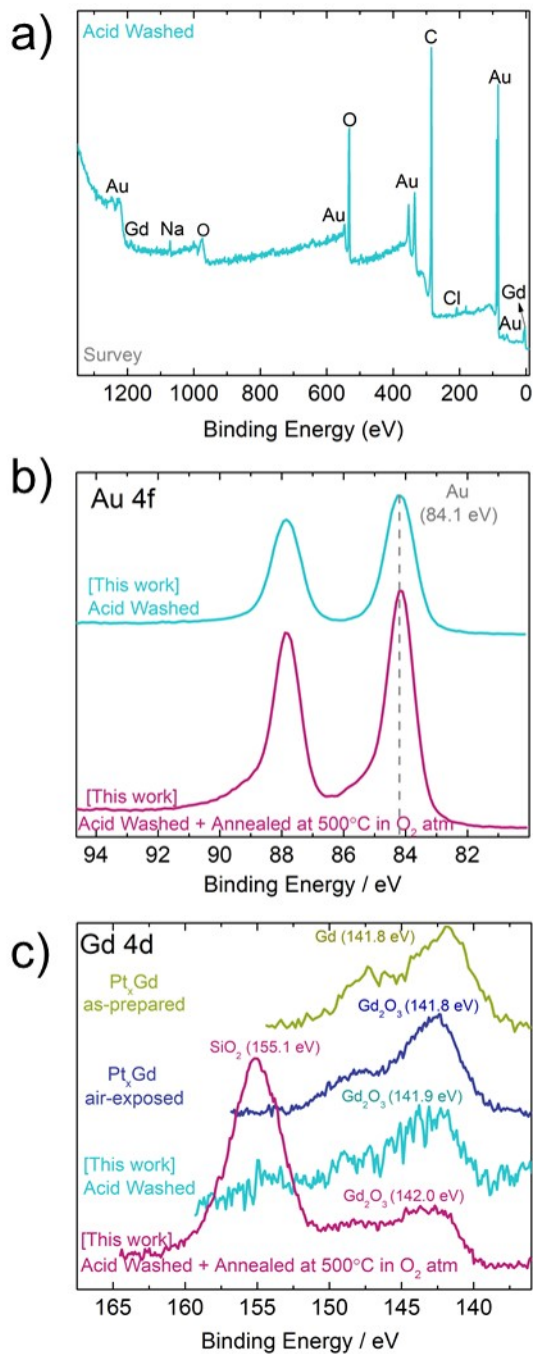


Figure 6.7: X-ray photoelectron spectroscopy of the sample obtained from the alkalide reduction technique. a) Survey, b) Au 4f and c) Gd 4d detail scans of the catalyst. The spectra of the Gd 4d obtained in this work is compared to one reported in [164]

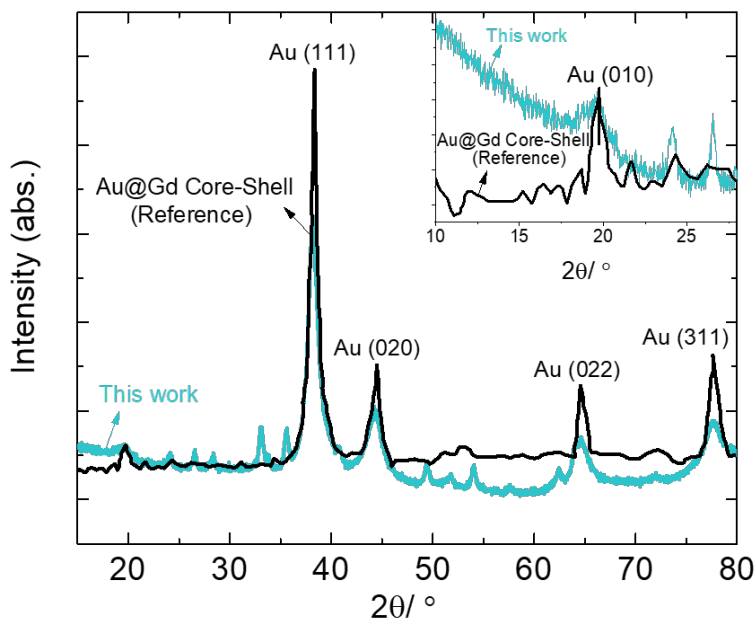


Figure 6.8: X-ray diffraction patterns of the core-shell Gd-Au nanoparticles from Wagner and co-workers (black line), and the material synthesized in this work (blue line).

The catalyst was also characterized with XRD. The XRD of the as-reported core-shell Gd-Au nanocrystals [214] (black line), and the sample obtained from our synthesis (blue line), are shown in Figure 6.8. The two sets of XRD data are, somewhat, similar. Au peaks associated with (111), (020), (022) and (311) reflections are observed, whereas no peaks corresponding to Gd or Gd_2O_3 are observed.

6.1.1 Discussion

The HRTEM, EDX line scans, XPS and XRD data all point to the fact that no core-shell Gd-Au nanocrystals were synthesized. The HRTEM (Figure 6.6) showed a very broad distribution in the size of the Au particles. While the XRD pattern of our synthesized sample is similar to the one reported, the XPS analysis does not show a Gd core and a Au shell. The proportion of GdCl_3 reduced into its metallic form is very small compared to the Si contamination, which was also present in the EDX spectrum reported by Wagner and co-workers, though it was not identified. We suspect the Si

contamination to come from i) the molecular sieves used to dry the THF, and ii) the glass beakers used for the synthesis. The incorporation of Si into the synthesized catalyst suggests that SiO₂ was reduced instead of GdCl₃, which explains the larger amount of Si as compare to Gd, detected with XPS. In an attempt to avoid Si contamination, we stopped using molecular sieves to conserve the dried THF, and replaced as much as possible of the glassware with Teflon (results not shown). Unfortunately, similar results to what was reported, though with smaller amount of Si, were obtained.

6.1.2 Conclusion

In conclusion, all the attempts to synthesize core-shell Gd-Au nanocrystals using the alkalide reduction method were unsuccessful. Following the procedure reported by Wagner and co-workers, we could only observe the formation of Au particles contaminated with Si, Na and K.

6.2 Cyanide Reduction Synthesis

Kenneth W. Lux and Elton J. Cairns proposed an aqueous route to obtain intermetallic compounds of Pt alloyed with Ce or Pr. In the synthesis method employed, the metal precursor containing Pt was chosen carefully. They selected H₂Pt(CN)₆ as Pt⁺ is complexed with CN⁻, which can lead to a volatile product, and can, therefore, be easily removed. The Pt precursor was then combined with the other metal cation, i.e. Ln(NO₃)₃, to form what they assumed as HLn[Pt(CN)₆]. The annealing of the precursor was done in 4% H₂ in He, and Pt₂Ce or Pt₂Pr were obtained.

X-ray diffraction patterns of the powders obtained from HLn[Pt(CN)₆] (Ln=Ce, Pr) precursors are presented in Figure 6.9. In Figure 6.9a, the peaks associated with Pt₂Pr have been assigned assuming a MgCu₂ Laves phase structure (space group Fd $\bar{3}m$; Strukturbericht designation: C15), as reported in the literature [218,219]. A small fraction of Pt₅Pr, marked with asterisks, is also identified. Pt₂Ce is isomorphic with Pt₂Pr, and as such, the peaks of Pt₂Ce can also be correlated to the MgCu₂ structure. The Pt₅Ce crystalline structure is identified with asterisks in Figure 6.9. Most importantly, in both cases, there are no peaks associated with polycrystalline Pt, which means that all the Pt contained in the precursor alloyed with Ce or Pr. Based on the XRD data, they claimed that an average particle size of ca. 25 nm were obtained for Pt₂Pr and Pt₂Ce.

To prevent the particles from sintering, it is reported that a salt can be added as separating media [220,221]. This salt act as a matrix, and is mixed with the precursor before the annealing. This technique was specifically developed for PtFe alloy nanoparticles, where NaCl was used as the salt

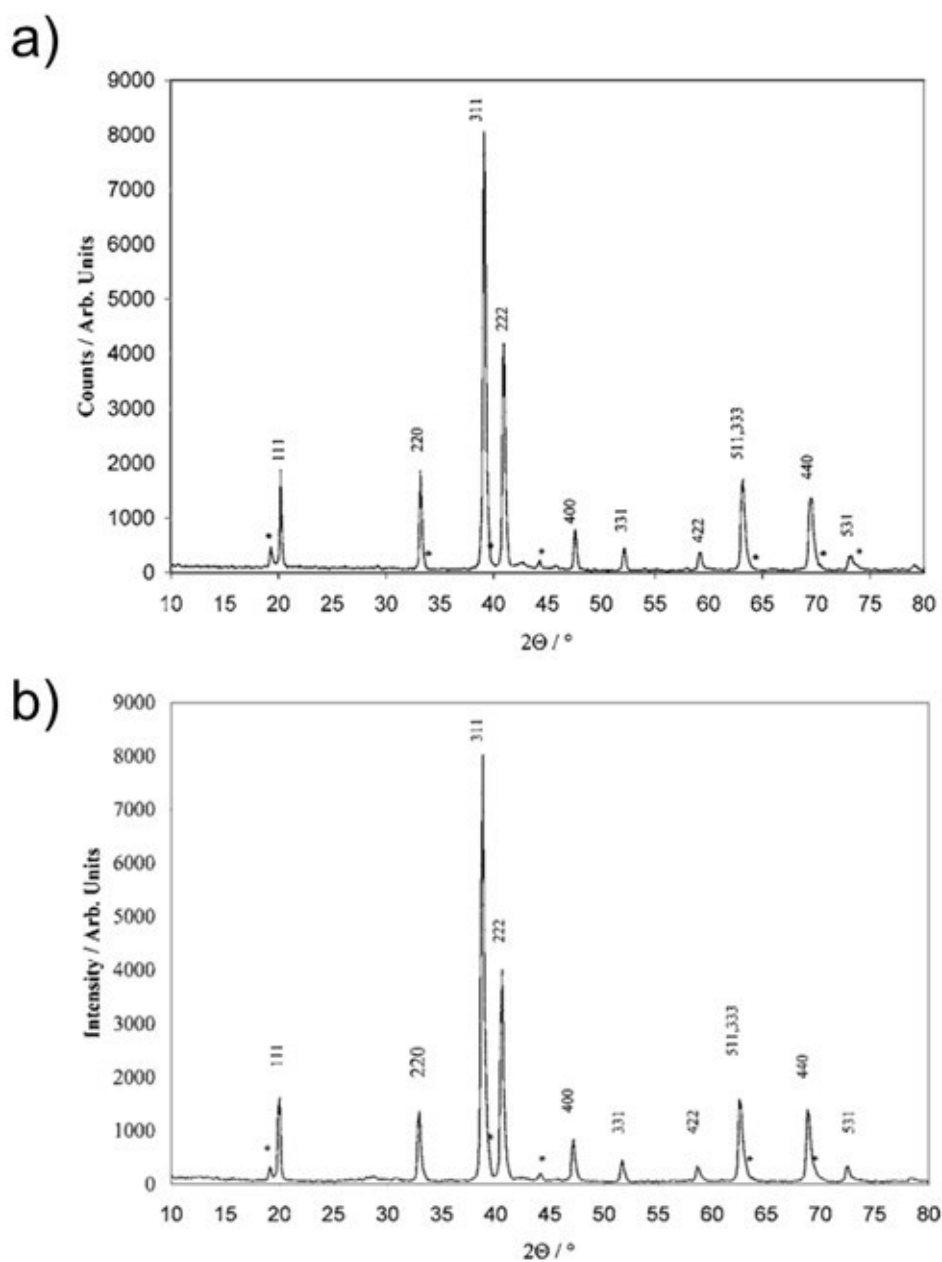


Figure 6.9: X-ray diffraction patterns of Pt-Pr and Pt-Ce powders obtained from the cyanide reduction method. Asterisks denote peaks associated with a) Pt₅Pr, and b) Pt₅Ce. Figures taken from [212]

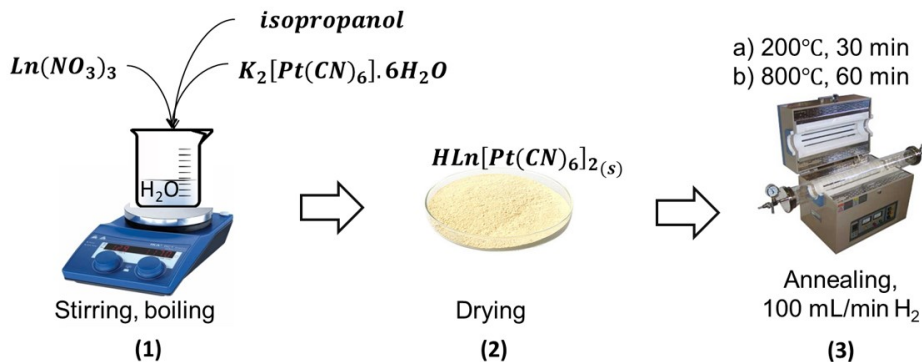


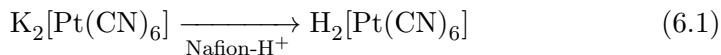
Figure 6.10: Schematic cyanide reduction protocol used in this work. Protocol taken from [212].

matrix. NaCl was chosen because it is chemically stable, and soluble in water, so that it can be easily removed after the annealing process by a water wash. Li and co-workers reported that for a NaCl-to-FePt ratio of 400:1, they could reduce the PtFe particle size from 15 nm to 4 nm in diameter [220].

6.2.1 Experimental Section

The experimental procedure used to obtain alloys of Pt and rare-earths was mostly taken from [212]. For practical and health reasons, we first tried $\text{K}_2\text{PtCl}_6 \cdot x\text{H}_2\text{O}$ as Pt precursor. We observed that when in solution, the $\text{K}_2\text{PtCl}_6 \cdot x\text{H}_2\text{O}$ started reducing already at 80°C, preventing us from using it as a platinum source. Therefore, we went back to the suggested Pt precursor, i.e. $\text{K}_2\text{Pt}(\text{CN})_6$ (Sigma Aldrich, 99.99% trace metal basis). Figure 6.10 summarizes the experimental procedure followed to obtain 1g of alloy:

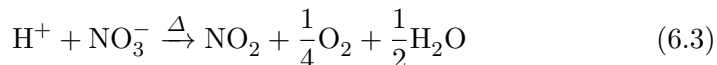
Step 1 First, 808.5 mg of $\text{K}_2\text{Pt}(\text{CN})_6$ (Alfa Aesar, 99.9%) was dissolved in 200 mL of ultra-pure water (Milli-Q, 18.2 M Ω). The solution was stirred for approximately 2h with four 6 cm x 6 cm pieces of protonised Nafion 117, to ion-exchange the potassium from $\text{K}_2\text{Pt}(\text{CN})_6$ with protons. As the ion-exchange between K^+ and H^+ generates a drop in pH, the exchange could be followed with a pH-meter. When, the pH became stable, it meant that $\text{H}_2[\text{Pt}(\text{CN})_6]$ was predominant, and the Nafion membranes were then removed.



~ 1.9 mmol of $\text{Ce}(\text{NO}_3)_3 \cdot 6\text{H}_2\text{O}$ (Sigma-aldrich, 99.999% trace metal basis) or $\text{Y}(\text{NO}_3)_3 \cdot 6\text{H}_2\text{O}$ (Sigma-aldrich, 99.8% trace metal basis), corresponding to a ratio of 1:2 Ln:Pt, was dissolved in ~ 15 mL of water, and added to the platinum solution.

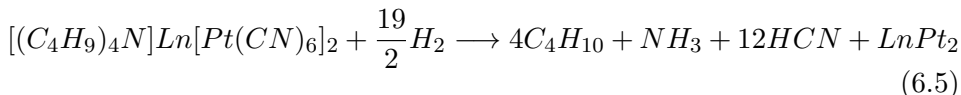
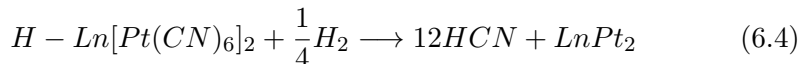


The solution was heated to its boiling point, and 2-propanol (Sigma-aldrich, 99.5%) was added to keep the liquid volume constant. This way, the water was slowly replaced with 2-propanol, and when the precursor was dried, the amount of intercalated water was minimized. Once the precursor was dried, ~ 20 mL of methanol was added three times to ensure that the nitrate ions from the precursor decomposed into NO_2 , and released as a gas, as described in equation (6.3). The precursor was then dried for a second time.



Step 2 The dried precursor resulted in a fine light-yellow powder. To ensure total dryness, an extra drying step at 60°C for 2h in air was performed.

Step 3 The precursor was then placed in a tube-furnace and purged for 1h. We initially tried purging with 5% H_2 gas, but had to switch to 100% H_2 at 100 mL/min for total precursor-to-alloy conversion. The precursor was first dried at 200°C in the H_2 atmosphere for 1h, and then annealed at 800°C . Lux and co-workers reported doing a "shock reduction" technique to avoid sintering, and favor the formation of smaller particle size. In the "shock reduction" technique, the furnace was first heated up to 800°C , and then the precursors was added. Unfortunately, this approach was not possible with the equipment at our disposal and, thus, we had to increase the temperature from room temperature to 800°C with the catalyst in the furnace. Once 800°C was reached, this temperature was maintained for 60 min. Equations (6.4) and (6.5) show the expected chemical transformation of the precursor to the alloy taking place under the experimental conditions described [212]. To investigate if the alloying process could also occur at lower annealing temperature, the precursor obtained from step 2 was also annealed at 500°C , 600°C and 700°C .



After the synthesis, the catalyst was recovered, and water- and acid-washed (0.1 M HClO₄) three times to remove the byproducts, as well as dissolve any remaining CeO₂ or Y₂O₃. The crystalline structure of the powder was probed using XRD. In situ XRD coupled to a mass spectrometer (MS) was also used. For the in situ XRD experiment, the system was purged with 98 % H₂/ 2 % Ar at 100 mL/min. The m/z=2 associated with H₂ was monitored, and once the signal detected was stable, we began the annealing procedure. For practical reasons, 700°C was the maximum temperature at which we could anneal with the in situ XRD setup. The temperature was increased from room temperature to 700°C, and a XRD pattern was recorded for every increase in temperature of 100°C.

Based on the positive results reported when using a salt matrix with PtFe particles, i.e. decrease of particle size, we decided to investigate if this method could be used to obtain smaller Pt_xLn particles [220,221]. Thus, the HLn[Pt(CN)₆]₂ precursor was mixed with NaCl in different ratios. To ensure that the precursor was well mixed with NaCl, a mortar and pestle were used. After annealing at 800°C, the powder was washed three times with water to completely dissolve the NaCl, after which the catalyst was characterized using XRD.

When tested as an oxygen reduction reaction (ORR) catalyst, the powder was dispersed in isopropanol, and drop-casted onto a glassy carbon (GC) electrode. The electrochemical ORR measurements were performed as described in Section 3.3.

6.2.2 Physical Characterization

To test the reproducibility of the synthesis method presented by Lux and co-workers [212], we first reproduced the synthesis of the Pt_xCe alloy. Figure 6.11 compares the XRD patterns of the Pt_xCe synthesized in this work (black line) to what was previously reported (grey line).

In both cases, the synthesis yields a complete precursor-to-alloy conversion, and no peaks associated with the reflection of polycrystalline Pt. The XRD pattern of the powder obtained by Lux and co-workers [212] shows an

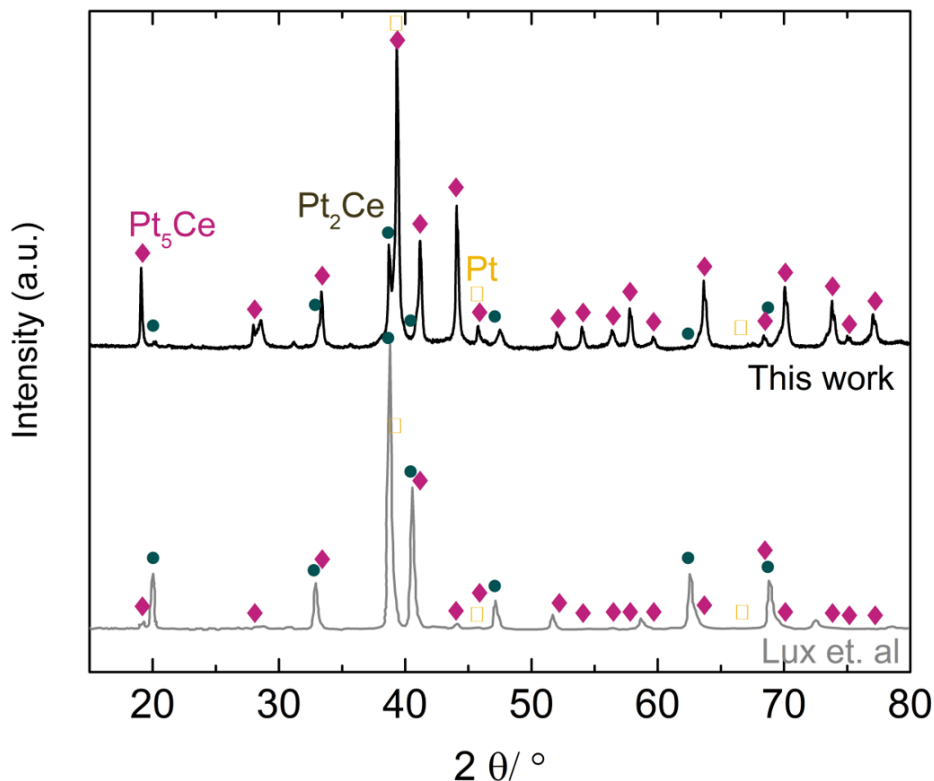


Figure 6.11: X-ray diffraction patterns of the platinum-cerium powder synthesized in this work (grey) and the reference [212] (black).

intense contribution from the Pt_2Ce phase with diffraction peaks at 20.0° , 32.9° , 38.8° , 40.6° , 47.2° , 62.5° and 68.8° . The XRD pattern of the Pt_xCe obtained in this work shows peaks at 19.8° , 39.3° , 41.2° and 44.1° associated with the Pt_5Ce crystalline structure [222]. We hypothesize that the differences in phase formation observed came from the slightly different synthesis protocols.

As the method was confirmed to be able to produce a Pt_xCe intermetallic compound, we extended the procedure to Pt_xY alloys, and replaced $\text{Ce}(\text{NO}_3)_3$ with $\text{Y}(\text{NO}_3)_3$. The annealing procedure was performed at 500°C , 600°C , 700°C and 800°C to investigate if a lower annealing temperature could be used in an effort to avoid sintering. Figure 6.12 presents the XRD patterns recorded for the materials obtained at different annealing temperatures.

The analysis of the XRD patterns indicates that Pt_3Y (green triangle) and hexagonal Pt_5Y , from the prototype structure Cu_5Ca , are all present in the Pt_xY catalysts. The most intense Pt_3Y peaks are observed for Pt_xY

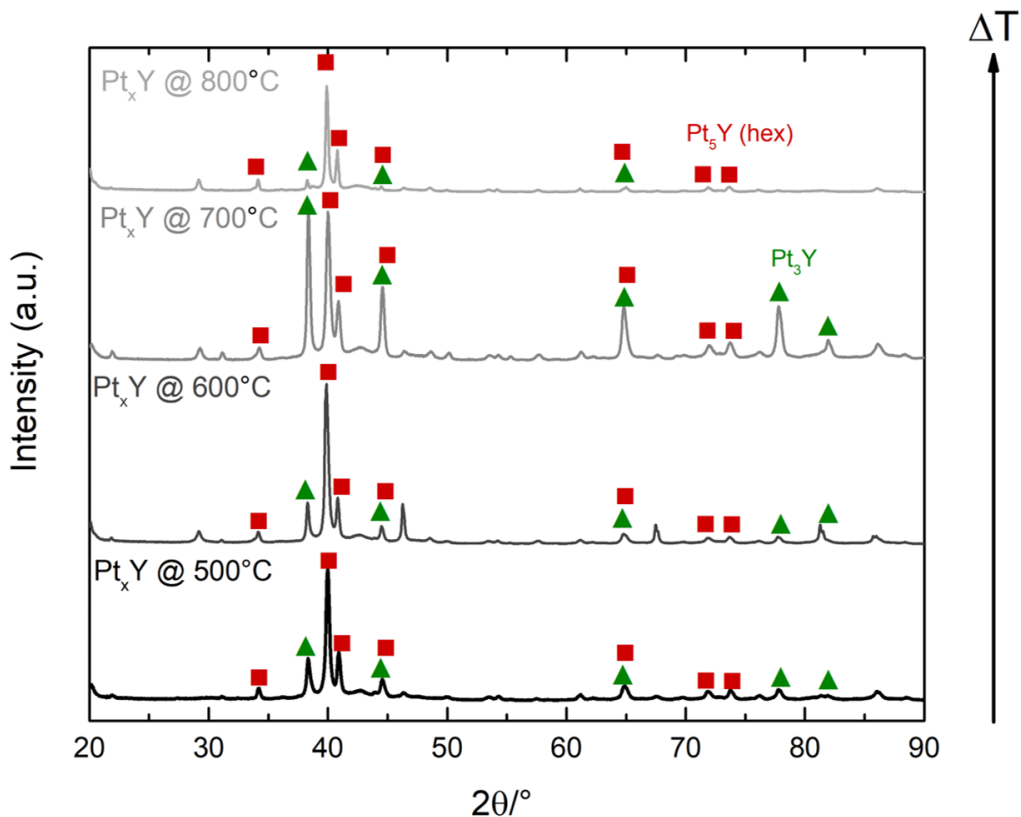


Figure 6.12: X-ray diffraction patterns of Pt_xY obtained for annealing at 500°C, 600°C, 700°C and 800°C.

(700°C) with peaks at 38.4°, 44.6°, 64.8°, 77.82° and 82.0°. Similarly, XRD patterns were recorded for Pt_xY annealed at 500°C, 600°C and 800°C. For these catalysts, most of the signal can be assigned to the hexagonal Pt₅Y, with the most intense peaks at 39.9° and 40.8°.

With the aim of getting more insight into the transitions occurring between the precursor and the alloy, in situ XRD was performed. Like previously, the in situ XRD was coupled to a MS where the products formed during the synthesis could be detected. The precursor was synthesized, and mounted in the in situ XRD setup where the annealing took place. The typical XRD patterns recorded and the masses detected from the products formation are presented in Figure 6.13a and b, respectively. We tried to assign the peaks from the XRD patterns taken from 40° to 300°C (Figure 6.13a), but were unsuccessful. Therefore, we can only assume that these peaks are related to HLn[Pt(CN)₆]₂, identified as the precursor [212]. The identification of the peaks observed in the XRD patterns recorded from

400°C to 700°C shows only polycrystalline Pt; no alloying process took place.

Selected m/z detected are presented in Figure 6.13b, where the temperature is labeled with grey dashed lines. The full MS spectrum is presented in Figure C.1. $m/z=2$, associated with H_2 (black line), is the gas used during the synthesis. When $HLn[Pt(CN)_6]_2$ is reduced, we expect CN^- to react with H_2 , and form HCN. The most abundant mass related to HCN is $m/z=27$ (purple line) due to the natural abundance of 1H , ^{12}C and ^{14}C . The peaks directly related to oxygen, $m/z = 16$ (green line), $m/z = 32$ (blue line), as well as H_2O ($m/z = 18$, red line), were also followed, as it is expected that the synthesis is sensitive to oxidizing species. The MS data indicates that HCN gas is produced even at low temperature, i.e. at 200°C. The highest intensity of HCN is detected for 500°C and 600°C, after which it is not detected anymore. This means that the reduction of platinum-cyanide starts already at 200°C even though most of it occurs at 500°C and 600°C.

The XRD pattern of the Pt_xY obtained when using NaCl as salt matrix during the annealing is presented in Figure 6.14 (black line), and compared to Pt_xY annealed according to the standard procedure. The NaCl-to-precursor ratio used in this work was 4:1. We observed no major differences in the full width half maximum of the main peak at 39.9°, which suggests that similar crystallite size was obtained. Additionally, we observed that the crystalline structure remains the same with, or without, NaCl. We tried higher ratios of NaCl-to-precursor (results not shown) but even when increasing the annealing time, it was impossible to alloy Pt and Y.

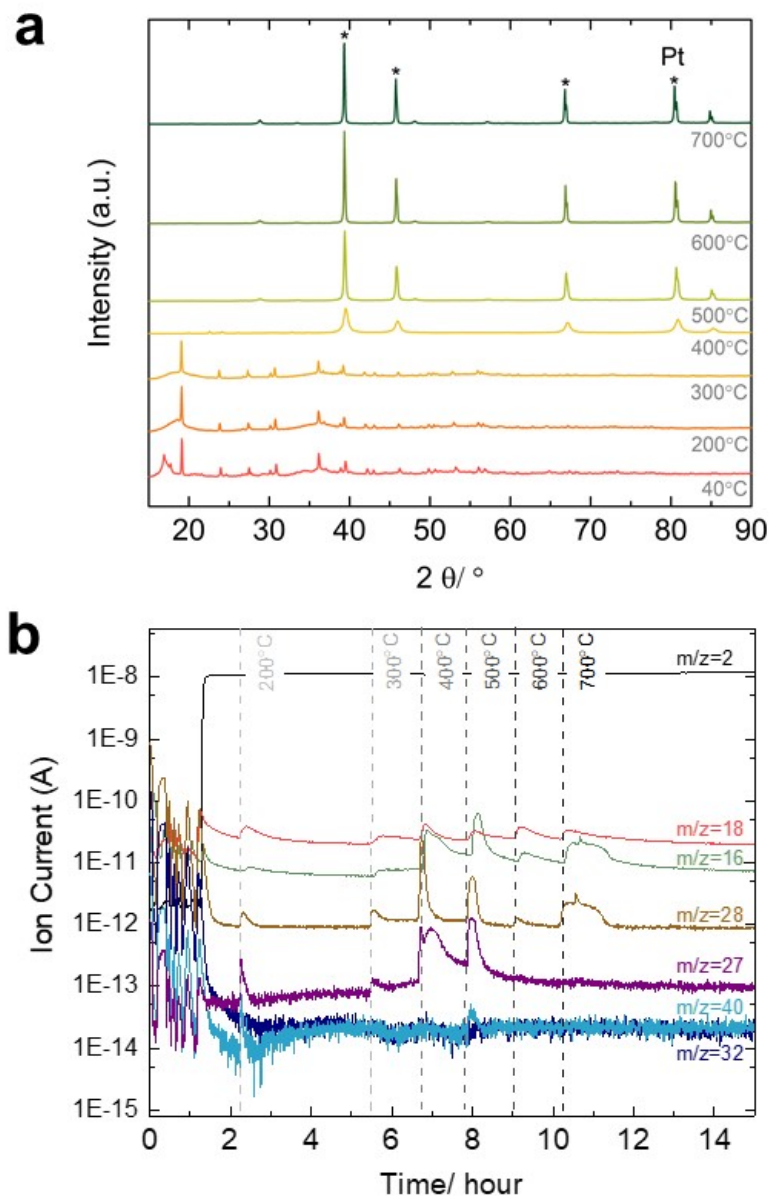


Figure 6.13: a) X-ray diffraction spectra of platinum cyanide and yttrium precursor at 40°C, 200°C, 300°C, 500°C, 600°C and 700°C, and b) Mass-spectrometer spectrum recorded during the annealing process.

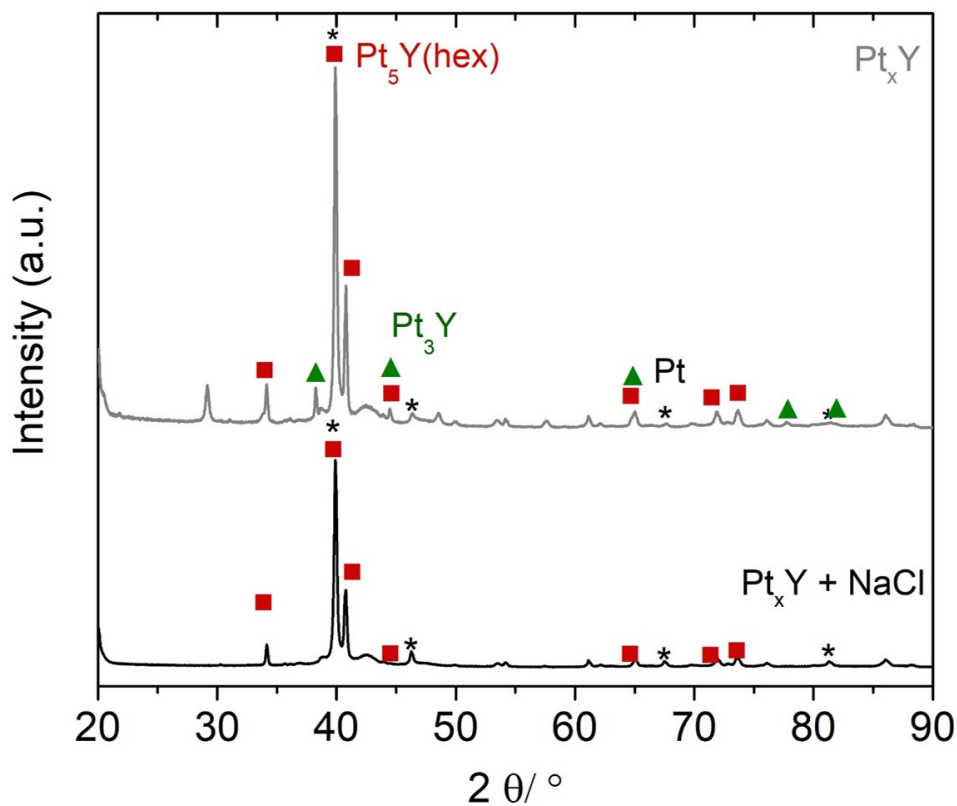


Figure 6.14: X-ray diffraction patterns of Pt_xY powder obtained from cyanide reduction synthesis (grey line) and with the addition of NaCl as salt matrix annealing (black line).

6.2.3 Electrochemical Oxygen Reduction

The Pt_xY powders annealed at 750°C and 800°C were tested for the ORR activity, and compared to a Pt/C nanoparticles catalyst, with average particle size > 50 nm. The catalysts were first cycled ~ 200 times at 200 mV/s in N_2 saturated 0.1 M HClO_4 before a stable cyclic voltammetry (CV) was obtained. This electrochemical step is associated to the formation of a Pt overlayer. An example of the CVs recorded and corresponding CO stripping measurement for the Pt_xY (800°C), is presented in Figure C.2. Once a stable CV was obtained, CVs in N_2 - and O_2 -saturated 0.1 M HClO_4 were recorded at 50 mV/s. Figure 6.15a shows representative anodic scans for Pt_xY (800°C) recorded in N_2 - and O_2 -saturated 0.1 M HClO_4 , where the background-corrected anodic scan is also shown (red curve).

The specific activities of the various catalysts are presented in Figure 6.15b. As shown, Pt_xY (750°C) (blue bar), and Pt_xY (800°C) (turquoise bar) have only slightly higher catalytic activity than the Pt/C nanoparticles. The current recorded for Pt_xY (800°C) is of 2.93 ± 0.2 $\text{mA}/\text{cm}_{\text{Pt}}^2$, compared to 2.0 ± 0.2 $\text{mA}/\text{cm}_{\text{Pt}}^2$ for Pt/C black. This is much smaller than the 10.7 $\text{mA}/\text{cm}_{\text{Pt}}^2$ measured on the polycrystalline Pt_3Y disk reported previously [162,168]. The activity normalized by the mass of Pt was not measured because we acknowledged that the average crystallite sizes of Pt_xY catalysts, suggested by the XRD patterns, are too big, and would undeniably translate to low mass activity.

6.2.4 Discussion

The synthesis of the Pt_xCe alloy using the cyanide reduction method reported by Lux and co-workers [212] was reproduced in this work (Figure 6.11). Our findings also show that the synthesis method can be extended to the formation of other types of Pt-Ln alloys, such as Pt_xY (Figure 6.12 and 6.14). We concluded that it was possible to form the alloy at lower temperatures than 800°C (Figure 6.12). More specifically, we observed that the alloying was taking place already at 500°C . This was supported by the in situ XRD experiment (Figure 6.13), where the most intense signal associated with $\text{Pt}(\text{CN})_6$ reduction was observed for 500°C . The crystalline structure of the Pt_5Ln annealed at 800°C , synthesized in this work, is different from the Pt_2Ln one reported. We suspect that minor differences in the experimental procedure could be the main reason behind this inconsistency. We also observed that the crystalline structure of the Pt_xY catalyst varied between Pt_5Y and Pt_3Y .

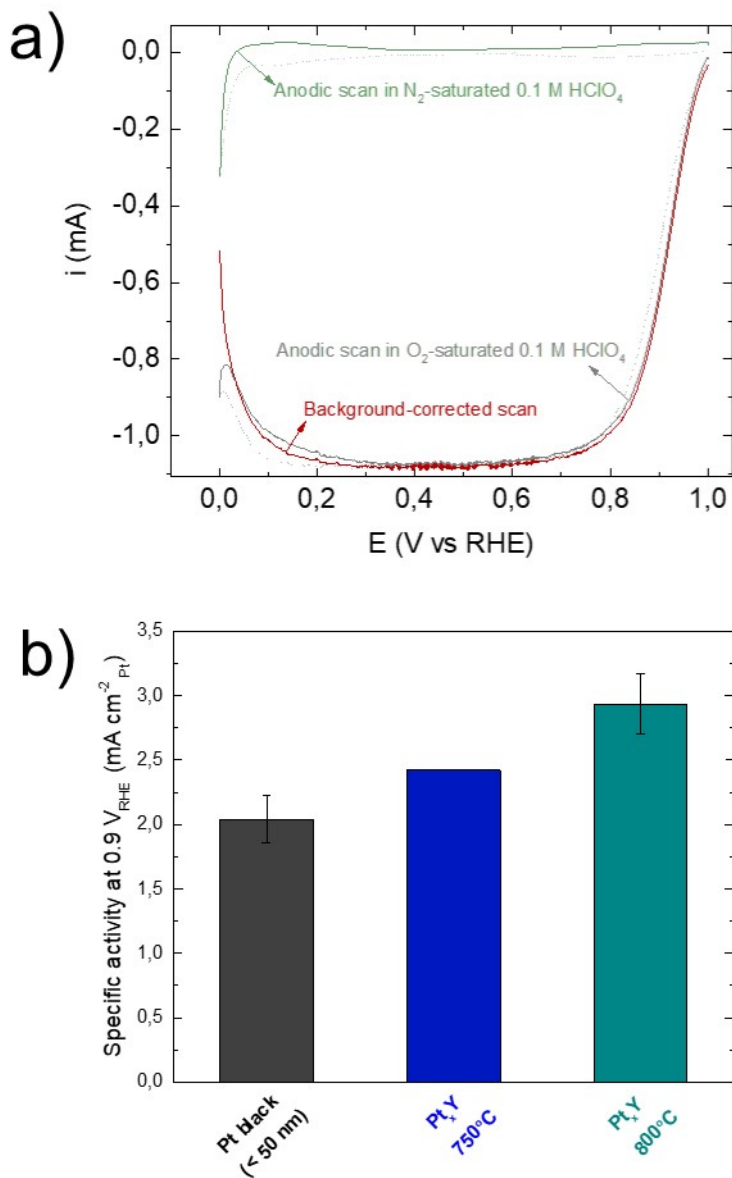


Figure 6.15: Oxygen reduction activity of Pt_xY catalyst obtained from the cyanide reduction method. The scan were recorded in 0.1 M $HClO_4$ at 1,600 rpm (dashed lines). a) The anodic scan (thick lines) related purely to the oxygen reduction (red) is obtained from the subtraction of the O_2 -saturated one (gray) to the N_2 -saturated one (green). b) The specific activity for the oxygen at 0.9 V_{RHE} is compared for Pt black (black), Pt_xY powder annealed at 750°C blue and 800°C (turquoise)

Pt_xY catalysts obtained from annealing treatment at 750°C and 800°C showed only slight improvement in specific activity in comparison to Pt black (Figure 6.15), and way lower specific activity than what was reported for polycrystalline Pt₃Y [162,168]. With the evidence we have, it is difficult to identify the reason for such low catalytic activity. However, part of it could be related to the formation of a Pt₅Y structure, instead of Pt₃Y. Finally, the use of NaCl as salt matrix during the annealing process did not decrease the average crystallite size, as shown in Figure 6.14. Unfortunately, we did not performed transmission electron microscopy (TEM) on the Pt_xY powder, which could have been useful to gain further understanding on the morphology of the Pt_xY powder with, and without, NaCl.

6.2.5 Conclusion

To summarize, we used the cyanide reduction method as reported by Lux and co-workers [212] to synthesize Pt_xCe and Pt_xY powders. We showed, using XRD, that the predominant crystalline structure obtained was Pt₅Ln (Ln=Ce, Y), when the annealing was done at 800°C. The Pt_xY catalysts obtained from annealing at 750°C and 800°C were tested for the ORR, and showed poor specific activity, compared to the expected 10.7 mA/cm²_{Pt} previously reported for polycrystalline Pt₃Y.

While it was relatively straightforward to obtain the Pt_xY alloy, the synthesis of well-defined nanoparticles supported on carbon using the cyanide reduction method is still a significant challenge. Also, the HCN gas produced during the annealing step could represent a safety issue if the catalyst had to be produced on larger scales. For these reasons, we decided to stop developing this method, and concentrated our efforts on the high temperature synthesis presented in Section 6.3.

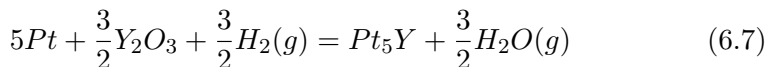
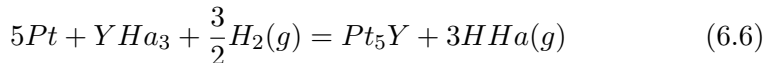
6.3 High Temperature Synthesis

The high temperature synthesis method consists of mixing Pt/C nanoparticles with rare-earth-based precursor, and anneal it at high temperature in a oxygen- and metal-free reactor to form alloy nanoparticles. The experimental conditions selected for the synthesis of Pt_xY were determined based on thermodynamics calculations. The newly synthesized Pt_xY nanoparticles were investigated with XRD, XPS and TEM. The thorough characterization of the nanoparticles are strong evidence that an alloy was formed and that the nanoparticle shape is conserved. Finally, the enhanced oxygen reduction activity registered reveals the great potential of this catalyst for future testing in a membrane electrode assembly.

6.3.1 Thermodynamics Calculations and Early Work

This section is a short introduction to the thermodynamic calculations used to develop the high temperature synthesis method. For a more detailed version of the calculations, and early experiments, please refer to [217] and [216].

Alloys of late transition metals such as Fe, Ni, Cu and Co are thermodynamically unstable under fuel-cell conditions [166,223,224]. The transition metal tends to dissolve which results in a surface that is Pt enriched. The more negative heat of enthalpy of Pt-rare-earth alloys, i.e. $\Delta H_{f(ally)} \sim -4$ eV versus -0.25 eV for the late transition metal elements [225], may stabilize the alloy against dealloying. However, the alloying energy of the rare-earths with the oxygen is much greater, i.e. approximately -10 eV [164]. Thus, the oxidation reaction will be favored over the alloying process with platinum, in case oxygen contamination is present. The synthesis route presented here is based on thermal annealing in a hydrogen atmosphere, which is a reducing gas. The thermodynamic calculations were done with the HSC Chemistry software package (version 6.1), developed by Outotod Technologies. The Pt-rare-earth data used with the software were extracted from experimental studies, where oxides of rare-earth are thermally reduced, and alloyed with Pt. In his thesis, Brian Knudsen and co-workers showed that the high temperature synthesis could be applied to many rare-earth elements [216]. For this work, however, we focused our effort on the synthesis of Pt_xY , as its catalytic activity is among the highest reported for the ORR [162,164]. To determine which yttrium precursor should be used in the synthesis, we calculated the variation in Gibbs free energy for the reduction of yttrium halides (YHa_3) (equation (6.6)), and yttrium oxides (equation (6.7)) under hydrogen atmosphere, to obtain the Pt_5Y alloy.



More specifically, the variation in Gibbs free energy (ΔG) to form Pt_5Y from oxide (Y_2O_3) and halide yttrium precursors (YI_3 , YF_3 and YCl_3), were used to evaluate which experimental conditions would allow the lowest annealing temperature and, therefore, more accessible experimental conditions. From Figure 6.16a, it can be seen that the relative ΔG values of Y_2O_3 and YF_3 are more positive than the one determined for YI_3 and YCl_3 , making the latter two more interesting choices for our synthesis. However, we observed that even for YI_3 and YCl_3 , temperatures above 1000°C are needed to have ΔG values < 0 , and favor the alloying process. As annealing

at a temperature as high as 1000°C should be avoided when working with nanoparticles because of sintering, we had to find a way to decrease the alloying temperature. One option to lower the temperature is to displace the equilibrium towards the product side by removing the gas product (HHa).

The equilibrium partial pressure of HHa produced by the annealing Pt with YCl_3 , YI_3 and YF_3 , in an H_2 atmosphere can be calculated using the following equation:

$$K_{HHa} = \frac{\left(\frac{P_{HHa}}{P}\right)^3}{\left(\frac{P_{H_2}}{P}\right)^{3/2}} \quad (6.8)$$

Where K_{HCl} is the equilibrium constant, P the overall pressure, P_{H_2} the partial pressure of oxygen and P_{HCl} the partial pressure of HCl gas. The equilibrium partial pressure of H_2O coming from the reduction of Y_2O_3 with H_2 gas was determined using equation (6.9).

$$K_{H_2O} = \left(\frac{\frac{P_{H_2O}}{P}}{\frac{P_{H_2}}{P}}\right)^{3/2} \quad (6.9)$$

Based on equation (6.9) and (6.8), the equilibrium partial pressure of HI, HCl, HF and H_2O were plotted as function of temperature, using the ideal gas law ($PV=nRT$) for 1 bar H_2 . As seen in Figure 6.16b, a relative partial pressure of 0.01 for HCl and HI is reached at approximately 600°C, while for the same temperature the partial pressure of HF and H_2O is in the order of 10^{-6} . The partial pressure of these gases can be related to the reaction rate, since higher partial pressure, means that a bigger amount of precursor is reduced. Based on this assumption, one can show that catalyst on a gram scale can be produced during 1h of experiment if YCl_3 or YI_3 are used as precursors [216,217].

As mentioned previously, the energy gained by the oxidation of yttrium is greater than that of alloying with Pt. Therefore, one should minimized all interaction with O_2 through air exposure and/or water. To illustrate the sensitivity of Y to O-containing species, the equilibrium partial pressure of H_2O generated from the reduction of Y_2O_3 in an H_2 atmosphere can also be used as the maximum limit of H_2O that can be in contact with Pt_xY , before it becomes $Pt-Y_2O_3$. For a water level below that threshold, the reducing environment will inhibit the oxygen contaminant, and the alloying reaction will take place. The higher the temperature, the higher the tolerance for H_2O . The tolerance for water at higher temperature is explained by the difference in reaction rate for the reduction of YCl_3 , and the oxidation of YCl_3 and/or Pt_xY . For example, we estimated that the H_2O/O_2 threshold at 600°C is of approx. 2 ppm, while it is of 50 ppm at 800°C.

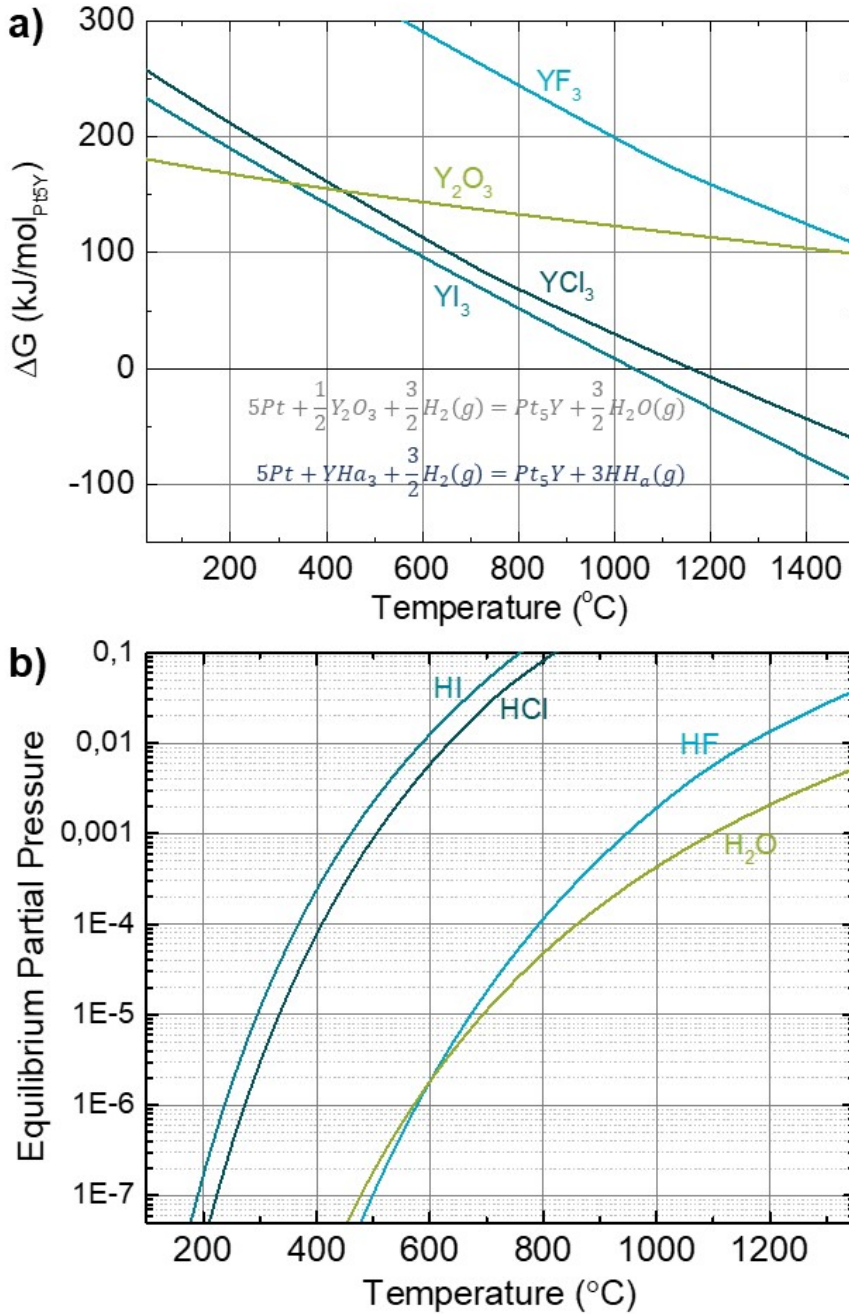


Figure 6.16: (A) Calculated variation in Gibbs free energy for forming Pt₅Y by annealing Pt assuming 1 bar of H₂ with Y₂O₃, YF₃, YCl₃, and YI₃. (B) Respective equilibrium partial pressures of gas products generated by the alloying process.

To verify the thermodynamic calculations described above, Christoffer Pedersen and co-workers [217] mixed Pt/C nanoparticles (TKK, ~ 7 nm diameter size) with YCl_3 , and annealed them in a quartz reactor under a H_2 flow of 10 mL/min at 700°C, 750°C, 800°C and 900°C. XRD patterns of the catalysts obtained from annealing at these temperatures were recorded, and are presented in Figure 6.17. Already at 700°C, i.e. a little below the melting point of YCl_3 (m.p. 721°C)[213], Pt_3Y and Pt_2Y are observed. However, a considerable contribution coming from Pt is also noted, which indicates that the annealing temperature must be higher for a full conversion. When annealing at 800°C and 900°C, the intensity associated to Pt decreases. At 800°C, the optimal composition is observed with intense peaks assigned to Pt_2 and Pt_3 , and relatively small Pt peaks. PtSi is observed at 900°C, but most likely originates from the glassware. From the results presented in Figure 6.17, we observed that the melting point of the yttrium precursor corresponds to start of the alloy formation. Based on that assumption, YCl_3 (m.p. 721°C) is much more suitable precursor than YI_3 , that has a melting point of 994°C. To summarize, based on the findings presented in Figure 6.17, the Pt_xY alloy can already be formed at 800°C with YCl_3 , limiting the sintering of Pt/C nanoparticles, and making YCl_3 a much better option than YI_3 .

To better understand how to control the alloying of Pt with Y, the formation of various Pt_xY crystalline phases was linked to HCl production. The HCl partial pressure plotted as a function of temperature in Figure 6.18a indicates whether Pt_3Y or Pt_5Y will be favored. Because of the limited experimental data available for Pt_2Y , this crystalline structure had to be left out. As illustrated in Figure 6.18, the alloy formation of that specific Pt_xY phase will occur if the HCl partial pressure is kept below the P_{HCl}/P equilibrium. For example, if the temperature is 400°C for a HCl partial pressure of 2×10^{-5} , the Pt/C nanoparticles will alloy with YCl_3 to form Pt_3 . Figure 6.18a is therefore highly useful for predicting the Pt_xY by varying the temperature and monitoring the HCl gas generated during the reaction.

The reaction time for the formation of Pt_3 and Pt_5 was also calculated. If the the alloying is limited by P_{HCl} , the reaction time can be measured using the ideal gas equation as presented below:

$$n_{\text{HCl}} = \frac{P_{\text{HCl}} \cdot Q \cdot t}{R \cdot T} \quad (6.10)$$

Where n_{HCl} is the number of moles of HCl generated, t the reaction time, Q the gas flow of H_2 , R the gas constant, and T the temperature of the gas. Using equation (6.6) and equation (6.10), where the number of mole of HCl, Pt_xY and Pt can be related.

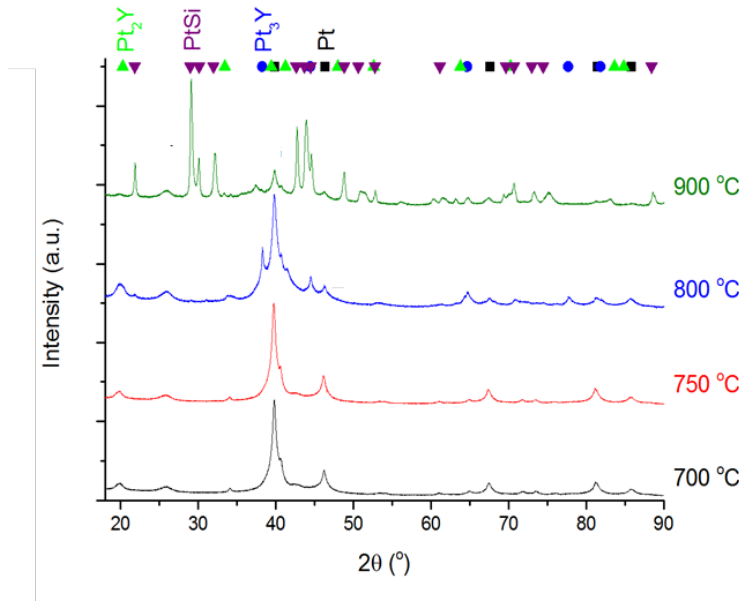


Figure 6.17: X-ray diffraction spectroscopy of Pt/C nanoparticles and YCl_3 precursor annealed at 700°C (black), 750°C (red), 800°C (blue) and 900°C (green). The synthesis was performed in a quartz reactor explaining the contamination with Si. Figure adapted from [217].

$$\frac{1}{3}n_{HCl} = n_{Pt_xY} = \frac{1}{x}n_{Pt_xY} = \frac{1}{x} \frac{w_{Pt}}{m_{Pt}} \quad (6.11)$$

Using the equation above, the alloying times of Pt_3Y and Pt_5Y can be obtained from:

$$t = \frac{3}{x} \frac{w_{Pt} \cdot R \cdot T}{m_{Pt} \cdot P_{HCl} \cdot Q} \quad (6.12)$$

As presented in Figure 6.18b, at 800°C the alloying of platinum into Pt_5Y and Pt_3Y takes between 50 to 140 minutes, respectively. This reaction time was calculated by assuming that the removal of HCl was the limiting factor (for chemical equilibrium).

6.3.2 Experimental Section

To satisfy the requirements needed for the alloying to occur, the handling of the chemicals, and the preparation steps took place in a glovebox (Omni-Lab system, Vacuum Atmospheres, <0.5 ppm of O_2 , <0.5 ppm of H_2O). A homemade gas-tight metal reactor was also built to fit the low O_2 concentration requirements [216]. The use of glass was also avoided to prevent

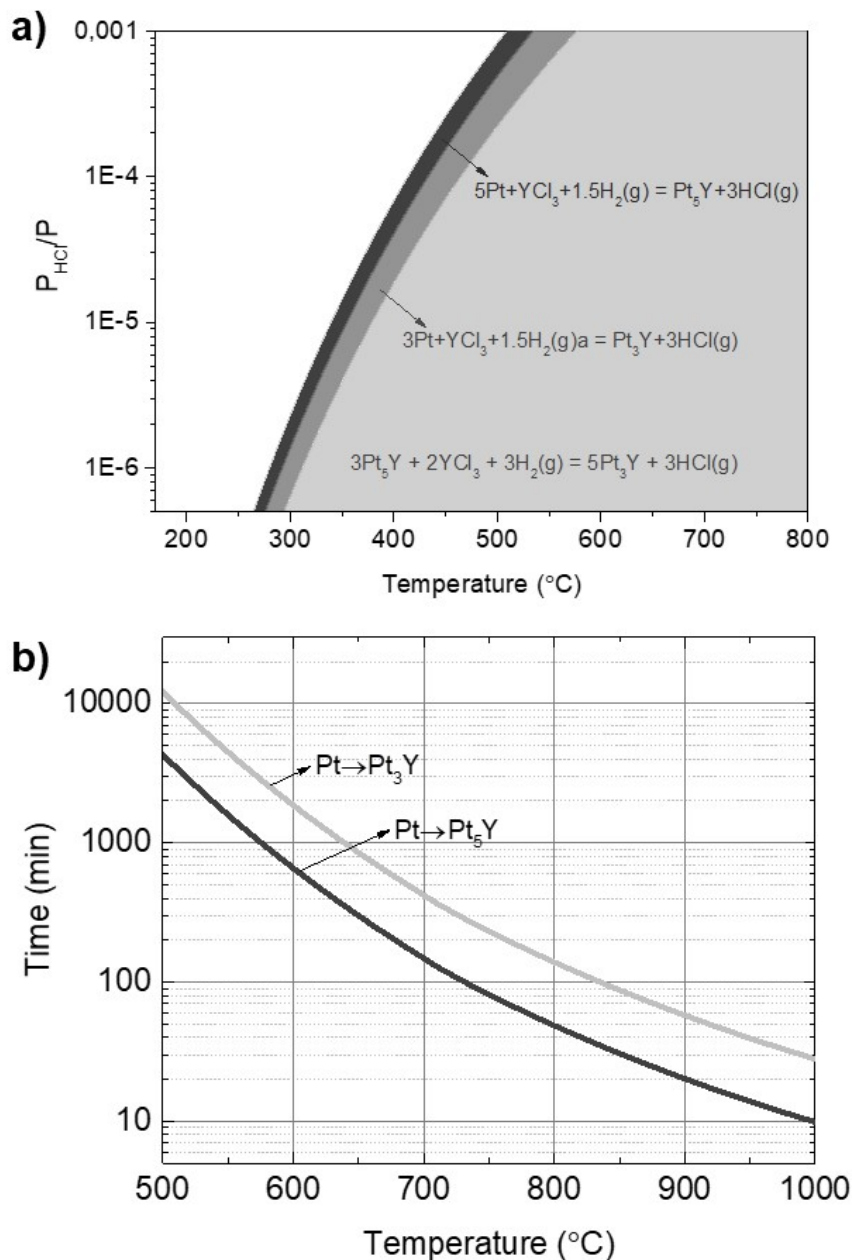


Figure 6.18: (A) Phase formation of Pt_3Y and Pt_5Y as a function of P_{HCl}/P and temperature. Insufficient data prevented us from calculating the phase formation of Pt_2Y . (B) Expected reaction time for 0.5 g of Pt in 10 mL/min 100% H_2 .

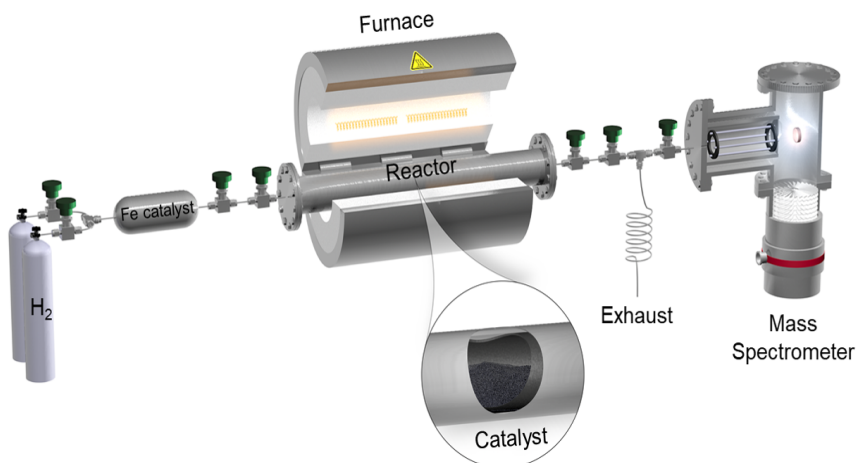


Figure 6.19: Metal reactor setup used for the high-temperature synthesis of $\text{Pt}_x\text{Y}/\text{C}$ nanoparticles

incorporation of Si in the Pt alloy [216]. A schematic of a simplified version of the setup is presented in Figure 6.19. The reactor was made of stainless steel, and closed from its surrounding via copper gaskets, and VCR valves located before and after the main chamber. The VCR valves were also used to handle the gas from the high-vacuum gas wall, where flows and atmosphere can be controlled. As seen in the schematic representation a Fe catalyst was installed before the reactor to reduce the amount of H_2O and/or O_2 contamination. The pressure inside the reactor was kept at 1 bar, and controlled using a pressure controller located at the end of the exhaust. The gas stream at the outlet was passed through a capillary sniffer that transferred the gas to a quadrupole mass spectrometer. Finally, a split-tubular furnace was used as the heating source.

The first step of the synthesis was to dry the Pt/C nanoparticles to remove trace amount of water from air exposure. To do so, the nanoparticles were placed in a graphite foil (99.8%, Alfa Aesar, 0.254 mm) in the middle of the reactor, and heated to 200°C in a 100 mL/min H_2 flow for 6h. The Pt/C nanoparticles were then taken out of the reactor. The Pt/C nanoparticles were then mixed with YCl_3 in ~ 20 mL of anhydrous acetonitrile (99.8%, Sigma-Aldrich, <10 ppm H_2O). The mixture was stirred overnight in an open beaker, enabling a slow evaporation of the solvent, and leaving behind a dry powder. The ratio of YCl_3 -to-Pt is of major importance to obtain the right crystalline structure, and limit the use of chloride precursor. According to our preliminary work, the optimal ratio was found to be 1.5:1 Pt: YCl_3

6.3. High Temperature Synthesis

Table 6.1: Parameters of the Thermal Treatment for the Synthesis of Pt_xY/C Nanoparticles

	Duration Steps (min)			
	25 → 400°C	400 → 600°C	600 → 800°C	800°C
Short annealing	10	20	30	60
Long annealing	10	20	30	360

[216]. The precursor, once dried, was put back in the graphite foil, and placed in the metal reactor for the alloying treatment. The reactor was put in the split-furnace, and connected to the gas wall and the MS. First, He was purged at 10 mL/min for 20 min. Then, the reactor was purged with H₂ at 100 mL/min for 60 min or until a stable signal was observed for m/z=2. Once the atmosphere in the reactor was saturated with H₂, the sample was heated to 800°C. This temperature was chosen because of the melting point of YCl₃ of 721°C, and based on the thermodynamic calculations presented in the previous section. The temperature programs used for the two synthesis are presented in Table 6.1. After the annealing, the gas flow was switched back to He for another 20 min at 10 mL/min, after which the reactor was brought back in the glovebox where the catalyst was recovered.

The as-synthesized catalyst was acid-washed (0.1 M HClO₄) and water-washed three times to remove the Pt-Y₂O₃/C layer that form when Pt_xY/C nanoparticles are exposed to air. The Y₂O₃ is unstable in acid electrolyte and will dissolve, leaving the strained Pt overlayer at the surface of the nanoparticles [162,164,171]. This procedure is also necessary to remove any unreacted traces of precursor. The water- and acid-washed are essential steps in the identification of the Pt-Y alloy using XPS analysis.

The crystalline structure of the powder recovered from the acid and water-washed was investigated using XRD (Panalytical X'Pert Pro/Empyrean). The samples were analyzed in a transmission spinner stage configuration on a zero-background plate. The 2θ angle was varied between 15° and 90°. The data treatment of the XRD pattern was done using Panalytical HighScore Plus software suite. The XPS characterization was performed to further confirm the alloy formation and identify possible contaminants coming from the synthesis process. The instrument used was a Theta-Probe (Thermo Scientific) under ultra-high vacuum (<10⁻⁸ mbar) and a monochromated Al Kα source was used. For all samples, the Pt 4f, Y 4d, O 1s, and C 1s region were investigated, where the C 1s at 284.6 eV was used for calibration. The atomic concentrations of Pt and Y were determined by integration of the Pt 4f and Y 4d peaks after removal of a Shirley-type background.

TEM was used to determine the size distribution of the Pt/C and Pt_xY/C nanoparticles (Tecnai T20 G2). The area of the nanoparticles on the pictures was measured manually using the software ImageJ and the diameter was estimated assuming perfectly spherical particles.

6.3.3 Results

As mentioned in subsection 6.3.2, a specific Pt_xY structure can be thermodynamically favored based on the HCl partial pressure. Using our calculations, catalyst prepared with different annealing times were obtained (see table 6.1). As presented, a longer (360 min), and a shorter (60 min) annealing treatment were chosen as annealing conditions. The 60 min annealing treatment was chosen based on the HCl signal detected by the MS during preliminary testing. More specifically, we monitored the HCl signal during the annealing process, and stopped heating once we observed that the intensity associated to HCl ($m/z=36$) was decreasing. In contrast, the 360 min annealing treatment is expected to reach relatively low HCl partial pressure and favor the formation of Pt₃Y.

Figure 6.20 shows the mass spectra of selected compounds detected with the mass spectrometer during the short-term synthesis (left axis). The full MS data of the short- and long-term synthesis are available in Figure C.3 and C.4, respectively. The time scale was adjusted so that time = 0 min is associated with the ramping in temperature. The temperature profile is also presented (dotted blue line, right axis). During the annealing treatment, we monitored the HCl signal as it has been defined as a way to follow the alloying process. $m/z=2$ and $m/z=36$, associated with H₂ and HCl, respectively, were selected as they are both involved in the alloying formation, as indicated in equation (6.6). The high signal detected for $m/z=2$ is associated to the high flow of H₂ used during the synthesis. $m/z=36$ is expected to be the strongest signal for HCl due to the high natural abundance of ³⁵Cl (76%), but could also be related to the production of tricarbon anion, a transient specie often associated to combustion reactions. To prove that $m/z=36$ is associated to the production of HCl, and is not a side product of combustion, CO₂ ($m/z=44$) is also plotted. While combustion-derived products seem to occur mainly at the beginning of the heating treatment ($t=9$ min), the $m/z=36$ signal starts increasing after $t=31$ min, when the temperature reaches approx. 600°C. Thus, Figure 6.20, the profiles of $m/z=36$ and 44 are different, and we can thus expect that most of the signal is associated to HCl. The HCl profile shows a maximum production at much higher temperature, i.e. around 800°C, $t=65$ min.

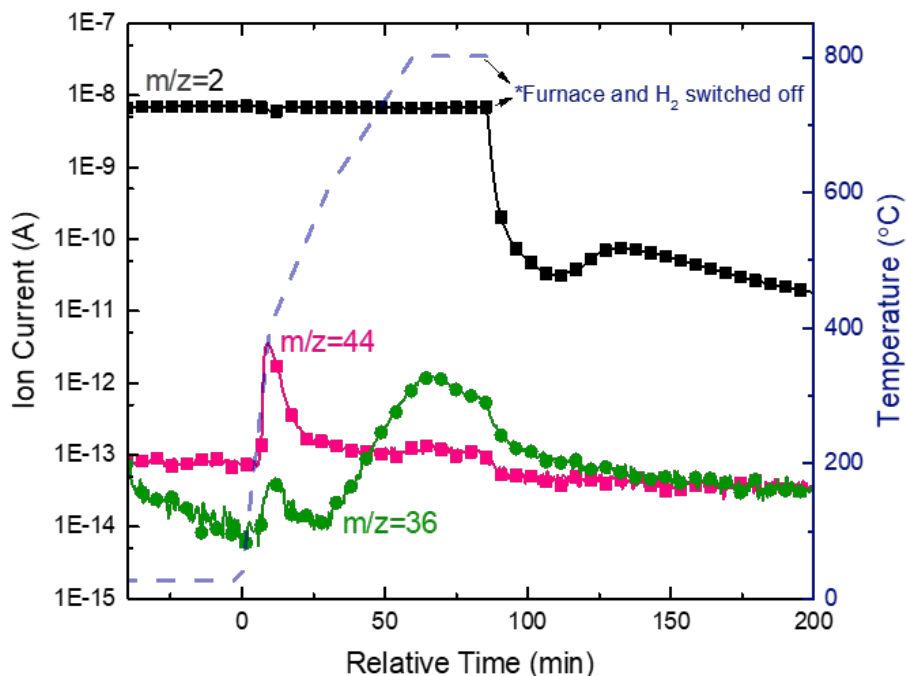


Figure 6.20: H_2 ($m/z = 2$), CO_2 ($m/z = 44$), and HCl ($m/z = 36$) detected by the mass spectrometer (MS) during the annealing of Pt/C nanoparticles and YCl_3 at 800°C under a H_2 atmosphere. The dotted lines are related to the ion current measured by the MS (left axis), and the dashed line is related to the temperature of the furnace (right axis).

6.3.4 Physical Characterization

Physical characterization of catalysts obtained after 60 and 360 min of annealing was done using XPS and XRD. XRD was used to evaluate if the experimental conditions described above lead to the formation of Pt_xY alloy, and to evaluate which crystalline structure can be identified in each sample. XPS was used to make sure that no contaminants were found in the materials and to confirm that the Pt_xY alloy was formed. Finally, we used TEM to investigate the variation in particle size before and after the synthesis, as sintering is expected when reaching high temperatures.

As shown in Figure 6.21, patterns of as-received Pt/C nanoparticles (black line), and $\text{Pt}_x\text{Y}/\text{C}$ obtained from 60 min (dark gray) and 360 min (light gray) annealing were recorded. The Pt/C nanoparticle's diffractogram shows peaks at 39.8° , 46.3° , 67.4° , 81.4° and 85.9° , associated to the (111), (200), (220), (311) and (211) plans. The identification of the Pt_xY crystalline structure in this work was done based on the information collected

from previous analysis on commercial polycrystalline disks of Pt₃Y, Pt₅ and Pt₂Y [168]. If we compare the 360 min synthesis to the Pt/C reference, only the peak associated with the (111) plane at 39.7° is observed. Therefore, the peak at 39.7° cannot be associated to Pt (111), as the relative intensities of the other polycrystalline Pt peaks would be violated. A face centered cubic (fcc) Pt₅Y, associated to the crystal prototype AuBe₅ [168], can be assigned with the reflections observed, showing its most intense reflection at 39.7° ((113) plane) and 41.42° ((222) plane). Pt₃Y is also clearly identified in the pattern. The peaks associated with the Pt₃Y crystalline structure are at 38.3°, 44.5°, and 64.4° and can be associated with the (111), (002), and (022) planes, respectively. Lastly, the Pt₂Y phase can also be identified. A low-intensity peak for the (004) plane is observed at 47.8°. In comparison, the Pt_xY/C sample obtained from the 60 min synthesis shows mainly fcc and/or hexagonal Pt₅Y structures. The most intense peak is observed for the (111) plane at 40.0°. This main peak could be attributed to both the FCC and/or hexagonal structure. At 40.9°, the (002) plane of the Pt₅Y hexagonal is identified. Other less intense peaks at high angles confirm that both the fcc, and hexagonal are present in the sample. The carbon support can also be identified in the patterns of all three samples with a broad peak at 25.8°.

To gain information on the chemical state of platinum and yttrium, detailed scans of the Pt 4f and Y 3d region were recorded. XPS is a surface sensitive technique, and will detect electrons originating from the atoms a few nm into the surface of the catalyst. For that reason, even if Pt overlayer is formed during acid-washed, a low signal from Y is expected. Figure 6.22 shows that metallic Pt (71.4 eV) is observed for both the catalyst obtained from the 60 and 360 min annealing. The deconvolution of Y 3d from the 360 min synthesis Pt_xY (Figure 6.22a), shows a mix of Pt_xY (156.5 eV), Pt₃Y (155.3 eV) and Y₂O₃ (157.8 eV). A small contamination associated with Si is also observed at 153.7 eV. The Y 3d analysis of the 60 min synthesis Pt_xY ((Figure 6.22b), only shows Y attributed to Pt_xY and Y₂O₃ compounds. Y₂O₃ can be detected if it is trapped in the nanoparticles, or if the acid-wash was not harsh enough to remove all the Y from the topmost layers.

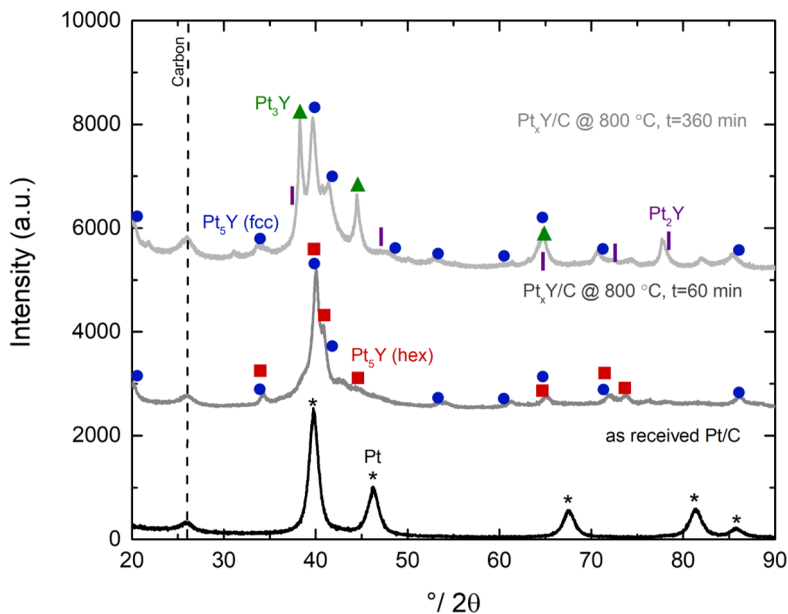
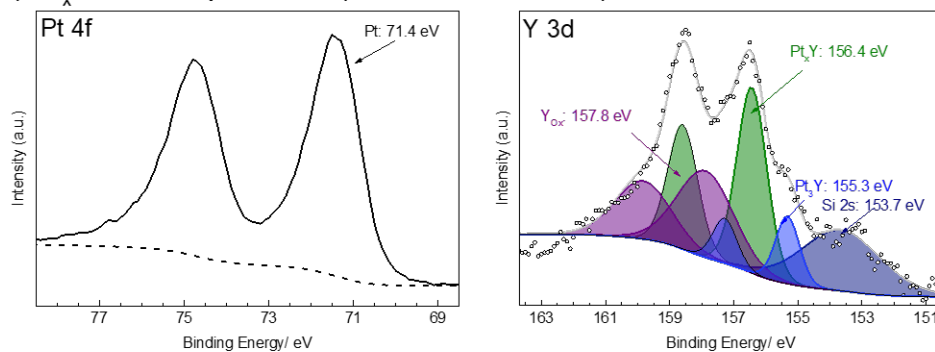


Figure 6.21: X-ray diffraction patterns of as-received Pt/C (black line), Pt_xY/C (60 min) (dark gray line), and Pt_xY/C (360 min) (light gray line) nanoparticles. The green triangles are associated with Pt_3Y structure, the blue circles to Pt_5Y (fcc), the red squares to Pt_5Y (hexagonal), the purple lines to Pt_2Y and the stars to Pt.

The TEM analysis was done on Pt/C, Pt_xY (60 min @ 800°C) and Pt_xY (360 min @ 800°C) nanoparticles. To clearly show how much catalyst was dedicated to each particle size, we decided to present the data as percentage of the total particles volume as function of particle diameter. Figure 6.23a shows the as-received Pt/C nanoparticles. The average particle size, calculated from a total of 225 particles, is 7.6 ± 3.4 nm. The particle size distributions of the Pt_xY obtained from 60 and 360 min annealing are presented in Figure 6.23b and c, respectively. The average size for the short synthesis is 9.9 ± 3.6 nm while 12.1 ± 4.4 nm was obtained for the long synthesis. Both Pt_xY/C catalysts show a fraction of very large nanoparticles with diameter > 25 nm in size.

The evaluation of the electrochemical activity for the ORR was performed at 50 mV/s in O_2 -saturated 0.1 M $HClO_4$ with a rotating disk electrode setup at 1600 rpm. The iR-corrected CVs are presented in Figure 6.24a. The kinetic current from the CVs was calculated, and the values at 0.9 V_{RHE} normalized by the electrochemical surface area and the mass of Pt are presented in Figures 6.24b and c, respectively. Pt/C nanoparticles present the lowest specific, and mass activity with 1 mA/cm² and 0.27 A/mg_{Pt}, respectively. Pt_xY (60 min @ 800°C) has intermediate activ-

A) Pt_xY/C nanoparticles (360 min at 800°C)



B) Pt_xY/C nanoparticles (60 min at 800°C)

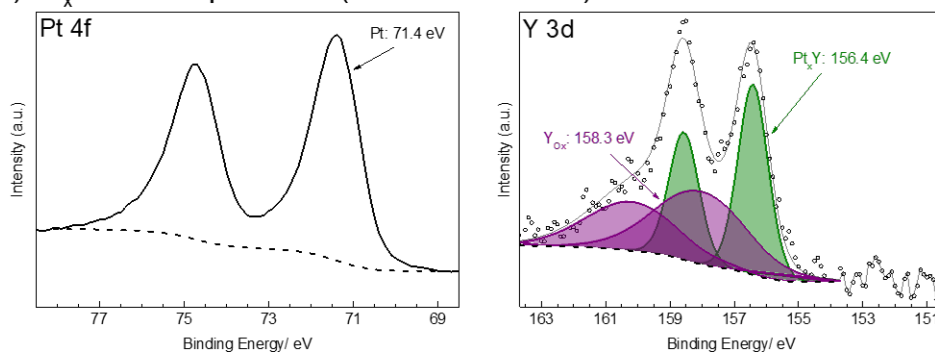


Figure 6.22: X-ray photoelectron spectra in the platinum 4f and yttrium 3d core level regions for Pt_xY obtained from (A) 360 min and (B) 60 min annealing at 800°C. The catalysts were washed three times with acid (0.1 M HClO₄) and water before XPS measurements.

6.3. High Temperature Synthesis

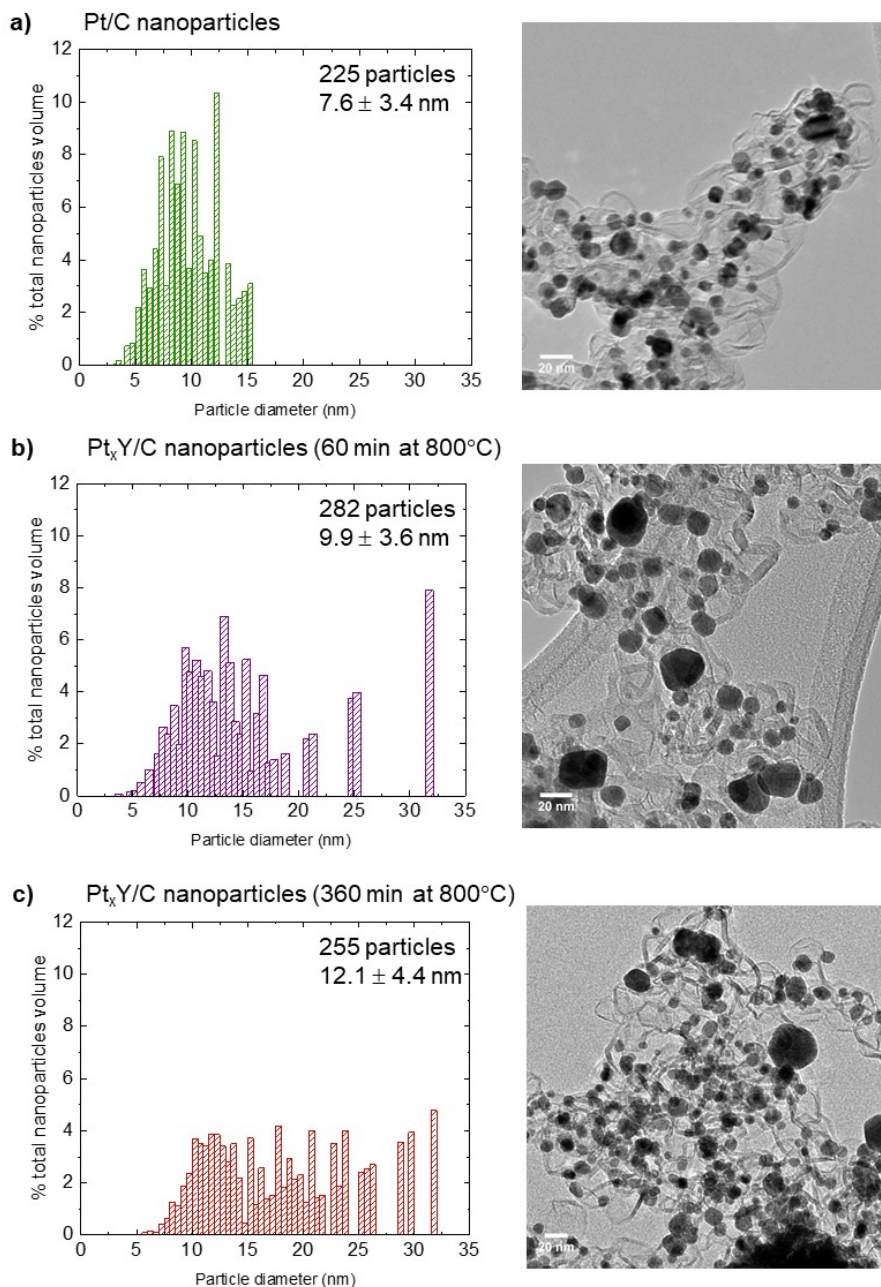


Figure 6.23: Particle size distributions and representative transmission electron micrographs for (A) the as-received Pt/C, (B) the 30 min annealed @ 800°C Pt_xY/C and (C) the 360 min annealed @ 800°C Pt_xY/C.

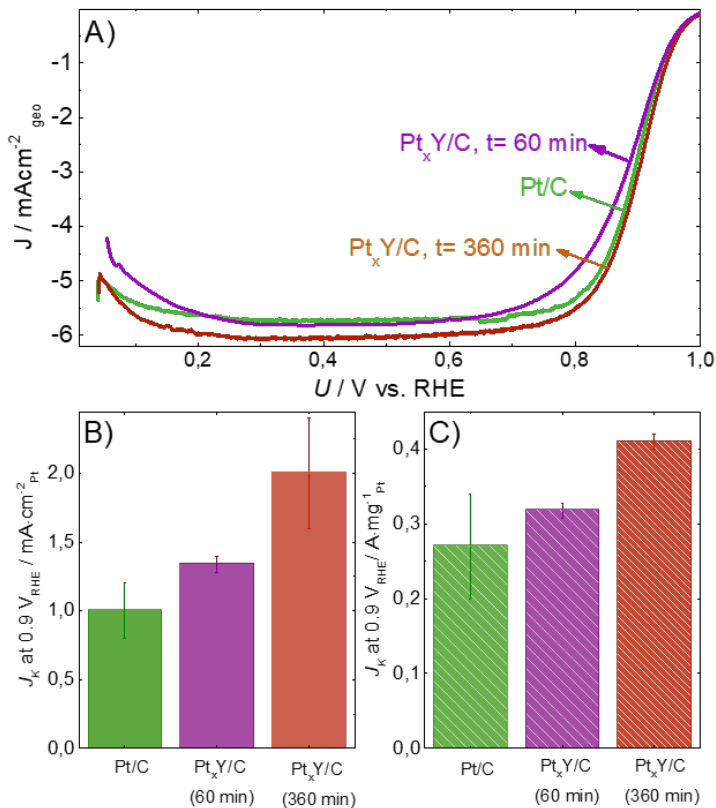


Figure 6.24: (A) RDE polarization curves at 1,600 rpm and 50 mV/s for the ORR on Pt/C (green curve), Pt_xY/C (60 min at 800°C) (purple curve), and Pt_xY/C (360 min at 800°C) (red curve) nanoparticle catalysts in O₂-saturated 0.1 M HClO₄. Kinetic current density normalized by (B) specific surface area and (C) mass of Pt at 0.9 V_{RHE} for Pt/C and Pt_xY/C annealed for 30 and 360 min at 800°C, on the basis of data from (A).

ity with 1.34 mA/cm² (specific activity) and 0.32 A/mg_{Pt} (mass activity). Finally, the highest specific activity (2 mA/cm²), and mass activity (0.41 A/mg_{Pt}) is obtained with Pt_xY/C (360 min @ 800°C).

Discussion

Both the XRD and XPS results confirm that the Pt_xY alloy was formed when using both the short and long thermal treatments. No peaks associated with metallic Pt was observed on Pt_x catalysts, confirming that all platinum was converted to an alloy. Pt_xY (60 min @ 800°C) shows only formation of Pt₅Y while Pt₃Y is also observed for Pt_xY (360 min @ 800°C) (Figure 6.22 and 6.21). The Pt₃Y crystalline phase of Pt_xY (360

min @ 800°C) corresponds to what was suggested in Figure 6.18. Indeed, for longer annealing time the HCl production decreases which favors the transition from Pt₅Y to Pt₃Y. The detailed scans of the Pt 4f and Y 3d region confirm what was previously reported for Pt_xY nanoparticles [162]. The Pt 4f peaks show an oxidation state of zero, and the Y 3d peaks are a mixture of Y₂O₃ and Pt_xY (Figure 6.22). The Pt-to-Y ratio between 3.5 and 3.9 fits with the reported value when a thick Pt overlayer is formed due to yttrium oxidation, and then leached when exposed to acid electrolyte [162]. A small Si contamination observed for the Pt_xY probably comes from the mixing of Pt/C nanoparticles and YCl₃ which took place in a glass beaker. It is possible that the longer annealing time favored the reduction of Si contaminant. In the future, to fully avoid Si contamination, one should prioritize teflon over glassware. However, since the signal intensity detected with the XPS was so low, we did not expect the Si to affect the measured electrochemical activity. To our knowledge, the high catalytic activity of Pt-Si was only reported for methanol oxidation reaction [226].

We argue that the lower specific and mass activity observed for Pt_xY (60 min @ 800°C) can be linked to two factors: the nature of the Pt_xY alloy and the nanoparticles size distribution. It was shown using polycrystalline Pt₂Y, Pt₃Y and Pt₅Y disks that the activity and stability vary greatly in-between the different crystalline structures. More specifically, Pt₃Y has the highest specific activity (9.4 mA/cm² at 0.9V_{RHE}), followed by Pt₅Y (5.9 mA/cm² at 0.9V_{RHE}) and, finally, Pt₂Y who's activity is closer to that of Pt and corrodes within the first few CVs [168].

As concluded from mass-selected studies, the specific activity increases with the increase in particle diameter until a maximum value is reached, i.e. the one from polycrystalline disk. The reason for this observation is that the alloy in the core strain the Pt overlayer, and once a certain size is achieved, the nanoparticles behave as the bulk. If this nanoparticle size is not reached, the Pt-Pt distance is closer to that of pure Pt. On the other hand, when looking at the mass activity, there is an optimum mass activity reached when a sufficient thickness of alloy is present in the bulk, but the particle diameter is still allow a high surface-to-bulk ratio. In this work, we showed that ca. 80% and ca. 92% of the Pt_xY particles obtained from 60 and 360 min annealing, respectively, have particle diameters greater than 10 nm (Figure 6.23). This high amount of nanoparticles with larger diameter significantly decreases the mass activity measured. Thus, this high percentage of particles with diameter larger than 10 nm explains why only 0.43 A/mg_{Pt} and 2.0 mA/cm²_{Pt} were measured at 0.9 V_{RHE}. We expect the remaining volume, having particle sizes between 2 and 9 nm, to have a mass activity that increases with volume, as presented in Figure 2.20.

Conclusion

In summary, the thermodynamic calculations for the reduction of Pt with rare-earth compounds under H_2 atmosphere allowed us to determine the experimental conditions required to form the Pt_xY alloy. The Pt-Y alloy was selected based on the already established high electrochemical activity for the oxygen reduction, and the lower temperature required to obtain the alloy. XRD and XPS data confirmed the Pt-Y alloy formation and showed how the annealing time can impact the crystalline structure favored. It is also, to our knowledge, the first time that chemically synthesized Pt-RE and Pt-Ln show improved mass activity for the oxygen reduction, when compared to Pt/C. The lower mass activity of the thermally synthesized nanoparticles as compared to the mass-selected Pt_xY could be improved by obtaining a more homogeneous size distribution, and a more pure Pt_3Y phase.

Conclusion and Outlook

7.1 Conclusion

This PhD work focused on the understanding and development of highly efficient and stable catalysts for the oxygen evolution and reduction reaction. This work was motivated by the replacement of fossil fuels with renewable energy sources through the development of hydrogen as energy carrier [5]. Electrolyzers hold a really important role in the future energy infrastructure, as it can be coupled to renewable energy sources, like wind and solar, to store energy in hydrogen bond. As of today, two electrolyzer technologies are in development. Polymer electrolyte membrane (PEM) electrolyzers are promising, but the acid electrolyte used limits catalyst materials to noble-metals [31]. On the other hand, alkaline electrolyzers are less efficient, but well-established technologies that use cheap and abundant catalysts [28]. The oxygen evolution reaction is the limiting reaction in water splitting [57], and hampers large-scale penetration of electrolyzer technologies on the market.

RuO_x are among the most active OER catalysts in acid electrolyte [34]. Using oriented thin films of RuO_2 developed by Shao-horn and co-workers [35,72,73], we investigated the stability in relation to the activity of these catalysts. We performed stability tests at 1.6 V_{RHE} in 0.05 M H_2SO_4 on (001), (111) and (101) oriented thin films, and compared it to (110) single crystal and commercial RuO_2 particles. The catalytic activity of the well-defined surface and particles scale as followed: (001) > (101) > (110) > (111) \sim particles. Our results suggest that surface structure has an important role in the activity, and also the corrosion. More specifically, we observed from our data that dissolution of Ru does not scale with the activity loss registered. In other words, we observed no relationship between activity and stability, in opposition to the universal activity-stability relationship

suggested by Markovic and co-workers [75,78,123,127]. More specifically, we hypothesized that undercoordinated sites like steps, edges and kinks are responsible of Ru corrosion, while we confirmed that the activity scaled with the density of Ru_{CUS}-O bounds.

We also investigated NiFeO_xH_y catalysts for the oxygen evolution in alkaline electrolyte. Using a well-defined mass-selected NiFeO_xH_y nanoparticles in 1 M KOH, we studied the effect of nanoparticle sizes on the catalytic activity. Our model system allowed the determination of the turnover frequencies normalized to the Ni and Fe atoms measured from the Ni redox peak, the surface of the particles and bulk of the NiFeO_xH_y nanoparticles. We accompanied our electrochemical measurements with X-ray photoelectron spectroscopy, low energy ion scattering and electron microscopy. To evaluate the participation of the lattice oxygen and intercalated water, we used in operando measurements where isotope labelling study was performed with electrochemical mass-spectrometry on NiFeO_xH_y nanoparticles and thin films. Our results showed no bulk activity and this confirm that only surface atoms are important for the OER activity.

The reverse reaction, the oxygen reduction reaction (ORR), was also investigated. ORR is limiting the conversion of hydrogen back to electricity in hydrogen fuel cell technologies. So far, only Pt-based materials showed promising activity and stability. More recently, our research group focused on a new class of materials: Pt-rare-earth alloys [56,171]. Based on the high catalytic activity obtained from mass-selected nanoparticles of Pt_xY and Pt_xGd [162,164], we decided to develop a synthesis that would allow the production of this type of alloys on a gram scale. In this work, we first investigated the alkali reduction method, and tried to reproduce Gd@Au nanocrystals using the protocol reported by Wagner and co-workers [214]. After many unsuccessful attempts, this method was abandoned. Then, we developed further the cyanide reduction method reported by Lux and co-workers [212], and formed the Pt_xY alloy from K₂Pt(CN)₆ and Y(NO₃)₃ precursors. The alloy formation was confirmed with X-ray diffraction. The catalytic activity for the oxygen reduction was measured but, unfortunately, we did not obtain any significant improvement compare to commercial Pt/C catalysts. Finally, we continued the work initiated by Brian Knudsen on the high temperature synthesis method [216]. We used thermodynamic calculations to determine the experimental conditions and showed that specific Pt_xY crystalline structure can be favored depending on the experimental conditions. The Pt_xY/C nanoparticles obtained from Pt/C nanoparticles and YCl₃ annealed at 800°C under hydrogen atmosphere was characterized with X-ray photoelectron spectroscopy, X-ray diffraction and transmission electron microscopy. Our electrochemical data show a two-fold improvement compare with commercial Pt/C nanoparticles.

7.2 Outlook

Despite the significant progress made on the OER and ORR sides in recent years, further improvement is still needed if we want the electrolyzers and hydrogen fuel cell to become competitive with fossil fuels. As presented in Chapter 4, we investigated well-defined surfaces of RuO₂ to gain understanding on the stability, and its relation to the activity. The understanding of the parameter controlling the stability is still in its early stage. It would be of great importance to observe how the surface reconstruct under OER conditions. Such characterization could be done with scanning tunneling microscopy for single-crystal catalysts, or with CO-temperature programmed desorption. In our experiments, we were limited by the detection limit of Ru with the ICP-MS because of the low Ru dissolution of our samples, and the relatively large volume of electrolyte used. Similar study to what was done in this work but using in situ technique could reveal extra information about the activity and stability over time under OER conditions.

Regarding the understanding of bulk activity of OER catalysts, a lot remains to be understood. From the different experimental conditions, and broad type of catalysts investigated, it is very difficult to draw general conclusions on the reasons behind participation of lattice oxygen. For that reason, I think it could be very insightful to study participation of lattice oxygen during the oxygen evolution in a more rigorous manner. As such, a parametric study using late transition metal catalysts, for example, could more easily reveal the conditions leading participation of lattice oxygen.

Finally, we showed that it was possible to synthesized Pt_xY/C nanoparticles on a gram scale using high temperature synthesis. We showed a relatively low specific and mass activity compared to what was reported for similar mass-selected Pt_xY nanoparticles [162]. In order to improve the catalytic activity of the catalyst, the first approach could be to focus on having a more homogeneous size distribution of nanoparticles. By doing the synthesis with Pt/C nanoparticles closer to 8-9 nm in diameter, one could try to annealed for shorter time, as we have learned that an alloy can be obtained for annealing time around 60 min. Also, another approach could be to focus on the synthesis of Pt_xGd/C nanoparticles. The melting point of GdCl₃ is of 609°C compared to 721°C for YCl₃. As such, the annealing could be done at lower temperature to prevent sintering.

Bibliography

- [1] “World Population Prospects,” tech. rep., United Nations, New York, 2017.
- [2] “BP Statistical Review of World Energy 2017,” Tech. Rep. 66, British Petroleum, 2017.
- [3] IPCC Panel, “Climate Change 2014: Synthesis Report,” tech. rep., Intergovernmental Panel on Climate Change, 2015.
- [4] U.S. Department of Energy, “Clean Energy.” <https://www.energy.gov/science-innovation/clean-energy>. 2018-03-19.
- [5] A. Zuttel, A. Remhof, A. Borgschulte, and O. Friedrichs, “Hydrogen: the future energy carrier,” *Philosophical Transactions of the Royal Society A: Mathematical, Physical and Engineering Sciences*, vol. 368, no. 1923, pp. 3329–3342, 2010.
- [6] Global Carbon Atlas, “CO₂ Emissions.” <http://www.globalcarbonatlas.org/en/CO2-emissions>. Accessed: 2017-11-16.
- [7] J. Fourier, “General Remarks on the Temperature of the Terrestrial Globe and the Planetary Spaces,” *American Journal of Science and Arts*, vol. 32, no. 1, pp. 1820–1879, 1837.
- [8] Stocker, V. B. T.F., D. Qin, G.-K. Plattner, M. Tignor, S.K. Allen, J. Boschung, A. Nauels, Y. Xia, and P. Midgley, “Summary for Policymakers. In: Climate Change 2013: The Physical Science Basis.

- Contribution of Working Group I to the Fifth Assessment Report of the Intergovernmental Panel on Climate Change,” *CEUR Workshop Proceedings*, vol. 1542, pp. 33–36, 2015.
- [9] M. E. Hauer, “Migration induced by sea-level rise could reshape the US population landscape,” *Nature Climate Change*, vol. 7, no. 5, pp. 321–325, 2017.
- [10] Australian Government, “Impacts of ocean acidification on the Reef.” <http://www.gbrmpa.gov.au/managing-the-reef/threats-to-the-reef/climate-change/how-climate-change-can-affect-the-reef/ocean-acidification>. 2018-05-03.
- [11] M. E. Mann, R. S. Bradley, and M. K. Hughes, “Northern hemisphere temperatures during the past millennium: Inferences, uncertainties, and limitations,” *Geophysical Research Letters*, vol. 26, no. 6, pp. 759–762, 1999.
- [12] T. Jackson, *Prosperity without growth. Economics for a finite planet*. London: Earthscan, 2009.
- [13] “Paris Agreement,” tech. rep., United Nations, 2015.
- [14] M. Meinshausen, N. Meinshausen, W. Hare, S. C. B. Raper, K. Frieler, R. Knutti, D. J. Frame, and M. R. Allen, “Greenhouse-gas emission targets for limiting global warming to 2°C,” *Nature*, vol. 458, no. 7242, pp. 1158–1162, 2009.
- [15] R. E. Smalley, “Future Global Energy Prosperity: The Terawatt Challenge,” *MRS Bull.*, vol. 30, pp. 412 – 417, 2005.
- [16] H. B. Gray, “Powering the planet with solar fuel,” *Nature Chemistry*, vol. 1, no. 1, p. 7, 2009.
- [17] EMD International A/S, “Elforbrug og vindmølleproduktion.” <http://www.emd.dk/el/>. 2017-10-10.
- [18] F. Díaz-González, A. Sumper, O. Gomis-Bellmunt, and R. Villafáfila-Robles, “A review of energy storage technologies for wind power applications,” *Renewable and Sustainable Energy Reviews*, vol. 16, no. 4, pp. 2154–2171, 2012.
- [19] H. Chen, T. N. Cong, W. Yang, C. Tan, Y. Li, and Y. Ding, “Progress in electrical energy storage system: A critical review,” *Progress in Natural Science*, vol. 19, no. 3, pp. 291–312, 2009.

-
- [20] “Global trends and outlook for hydrogen,” tech. rep., International Energy Agency, 2017.
- [21] “Hydrogen and Fuel Cell Overview,” tech. rep., U.S. Department of Energy, Tokyo, 2016.
- [22] B. A. Pinaud, J. D. Benck, L. C. Seitz, A. J. Forman, Z. Chen, T. G. Deutsch, B. D. James, K. N. Baum, G. N. Baum, S. Ardo, H. Wang, E. Miller, and T. F. Jaramillo, “Technical and economic feasibility of centralized facilities for solar hydrogen production via photocatalysis and photoelectrochemistry,” *Energy & Environmental Science*, vol. 6, no. 7, p. 1983, 2013.
- [23] M. Balat, “Potential importance of hydrogen as a future solution to environmental and transportation problems,” *International Journal of Hydrogen Energy*, vol. 33, no. 15, pp. 4013–4029, 2008.
- [24] P. Tseng, J. Lee, and P. Friley, “A hydrogen economy: Opportunities and challenges,” *Energy*, vol. 30, no. 14, pp. 2703–2720, 2005.
- [25] “Technology Roadmap,” tech. rep., International Energy Agency, 2015.
- [26] A. Ursua, L. Gandia, and P. Sanchis, “Hydrogen Production From Water Electrolysis: Current Status and Future Trends,” *Proceedings of the IEEE*, vol. 100, no. 2, pp. 410–426, 2012.
- [27] State of Green, “Denmark is heading towards 60% wind energy.” <https://stateofgreen.com/en/profiles/state-of-green/news/denmark-is-heading-towards-60-wind-energy>. 2017-12-12.
- [28] M. Carmo, D. L. Fritz, J. Mergel, and D. Stolten, “A comprehensive review on PEM water electrolysis,” *International Journal of Hydrogen Energy*, vol. 38, no. 12, pp. 4901–4934, 2013.
- [29] “The production of hydrogen and oxygen through the electrolysis of water,” Tech. Rep. 312, New York, NY, 1891.
- [30] C. C. L. McCrory, S. Jung, I. M. Ferrer, S. M. Chatman, J. C. Peters, and T. F. Jaramillo, “Benchmarking Hydrogen Evolving Reaction and Oxygen Evolving Reaction Electrocatalysts for Solar Water Splitting Devices,” *Journal of the American Chemical Society*, vol. 137, no. 13, pp. 4347–4357, 2015.
- [31] K.E. Ayers, E.E. Anderson, C.B. Capuano, B.D. Carter, L.T. Dalton, G. Hanlon, J. Manco and M. Niedzwiecki, “Research Advances

- towards Low Cost, High Efficiency PEM Electrolysis,” *ECS Transactions*, vol. 33, no. 1, pp. 3–15, 2010.
- [32] D. J. Walton, L. D. Burket, and M. M. Murphy, “Sonoelectrochemistry : and Oxygen Evolution Chlorine , Hydrogen At Platinised Platinum,” *Evolution*, vol. 41, no. 17, pp. 2747–2751, 1996.
- [33] E. Kemppainen, A. Bodin, B. Sebok, T. Pedersen, B. Seger, B. Mei, D. Bae, P. C. K. Vesborg, J. Halme, O. Hansen, P. D. Lund, and I. Chorkendorff, “Scalability and feasibility of photoelectrochemical H₂ evolution: the ultimate limit of Pt nanoparticle as an HER catalyst,” *Energy Environ. Sci.*, vol. 8, no. 10, pp. 2991–2999, 2015.
- [34] E. A. Paoli, F. Masini, R. Frydendal, D. Deiana, C. Schlaup, M. Malizia, T. W. Hansen, S. Horch, I. E. L. Stephens, and I. Chorkendorff, “Oxygen evolution on well-characterized mass-selected Ru and RuO₂ nanoparticles,” *Chem. Sci.*, vol. 6, no. 1, pp. 190–196, 2015.
- [35] K. A. Stoerzinger, L. Qiao, M. D. Biegalski, and Y. Shao-Horn, “Orientation-dependent oxygen evolution activities of rutile IrO₂ and RuO₂,” *Journal of Physical Chemistry Letters*, vol. 5, no. 10, pp. 1636–1641, 2014.
- [36] W. Sheng, H. A. Gasteiger, and Y. Shao-Horn, “Hydrogen Oxidation and Evolution Reaction Kinetics on Platinum: Acid vs Alkaline Electrolytes,” *Journal of The Electrochemical Society*, vol. 157, no. 11, p. B1529, 2010.
- [37] W. T. Hong, M. Risch, K. A. Stoerzinger, A. Grimaud, J. Suntivich, and Y. Shao-Horn, “Toward the rational design of non-precious transition metal oxides for oxygen electrocatalysis,” *Energy & Environmental Science*, vol. 8, pp. 1404–1427, 2015.
- [38] Department of Energy, “Comparison of Fuel Cell Technologies.” <https://www.energy.gov/eere/fuelcells/about-fuel-cell-technologies-office>. 2018-05-14.
- [39] P. to a Competitive European Fuel Cell micro Cogeneration Market (PACE), “Fuel Cell micro-Cogeneration–Heating and Powering your Home.” <http://www.pace-energy.eu/about-pace/>. 2018-03-21.
- [40] W. Sussex, ed., *Fuel Cell System Explained*. Chichester: Wiley & Sons, Ltd, second ed., 2003.
- [41] F. W. to Energy, “Technology electrolyser,” 2017.

-
- [42] W. Vielstich, A. Lamm, and H. Gasteiger, *Handbook of Fuel Cells: Fundamentals, Technology, Applications*. John Wiley & Sons, Ltd, 2003.
- [43] International Organization of Motor Vehicle Manufacturers (OICA), “2016 production statistics,” 2017.
- [44] L. Dubau, L. Castanheira, F. Maillard, M. Chatenet, O. Lottin, G. Maranzana, J. Dillet, A. Lamibrac, J. C. Perrin, E. Moukheiber, A. Elkaddouri, G. De Moor, C. Bas, L. Flandin, and N. Caqué, “A review of PEM fuel cell durability: Materials degradation, local heterogeneities of aging and possible mitigation strategies,” *Wiley Interdisciplinary Reviews: Energy and Environment*, vol. 3, no. 6, pp. 540–560, 2014.
- [45] H. a. Gasteiger, S. S. Kocha, B. Sompalli, and F. T. Wagner, “Activity benchmarks and requirements for Pt, Pt-alloy, and non-Pt oxygen reduction catalysts for PEMFCs,” *Applied Catalysis B: Environmental*, vol. 56, no. 1-2 SPEC. ISS., pp. 9–35, 2005.
- [46] S. Chen, H. A. Gasteiger, K. Hayakawa, T. Tada, and Y. Shao-Horn, “Platinum-Alloy Cathode Catalyst Degradation in Proton Exchange Membrane Fuel Cells: Nanometer-Scale Compositional and Morphological Changes,” *Journal of The Electrochemical Society*, vol. 157, no. 1, p. A82, 2010.
- [47] J. Greeley and N. M. Markovic, “The road from animal electricity to green energy: combining experiment and theory in electrocatalysis,” *Energy & Environmental Science*, vol. 5, no. 11, p. 9246, 2012.
- [48] H. a. Gasteiger, S. S. Kocha, B. Sompalli, and F. T. Wagner, “Activity benchmarks and requirements for Pt, Pt-alloy, and non-Pt oxygen reduction catalysts for PEMFCs,” *Applied Catalysis B: Environmental*, vol. 56, no. 1-2 SPEC. ISS., pp. 9–35, 2005.
- [49] A. J. Bard and L. R. Faulkner, *Electrochemical Methods: Fundamentals and Applications*. second ed., 1944.
- [50] J. Larminie and A. Dicks, “Efficiency and Open Circuit Voltage,” in *Fuel Cell Systems Explained*, pp. 25–43, Wiley & Sons, Ltd, second ed., 2003.
- [51] I. Chorkendorff and J. Niemantsverdriet, *Concept of Modern Catalysis and Kinetic*. Weinheim: Wiley-vch, 2003.

- [52] J. K. Nørskov, J. Rossmeisl, A. Logadottir, L. Lindqvist, J. R. Kitchin, T. Bligaard, and H. Jónsson, “Origin of the overpotential for oxygen reduction at a fuel-cell cathode,” *Journal of Physical Chemistry B*, vol. 108, no. 46, pp. 17886–17892, 2004.
- [53] J. Rossmeisl, Z. W. Qu, H. Zhu, G. J. Kroes, and J. K. Nørskov, “Electrolysis of water on oxide surfaces,” *Journal of Electroanalytical Chemistry*, vol. 607, no. 1-2, pp. 83–89, 2007.
- [54] I. C. Man, H. Y. Su, F. Calle-Vallejo, H. A. Hansen, J. I. Martínez, N. G. Inoglu, J. Kitchin, T. F. Jaramillo, J. K. Nørskov, and J. Rossmeisl, “Universality in Oxygen Evolution Electrocatalysis on Oxide Surfaces,” *ChemCatChem*, vol. 3, no. 7, pp. 1159–1165, 2011.
- [55] J. Rossmeisl, A. Logadottir, and J. K. Nørskov, “Electrolysis of water on (oxidized) metal surfaces,” *Chemical Physics*, vol. 319, no. 1-3, pp. 178–184, 2005.
- [56] I. E. L. Stephens, A. S. Bondarenko, U. Grønbjerg, J. Rossmeisl, and I. Chorkendorff, “Understanding the electrocatalysis of oxygen reduction on platinum and its alloys,” *Energy & Environmental Science*, vol. 5, no. 5, p. 6744, 2012.
- [57] Z. W. Seh, J. Kibsgaard, C. F. Dickens, I. Chorkendorff, J. K. Nørskov, and T. F. Jaramillo, “Combining theory and experiment in electrocatalysis: Insights into materials design,” *Science*, vol. 355, no. 6321, p. eaad4998, 2017.
- [58] M. Lischka, C. Mosch, and A. Groß, “Tuning catalytic properties of bimetallic surfaces: Oxygen adsorption on pseudomorphic Pt/Ru overlayers,” *Electrochimica Acta*, vol. 52, no. 6, pp. 2219–2228, 2007.
- [59] H. E. Hoster, O. B. Alves, and M. T. Koper, “Tuning adsorption via strain and vertical ligand effects,” *ChemPhysChem*, vol. 11, no. 7, pp. 1518–1524, 2010.
- [60] M. Mavrikakis, B. Hammer, and J. K. Nørskov, “Effect of Strain on the Reactivity of Metal Surfaces,” *Physical Review Letters*, vol. 81, no. 13, pp. 2819–2822, 1998.
- [61] A. S. Bandarenka, A. S. Varela, M. Karamad, F. Calle-Vallejo, L. Bech, F. J. Perez-Alonso, J. Rossmeisl, I. E. L. Stephens, and I. Chorkendorff, “Design of an active site towards optimal electrocatalysis: Overlayers, surface alloys and near-surface alloys of Cu/Pt(111),” *Angewandte Chemie - International Edition*, vol. 51, no. 47, pp. 11845–11848, 2012.

- [62] K. D. Jensen, J. Tymoczko, J. Rossmeisl, A. S. Bandarenka, I. Chorkendorff, M. Escudero-Escribano, and I. E. Stephens, "Elucidation of the Oxygen Reduction Volcano in Alkaline Media using a Copper–Platinum(111) Alloy," *Angewandte Chemie - International Edition*, vol. 57, no. 11, pp. 2800–2805, 2018.
- [63] A. Bodin, *Synthesis of Nanoparticles Model Systems for Sustainable Catalysis by Gas Aggregation*. PhD thesis, Technical University of Denmark, 2017.
- [64] S. Cherevko, S. Geiger, O. Kasian, N. Kulyk, J. P. Grote, A. Savan, B. R. Shrestha, S. Merzlikin, B. Breitbach, A. Ludwig, and K. J. J. Mayrhofer, "Oxygen and hydrogen evolution reactions on Ru, RuO₂, Ir, and IrO₂ thin film electrodes in acidic and alkaline electrolytes: A comparative study on activity and stability," *Catalysis Today*, vol. 262, pp. 170–180, 2016.
- [65] L. C. Seitz, C. F. Dickens, K. Nishio, Y. Hikita, J. Montoya, A. Doyle, C. Kirk, A. Vojvodic, H. Y. Hwang, J. K. Nørskov, and T. F. Jaramillo, "A highly active and stable IrO_x/SrIrO₃ catalyst for the oxygen evolution reaction," *Science*, vol. 353, no. 6303, 2016.
- [66] T. Reier, M. Oezaslan, and P. Strasser, "Electrocatalytic oxygen evolution reaction (OER) on Ru, Ir, and Pt catalysts: A comparative study of nanoparticles and bulk materials," *ACS Catalysis*, vol. 2, no. 8, pp. 1765–1772, 2012.
- [67] M. K. Debe, S. M. Hendricks, G. D. Vernstrom, M. Meyers, M. Brostrom, M. Stephens, Q. Chan, J. Willey, M. Hamden, C. K. Mittelsteadt, C. B. Capuano, K. E. Ayers, and E. B. Anderson, "Initial Performance and Durability of Ultra-Low Loaded NSTF Electrodes for PEM Electrolyzers," *Journal of The Electrochemical Society*, vol. 159, no. 6, p. K165, 2012.
- [68] R. Frydendal, E. A. Paoli, B. P. Knudsen, B. Wickman, P. Malacrida, I. E. L. Stephens, and I. Chorkendorff, "Benchmarking the Stability of Oxygen Evolution Reaction Catalysts: The Importance of Monitoring Mass Losses," *ChemElectroChem*, vol. 1, no. 12, pp. 2075–2081, 2014.
- [69] Y. Lee, J. Suntivich, K. J. May, E. E. Perry, and Y. Shao-Horn, "Synthesis and Activities of Rutile IrO₂ and RuO₂ Nanoparticles for Oxygen Evolution in Acid and Alkaline Solutions," *The Journal of Physical Chemistry Letters*, no. pH 1, pp. 399–404, 2012.

- [70] R. Forgie, G. Bugosh, K. C. Neyerlin, Z. Liu, and P. Strasser, "Bimetallic Ru Electrocatalysts for the OER and Electrolytic Water Splitting in Acidic Media," *Electrochemical and Solid-State Letters*, vol. 13, no. 4, p. B36, 2010.
- [71] K. Macounova, M. Makarova, and P. Krtil, "Oxygen evolution on nanocrystalline RuO₂ and Ru_{0.9}Ni_{0.1}O_{2-δ} electrodes - DEMS approach to reaction mechanism determination," *Electrochemistry Communications*, vol. 11, no. 10, pp. 1865–1868, 2009.
- [72] K. A. Stoerzinger, R. R. Rao, X. R. Wang, W. T. Hong, C. M. Rouleau, and Y. Shao-Horn, "The Role of Ru Redox in pH-Dependent Oxygen Evolution on Rutile Ruthenium Dioxide Surfaces," *Chem*, vol. 2, no. 5, pp. 668–675, 2017.
- [73] K. A. Stoerzinger, O. Diaz-Morales, M. Kolb, R. R. Rao, R. Fryden-dal, L. Qiao, X. R. Wang, N. B. Halck, J. Rossmesl, H. A. Hansen, T. Vegge, I. E. L. Stephens, M. T. M. Koper, and Y. Shao-Horn, "Orientation-Dependent Oxygen Evolution on RuO₂ without Lattice Exchange," *ACS Energy Letters*, vol. 2, no. 4, pp. 876–881, 2017.
- [74] M. Escudero-Escribano, A. F. Pedersen, E. A. Paoli, R. Fryden-dal, D. Friebel, P. Malacrida, J. Rossmesl, I. E. L. Stephens, and I. Chorkendorff, "The Importance of Surface IrO_x in Stabilizing RuO₂ for Oxygen Evolution," *The Journal of Physical Chemistry B*, vol. 122, no. 2, pp. 947–955, 2018.
- [75] N. Danilovic, R. Subbaraman, K. C. Chang, S. H. Chang, Y. Kang, J. Snyder, A. P. Paulikas, D. Strmcnik, Y. T. Kim, D. Myers, V. R. Stamenkovic, and N. M. Markovic, "Using surface segregation to design stable Ru-Ir oxides for the oxygen evolution reaction in acidic environments," *Angewandte Chemie - International Edition*, vol. 53, no. 51, pp. 14016–14021, 2014.
- [76] A. C. C. Tseung and S. Jasem, "Oxygen evolution on semiconducting oxides," *Electrochimica Acta*, vol. 22, no. 1, pp. 31–34, 1977.
- [77] R. R. Rao, M. J. Kolb, N. B. Halck, A. F. Pedersen, A. Mehta, H. You, K. A. Stoerzinger, Z. Feng, H. A. Hansen, H. Zhou, L. Giordano, J. Rosmeisl, T. Vegge, I. Chorkendorff, I. Stephens, and Y. Shao-horn, "Towards identifying the active sites on RuO₂ (110) in catalyzing oxygen evolution," *Energy & Environmental Science*, pp. 0–13, 2017.
- [78] S. H. Chang, N. Danilovic, K.-C. Chang, R. Subbaraman, A. P. Paulikas, D. D. Fong, M. J. Highland, P. M. Baldo, V. R. Stamenkovic,

- J. W. Freeland, J. a. Eastman, and N. M. Markovic, "Functional links between stability and reactivity of strontium ruthenate single crystals during oxygen evolution," *Nature Communications*, vol. 5, no. 4191, pp. 1–9, 2014.
- [79] N. Hodnik, P. Jovanovič, A. Pavlišič, B. Jozinovič, M. Zorko, M. Bele, V. S. Šelih, M. Šala, S. Hočevar, and M. Gaberšček, "New insights into corrosion of ruthenium and ruthenium oxide nanoparticles in acidic media," *Journal of Physical Chemistry C*, vol. 119, no. 18, pp. 10140–10147, 2015.
- [80] H. Tamura and C. Iwakura, "Metal oxide anodes for oxygen evolution," *International Journal of Hydrogen Energy*, vol. 7, no. 11, pp. 857–865, 1982.
- [81] M. Vukovic, "Rotating Ring-Disc Electrode Study of the Enhanced Oxygen Evolution on an Activated Ruthenium Electrode," *J. Chem. Soc., Faraday Trans*, vol. 86, no. 22, pp. 3743–3746, 1990.
- [82] B. J. Kim, D. F. Abbott, X. Cheng, E. Fabbri, M. Nachtegaal, F. Bozza, I. E. Castelli, D. Lebedev, R. Schäublin, C. Copéret, T. Graule, N. Marzari, and T. J. Schmidt, "Unraveling Thermodynamics, Stability, and Oxygen Evolution Activity of Strontium Ruthenium Perovskite Oxide," *ACS Catalysis*, vol. 7, no. 5, pp. 3245–3256, 2017.
- [83] E. A. Paoli, F. Masini, R. Frydendal, D. Deiana, P. Malacrida, T. W. Hansen, I. Chorkendorff, and I. E. L. Stephens, "Fine-tuning the activity of oxygen evolution catalysts: The effect of oxidation pre-treatment on size-selected Ru nanoparticles," *Catalysis Today*, vol. 262, pp. 57–64, 2016.
- [84] M. S. Burke, S. Zou, L. J. Enman, J. E. Kellon, C. A. Gabor, E. Pledger, and S. W. Boettcher, "Revised Oxygen Evolution Reaction Activity Trends for First-Row Transition-Metal (Oxy)hydroxides in Alkaline Media," *Journal of Physical Chemistry Letters*, vol. 6, no. 18, pp. 3737–3742, 2015.
- [85] J. W. D. Ng, M. García-Melchor, M. Bajdich, P. Chakhranont, C. Kirk, A. Vojvodic, and T. F. Jaramillo, "Gold-supported cerium-doped NiOx catalysts for water oxidation," *Nature Energy*, vol. 1, no. 5, p. 16053, 2016.
- [86] B. M. Hunter, J. D. Blakemore, M. Deimund, H. B. Gray, J. R. Winkler, and A. M. Müller, "Highly active mixed-metal nanosheet water

- oxidation catalysts made by pulsed-laser ablation in liquids,” *Journal of the American Chemical Society*, vol. 136, no. 38, pp. 13118–13121, 2014.
- [87] J. D. Blakemore, H. B. Gray, J. R. Winkler, and A. M. Müller, “Co₃O₄ nanoparticle water-oxidation catalysts made by pulsed-laser ablation in liquids,” *ACS Catalysis*, vol. 3, no. 11, pp. 2497–2500, 2013.
- [88] B. Zhang, X. Zheng, O. Voznyy, R. Comin, M. Bajdich, M. Garcia-Melchor, L. Han, J. Xu, M. Liu, L. Zheng, F. P. Garcia de Arquer, C. T. Dinh, F. Fan, M. Yuan, E. Yassitepe, N. Chen, T. Regier, P. Liu, Y. Li, P. De Luna, A. Janmohamed, H. L. Xin, H. Yang, A. Vojvodic, and E. H. Sargent, “Homogeneously dispersed multimetal oxygen-evolving catalysts,” *Science*, vol. 352, no. 6283, pp. 333–337, 2016.
- [89] A. Grimaud, K. J. May, C. E. Carlton, Y.-L. Lee, M. Risch, W. T. Hong, J. Zhou, and Y. Shao-Horn, “Double perovskites as a family of highly active catalysts for oxygen evolution in alkaline solution,” *Nature Communications*, vol. 4, no. May, pp. 1–7, 2013.
- [90] R. Frydendal, M. Busch, N. B. Halck, E. A. Paoli, P. Krtil, I. Chorkendorff, and J. Rossmeisl, “Enhancing activity for the oxygen evolution reaction: The beneficial interaction of gold with manganese and cobalt oxides,” *ChemCatChem*, vol. 7, no. 1, pp. 149–154, 2015.
- [91] P. Chakthranont, J. Kibsgaard, A. Gallo, J. Park, M. Mitani, D. Sokaras, T. Kroll, R. Sinclair, M. B. Mogensen, and T. F. Jaramillo, “Effects of Gold Substrates on the Intrinsic and Extrinsic Activity of High-Loading Nickel-Based Oxyhydroxide Oxygen Evolution Catalysts,” *ACS Catalysis*, vol. 7, no. 8, pp. 5399–5409, 2017.
- [92] Jin Suntivich and Kevin J. May and Hubert A. Gasteiger and John B. Goodenough and Y. Shao-Horn, “A Perovskite Oxide Optimized for Oxygen Evolution Catalysis from Molecular Orbital Principles,” *Science*, vol. 6061, pp. 1383–1385, 2011.
- [93] R. Tang, Y. Nie, J. K. Kawasaki, D.-Y. Kuo, G. Petretto, G. Hautier, G.-M. Rignanese, K. M. Shen, D. G. Schlom, and J. Suntivich, “Oxygen evolution reaction electrocatalysis on SrIrO₃ grown using molecular beam epitaxy,” *J. Mater. Chem. A*, pp. –, 2016.
- [94] L. Trotochaud, J. K. Ranney, K. N. Williams, and S. W. Boettcher, “Solution-cast metal oxide thin film electrocatalysts for oxygen evolution,” *Journal of the American Chemical Society*, vol. 134, no. 41, pp. 17253–17261, 2012.

- [95] L. Trotochaud, S. L. Young, J. K. Ranney, and S. W. Boettcher, "Nickel-Iron oxyhydroxide oxygen-evolution electrocatalysts: The role of intentional and incidental iron incorporation," *Journal of the American Chemical Society*, vol. 136, no. 18, pp. 6744–6753, 2014.
- [96] M. S. Burke, L. J. Enman, A. S. Batchellor, S. Zou, and S. W. Boettcher, "Oxygen Evolution Reaction Electrocatalysis on Transition Metal Oxides and (Oxy)hydroxides: Activity Trends and Design Principles," *Chemistry of Materials*, vol. 27, no. 22, pp. 7549–7558, 2015.
- [97] L. J. Enman, M. S. Burke, A. S. Batchellor, and S. W. Boettcher, "Effects of Intentionally Incorporated Metal Cations on the Oxygen Evolution Electrocatalytic Activity of Nickel (Oxy)hydroxide in Alkaline Media," *ACS Catalysis*, vol. 6, no. 4, pp. 2416–2423, 2016.
- [98] S. Klaus, Y. Cai, M. W. Louie, L. Trotochaud, and A. T. Bell, "Effects of Fe electrolyte impurities on Ni(OH)₂/NiOOH structure and oxygen evolution activity," *Journal of Physical Chemistry C*, vol. 119, no. 13, pp. 7243–7254, 2015.
- [99] D. A. Corrigan, "The Catalysis of the Oxygen Evolution Reaction by Iron Impurities in Thin Film Nickel Oxide Electrodes," *Journal of The Electrochemical Society*, vol. 134, no. 2, p. 377, 1987.
- [100] D. Friebel, M. W. Louie, M. Bajdich, K. E. Sanwald, Y. Cai, A. M. Wise, M. J. Cheng, D. Sokaras, T. C. Weng, R. Alonso-Mori, R. C. Davis, J. R. Bargar, J. K. Nørskov, A. Nilsson, and A. T. Bell, "Identification of highly active Fe sites in (Ni,Fe)OOH for electrocatalytic water splitting," *Journal of the American Chemical Society*, vol. 137, no. 3, pp. 1305–1313, 2015.
- [101] M. W. Louie and A. T. Bell, "An Investigation of Thin-Film Ni-Fe Oxide Catalysts for the Electrochemical Evolution of Oxygen," *Journal of the American Chemical Society*, vol. 135, pp. 12329–12337, 2013.
- [102] X. Li, F. C. Walsh, and D. Pletcher, "Nickel based electrocatalysts for oxygen evolution in high current density, alkaline water electrolyzers," *Phys. Chem. Chem. Phys.*, vol. 13, no. 3, pp. 1162–1167, 2011.
- [103] N. Li, D. K. Bediako, R. G. Hadt, D. Hayes, T. J. Kempa, F. von Cube, D. C. Bell, L. X. Chen, and D. G. Nocera, "Influence of iron doping on tetravalent nickel content in catalytic oxygen evolving films," *Proceedings of the National Academy of Sciences*, vol. 114, no. 7, pp. 1486–1491, 2017.

- [104] M. Görlin, P. Chernev, J. F. De Araujo, T. Reier, S. Dresp, B. Paul, R. Krähnert, H. Dau, and P. Strasser, "Oxygen evolution reaction dynamics, faradaic charge efficiency, and the active metal redox states of Ni-Fe oxide water splitting electrocatalysts," *Journal of the American Chemical Society*, vol. 138, no. 17, pp. 5603–5614, 2016.
- [105] F. Dionigi and P. Strasser, "NiFe-Based (Oxy)hydroxide Catalysts for Oxygen Evolution Reaction in Non-Acidic Electrolytes," *Advanced Energy Materials*, vol. 6, p. 1600621, 2016.
- [106] M. Pourbaix, *Atlas of electrochemical equilibria in aqueous solutions*. National Association of Corrosion, second ed., 1974.
- [107] M. Morishita, S. Ochiai, T. Kakeya, T. Ozaki, Y. Kawabe, M. Watada, S. Tanase, and T. Sakai, "Phase Transformation in the Charge-Discharge Process and the Structural Analysis by Synchrotron XAFS and XRD for Nickel Hydroxide Electrode," *Electrochemistry*, vol. 76, no. 11, pp. 802–807, 2008.
- [108] M. Wehrens-Dijksma and P. H. Notten, "Electrochemical Quartz Microbalance characterization of Ni(OH)₂-based thin film electrodes," *Electrochimica Acta*, vol. 51, no. 18, pp. 3609–3621, 2006.
- [109] R. L. Doyle, I. J. Godwin, M. P. Brandon, and M. E. G. Lyons, "Redox and electrochemical water splitting catalytic properties of hydrated metal oxide modified electrodes," *Physical Chemistry Chemical Physics*, vol. 15, no. 33, p. 13737, 2013.
- [110] O. Diaz-Morales, F. Calle-Vallejo, C. de Munck, and M. T. M. Koper, "Electrochemical water splitting by gold: evidence for an oxide decomposition mechanism," *Chemical Science*, vol. 4, no. 6, p. 2334, 2013.
- [111] S. Fierro, T. Nagel, H. Baltruschat, and C. Comninellis, "Investigation of the oxygen evolution reaction on Ti/IrO₂ electrodes using isotope labelling and on-line mass spectrometry," *Electrochemistry Communications*, vol. 9, no. 8, pp. 1969–1974, 2007.
- [112] H. M. A. Amin and H. Baltruschat, "How many surface atoms in Co₃O₄ take part in oxygen evolution? Isotope labeling together with differential electrochemical mass spectrometry," *Phys. Chem. Chem. Phys.*, vol. 19, no. 37, pp. 25527–25536, 2017.
- [113] M. Wohlfahrt-Mehrens and J. Heitbaum, "Oxygen evolution on Ru and RuO₂ electrodes studied using isotope labelling and on-line mass

- spectrometry,” *Journal of Electroanalytical Chemistry and Interfacial Electrochemistry*, vol. 237, pp. 251–260, 1987.
- [114] A. Grimaud, O. Diaz-Morales, B. Han, W. T. Hong, Y.-L. Lee, L. Giordano, K. A. Stoerzinger, M. T. M. Koper, and Y. Shao-Horn, “Activating lattice oxygen redox reactions in metal oxides to catalyze oxygen evolution,” *Nature Chemistry*, vol. 9, no. 5, pp. 457–465, 2017.
- [115] A. D. Doyle, M. Bajdich, and A. Vojvodic, “Theoretical Insights to Bulk Activity Towards Oxygen Evolution in Oxyhydroxides,” *Catalysis Letters*, vol. 147, no. 6, pp. 1533–1539, 2017.
- [116] A. S. Batchellor and S. W. Boettcher, “Pulse-Electrodeposited Ni-Fe (Oxy)hydroxide Oxygen Evolution Electrocatalysts with High Geometric and Intrinsic Activities at Large Mass Loadings,” *ACS Catalysis*, vol. 5, no. 11, pp. 6680–6689, 2015.
- [117] C. G. Morales-Guio, M. T. Mayer, A. Yella, S. D. Tilley, M. Graetzel, and X. Hu, “An Optically Transparent Iron Nickel Oxide Catalyst for Solar Water Splitting,” *Journal of the American Chemical Society*, vol. 137, no. 31, pp. 9927–9936, 2015.
- [118] C. C. L. McCrory, S. Jung, J. C. Peters, and T. F. Jaramillo, “Benchmarking Heterogeneous Electrocatalysts for the Oxygen Evolution Reaction,” *Journal of the American Chemical Society*, vol. 135, no. 45, pp. 16977–16987, 2013.
- [119] R. Frydendal, E. A. Paoli, I. Chorkendorff, J. Rossmeisl, and I. E. L. Stephens, “Toward an Active and Stable Catalyst for Oxygen Evolution in Acidic Media: Ti-Stabilized MnO_2 ,” *Advanced Energy Materials*, vol. 5, no. 22, 2015.
- [120] R. Jinnouchi, E. Toyoda, T. Hatanaka, and Y. Morimoto, “First principles calculations on site-dependent dissolution potentials of supported and unsupported Pt particles,” *Journal of Physical Chemistry C*, vol. 114, no. 41, pp. 17557–17568, 2010.
- [121] I. C. Man, *Theoretical Study of Electro-catalysts for oxygen evolution*. PhD thesis, Technical University of Denmark, 2011.
- [122] N. Danilovic, R. Subbaraman, K. C. Chang, S. H. Chang, Y. J. Kang, J. Snyder, A. P. Paulikas, D. Strmcnik, Y. T. Kim, D. Myers, V. R. Stamenkovic, and N. M. Markovic, “Activity-stability trends for the oxygen evolution reaction on monometallic oxides in acidic environments,” *Journal of Physical Chemistry Letters*, vol. 5, no. 14, pp. 2474–2478, 2014.

- [123] P. P. Lopes, D. Strmcnik, D. Tripkovic, J. G. Connell, V. Stamenkovic, and N. M. Markovic, "Relationships between Atomic Level Surface Structure and Stability/Activity of Platinum Surface Atoms in Aqueous Environments," *ACS Catalysis*, vol. 6, no. 4, pp. 2536–2544, 2016.
- [124] S. Cherevko, T. Reier, A. R. Zeradjanin, Z. Pawolek, P. Strasser, and K. J. J. Mayrhofer, "Stability of nanostructured iridium oxide electrocatalysts during oxygen evolution reaction in acidic environment," *Electrochemistry Communications*, vol. 48, pp. 81–85, 2014.
- [125] S. Cherevko, A. R. Zeradjanin, A. a. Topalov, N. Kulyk, I. Katsounaros, and K. J. J. Mayrhofer, "Dissolution of noble metals during oxygen evolution in acidic media," *ChemCatChem*, vol. 6, no. 8, pp. 2219–2223, 2014.
- [126] T. Reier, H. N. Nong, D. Teschner, R. Schlögl, and P. Strasser, "Electrocatalytic Oxygen Evolution Reaction in Acidic Environments - Reaction Mechanisms and Catalysts," *Advanced Energy Materials*, vol. 7, no. 1, 2017.
- [127] S. H. Chang, J. G. Connell, N. Danilovic, R. Subbaraman, K.-C. Chang, V. R. Stamenkovic, and N. M. Markovic, "Activity–stability relationship in the surface electrochemistry of the oxygen evolution reaction," *Faraday Discuss.*, vol. 176, no. 0, pp. 125–133, 2014.
- [128] F. T. Wagner, B. Lakshmanan, and M. F. Mathias, "Electrochemistry and the future of the automobile," *Journal of Physical Chemistry Letters*, vol. 1, no. 14, pp. 2204–2219, 2010.
- [129] S. Mukerjee, "Role of Structural and Electronic Properties of Pt and Pt Alloys on Electrocatalysis of Oxygen Reduction," *Journal of The Electrochemical Society*, vol. 142, no. 5, p. 1409, 1995.
- [130] S. Mukerjee and J. McBreen, "Effect of particle size on the electrocatalysis by carbon-supported Pt electrocatalysts: An in situ XAS investigation," *Journal of Electroanalytical Chemistry*, vol. 448, no. 2, pp. 163–171, 1998.
- [131] S. Mukerjee and S. Srinivasan, "Enhanced electrocatalysis of oxygen reduction on platinum alloys in proton-exchange membrane fuel-cells," *Journal of Electroanalytical Chemistry*, vol. 357, no. 1-2, pp. 201–224, 1993.
- [132] V. Stamenković, T. J. Schmidt, P. N. Ross, and N. M. Marković, "Surface Composition Effects in Electrocatalysis: Kinetics of Oxygen

- Reduction on Well-Defined Pt₃Ni and Pt₃Co Alloy Surfaces,” *The Journal of Physical Chemistry B*, vol. 106, no. 46, pp. 11970–11979, 2002.
- [133] V. Stamenkovic, B. S. Mun, K. J. Mayrhofer, P. N. Ross, N. M. Markovic, J. Rossmeisl, J. Greeley, and J. K. Nørskov, “Changing the Activity of Electrocatalysts for Oxygen Reduction by Tuning the Surface Electronic Structure,” *Angewandte Chemie International Edition*, vol. 45, no. 18, pp. 2897–2901, 2006.
- [134] V. R. Stamenkovic, B. S. Mun, M. Arenz, K. J. Mayrhofer, C. A. Lucas, G. Wang, P. N. Ross, and N. M. Markovic, “Trends in electrocatalysis on extended and nanoscale Pt-bimetallic alloy surfaces,” *Nature Materials*, vol. 6, no. 3, pp. 241–247, 2007.
- [135] C. Wang, M. Chi, D. Li, D. Strmcnik, D. Van Der Vliet, G. Wang, V. Komanicky, K. C. Chang, A. P. Paulikas, D. Tripkovic, J. Pearson, K. L. More, N. M. Markovic, and V. R. Stamenkovic, “Design and synthesis of bimetallic electrocatalyst with multilayered Pt-skin surfaces,” *Journal of the American Chemical Society*, vol. 133, no. 36, pp. 14396–14403, 2011.
- [136] V. R. Stamenkovic, B. Fowler, B. S. Mun, G. Wang, P. N. Ross, C. a. Lucas, and N. M. Marković, “Improved oxygen reduction activity on Pt₃Ni(111) via increased surface site availability,” *Science*, vol. 315, no. 5811, pp. 493–497, 2007.
- [137] C. Chen, Y. Kang, Z. Huo, Z. Zhu, W. Huang, H. L. Xin, J. D. Snyder, D. Li, J. A. Herron, M. Mavrikakis, M. Chi, K. L. More, Y. Li, N. M. Markovic, G. A. Somorjai, P. Yang, and V. R. Stamenkovic, “Highly Crystalline Multimetallic Nanoframes with Three-Dimensional Electrocatalytic Surfaces,” *Science*, vol. 343, no. 6177, pp. 1339–1343, 2014.
- [138] X. Huang, Z. Zhao, L. Cao, Y. Chen, E. Zhu, Z. Lin, M. Li, A. Yan, A. Zettl, Y. M. Wang, X. Duan, T. Mueller, and Y. Huang, “High-performance transition metal – doped Pt₃Ni octahedra for oxygen reduction reaction,” *Science*, vol. 348, no. 2009, pp. 1230–1234, 2015.
- [139] C. Baldizzone, S. Mezzavilla, H. W. P. Carvalho, J. C. Meier, A. K. Schuppert, M. Heggen, C. Galeano, J. D. Grunwaldt, F. Schüth, and K. J. J. Mayrhofer, “Confined-space alloying of nanoparticles for the synthesis of efficient PtNi fuel-cell catalysts,” *Angewandte Chemie - International Edition*, vol. 53, no. 51, pp. 14250–14254, 2014.

- [140] S. Chen, P. J. Ferreira, W. Sheng, N. Yabuuchi, L. F. Allard, and Y. Shao-Horn, "Enhanced Activity for Oxygen Reduction Reaction on "Pt₃Co" Nanoparticles: Direct Evidence of Percolated and Sandwich-Segregation Structures," *Journal of the American Chemical Society*, vol. 130, no. 42, pp. 13818–13819, 2008.
- [141] S. Chen, W. Sheng, N. Yabuuchi, P. J. Ferreira, L. F. Allard, and Y. Shao-Horn, "Origin of Oxygen Reduction Reaction Activity on "Pt 3 Co" Nanoparticles: Atomically Resolved Chemical Compositions and Structures," *The Journal of Physical Chemistry C*, vol. 113, no. 3, pp. 1109–1125, 2009.
- [142] P. Mani, R. Srivastava, and P. Strasser, "Dealloyed Pt-Cu core-shell nanoparticle electrocatalysts for use in PEM fuel cell cathodes," *Journal of Physical Chemistry C*, vol. 112, no. 7, pp. 2770–2778, 2008.
- [143] K. C. Neyerlin, R. Srivastava, C. Yu, and P. Strasser, "Electrochemical activity and stability of dealloyed Pt-Cu and Pt-Cu-Co electrocatalysts for the oxygen reduction reaction," *Journal of Power Sources*, vol. 186, no. 2, pp. 261–267, 2009.
- [144] B. Han, C. E. Carlton, A. Kongkanand, R. S. Kukreja, B. R. Theobald, L. Gan, R. O'Malley, P. Strasser, F. T. Wagner, and Y. Shao-Horn, "Record activity and stability of dealloyed bimetallic catalysts for proton exchange membrane fuel cells," *Energy Environ. Sci.*, vol. 8, no. 1, pp. 258–266, 2015.
- [145] P. Strasser, S. Koh, T. Anniyev, J. Greeley, K. More, C. Yu, Z. Liu, S. Kaya, D. Nordlund, H. Ogasawara, M. F. Toney, and A. Nilsson, "Lattice-strain control of the activity in dealloyed core-shell fuel cell catalysts," *Nature Chemistry*, vol. 2, no. 6, pp. 454–460, 2010.
- [146] S. Koh and P. Strasser, "Electrocatalysis on bimetallic surfaces: Modifying catalytic reactivity for oxygen reduction by voltammetric surface dealloying," *Journal of the American Chemical Society*, vol. 129, no. 42, pp. 12624–12625, 2007.
- [147] P. Strasser, Z. C. Liu, and S. Koh, "Aging studies of Voltammetrically dealloyed Pt-Cu nanoparticle ORR electrocatalysts," *Proton Exchange Membrane Fuel Cells 8, Pts 1 and 2*, vol. 16, no. 2, pp. 515–522, 2008.
- [148] F. Hasché, M. Oezaslan, and P. Strasser, "Activity and Structure of Dealloyed PtNi₃ Nanoparticle Electrocatalyst for Oxygen Reduction

- Reaction in PEMFC,” *ECS Transactions*, vol. 41, no. 1, pp. 1079–1088, 2011.
- [149] T. Asset, R. Chattot, M. Fontana, B. Mercier-Guyon, N. Job, L. Dubau, and F. Maillard, “A Review on Recent Developments and Prospects for Oxygen Reduction Reaction on Hollow Pt-alloy Nanoparticles,” *ChemPhysChem*, 2018.
- [150] A. Smigelskas and E. Kirkendall, “Zinc Diffusion in Alpha Brass,” *Claaa E Metal’s Technology*, vol. XIII, no. 1942, p. 2071, 1946.
- [151] A. S. B. Federico Calle-Vallejo, Jakub Tymoczko, Viktor Colic, Quang Huy Vu, Marcus D. Pohl, karina Morgenstern, David Loffreda, Philippe Sautet, Wolfgang Schuhmann, “Finding optimal surface sites on heterogeneous catalysts by counting nearest neighbors,” *Science*, vol. 350, no. 6257, pp. 185–190, 2015.
- [152] I. Erfye, L. Stephens, and J. Rossmeisl, “Toward sustainable fuel cells Improved,” *Science*, vol. 354, no. 63, pp. 9–11, 2016.
- [153] C. M. Pedersen, M. Escudero-escribano, A. Velázquez-Palenzuela, L. H. Christensen, I. Chorkendorff, and I. E. Stephens, “Benchmarking Pt-based electrocatalysts for low temperature fuel cell reactions with the rotating disk electrode: oxygen reduction and hydrogen oxidation in the presence of CO (review article),” *Electrochimica Acta*, vol. 179, pp. 1–11, 2015.
- [154] A. Bonakdarpour, K. Stevens, G. D. Vernstrom, R. Atanasoski, A. K. Schmoeckel, M. K. Debe, and J. R. Dahn, “Oxygen reduction activity of Pt and Pt-Mn-Co electrocatalysts sputtered on nano-structured thin film support,” *Electrochimica Acta*, vol. 53, no. 2, pp. 688–694, 2007.
- [155] K. Sasaki, H. Naohara, Y. Cai, Y. M. Choi, P. Liu, M. B. Vukmirovic, J. X. Wang, and R. R. Adzic, “Core-protected platinum monolayer shell high-stability electrocatalysts for fuel-cell cathodes,” *Angewandte Chemie - International Edition*, vol. 49, no. 46, pp. 8602–8607, 2010.
- [156] D. Wang, H. L. Xin, R. Hovden, H. Wang, Y. Yu, D. A. Muller, F. J. Disalvo, and H. D. Abruña, “Structurally ordered intermetallic platinum-cobalt core-shell nanoparticles with enhanced activity and stability as oxygen reduction electrocatalysts,” *Nature Materials*, vol. 12, no. 1, pp. 81–87, 2013.

- [157] C. Wang, D. Van Der Vliet, K. L. More, N. J. Zaluzec, S. Peng, S. Sun, H. Daimon, G. Wang, J. Greeley, J. Pearson, A. P. Paulikas, G. Karapetrov, D. Strmcnik, N. M. Markovic, and V. R. Stamenkovic, "Multimetallic Au/FePt₃ nanoparticles as highly durable electrocatalyst," *Nano Letters*, vol. 11, no. 3, pp. 919–926, 2011.
- [158] S. Guo, D. Li, H. Zhu, S. Zhang, N. M. Markovic, V. R. Stamenkovic, and S. Sun, "FePt and CoPt nanowires as efficient catalysts for the oxygen reduction reaction," *Angewandte Chemie - International Edition*, vol. 52, no. 12, pp. 3465–3468, 2013.
- [159] J. X. Wang, C. Ma, Y. Choi, D. Su, Y. Zhu, P. Liu, R. Si, M. B. Vukmirovic, Y. Zhang, and R. R. Adzic, "Kirkendall effect and lattice contraction in nanocatalysts: A new strategy to enhance sustainable activity," *Journal of the American Chemical Society*, vol. 133, no. 34, pp. 13551–13557, 2011.
- [160] W. Liu, P. Rodriguez, L. Borchardt, A. Foelske, J. Yuan, A. K. Herrmann, D. Geiger, Z. Zheng, S. Kaskel, N. Gaponik, R. Kötz, T. J. Schmidt, and A. Eychmüller, "Bimetallic aerogels: High-performance electrocatalysts for the oxygen reduction reaction," *Angewandte Chemie - International Edition*, vol. 52, no. 37, pp. 9849–9852, 2013.
- [161] S. I. Choi, M. Shao, N. Lu, A. Ruditskiy, H. C. Peng, J. Park, S. Guerrero, J. Wang, M. J. Kim, and Y. Xia, "Synthesis and characterization of Pd@Pt-Ni core-shell octahedra with high activity toward oxygen reduction," *ACS Nano*, vol. 8, no. 10, pp. 10363–10371, 2014.
- [162] P. Hernandez-Fernandez, F. Masini, D. N. McCarthy, C. E. Strebler, D. Friebel, D. Deiana, P. Malacrida, A. Nierhoff, A. Bodin, A. M. Wise, J. H. Nielsen, T. W. Hansen, A. Nilsson, I. E. L. Stephens, and I. Chorkendorff, "Mass-selected nanoparticles of Pt_xY as model catalysts for oxygen electroreduction," *Nature Chemistry*, vol. 6, no. 8, pp. 732–738, 2014.
- [163] S. I. Choi, S. Xie, M. Shao, J. H. Odell, N. Lu, H. C. Peng, L. Protsailo, S. Guerrero, J. Park, X. Xia, J. Wang, M. J. Kim, and Y. Xia, "Synthesis and characterization of 9 nm Pt-Ni octahedra with a record high activity of 3.3 A/mg_{Pt} for the oxygen reduction reaction," *Nano Letters*, vol. 13, no. 7, pp. 3420–3425, 2013.
- [164] A. Velázquez-Palenzuela, F. Masini, A. F. Pedersen, M. Escudero-Escribano, D. Deiana, P. Malacrida, T. W. Hansen, D. Friebel, A. Nilsson, I. E. Stephens, and I. Chorkendorff, "The enhanced activity

- of mass-selected Pt_xGd nanoparticles for oxygen electroreduction,” *Journal of Catalysis*, vol. 328, pp. 297–307, aug 2015.
- [165] M. Li, Z. Zhao, T. Cheng, A. Fortunelli, C.-Y. Chen, R. Yu, Q. Zhang, L. Gu, B. V. Merinov, Z. Lin, E. Zhu, T. Yu, Q. Jia, J. Guo, L. Zhang, W. A. Goddard, Y. Huang, and X. Duan, “Ultrafine jagged platinum nanowires enable ultrahigh mass activity for the oxygen reduction reaction,” *Science*, vol. 354, pp. 1414–1419, dec 2016.
- [166] L. Dubau, M. Lopez-Haro, L. Castanheira, J. Durst, M. Chatenet, P. Bayle-Guillemaud, L. Guétaz, N. Caqué, E. Rossinot, and F. Mailard, “Probing the structure, the composition and the ORR activity of Pt₃Co/C nanocrystallites during a 3422 h PEMFC ageing test,” *Applied Catalysis B: Environmental*, vol. 142-143, pp. 801–808, 2013.
- [167] J. Greeley, I. E. L. Stephens, A. S. Bondarenko, T. P. Johansson, H. A. Hansen, T. F. Jaramillo, J. Rossmeisl, I. Chorkendorff, and J. K. Nørskov, “Alloys of platinum and early transition metals as oxygen reduction electrocatalysts,” *Nature chemistry*, vol. 1, no. 7, pp. 552–556, 2009.
- [168] I. E. L. Stephens, A. S. Bondarenko, L. Bech, and I. Chorkendorff, “Oxygen Electroreduction Activity and X-Ray Photoelectron Spectroscopy of Platinum and Early Transition Metal Alloys,” *Chem-CatChem*, vol. 4, pp. 341–349, mar 2012.
- [169] M. Escudero-Escribano, A. Verdaguer-Casadevall, P. Malacrida, U. Grønbjerg, B. P. Knudsen, A. K. Jepsen, J. Rossmeisl, I. E. L. Stephens, and I. Chorkendorff, “Pt₅Gd as a highly active and stable catalyst for oxygen electroreduction,” *Journal of the American Chemical Society*, vol. 134, no. 40, pp. 16476–16479, 2012.
- [170] U. G. Vej-Hansen, J. Rosmeisl, I. E. L. Stephens, J. Schiøtz, J. Rossmeisl, I. E. L. Stephens, J. Schiøtz, J. Rosmeisl, I. E. L. Stephens, and J. Schiøtz, “Correlation between diffusion barriers and alloying energy in binary alloys,” *Phys. Chem. Chem. Phys.*, vol. 18, no. 4, pp. 3302–3307, 2016.
- [171] M. Escudero-Escribano, P. Malacrida, M. Hangaard Hansen, U. Grønbjerg Vej-Hansen, A. A. Velazquez-Palenzuela, V. Tripkovic, J. Schiøtz, J. Rossmeisl, I. E. Stephens, and I. Chorkendorff, “Tuning the activity of pt alloy electrocatalysts by means of the lanthanide contraction,” *Science*, vol. 352, pp. 73–76, apr 2016.

- [172] U. G. Vej-Hansen, M. Escudero-Escribano, A. Velázquez-Palenzuela, P. Malacrida, J. Rossmeisl, I. E. L. Stephens, I. Chorkendorff, and J. Schiøtz, “New Platinum Alloy Catalysts for Oxygen Electroreduction Based on Alkaline Earth Metals,” *Electrocatalysis*, no. April, 2017.
- [173] N. Todoroki, Y. Iijima, R. Takahashi, Y. Asakimori, and T. Wadayama, “Structure and Electrochemical Stability of Pt-Enriched Ni/Pt(111) Topmost Surface Prepared by Molecular Beam Epitaxy,” *Journal of the Electrochemical Society*, vol. 160, no. 6, pp. F591–F596, 2013.
- [174] M. Tsuji, K. Uto, T. Nagami, A. Muto, H. Fukushima, and J.-i. Hayashi, “Synthesis of Carbon-Supported Pt- YO_x and PtY Nanoparticles with High Catalytic Activity for the Oxygen Reduction Reaction Using a Microwave-based Polyol Method,” *ChemCatChem*, vol. 9, no. 6, pp. 962–970, 2017.
- [175] R. Cui, L. Mei, G. Han, J. Chen, G. Zhang, and Y. Quan, “Facile Synthesis of Nanoporous Pt-Y alloy with Enhanced Electrocatalytic Activity and Durability,” *Scientific Reports*, vol. 7, no. 41826, 2017.
- [176] R. Brandiele, C. Durante, E. Grądzka, G. A. Rizzi, J. Zheng, D. Badocco, P. Centomo, P. Pastore, G. Granozzi, and A. Gennaro, “One step forward to a scalable synthesis of platinum–yttrium alloy nanoparticles on mesoporous carbon for the oxygen reduction reaction,” *J. Mater. Chem. A*, vol. 4, no. 31, pp. 12232–12240, 2016.
- [177] S. B. Han, D. H. Kwak, Y. W. Lee, S. J. Kim, J. Y. Lee, S. Lee, H. J. Kwon, and K. W. Park, “Electrodeposited nanoporous PtY alloy electrodes with enhanced oxygen reduction reaction,” *International Journal of Electrochemical Science*, vol. 11, no. 5, pp. 3803–3814, 2016.
- [178] S. J. Yoo, K.-S. Lee, S. J. Hwang, Y.-H. Cho, S.-K. Kim, J. W. Yun, Y.-E. Sung, and T.-H. Lim, “Pt₃Y electrocatalyst for oxygen reduction reaction in proton exchange membrane fuel cells,” *International Journal of Hydrogen Energy*, vol. 37, no. 12, pp. 9758–9765, 2012.
- [179] J. S. Kanady, P. Leidinger, A. Haas, S. Titlbach, S. Schunk, K. Schierle-Arndt, E. J. Crumlin, C. H. Wu, and A. P. Alivisatos, “Synthesis of Pt₃Y and Other Early-Late Intermetallic Nanoparticles by Way of a Molten Reducing Agent,” *Journal of the American Chemical Society*, vol. 139, no. 16, pp. 5672–5675, 2017.

-
- [180] B. Von Issendorff and R. E. Palmer, “A new high transmission infinite range mass selector for cluster and nanoparticle beams,” *Review of Scientific Instruments*, vol. 70, no. 12, pp. 4497–4501, 1999.
- [181] R. Eason, *Pulsed Laser Deposition of Thin Films : Applications-Led Growth of Functional Materials*. New-York: John Wiley & Sons Inc, 2006.
- [182] C. D. Gardini, Diego; Wagner, Jakob Birkedal; Damsgaard, *In situ and ex situ electron microscopy and X-ray diffraction characterization of the evolution of a catalytic system - from synthesis to deactivation*. PhD thesis, Technical University of Denmark, 2015.
- [183] P. Malacrida, *Alloys of Pt and Rare Earths for the Oxygen Electrorreduction Reaction*. PhD thesis, Technical University of Denmark, 2014.
- [184] C. V. Cushman, P. Brüner, J. Zakel, G. H. Major, B. M. Lunt, N. J. Smith, T. Grehl, and M. R. Linford, “Low energy ion scattering (LEIS). A practical introduction to its theory, instrumentation, and applications,” *Analytical Methods*, vol. 8, no. 17, pp. 3419–3439, 2016.
- [185] H. H. Brongersma, T. Grehl, E. R. Schofield, R. A. Smith, and H. R. Ter Veen, “Analysis of the outer surface of platinum-gold catalysts by low-energy ion scattering,” *Platinum Metals Review*, vol. 54, no. 2, pp. 81–87, 2010.
- [186] L. Reimer and H. Kohl, *Transmission Electron Microscopy Physics of Image Formation*, vol. 51. Springer, 2008.
- [187] K. D. Jensen, *Electrochemical insights into platinum catalysts for fuel cells*. PhD thesis, Technical University of Denmark, 2017.
- [188] E. R. Savinova and U. Stimming, “CO monolayer oxidation on Pt nanoparticles : Further insights into the particle size effects,” *Journal of Electroanalytical Chemistry*, vol. 599, pp. 221–232, 2007.
- [189] M. Watanabe, Y. Zhu, and H. Uchida, “Oxidation of CO on a PtFe Alloy Electrode Studied by Surface Enhanced Infrared Reflection-Absorption Spectroscopy,” *The Journal of Physical Chemistry B*, vol. 104, no. 8, pp. 1762–1768, 2000.
- [190] D. F. Van Der Vliet, C. Wang, D. Li, A. P. Paulikas, J. Greeley, R. B. Rankin, D. Strmcnik, D. Tripkovic, N. M. Markovic, and V. R. Stamenkovic, “Unique electrochemical adsorption properties of Pt-skin surfaces,” *Angewandte Chemie - International Edition*, vol. 51, no. 13, pp. 3139–3142, 2012.

- [191] D. B. Trimarco, S. B. Scott, A. H. Thilsted, and J. Y. Pan, “Enabling real-time detection of electrochemical desorption phenomena with sub-monolayer sensitivity,” *Electrochimica Acta*, pp. 1–25, 2018.
- [192] T. E. Lister, Y. Chu, W. Cullen, H. You, R. M. Yonco, J. F. Mitchell, and Z. Nagy, “Electrochemical and X-ray scattering study of well defined RuO₂ single crystal surfaces,” *Journal of Electroanalytical Chemistry*, vol. 524-525, pp. 201–218, 2002.
- [193] K. A. Stoerzinger, *Understanding the Catalytic Activity of Oxides through their Electronic Structure and Surface Chemistry* by. PhD thesis, Massachusetts Institute of Technology, 2016.
- [194] T. E. Lister, Y. V. Tolmachev, Y. Chu, W. G. Cullen, H. You, R. Yonco, and Z. Nagy, “Cathodic activation of RuO₂ single crystal surfaces for hydrogen-evolution reaction,” *Journal of Electroanalytical Chemistry*, vol. 554-555, no. 1, pp. 71–76, 2003.
- [195] V. R. Stamenkovic, D. Strmcnik, P. P. Lopes, and N. M. Markovic, “Energy and fuels from electrochemical interfaces,” *Nature Materials*, vol. 16, no. 1, pp. 57–69, 2016.
- [196] H. Hussain, G. Tocci, T. Woolcot, X. Torrelles, C. L. Pang, D. S. Humphrey, C. M. Yim, D. C. Grinter, G. Cabailh, O. Bikondoa, R. Lindsay, J. Zegenhagen, A. Michaelides, and G. Thornton, “Structure of a model TiO₂ photocatalytic interface,” *Nature Materials*, vol. 16, no. 4, pp. 461–466, 2016.
- [197] T. Li, O. Kasian, S. Cherevko, S. Zhang, S. Geiger, C. Scheu, P. Felfer, D. Raabe, B. Gault, and K. J. J. Mayrhofer, “Atomic-scale insights into surface species of electrocatalysts in three dimensions,” *Nature Catalysis*, vol. 1, no. April, pp. 300–305, 2018.
- [198] M. Nesselberger, M. Roefzaad, R. Fayçal Hamou, P. Ulrich Biedermann, F. F. Schweinberger, S. Kunz, K. Schloegl, G. K. H. Wiberg, S. Ashton, U. Heiz, K. J. J. Mayrhofer, and M. Arenz, “The effect of particle proximity on the oxygen reduction rate of size-selected platinum clusters,” *Nat. Mater.*, vol. 12, no. 10, pp. 919–924, 2013.
- [199] H. Mistry, F. Behafarid, R. Reske, A. S. Varela, P. Strasser, and B. Roldan Cuenya, “Tuning Catalytic Selectivity at the Mesoscale via Interparticle Interactions,” *ACS Catalysis*, vol. 6, no. 2, pp. 1075–1080, 2016.

- [200] M. C. Biesinger, L. W. M. Lau, A. R. Gerson, and R. S. C. Smart, "The role of the Auger parameter in XPS studies of nickel metal, halides and oxides," *Physical Chemistry Chemical Physics*, vol. 14, no. 7, p. 2434, 2012.
- [201] M. C. Biesinger, B. P. Payne, A. P. Grosvenor, L. W. Lau, A. R. Gerson, and R. S. C. Smart, "Resolving surface chemical states in XPS analysis of first row transition metals, oxides and hydroxides: Cr, Mn, Fe, Co and Ni," *Applied Surface Science*, vol. 257, no. 7, pp. 2717–2730, 2011.
- [202] A. P. Grosvenor, M. C. Biesinger, R. S. C. Smart, and N. S. McIntyre, "New interpretations of XPS spectra of nickel metal and oxides," *Surface Science*, vol. 600, no. 9, pp. 1771–1779, 2006.
- [203] P. J. Ferreira, G. J. la O', Y. Shao-Horn, D. Morgan, R. Makharia, S. Kocha, and H. A. Gasteiger, "Instability of Pt/C Electrocatalysts in Proton Exchange Membrane Fuel Cells," *Journal of The Electrochemical Society*, vol. 152, no. 11, p. A2256, 2005.
- [204] J. C. Meier, C. Galeano, I. Katsounaros, J. Witte, H. J. Bongard, A. A. Topalov, C. Baldizzone, S. Mezzavilla, F. Sch??th, and K. J. J. Mayrhofer, "Design criteria for stable Pt/C fuel cell catalysts," *Beilstein Journal of Nanotechnology*, vol. 5, no. 1, pp. 44–67, 2014.
- [205] T. Binninger, R. Mohamed, K. Waltar, E. Fabbri, P. Levecque, R. K??tz, and T. J. Schmidt, "Thermodynamic explanation of the universal correlation between oxygen evolution activity and corrosion of oxide catalysts," *Scientific Reports*, vol. 5, no. 1, p. 12167, 2015.
- [206] C. Sp??ri, J. T. H. Kwan, A. Bonakdarpour, D. P. Wilkinson, and P. Strasser, "The Stability Challenges of Oxygen Evolving Catalysts: Towards a Common Fundamental Understanding and Mitigation of Catalyst Degradation," *Angewandte Chemie - International Edition*, vol. 56, no. 22, pp. 5994–6021, 2017.
- [207] H. Silva, M. G. Nielsen, E. M. Fiordaliso, C. D. Damsgaard, C. Gundlach, T. Kasama, I. B. Chorkendorff, and D. Chakraborty, "Synthesis and characterization of Fe-Ni/ χ -Al₂O₃ egg-shell catalyst for H₂ generation by ammonia decomposition," *Applied Catalysis A: General*, vol. 505, pp. 548–556, 2015.
- [208] S. W. Boettcher, "ACS Energy Letters: Elevating Solar Fuels and Electrocatalysis Research," *ACS Energy Letters*, no. 5, pp. 920–921.

- [209] F. Song and X. Hu, “Exfoliation of layered double hydroxides for enhanced oxygen evolution catalysis,” *Nature Communications*, vol. 5, pp. 1–9, 2014.
- [210] M. Gong, Y. Li, H. Wang, Y. Liang, J. Z. Wu, J. Zhou, J. Wang, T. Regier, F. Wei, and H. Dai, “An advanced Ni-Fe layered double hydroxide electrocatalyst for water oxidation,” *Journal of the American Chemical Society*, vol. 135, no. 23, pp. 8452–8455, 2013.
- [211] X. Long, J. Li, S. Xiao, K. Yan, Z. Wang, H. Chen, and S. Yang, “A strongly coupled graphene and FeNi double hydroxide hybrid as an excellent electrocatalyst for the oxygen evolution reaction,” *Angewandte Chemie - International Edition*, vol. 53, no. 29, pp. 7584–7588, 2014.
- [212] K. W. Lux and E. J. Cairns, “Lanthanide–Platinum Intermetallic Compounds as Anode Electrocatalysts for Direct Ethanol PEM Fuel Cells,” *Journal of The Electrochemical Society*, vol. 153, no. 6, p. A1132, 2006.
- [213] D. R. Lide, *CRC Handbook of Chemistry and Physics*. CRC Press, 2005.
- [214] C. Yan and M. J. Wagner, “Air and Water Stable Gold Coated Gadolinium Metal Nanocrystals,” *Nano letters*, vol. 13, no. 6, pp. 2611–2614, 2013.
- [215] M. J. Wagner, “Inorganic Nanomaterials Synthesis Using Alkalide Reduction,” in *Nanomaterials: Inorganic and Bioinorganic Perspectives* (R. A. Lukehart, C. M., Scott, ed.), p. 357, Chichester, UK: John Wiley & Sons, Ltd, 2008.
- [216] B. P. Knudsen, *Synthesis of Platinum Rare Earth Alloy Catalysts for Fuel Cells PhD dissertation by*. PhD thesis, Technical University of Denmark, 2016.
- [217] C. M. Pedersen, *New catalysts for miniaturized methanol fuel cells*. PhD thesis, Technical University of Denmark, 2015.
- [218] L. K. T.B. Massalski, H. Okamoto, P.R. Subramanian, ed., *Binary Alloy Phase Diagrams*. ASM International, 2nd editio ed., 1990.
- [219] V. B. Compton and B. T. Matthias, “Laves phase compounds of rare earths and hafnium with noble metals,” *Acta Crystallographica*, vol. 12, no. 9, pp. 651–654, 1959.

-
- [220] D. Li, N. Poudyal, V. Nandwana, Z. Jin, K. Elkins, and J. P. Liu, "Hard magnetic FePt nanoparticles by salt-matrix annealing," *Journal of Applied Physics*, vol. 99, no. 8, pp. 100–102, 2006.
- [221] K. Elkins, D. Li, N. Poudyal, V. Nandwana, Z. Jin, K. Chen, and J. P. Liu, "Monodisperse face-centred tetragonal FePt nanoparticles with giant coercivity," *Journal of Physics D: Applied Physics*, vol. 38, no. 14, pp. 2306–2309, 2005.
- [222] Q. E. Barberis and D. Davidov, "Electron-Spin-Resonance and Lattice-Parameter Study of Cerium Cubic Laves-Phase Compounds: Evidence for Intermediate-Valence State," *Journal of Physical Review Letters*, vol. 45, no. 24, pp. 1966–1970, 1980.
- [223] J. Zhang, M. B. Vukmirovic, Y. Xu, M. Mavrikakis, and R. R. Adzic, "Controlling the Catalytic Activity of Platinum- Monolayer Electrocatalysts for Oxygen Reduction with Different Substrates," *Angew. Chem., Int. Ed.*, vol. 117, pp. 2170 –2173, 2005.
- [224] H. L. Xin, J. A. Mundy, Z. Liu, R. Cabezas, R. Hovden, L. F. Kourkoutis, J. Zhang, N. P. Subramanian, R. Makharia, F. T. Wagner, and D. A. Muller, "Atomic-resolution spectroscopic imaging of ensembles of nanocatalyst particles across the life of a fuel cell," *Nano Letters*, vol. 12, no. 1, pp. 490–497, 2012.
- [225] P. Malacrida, M. Escudero-Escribano, A. Verdaguer-Casadevall, I. E. L. Stephens, and I. Chorkendorff, "Enhanced activity and stability of Pt–La and Pt–Ce alloys for oxygen electroreduction: the elucidation of the active surface phase," *Journal of Materials Chemistry A*, vol. 2, no. 12, p. 4234, 2014.
- [226] A. A. Permyakova, B. Han, J. O. Jensen, N. J. Bjerrum, and Y. Shao-Horn, "Pt - Si bifunctional surfaces for CO and methanol electro-oxidation," *Journal of Physical Chemistry C*, vol. 119, no. 15, pp. 8023–8031, 2015.

Appendices

Supplementary Materials Chapter 4

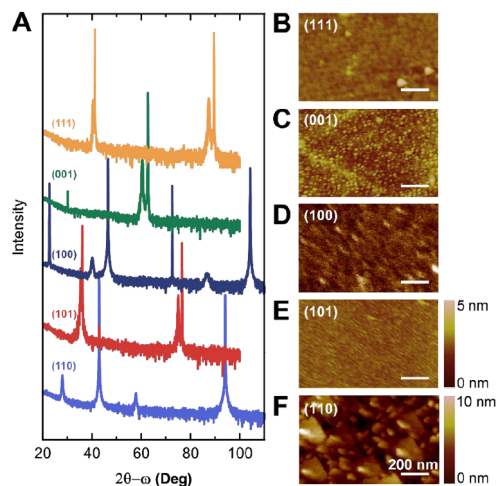


Figure A.1: (A) X-ray diffraction spectra of (111), (001), (100), (101) and (110) RuO₂ oriented thin films. (B-F) Atomic force microscopy image of representative samples after deposition. (B) (111), (C) (001), (D) (100), (E) (101), (F) (110) RuO₂. The scale bar is 200 nm for all images, and contrast scale is 0 to 5 nm for (B-E). Taken from [193]

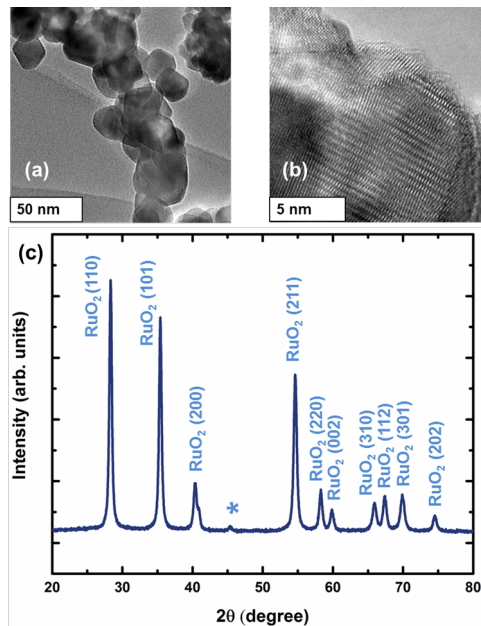


Figure A.2: (a-b) Transmission electron microscopy images and c) X-ray diffraction spectrum of commercial RuO₂ particles (Sigma-Aldrich). Courtesy of Binghong Han.

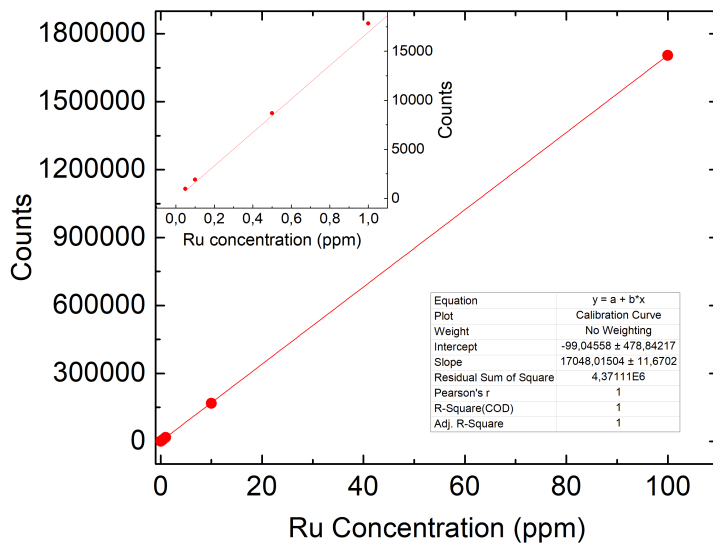


Figure A.3: Representative calibration curve for Ru quantification in 0.05 M H₂SO₄ using inductively-coupled plasma mass spectrometry

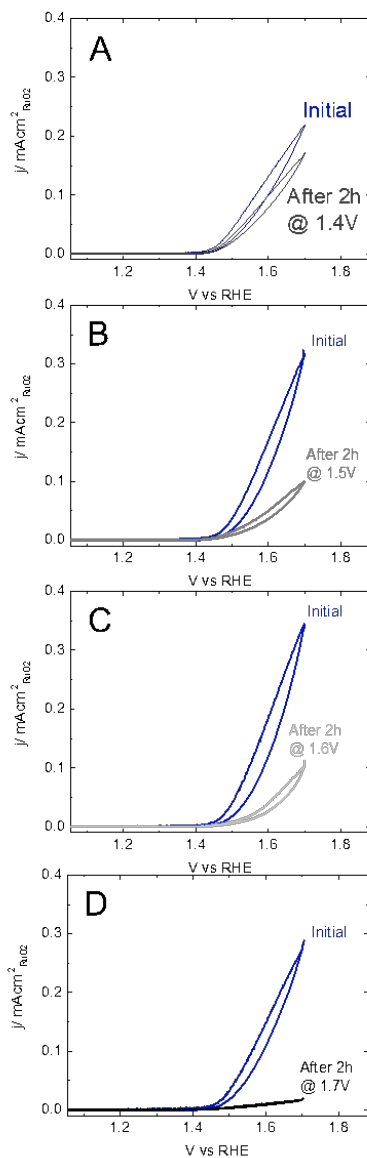


Figure A.4: Characteristic cyclic voltammetry at 10 mV/s in 0.05 M HV_2SOV_4 before (blue) and after (grey) stability test at (A) 1.4 (B), 1.5 (C), 1.6 and (D) 1.7 V_{RHE}

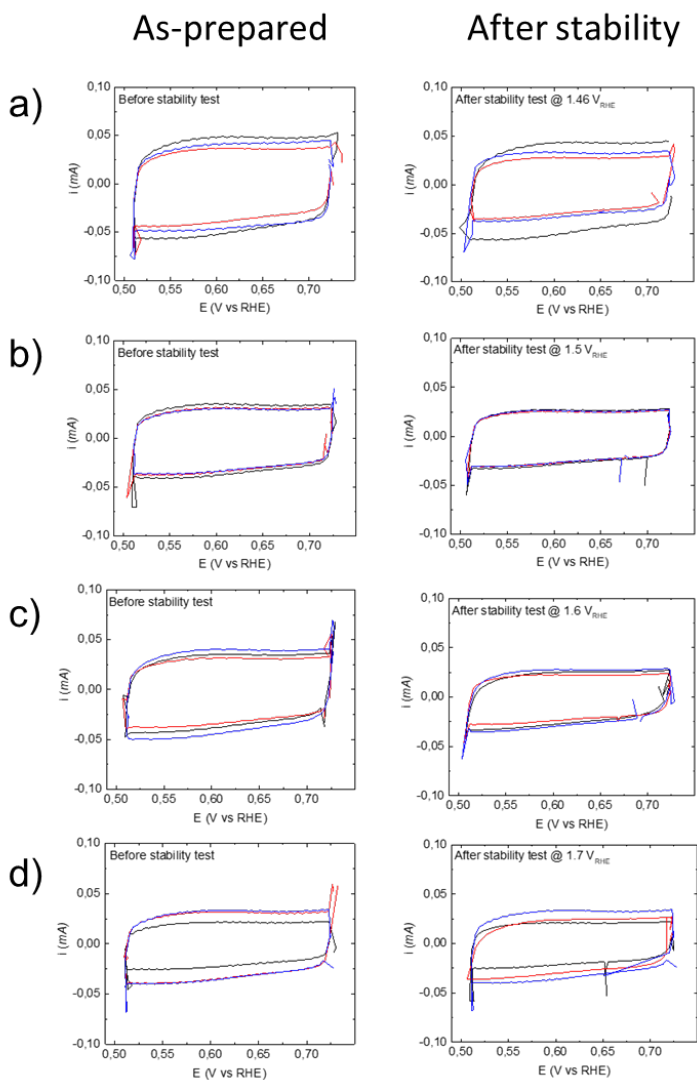


Figure A.5: Capacitance measurements of the RuO₂ nanoparticles before and after stability test at a) 1.46 V_{RHE} , b) 1.5 V_{RHE} , c) 1.6 V_{RHE} and d) 1.7 V_{RHE} . The capacitance was recorded at 100 mV/s in 0.05 M H₂SO₄

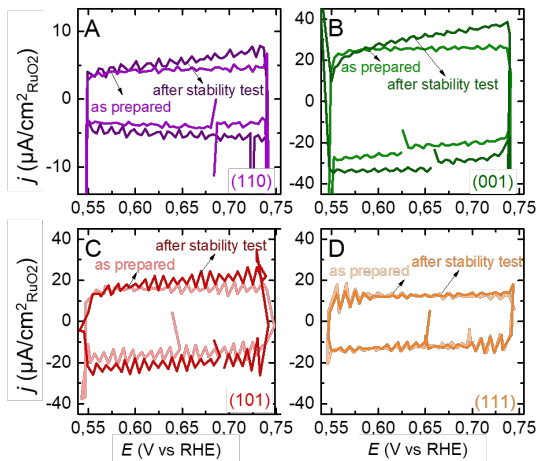


Figure A.6: Capacitance measurement of the (110), (001), (101) and (111) RuO₂ well-defined surfaces at 100 mV/s in 0.05 M H₂SO₄ before and after the first stability measurement at 1.6 v_{RHE}

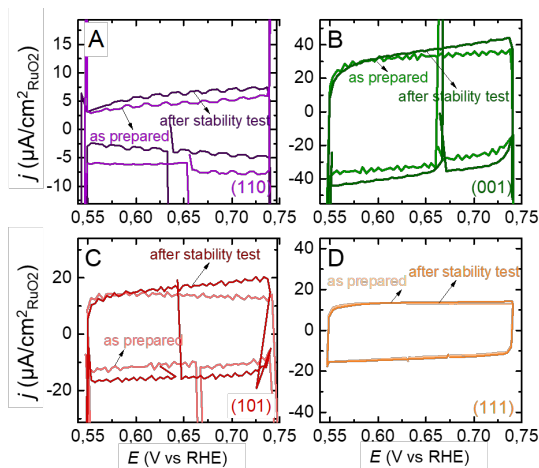


Figure A.7: Capacitance measurement of the (110), (001), (101) and (111) RuO₂ well-defined surfaces at 100 mV/s in 0.05 M H₂SO₄ before and after the second stability measurement at 1.6 v_{RHE}

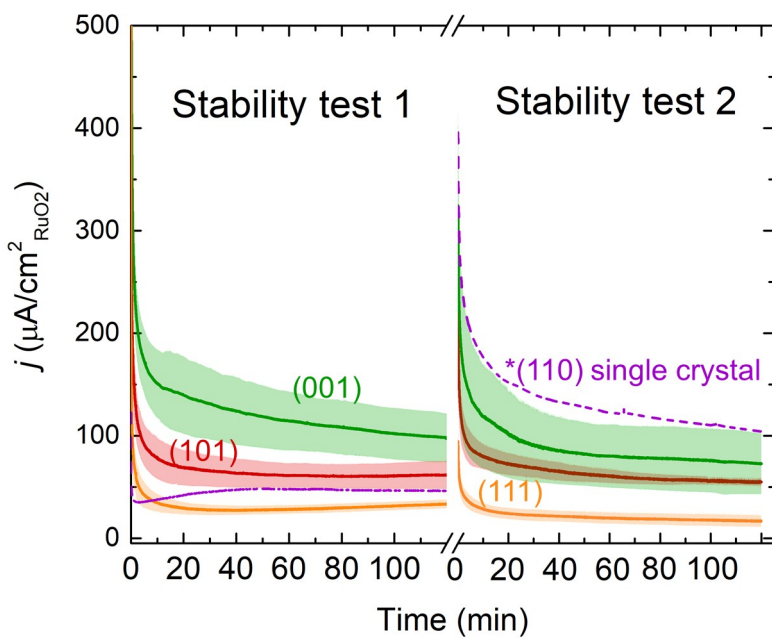


Figure A.8: Two-hour potentiostatic measurements at $1.6 V_{RHE}$ in $0.05 \text{ M H}_2\text{SO}_4$ from stability test 1 (left) and stability test 2 (right) for the RuO_2 (111), (101), (110) and (001) surfaces.

Supplementary Materials Chapter 5

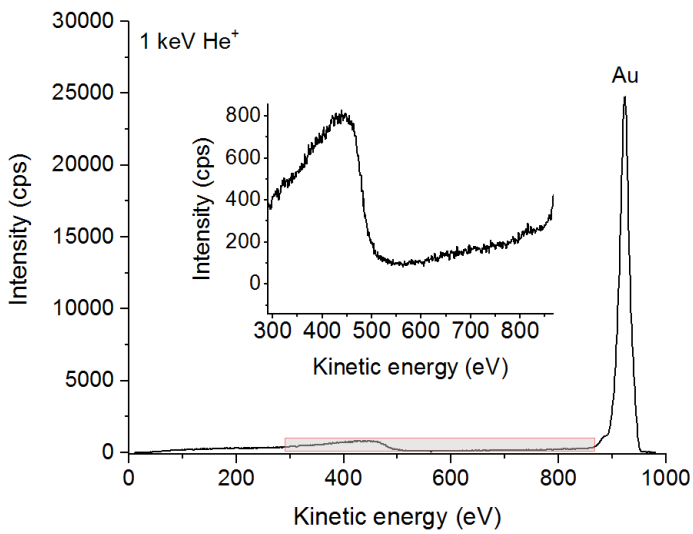


Figure B.1: Low-energy ion scattering spectra of the bare Au substrate

Mass transport model of a NiFe nanoparticle

The Nernst-Planck mass transport equation reads

$$\vec{j}_i = -D_i \nabla c_i - z_i \mu_i c_i \nabla U, \quad (1)$$

Where j_i is flux of species i (mol/(m²s)), c_i is its concentration (mol/m³), D_i its diffusion constant (m²/s, z_i its charge number, and μ_i its electronic mobility (m²/Vs)). U is the electrical potential (V). The first term on the right side of Equation 1 is due to diffusive transport down a concentration gradient and the second term is due to migration down an electrical potential energy gradient.

D_i and μ_i are always related by the Stokes-Einstein equation,

$$\mu_i = \frac{|z_i| \mathcal{F}}{RT} D_i, \quad (2)$$

where \mathcal{F} is Faraday's constant (C/mol), R is the gas constant (J/(molK)), and T is the absolute temperature (K).

The charge flux is the sum of the flux of each species times its charge number. For a single NP on a substrate with hemispherical symmetry in steady state, the charge flux integrated over a shell of any radius is related to the electrical current through that nanoparticle.

$$\vec{j} = \sum_i z_i \vec{j}_i = \frac{I_0}{2\pi r^2 \mathcal{F}} \hat{r} = \frac{I}{2\pi r^2 \mathcal{F} N} \hat{r} \quad (3)$$

Here, I_0 is the current through an individual nanoparticle (A), I is the total current (I), and N is the number of nanoparticles.

In 0.1 M KOH, there are two species of appreciable concentration, K⁺ and OH⁻. Charge neutrality demands that their concentrations are equal at any point.

$$c_{\text{OH}} = c_{\text{K}} = c \quad (4)$$

During the oxygen evolution reaction, K⁺ is neither consumed nor destroyed. Setting its flux to zero in Equation 1 results in a simple relationship between the concentration, the concentration gradient, and the electrical potential gradient.

$$\vec{j}_{\text{K}} = -D_{\text{K}} \nabla c - \mu_{\text{K}} c \nabla U = 0, \text{ or} \quad (5)$$

$$\nabla U = -\frac{D_{\text{K}}}{\mu_{\text{K}}} \frac{\nabla c}{c} = -\frac{RT}{\mathcal{F}} \frac{\nabla c}{c} \quad (6)$$

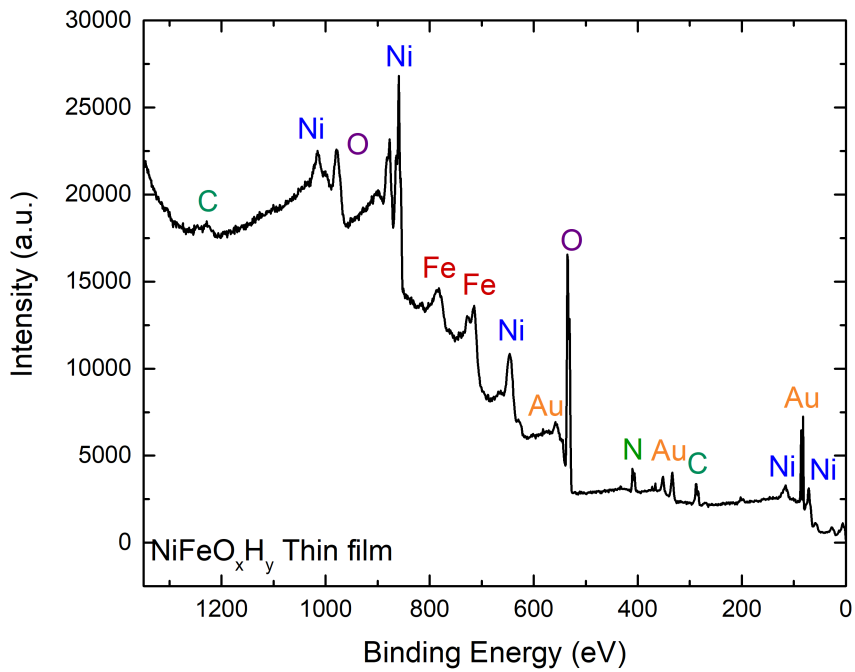
Meanwhile, during OER, OH is consumed at the electrode (or, equivalently, neutralized by H⁺ produced at the electrode) at a rate equivalent in magnitude to the charge flux. In OER, the current, and thus the charge flux, originating at the nanoparticle and moving out radially, is positive, while the OH⁻ flux is towards the electrode.

$$\vec{j}_{\text{OH}} = -D_{\text{OH}} \nabla c + \mu_{\text{OH}} c \nabla U = -\vec{j} \quad (7)$$

Substituting Equation 6 into Equation 7, using 2, and $D = D_{\text{OH}^-}$, yields

$$\vec{j} = 2D \nabla c \quad (8)$$

Remarkably, the transport of OH⁻ is due in equal parts to the concentration gradient and the potential gradient, while for K⁺ the two driving forces exactly cancel. Physics is cool.



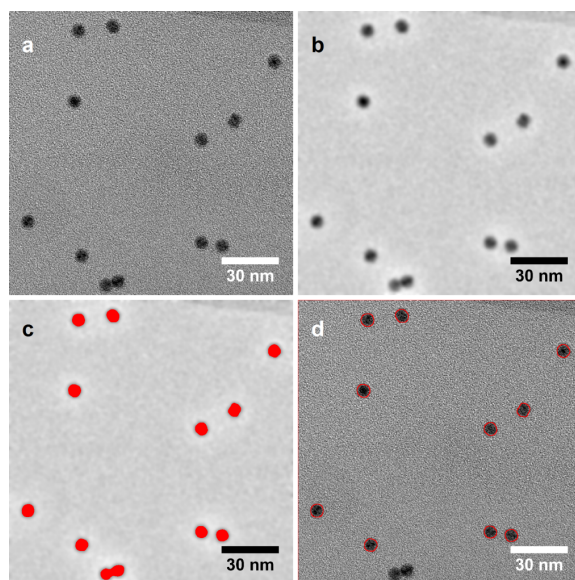


Figure B.3: Example of the determination of particle size distribution taken for 6.7 nm NiFe particles. a: original image, b: after band-pass filtering, c: after thresholding and d: the outlines of the found particles overlaid on the original image.

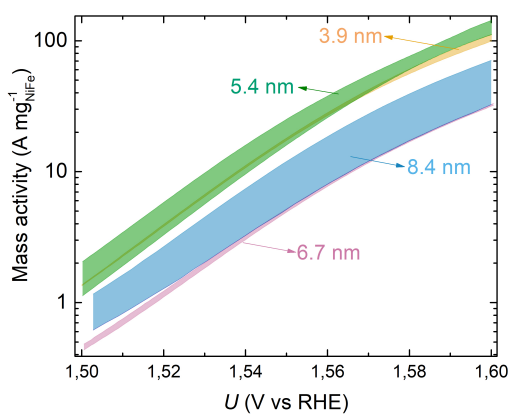


Figure B.4: Polarization curves of 3.9 nm, 5.4 nm, 6.7 nm and 8.4 nm NiFeO_xH_y taken from 10 mV/s cyclic voltammeteries in 1 M KOH at 1,600 rpm. The average current was measured over three independent samples.

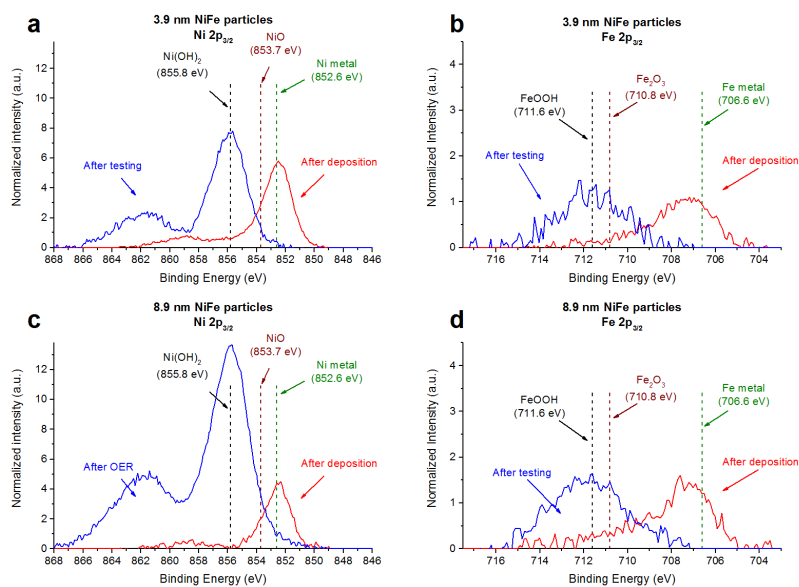


Figure B.5: X-ray photoelectron spectroscopy of the Ni 2p and Fe 2p region of the as-prepared (blue) and after OER (red) 3.9 nm (smallest size) and 8.4 nm (biggest size) NiFeO_xH_y nanoparticles

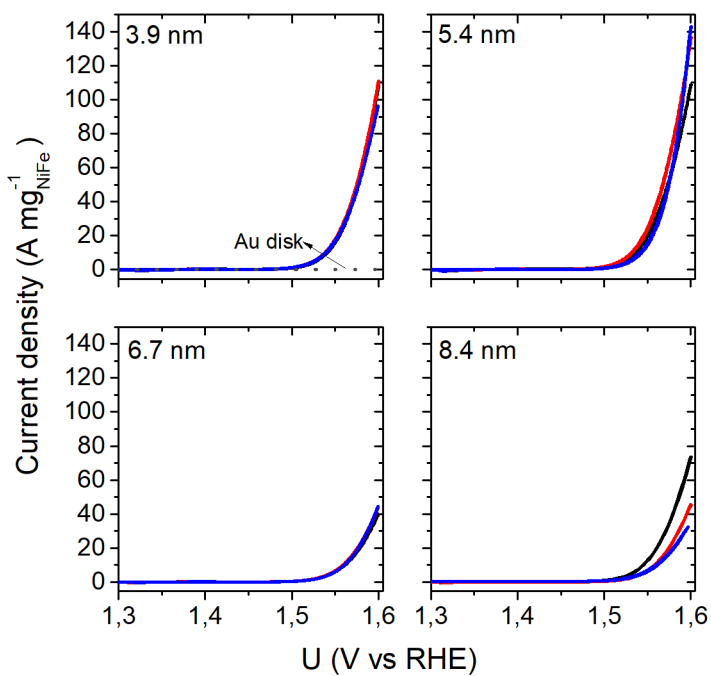


Figure B.6: Cyclic voltammeteries of the 3.9 nm, 5.4 nm, 6.7 nm and 8.4 nm as-prepared NiFeO_xH_y nanoparticles (3 samples each) at 10 mV/s on Au disks in N₂-saturated 1 M KOH at 1,600 rpm and iR-corrected.

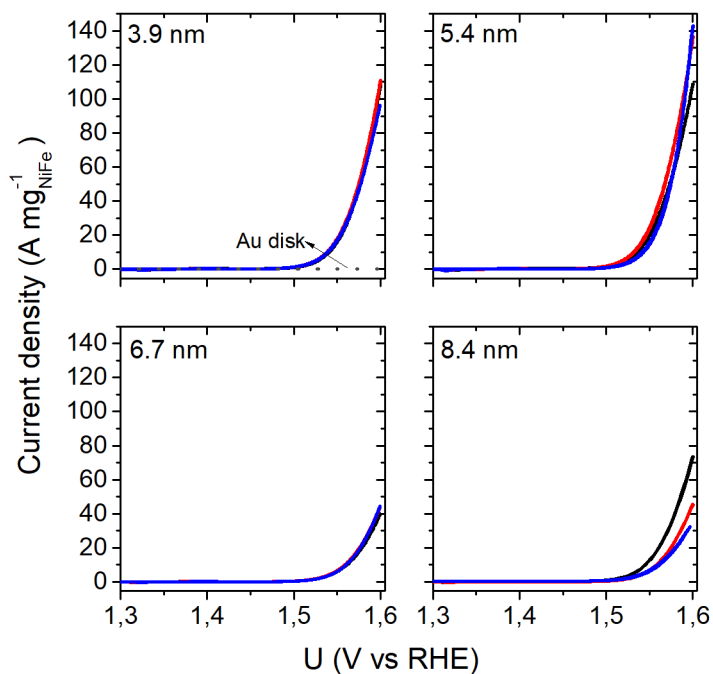


Figure B.7: Cyclic voltammeteries of the 3.9 nm, 5.4 nm, 6.7 nm and 8.4 nm NiFeO_xH_y nanoparticles (3 samples each) at 10 mV/s on Au disks in N₂-saturated 1 M KOH at 1,600 rpm and iR-corrected. The CVs were recorded after 2 hours at 1.6 V_{RHE} in 1 M KOH at 1,600 rpm.

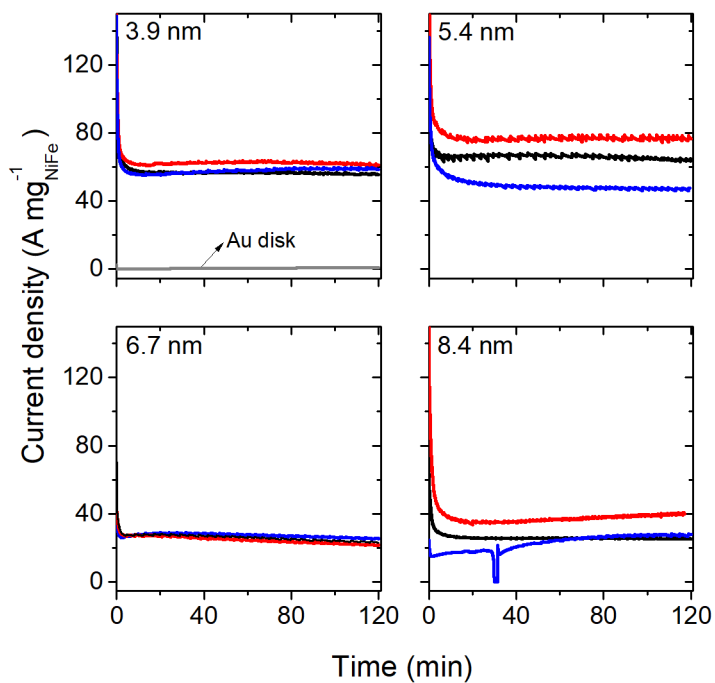


Figure B.8: Chronoamperometry of the NiFeO_xH_y nanoparticles at 1.6 V_{RHE} for 2h in 1 M KOH in N_2 -saturated at 1,600 rpm. The catalytic activity of a gold disk, the substrate, is also plotted (dotted line) to show its minor contribution to the total catalytic activity.

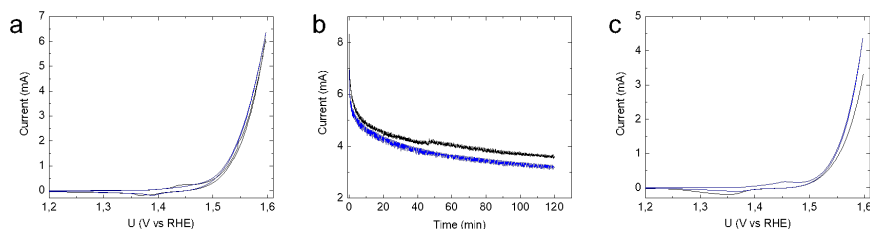


Figure B.9: a) Cyclic voltammeteries (CVs) of the as-prepared electrodeposited NiFeO_xH_y thin films at 10 mV/s b) Chronoamperometry at 1.6 V_{RHE} for 2h c) CVs after OER at 10 mV/s. All electrochemical measurements were performed in N_2 -saturated 1 M KOH at 1,600 rpm and iR-corrected.

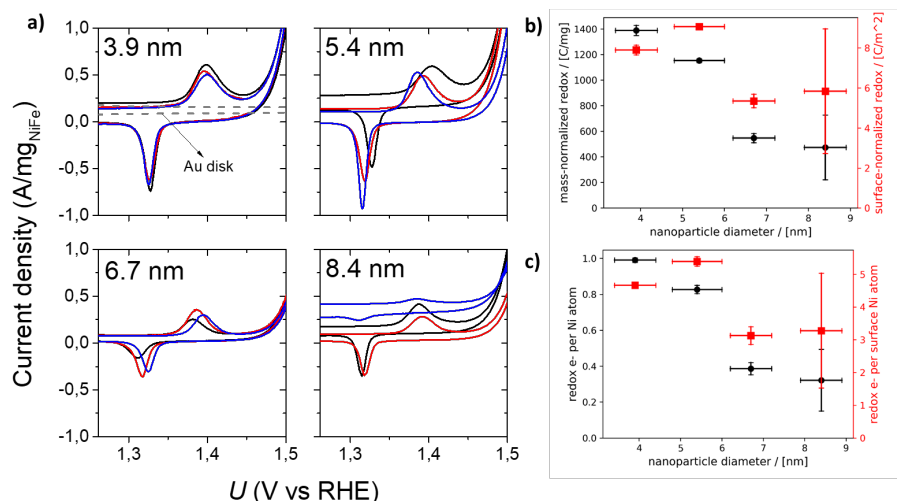


Figure B.10: (a) Cyclic voltammeteries with zoom on the $\text{Ni}^{2+}/\text{Ni}^{3+/4+}$ redox feature all nanoparticle samples. (b) Area of the Ni reduction peak normalized to mass loading (circles, left y-axis) and to nanoparticle surface area estimated from current deposition (squares, right y-axis). (c) Number of electrons transferred during Ni reduction wave normalized to the total loading of Ni atoms (circles, right y-axis) and to the calculated number of surface Ni atoms (squares, right y-axis). Vertical error bars represent the standard deviation between three samples.

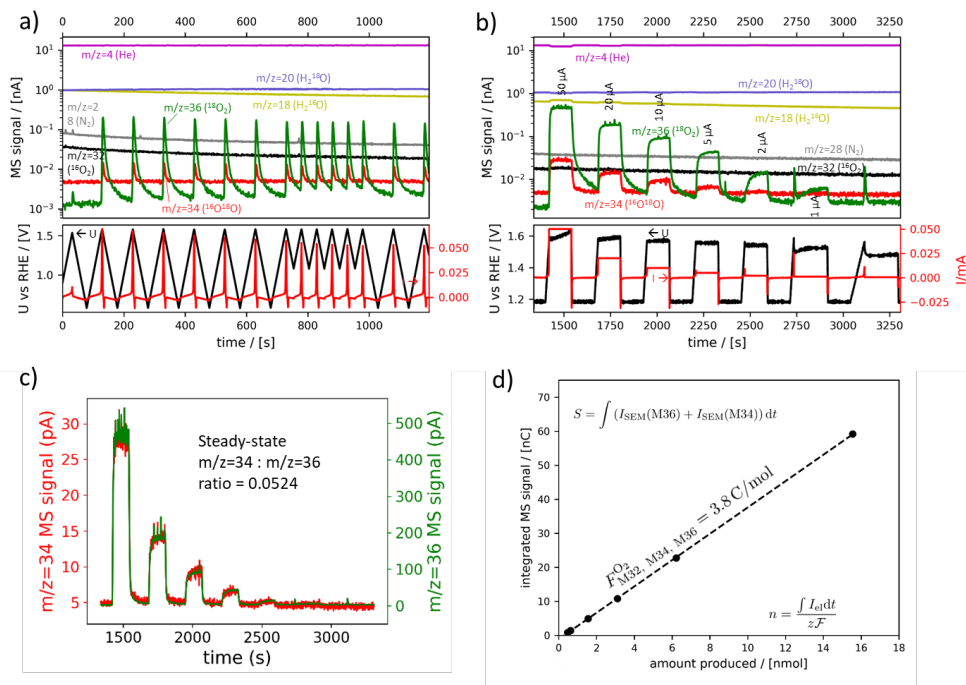


Figure B.11: (a) The first half of the raw data, cyclic voltammetry, as an EC-MS plot. Raw QMS signals are plotted in the top frame and electrochemical potential (black) and current (red) are plotted in the bottom frame. (b) The second half of the raw data, constant-current steps for calibration, as an EC-MS plot. The $m/z=34$ and $m/z=36$ signals are replotted in (c) on two linear axes, to show that the ratio is constant. (d) The results of the calibration showing linear response

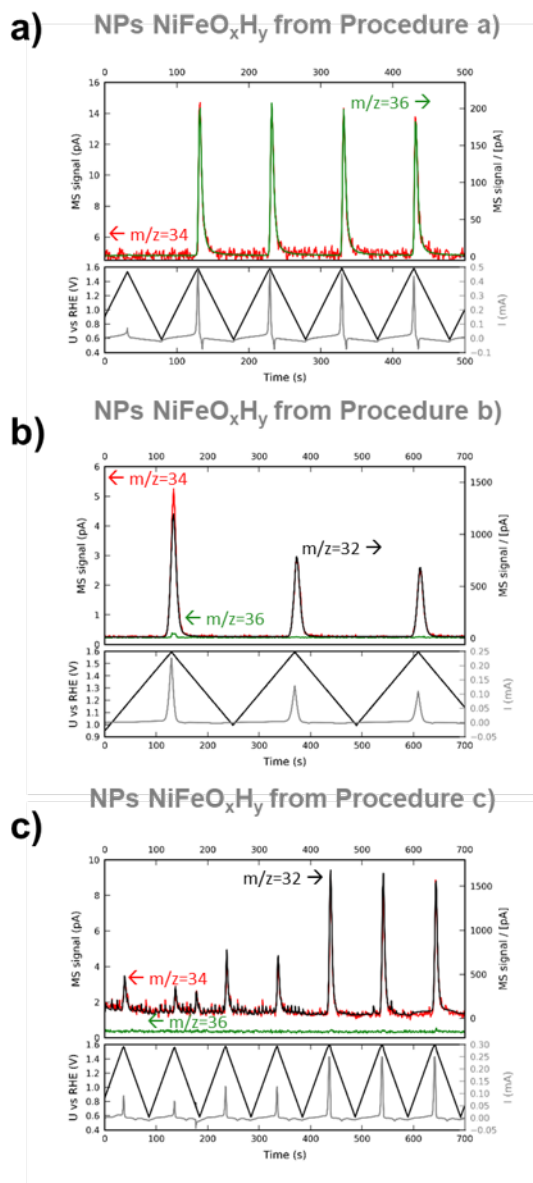


Figure B.12: Comparison of EC-MS results from isotope experiments. EC-MS results for isotope experiments on NiFeO_xH_y nanoparticles from procedure *a*, *b* and *c*.

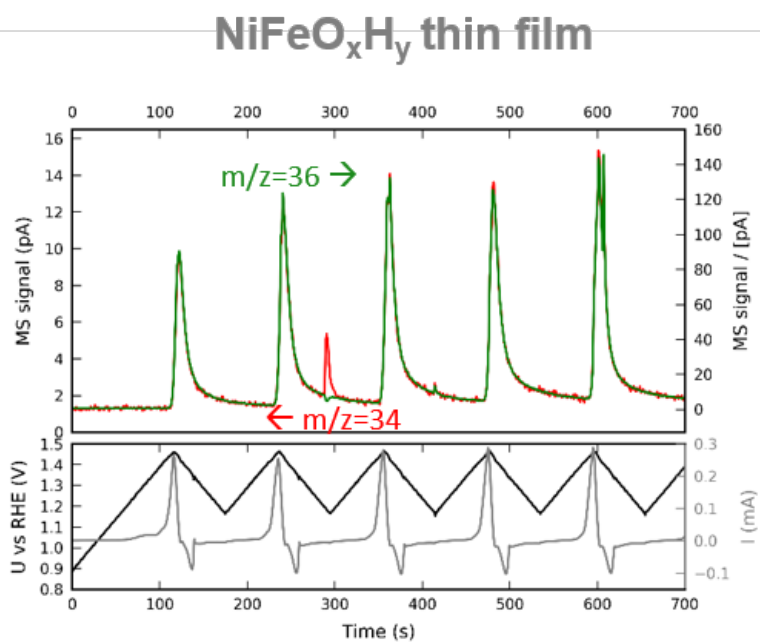


Figure B.13: EC-MS results for isotope experiments on an NiFeO_xH_y thin film obtained from electrodeposition.

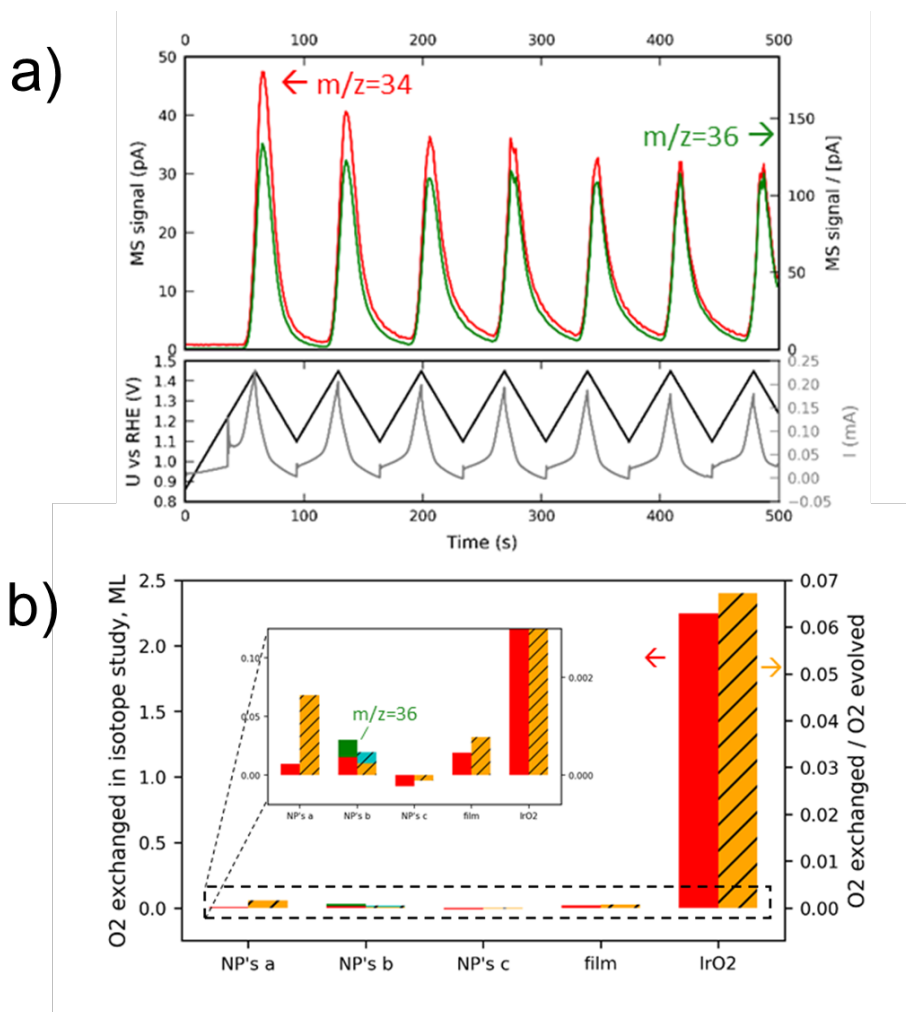


Figure B.14: a) EC-MS results for isotope experiments on an IrO₂ thin film produced by thermal decomposition. The experiment starts with the first scan, from open-circuit potential. The majority O₂ isotope produced by the electrolyte is plotted on the right y-axis and the minority O₂ isotope(s) on the left y-axis. m/z=32 is omitted as a minority isotope since the background is too high. b) The excess minority isotope is quantified and normalized to the number of surface atoms in the catalyst (solid bars, left y-axis) and the total O₂ evolved during the part of the experiment shown here (hashed bars, right y-axis).

Supplementary Materials Chapter 6

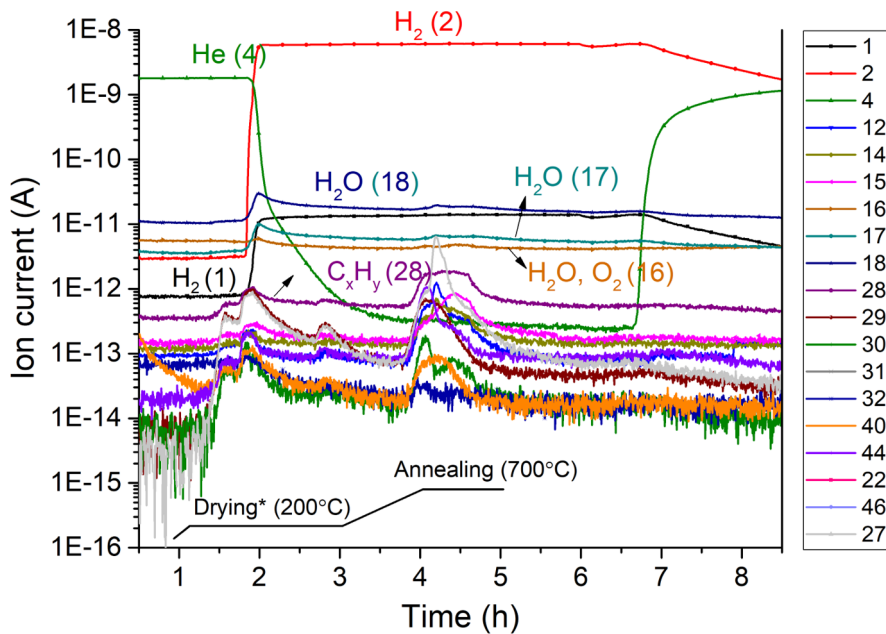


Figure C.1: Full mass-spectrometer data recorded during the annealing process of the cyanide reduction method

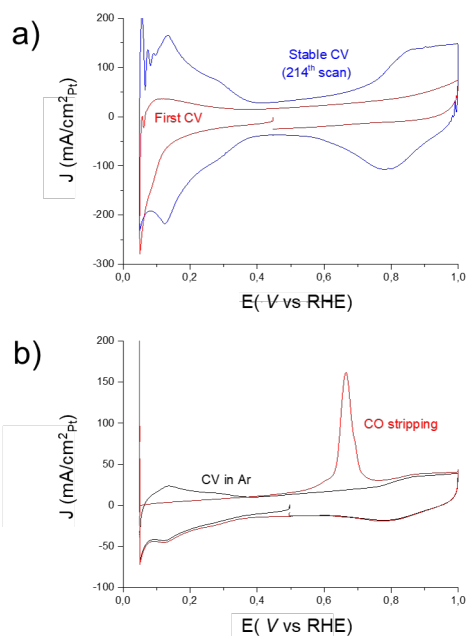


Figure C.2: a) Cyclic voltammery recorded at 200 mV/s in N₂-saturated 0.1 M HClO₄ after the first and 214th cycle, and b) CO stripping experiment at 10 mV/s. The electrochemical characterization was performed on Pt_xY (800°C) at 1,600 rpm.

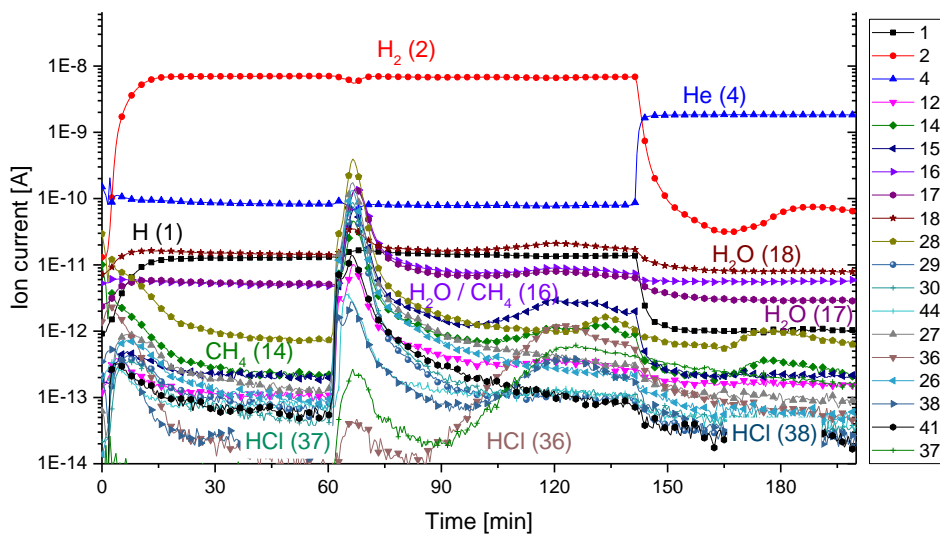


Figure C.3: Full mass-spectrometer data recorded during the 60 min annealing process of the high temperature synthesis

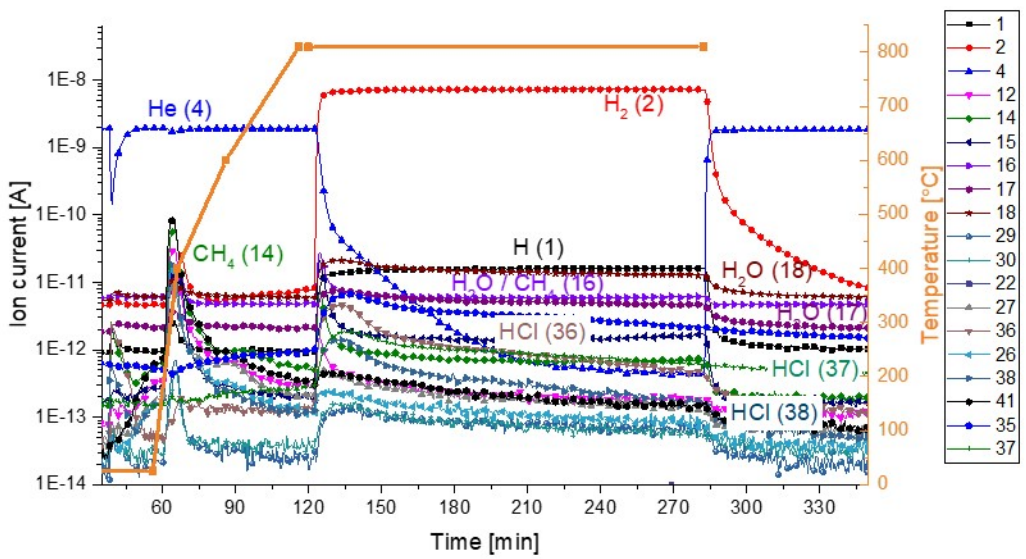


Figure C.4: Full mass-spectrometer data recorded during the 360 min annealing process of the high temperature synthesis



Appended Articles

Paper I

**Scalable Synthesis of Carbon-Supported
Platinum-Lanthanide and Rare Earth Alloys for
Oxygen Reduction**

Scalable Synthesis of Carbon-Supported Platinum–Lanthanide and –Rare-Earth Alloys for Oxygen Reduction

Claudie Roy,[†] Brian P. Knudsen,[†] Christoffer M. Pedersen,^{†,‡} Amado Velázquez-Palenzuela,^{†,‡} Leif H. Christensen,[‡] Christian Danvad Damsgaard,[§] Ifan E. L. Stephens,^{†,||} and Ib Chorkendorff^{*,†,||}

[†]Surface Physics and Catalysis, Department of Physics, Technical University of Denmark, DK-2800 Kgs. Lyngby, Denmark

[‡]Center for Nano- and Micro technology, Danish Technological Institute (DTI), Gregersensvej, DK-2630 Taastrup, Denmark

[§]Center for Electron Nanoscopy, Department of Physics, Technical University of Denmark, DK-2800 Kgs. Lyngby, Denmark

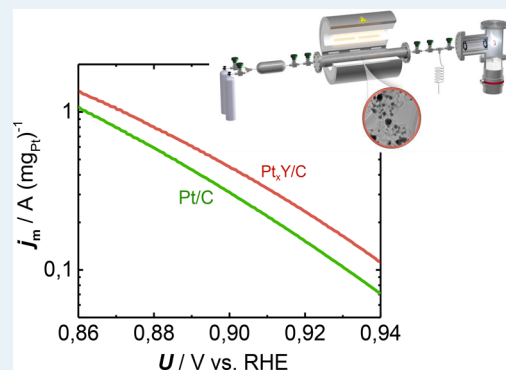
^{||}Department of Materials, Imperial College London, London SW7 2AZ, United Kingdom

Supporting Information

ABSTRACT: Platinum–rare-earth alloys have proven to be both active and stable under accelerated stability tests in their bulk polycrystalline form. However, a scalable method for the synthesis of a high-surface-area supported catalyst of these alloys has so far not been presented. Herein we discuss the thermodynamics relevant for the reduction conditions of the rare earths to form alloys with platinum. We show how the tolerance for water and oxygen severely limits the synthesis parameters and how under certain conditions the thermal reduction of YCl_3 with H_2 is possible from 500 °C. From the insight gained, we synthesized a $\text{Pt}_x\text{Y}/\text{C}$ catalyst by modifying a Pt/C catalyst and confirmed alloy formation by both X-ray diffraction and X-ray photoelectron spectroscopy measurements. These reveal crystalline intermetallic phases and the metallic state of yttrium. Without any optimization of the method, the catalyst has an improved mass activity in comparison to the unmodified catalyst, proving the viability of the method.

Initial work based on thermodynamic equilibrium calculations on reduction time show promise in controlling the phase formed by tuning the parameters of time, temperature, and gas composition.

KEYWORDS: synthesis, rare earths, platinum, alloy, oxygen reduction reaction, proton exchange membrane fuel cell, nanoparticles



INTRODUCTION

Proton exchange membrane fuel cells (PEMFCs) are among the most promising renewable energy technologies, capable of producing electricity through electrochemical reactions of hydrogen and oxygen fuels at near room temperature (<80 °C) operating conditions.^{1–4} However, the high platinum loading at the cathode side strongly limits the expansion of hydrogen vehicles on the market.⁵ Over the years, the loading at the anode could be reduced to 0.05 mg cm^{-2} . The major kinetic losses at the cathode side still result in a high loading of Pt: i.e., 0.4 mg cm^{-2} of Pt in a state of the art fuel cell.⁴ One of the tools available for improving the catalytic activity is to optimize the bond strength of the oxygen reduction intermediate (ORR)^{6,7} to the catalyst's active sites. Among the materials studied, the alloys of Pt with late transition metals such as Ni and Co have demonstrated among the highest catalytic activities reported.^{8–10} One of the pillars that made fuel cell electric vehicles (FCEVs) possible is the commercial use of a Pt–Co alloy that significantly increases the mass activity of the catalyst in comparison to previous-generation vehicles.¹¹ When they are implemented in fuel cells, alloys of Pt with late transition metals tend to dealloy over time.^{12–14} The less noble metal dissolves into the acidic electrolytes, first from

the surface and then from the bulk in the long term.^{12,15} Even so, there have been numerous recent studies that report novel forms of Pt–Ni based catalysts with outstanding activity and stability in accelerated degradation tests.^{8,10,16,17}

Another group of alloys pioneered by our group are those of Pt and lanthanide and/or rare-earth elements.^{18–20} It was suggested that the alloying energy, or the negative enthalpy of formation, could also be used as a descriptor for stability against dissolution for the Pt-based catalysts. These alloys, such as Pt_xY and Pt_xGd , have been shown to be both active and stable in polycrystalline,²¹ single-crystal,^{22,23} and nanoparticulate forms obtained from magnetron sputtering,^{24,25} with the increase in activity originating from a compressed Pt overlayer.²⁰ The more reactive solute metal will tend to dissolve in the acid electrolyte of a PEMFC, resulting in the formation of a thick and strained Pt overlayer.²⁰ The tradeoff between this strained structure and the optimization of surface to bulk ratio obtained with small particle size explains the observed maximum mass activity of nanoparticles of Pt_xY and Pt_xGd at around 8–9 nm.²⁴

Received: November 21, 2017

Revised: January 10, 2018

Published: January 17, 2018

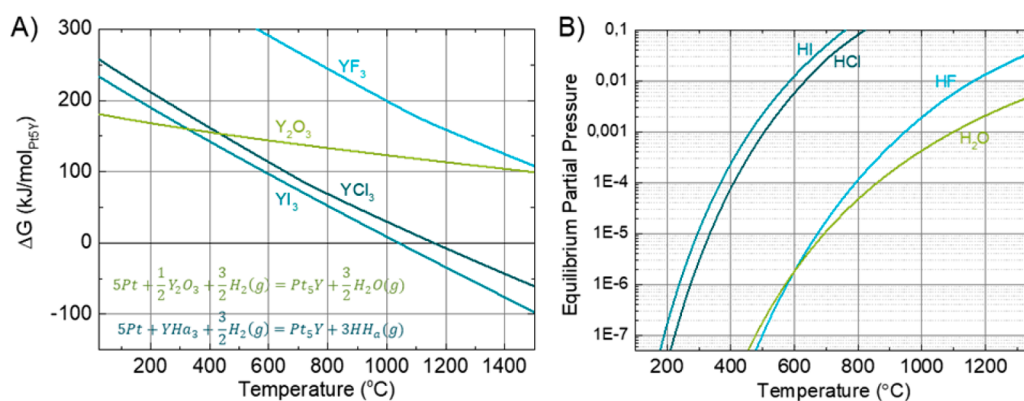


Figure 1. (A) Calculated variation in Gibbs free energy for forming Pt₅Y by annealing Pt assuming 1 bar of H₂ with Y₂O₃, YF₃, YCl₃, and YI₃. (B) Respective equilibrium partial pressures of gas products generated by the alloying process.

Technological limitations on the magnetron sputtering, i.e. the slow deposition rate and the production limited to a few nanograms, prohibit scale-up production of mass-selected nanoparticles of Pt_xY and/or Pt_xGd and impede their implementation into membrane electrode assembly. For this, a chemical synthesis technique scalable up to the gram scale is needed. Chemical synthesis including lanthanide and/or rare-earth elements is a real challenge, partially because of the oxophilicity of these compounds. The significant difference in reduction potential of Pt²⁺/Pt being +1.18 V vs those of the rare earths such as Y³⁺/Y at −2.37 V²⁶ is also an important obstacle in the alloying process.

Many have attempted to chemically synthesize these nanoparticles^{27–33} but without showing any real evidence of Pt–Y alloy formation: i.e., an X-ray diffraction spectrum showing only Pt peaks and/or no X-ray photoelectron spectroscopic analysis of the Y 3d region. Kanady et al. are the first, to our knowledge, that showed clear the formation of intermetallic Pt₃Y nanoparticles. In that work, molten borohydride was both the reducing agent and reaction medium.³⁴ Unfortunately, the catalyst was not tested for the electrochemical reduction of oxygen, and the activity cannot be compared to that reported by our model study.

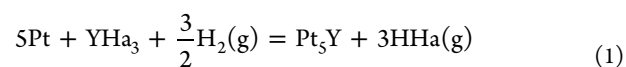
Before we were able to obtain Pt_xY/C via a thermal process, we tried other different types of synthesis methods. It was reported that it is possible to synthesize gold-coated gadolinium nanoparticles by alkali reduction.³⁵ With the ultimate goal of replacing Au with Pt, we reproduced the protocol reported by Yan et al.³⁵ Even after many attempts, we observed that only a small portion of Gd was actually reduced and incorporated into the gold nanoparticles, while most of the core was made of Si coming from the glassware. We also investigated the cyanide reduction techniques reported by Lux and Cairns.³⁶ In their protocol, they used Pt(CN)₂ and Ce(NO₃)₃·6H₂O as precursors that they mixed in water and annealed in H₂ to obtain a Pt_xCe alloy. By following the same procedure but substituting a Ce- with a Y-based precursor, we successfully obtained Pt_xY powder. Unfortunately, we did not manage to optimize the powder to favor the formation of nanoparticles. In addition, the large production of Pt_xY alloy would certainly represent a safety concern, as HCN is one of the byproducts.

In this work, we have successfully scaled up the synthesis of the intermetallic alloys of Pt_xY nanoparticles supported on carbon on a gram scale. The alloy was obtained by annealing nanoparticles of Pt/C with YCl₃ under a hydrogen atmosphere.

We provide thermodynamic calculations of the thermal reduction of halide salts of the rare-earth metals by hydrogen that represent an important step forward the understanding of Pt–lanthanide and –rare-earth alloy formation. Using these calculations, it was also possible to predict the formation of the most active Pt_xY crystalline phase. The structures of all alloys have been confirmed by X-ray diffraction spectroscopy (XRD), X-ray photoelectron spectroscopy (XPS), and transmission electron microscopy (TEM) techniques. The catalyst was tested using a rotating disk electrode setup for the oxygen reduction reaction (ORR) in acid electrolyte. To our knowledge, this is the first time that a Pt_xY/C alloy synthesized on a gram scale has exhibited enhanced mass activity, in comparison to the commercially available supported Pt catalyst. The thermal synthesis method used for the synthesis lends itself to efficient control of the alloy phase formed and could be extended to other elements of the lanthanide and rare-earth family.

THEORETICAL CALCULATIONS

As mentioned above, the energy gained by the rare-earth elements upon alloying with Pt is close to 4 eV, which is much greater than that of the late transition metals, which only gain around 0.25 eV.¹⁹ However, the alloying energy gained by the rare earth and lanthanide elements when they form their respective oxide is close to 10 eV,²⁴ making the oxidation the favored reaction on contact with any oxidizing agent. In this work, we investigate alloy synthesis using thermal reduction under an H₂ atmosphere. We utilized the HSC Chemistry software package (version 6.1) developed by Outotec Technologies. The data related to Pt–rare-earth/lanthanide alloys were not part of the database and were extracted from experimental studies where oxide precursors were reduced thermally to alloy with Pt.^{37–40} An understanding of the reactivity of the rare-earth/lanthanide precursors and oxides is crucial for the synthesis of Pt alloys. Because of the great ORR activity obtained from model Pt_xY nanoparticles and thin films, we decided to start investigating that specific system. We have calculated the variation in Gibbs free energy for (1) the reduction of yttrium halides (YHa₃) and (2) yttrium oxide (Y₂O₃) to form Pt₅Y alloys. The reaction to form Pt₅Y from Pt metal and YHa₃ under an H₂ atmosphere is



and the reaction to reduce Y₂O₃ with Pt₅Y is

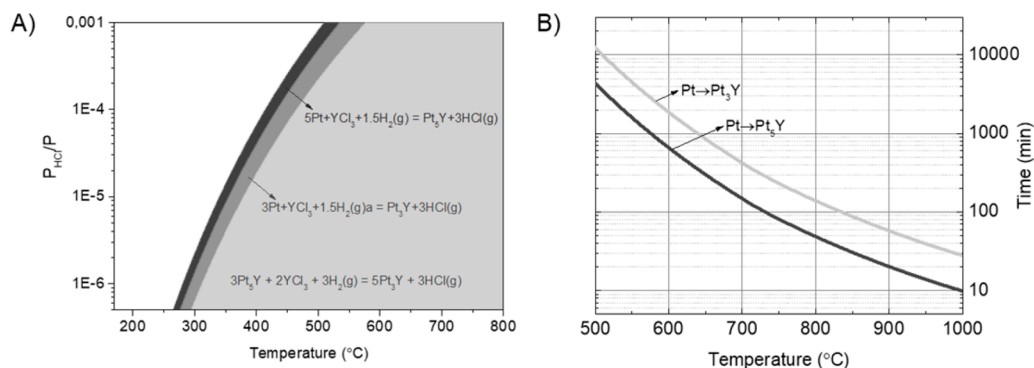
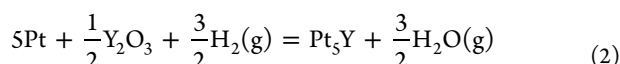


Figure 2. (A) Phase formation of Pt_3Y and Pt_5Y as a function of P_{HCl}/P and temperature. Insufficient data prevented us from calculating the phase formation of Pt_2Y . (B) Expected reaction time for 0.5 g of Pt in 10 mL/min 100% H_2 .



The determination of the change in Gibbs free energy (ΔG) for the Pt_5Y system obtained from Y_2O_3 and also YI_3 , YF_3 , and YCl_3 is of great interest to find the conditions favoring the alloying process at the lowest temperature and most accessible experimental conditions. The ΔG values related to the different precursors are shown in Figure 1a as a function of temperature. The formations of Pt_5Y with chlorides and iodides have similar ΔG values, whereas the reactions with fluorides and oxides have more positive ΔG values, ruling out the latter. However, even with YI_3 and YCl_3 , temperatures above 1000 °C are necessary to favor the alloying ($\Delta G \leq 0$), which seems problematic with nanoparticles, as we want to avoid agglomeration. The way around this problem is to keep the reaction out of equilibrium by removing the gas product, which enables the reaction to run at lower temperatures. The equilibrium partial pressure for the gas product from halide precursors can be calculated by solving the following equation, where K_{HHa} is the equilibrium constant for the reduction of Pt metal with YHa_3 , P is the pressure, and P_{H_2} and P_{HHa} are the partial pressures of H_2 and HHa , respectively:

$$K_{\text{HHa}} = \frac{\left(\frac{P_{\text{HHa}}}{P}\right)^3}{\left(\frac{P_{\text{H}_2}}{P}\right)^{3/2}} \quad (3)$$

Similarly, the sensitivity for H_2O can be found from the relation between the equilibrium constant for reaction 2 and the partial pressure of water vapor $P_{\text{H}_2\text{O}}$ and hydrogen P_{H_2} :

$$K_{\text{H}_2\text{O}} = \left(\frac{\frac{P_{\text{H}_2\text{O}}}{P}}{\frac{P_{\text{H}_2}}{P}}\right)^{3/2} \quad (4)$$

The solutions to eqs 3 and 4 are plotted for the Pt_5Y system with 1 bar of H_2 on Figure 1b. At 600 °C, the equilibrium partial pressure of HCl and HI is around 0.01. The concentration/production of HCl and HI is directly linked to the alloying process. For such high partial pressure, the alloying process is fast and the catalyst on a gram scale can be produced in 1 h. Preliminary results also shows that very little is converted below the melting point of the precursor (see Figure S2). For that reason, YCl_3 (mp 721 °C) is of greater interest than YI_3 (mp 994 °C).

The determination of ΔG and the equilibrium constant for the alloying process can be extended to other chloride precursors. Figure S1a,b show the calculated values for the alloying of Pt_xM , where $\text{M} = \text{Dy}$, Tb , Tm , Sm , Gd , Ce , La , Ca , as a function of temperature. There is a general trend where “late” lanthanides have a higher reaction constant and thus produce a higher concentration of gas as the side product in comparison with “early” lanthanides. Thus, for the “late” lanthanide, an alloying rate enabling the production of grams of materials is possible at lower temperature.

Using the same approach, and assuming a constant H_2 pressure of 1 bar, the partial pressure of HCl for forming different crystal structures of Pt_xY was calculated. The H_2 partial pressure for the alloy formation of Pt_5Y and Pt_3Y is presented in Figure 2a. A lack of data restrained us from calculating the alloy formation of Pt_2Y . If the system is kept below the equilibrium partial pressure of hydrochloric acid, the formation of alloy will proceed. In turn this entails that, for a given partial pressure above the equilibrium for the Pt_3Y , but below the equilibrium for Pt_5Y , only the latter will be formed. From this, it is seen that Pt_5Y has the highest equilibrium pressure. The same observation was made for all Pt_xM alloys in comparison with their respective Pt_3M phases, and thus the formed phase could be controlled by controlling the partial pressure of HCl.

Because of the oxophilicity of the rare earths and lanthanides, it is worth discussing the effect of water and oxygen contamination, which could potentially hinder alloy formation. When they are in contact with oxygen, rare-earth and lanthanide elements will oxidize rather than alloy with Pt because of the more negative enthalpy of formation (10 eV per atom). Thus, the oxygen concentration when Pt is annealed with rare-earth/lanthanide elements should be minimized. The maximum limit of H_2O that can be in contact with Y_2O_3 is presented in Figure 1b. Below that H_2O partial pressure, the reductive environment will inhibit the oxidation reaction and the alloying will still occur. Above the H_2O partial pressure, the concentration is too high and the reducing atmosphere is not enough to inhibit the oxidation of the precursor or the Pt-based alloy. The $\text{H}_2\text{O}/\text{O}_2$ concentration threshold increases with temperature: for example, it is about 2 ppm at 600 °C and about 50 ppm at 800 °C for Pt_5Y alloys. The higher limit is set by the difference in reaction rate for reduction of YCl_3 and oxidation of YCl_3 or Pt_5Y , due to the difference in equilibrium partial pressure limits which can be different by orders of magnitude, as is also seen in Figure 1. The reaction time can be calculated by assuming that the reactions are limited by the gas

product (HCl) removal (i.e., assuming chemical equilibrium at all times). As mentioned above, the limit is linked to the partial pressure level of HCl and the speed at which the gas product can be removed. In the regime where the alloying is limited by the HCl partial pressure, we can approximate the reaction time by applying the ideal gas equation

$$n_{\text{HCl}} = \frac{P_{\text{HCl}}Qt}{RT} \quad (5)$$

where n_{HCl} is the moles of HCl gas, P_{HCl} the partial pressure of HCl from eq 3, Q the gas flow, t the time, R the gas constant, and T the temperature of the gas where the flow is measured. From eq 1, we can relate the number of moles of HCl, Pt_xY , and Pt

$$\frac{1}{3}n_{\text{HCl}} = n_{\text{Pt}_x\text{Y}} = \frac{1}{x}n_{\text{Pt}} = \frac{1}{x} \frac{w_{\text{Pt}}}{m_{\text{Pt}}} \quad (6)$$

and associate the formation of Pt_5Y to the ideal gas equation

$$t = \frac{3}{x} \frac{w_{\text{Pt}}RT}{m_{\text{Pt}}P_{\text{HCl}}Q} \quad (7)$$

Using eq 7, it is possible to approximate the reaction time for the formation of Pt_5Y and Pt_3Y from 0.5 g of Pt and an excess of YCl_3 under 1 bar of H_2 flowing at 10 mL/min. This shows that 1 g of 50 wt % Pt/C can be converted into Pt_5Y and Pt_3Y in about 50 and 140 min, respectively, at 800 °C under these experimental conditions (Figure 2b). This simple model does not include kinetics effects or mass transport limitations of the rare-earth or lanthanide species into the bulk of the platinum. However, our main interest is in the region where the reaction is limited by the removal of gas product, as it enables control over the formed alloy phases.

From this, it is possible to conclude that Pt_xY alloy formation with metallic Pt is feasible using a chloride precursor under 1 bar of H_2 at temperatures higher than 600 °C. The reaction is sensitive to H_2O and O_2 , which should be kept below 1 ppm at 600 °C and 20 ppm at 800 °C, which can be achieved with instrumental grade hydrogen and a leak-free system.

EXPERIMENTAL SECTION

Synthesis of $\text{Pt}_x\text{Y/C}$ Nanoparticles. The high oxophilicity of the rare-earth and lanthanide elements requires minimal to no air exposure. For that reason, handling of the chemicals prior to and after thermal reduction took place in a glovebox (Omni-Lab system, Vacuum Atmospheres, <0.5 ppm of O_2 , <0.5 ppm of H_2O). A homemade gastight metal reactor was designed for the preparation of the $\text{Pt}_x\text{Y/C}$ nanoparticles, and a simplified version is presented on Figure 3. The stainless steel reactor was put into a split-tubular furnace. For gas handling, VCR valves on the reactor were used for connecting to the high-vacuum gas wall where gas flows and composition were controlled. An iron catalyst was placed before the metal reactor to prevent water and/or oxygen from entering the reactor and reacting with the precursors. The system was operated at 1 bar and controlled by a pressure controller on the back end of the setup. The gas stream from the thermal reduction was passed by a glass capillary sniffer that allowed direct transfer to a quadrupole mass spectrometer for monitoring of the products.

Using the synthesis setup, the Pt/C nanoparticles were first dried at 200 °C in 100 mL of H_2 for 6 h to remove trace amounts of H_2O from air exposure. Once the drying procedure was over, YCl_3 was mixed with the Pt/C nanoparticles. YCl_3

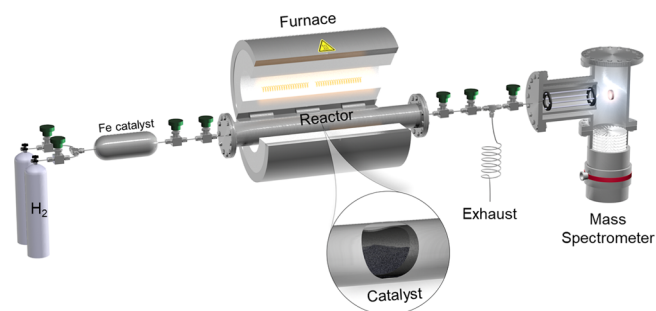


Figure 3. Metal reactor setup used for the high-temperature synthesis of $\text{Pt}_x\text{Y/C}$ nanoparticles.

was first dissolved in anhydrous acetonitrile (99.8%, Sigma-Aldrich, <10 ppm of H_2O) before the Pt/C nanoparticles were added. The mixture was partially covered and stirred overnight, and a dry powder was obtained. An optimal mixing of the YCl_3 precursor with the Pt/C nanoparticles is essential to improve the phase selectivity and limit the use of chloride precursor. For that reason, a ratio of Pt nanoparticles to YCl_3 of 1.5:1 was used.

The dry powder was spread evenly in the middle of a graphite foil (99.8%, Alfa Aesar, 0.254 mm) before being introduced into the metal reactor. The graphite foil was used to avoid contact between the precursors and the metal reactor. Finally, the metal reactor was sealed with a copper head gasket and connected to the stainless steel tubes. Helium was purged to the reactor at 10 mL/min for 20 min. The reactor was then filled with hydrogen for 60 min at 100 mL/min. The hydrogen flow was kept at 100 mL/min during the annealing procedure. The high H_2 flow was selected on the basis of the thermodynamic calculations. Hydrogen, a reducing gas, prevents the oxidation of the yttrium by O_2 , assuming minimal leaks in the setup. The temperature was monitored using a thermocouple placed in the middle of the furnace. The annealing temperature of 800 °C was chosen in order to be slightly above the melting point of the YCl_3 precursor (mp 721 °C),²⁶ as explained above.

Physical Characterizations. Prior to any characterization, the as-synthesized catalyst was acid-washed (0.1 M HClO_4) and water-washed three times. When the $\text{Pt}_x\text{Y/C}$ nanoparticles were formed and exposed to air, the first few monolayers of yttrium were oxidized and the surface became $\text{Pt-Y}_2\text{O}_3/\text{C}$. As the Y_2O_3 is unstable in acid electrolyte, the surface was cleaned from the oxide layer using 0.1 M HClO_4 , resulting in a strained Pt overlayer with high activity for the ORR. The acid electrolyte and water also removed any unreacted traces of precursor. The acid and water wash is essential to identify metallic yttrium under the Pt overlayer using XPS. The catalyst was then recovered by suspension in ethanol and dried at 60 °C.

Acid-washed $\text{Pt}_x\text{Y/C}$ catalysts were subjected to XRD analysis in order to confirm the formation of intermetallic compounds with a long-range ordered structure. For such purposes, the powder catalyst was loaded on a zero-background plate and mounted in the equipment (Panalytical X'Pert Pro/Empyrean) in a transmission spinner stage configuration. The 2θ angle was varied between 15 and 90° in continuous mode. For each batch of measurements, a silicon reference was measured and used as calibration. Data treatment of the collected XRD patterns was performed with the Panalytical HighScore Plus software suite, which also provided a database with the experimental XRD patterns used as reference.

Additional XRD patterns for comparison purposes were taken from the online Inorganic Crystal Structure Database (ICSD)-Karlsruhe and in-house measurements on polycrystalline alloy stubs from MaTeck used in previous works.^{3,21}

The catalysts were characterized using X-ray photoelectron spectroscopy (XPS) to further confirm the alloy formation over the oxide. The samples were mounted on carbon tape attached to aluminum foil for a better contact. XPS measurements were acquired under ultrahigh-vacuum (UHV) conditions ($<10^{-8}$ millibar) in a Theta-Probe instrument (Thermo Scientific). This instrument is equipped with a monochromated Al K α source (emission line at 1486.7 eV), and XPS spectra were obtained at an analyzer pass energy of 100 eV. In all cases, the atomic concentrations were quantified by integration of the Pt 4f, Y 4d, O 1s, and C 1s peaks after removal of a Shirley-type background. The scans were calibrated according to the C 1s peak (284.6 eV). Reference XPS spectra for comparison were obtained from the NIST X-ray Photoelectron Spectroscopy Database and in-house measurements on polycrystalline alloy stubs from MaTeck. The size distribution of the deposited nanoparticles was determined with ex situ TEM imaging (Tecnai T20 G2). The area of the nanoparticles on the pictures was measured manually using the software ImageJ. The diameter was estimated assuming perfectly spherical particles.

Electrochemical Characterizations. The electrochemical experiments were carried out in a custom-made three-electrode glass cell at 23 °C using the rotating disk electrode method.^{41–44} Prior to the measurements all glassware was cleaned in piranha solution (98% H₂SO₄ (Merck, Emsure) and 30% H₂O₂ (Merck, Emsure), 3/1 v/v) for 24 h and rinsed several times with Milli-Q water at 80 °C. The electrochemical cell includes the working electrode which was mounted on a Pine Instruments rotator, a Pt wire (Chempur, 99.9%, 0.5 mm diameter) to act as a counter electrode, and an Hg|Hg₂SO₄ (0.6 M H₂SO₄) reference electrode (Schott Instruments), the last electrode being separated from the working electrode compartment using a ceramic frit. The electrochemical experiments were performed in 0.1 M HClO₄ electrolyte (70% HClO₄, Merck, Suprapur and Millipore Milli-Q, resistivity >18.2 M Ω cm, TOC <3 ppb). The gases used were supplied by AGA with Instrument 5.0 purity for Ar, N₂, and O₂ gases, Instrument 4.5 purity for the H₂ gas, and Instrument 3.7 purity for the CO. All of the potentials are reported versus the reversible hydrogen electrode (RHE) and corrected for Ohmic drop. The Ohmic resistance was determined from the fitted high-frequency intercept measured using electrochemical impedance spectroscopy.⁴⁵ The measured Ohmic resistance ranged from 25 to 30 Ω . The RHE potential was measured by bubbling H₂ over the Pt electrode in the electrolyte at 1600 rpm and measuring the mean of the intersection value while the electrode was cycled from 0.02 to 0.3 V_{RHE} at 10 mV/s.

The ink preparation of the Pt/C catalyst was carried out as previously described.⁴² The Pt_xY/C catalyst inks were based on isopropyl alcohol. A 5 mm diameter glassy-carbon electrode (Pine Instruments) was used as the substrate. The glassy-carbon disks were polished beforehand using Buehler Micro-Polish™ 0.05 mm alumina particles on a Buehler MicroCloth PSA and then ultrasonicated twice in both isopropyl alcohol and deionized water. The electrodes were prepared by first mounting the polished and cleaned glassy-carbon disk in a custom-made Teflon holder and then drop-casting 10 μ L of the prepared ink on a glassy-carbon disk. The deposited aliquot was allowed to dry in air (or under a lamp heating up to 40–50

°C), and then the electrode was coupled to a Pine Instruments rotating-disk electrode Teflon shaft that was attached to a rotator device (also from Pine) provided with a rotation speed controller upon the electrochemical measurement.

The working electrode was immersed into the electrochemical cell under potential control at 0.10 V_{RHE} and cycled at 200 mV/s in a N₂-saturated electrolyte until a stable CV was obtained (typically after ca. 200 cycles). Following this, the ORR performance of the Pt_xY/C catalysts was evaluated in O₂-saturated solution at 50 mV s⁻¹ and 1600 rpm until a stable current was reached. The electrochemical surface area (ECSA) was evaluated using the CO-stripping method.⁴⁶ For this purpose, CO gas was first bubbled into the electrolyte for 2 min, while the working electrode potential was kept at 0.05 V_{RHE}. The remaining CO dissolved in solution was removed by flushing Ar for 15 min while the potential control was maintained. Afterward, the potential was scanned up to 1.00 V in CO-free Ar-purged solution at 50 mV s⁻¹. The corresponding electrochemical active surface area (ECSA) of the Pt_xY/C catalysts was estimated assuming a ratio of 420 μ C cm⁻²,⁴⁷ for reasons of consistency with previous works.^{25,48,49}

RESULTS AND DISCUSSION

Physical and Chemical Characterizations. As presented earlier, specific Pt_xY phase can be thermodynamically favored, and the progression can be monitored using the partial pressure of HCl (eq 7). With the aim of testing this theory, we synthesized Pt_xY using two different annealing times (Table 1).

Table 1. Parameters of the Thermal Treatment for the Synthesis of Pt_xY/C Nanoparticles

experiment	duration of step (min)			
	25 °C → 400 °C	400 °C → 600 °C	600 °C → 800 °C	800 °C
short-term annealing	10	20	30	60
long-term annealing	10	20	30	360

An annealing of 360 min at 800 °C was chosen and compared with a 60 min annealing time. The shorter treatment was chosen on the basis of the production of HCl detected by the MS placed at the end of the reactor.

Figure 4 shows the mass spectrum signals of some of the products detected by the mass spectrometer while performing a synthesis. The zero value of the time scale was calibrated with the beginning of the annealing treatment. The temperature ramping is also presented (blue dashed line). H₂ and HCl are presented, as both products are involved in the alloy formation reaction (eq 1). The most abundant isotope of chlorine being 35, we expect that production of HCl should be detected when m/z 36 is monitored. H₂ is correlated with a signal at m/z 2. The elevated H₂ signal detected corresponds to the high flow of 100 mL H₂/min used during the annealing process.

Detection of molecular weight 36 can also be related to the detection of tricarbon anion (C₃⁻), a transient species often observed in combustion reactions. To dissociate HCl production from a combustion-related product, CO₂ (m/z 44) is also plotted: m/z 44 (CO₂) and m/z 36 (HCl) show much lower current intensity in comparison with m/z 2 (H₂). For both species, two more intense features are observed over the annealing period. For m/z 44 (CO₂), a sharp peak is

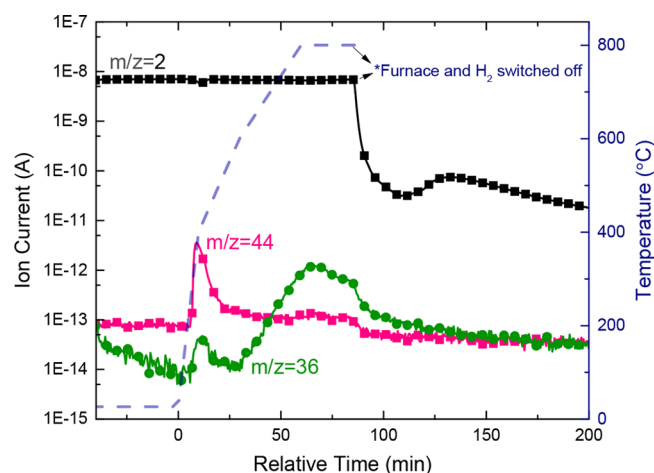


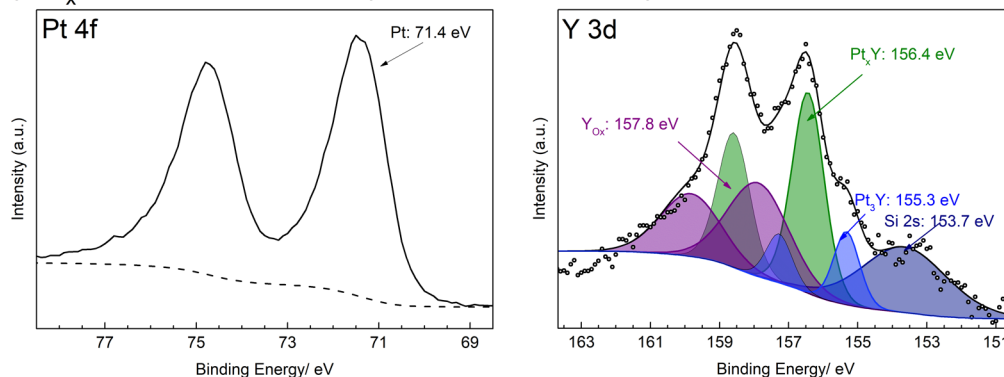
Figure 4. H_2 (m/z 2), CO_2 (m/z 44), and HCl (m/z 36) detected by the mass spectrometer (MS) during the annealing of Pt/C nanoparticles and YCl_3 at 800°C under a H_2 atmosphere. The dotted lines are related to the ion current measured by the MS (left axis), and the dashed line is related to the temperature of the furnace (right axis).

detected at $t = 9$ min, and a shoulder is seen between $t = 63$ min and $t = 85$ min. A much smaller peak is observed at $t = 11$ min for m/z 36 (HCl), but a rather intense and broad peak is noted at ca. $t = 65$ min. For both m/z 44 (CO_2) and 36 (HCl), the decrease in signal from the second peak seems to be correlated to the furnace being stopped and hydrogen being replaced by helium. A drastic decrease is observed when the

hydrogen flow and furnace are switched off. The mass spectrum signals of all detected species are available in the [Supporting Information](#).

The surface composition of the synthesized catalysts was characterized by XPS. In [Figure 5](#) are displayed detailed Pt 4f and Y 3d scans of the acid- and water-washed Pt_xY annealed for 360 min (A) and 60 min (B), respectively. As observed previously, the Pt 4f signal of a Pt_xY alloy remains unchanged in comparison to that of bare Pt.²⁵ Indeed, the main Pt peaks of the 4f core level region at 71.4 eV indicate a metallic state for both samples. The XPS spectrum of the Y 3d core-level region was deconvoluted by more than a single set of peaks, which suggests that Y is in more than one chemical state. The deconvolution of the Y 3d peak from the long-term annealed Pt_xY shows the contribution of three different oxidation states of Y: Pt_xY (156.4 eV), Pt_3Y (155.3 eV), and Y_2O_3 (157.8 eV). The peak at 156.4 eV was also observed when the Pt_xY mass-selected nanoparticles were measured²⁵ and is associated with alloy formation between yttrium and platinum. A small Si contamination (153.7 eV) was also observed in the Y 3d region. This contamination was further confirmed by a peak with very small intensity around 103 eV. We suspect that this contamination came from the mixing of Pt/C nanoparticles and YCl_3 in a glass beaker. On the other hand, the deconvolution of the Y 3d region from the Pt_xY (60 min at 800°C) ([Figure 5B](#)) shows a mix of Pt_xY (156.4 eV) and Y_2O_3 (158.3 eV). The Pt:Y ratio varies between 3.5 and 3.9 for the long- and short-term syntheses, respectively. Similarly, the XPS spectra of the Y 3d region of the Pt_3Y obtained by the molten reducing agent method³⁴ after acid wash shows Y_2O_3 and

A) $\text{Pt}_x\text{Y}/\text{C}$ nanoparticles (360 min at 800°C)



B) $\text{Pt}_x\text{Y}/\text{C}$ nanoparticles (60 min at 800°C)

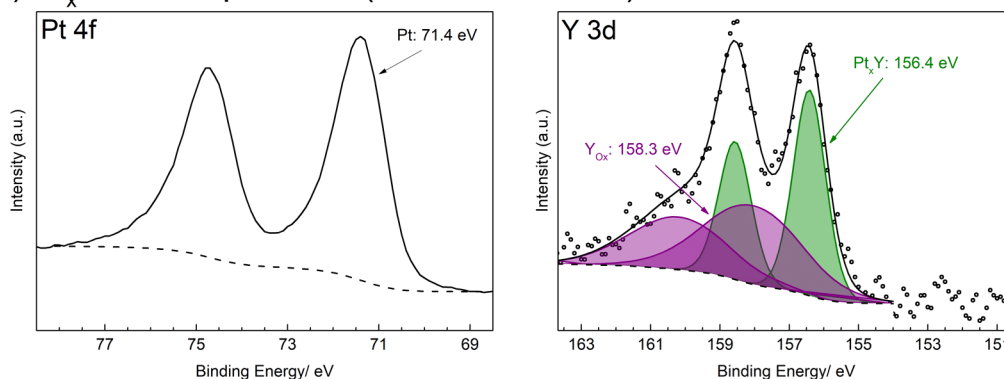


Figure 5. XPS spectra in the platinum 4f and yttrium 3d core level regions for Pt_xY obtained from (A) 360 min and (B) 60 min annealing at 800°C . The catalysts were washed three times with acid (0.1 M HClO_4) and water before XPS measurements.

metallic Y. Unlike what we report, the previous study could only identify one metallic Y species.

Intermetallic phase formation for the Pt_xY catalysts obtained by high-temperature synthesis was also confirmed by XRD (Figure 6). A comparison of the XRD patterns of the as-

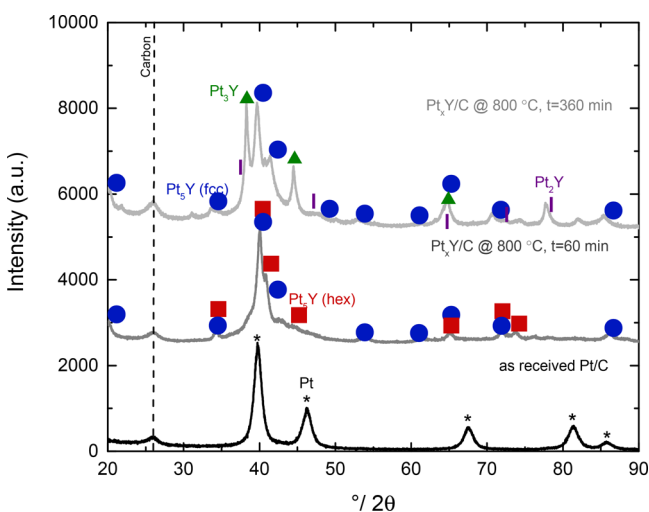


Figure 6. XRD patterns of as-received Pt/C (black line), Pt_xY/C (60 min) (dark gray line), and Pt_xY/C (360 min) (light gray line) nanoparticles.

received Pt/C reference (black line) and the synthesized catalyst (dark and light gray lines) shows many discrepancies, ensuring that no metallic Pt is contained in the synthesized catalyst. Indeed, if we compare the long-term synthesis with the Pt/C reference, we observe that, even though the peak at 39.7° could be related to the (111) Pt reflection, no other peaks related to the Pt reference are observed. The crystalline structure of the Pt_xY annealed for 360 min shows reflections associated with three different Pt_xY phases. The identification of the measured reflections was done on the basis of previous work,³ where bulk polycrystalline Pt₂Y, Pt₃Y, and Pt₃Y were characterized. Pt₃Y shows intense peaks at 38.3, 44.5, and 64.4° associated with the (111), (002), and (022) planes, respectively. A face-centered-cubic (FCC) Pt₃Y from the crystal prototype AuBe₃³ is also observed and shows characteristic peaks at 39.7° ((113) facets) and 41.42° ((222) facets). Finally, the Pt₂Y phase shows a low-intensity peak for the (004) plane at 47.8°. The XRD pattern of the Pt_xY obtained from short annealing only shows reflections associated with the FCC and/or hexagonal Pt₃Y, from the prototype structure Cu₅Ca. The most intense peak at 40.0° could be related to the (111) reflection of the FCC and/or hexagonal Pt₃Y. A shoulder fitting with the position of the (002) facets of the hexagonal Pt₃Y is noted. In addition, a much less intense peak associated with the Pt₃Y is observed at higher degrees of reflection. Many peaks of the FCC and hexagonal structures are overlapping, making it difficult to fully differentiate them. The carbon support shows a peak in all of the XRD patterns at 25.8°.

The particle-size distribution (PSD) histograms of the catalysts were determined using TEM and are plotted in Figure 7. The Y axis plotted is the percentage volume of nanoparticles of a specific size. This value was obtained from the number of nanoparticles for a defined size multiplied by its volume. From Figure 7a, it is observed that the as-received Pt/C catalyst already has a relatively broad size distribution with an

average of 7.6 ± 3.4 nm. Only one large particle (~ 35 nm) was observed but is not represented on the TEM picture. The average of the Pt_xY/C nanoparticles obtained from the short-term synthesis is slightly higher than that for the as-received Pt particles with a PSD of 9.9 ± 3.6 nm. We can see that for this catalyst $\sim 80\%$ of the particles have diameter size >10 nm. The Pt_xY/C synthesis obtained from 360 min annealing shows the highest PSD (12.1 ± 4.4 nm), and $\sim 92\%$ of the nanoparticles have particle diameters above 10 nm.

Oxygen Reduction Reaction. The activity for oxygen reduction of the Pt_xY catalysts is presented in Figure 8. Typical cyclic voltammograms in O₂-saturated 0.1 M HClO₄ solution at 50 mV s⁻¹ are shown in Figure 8a. The Pt/C nanoparticles used for the synthesis were measured and used as reference. We chose the Pt/C nanoparticles to compare the catalytic activity of Pt_xY catalysts with similar nanoparticle sizes. Comparison with commercial Pt/C TKK 60% is also available in Figure S3 in the Supporting Information. In the potential region of mixed kinetic and mass transport, there is a positive shift for the longer annealed Pt_xY nanoparticles, relative to Pt. This represents a substantial decrease in the overpotential for the alloy surface. The kinetic activity at 0.9 V_{RHE} normalized by the specific surface area and mass fraction of platinum is plotted in Figure 8b,c, respectively. As expected, the activity reported for our Pt/C reference catalyst is lower than that of the state of the art Pt/C nanoparticles reported previously.⁴² The lower kinetic activity of the Pt/C electrode measured in this work is related to the larger particle size of the Pt catalyst.⁴⁹ The greatest increase in specific and mass activity is obtained with Pt_xY annealed for 360 min at 800 °C. An increase in mass activity, the most relevant activity descriptor when implementation in fuel cell devices is considered, of roughly 40% in comparison to our Pt/C reference is shown. Very similar mass activity is obtained with Pt_xY nanoparticles annealed for 60 min at 800 °C.

Discussion. XPS results show that intermetallic Pt_xY was successfully formed. For both catalysts, Pt_xY was observed. A Pt₃Y phase, corresponding to the respective XRD pattern, was also observed for the Pt_xY/C annealed for 360 min. The metallic Pt peaks observed for both Pt_xY catalysts are those that were previously reported for Pt–Y alloy formation.²⁵ The ratios of Pt and Y signals of 3.5–3.9 correspond to the values already reported for the formation of a “thick” Pt overlayer due to yttrium oxidation and leaching on exposure to air and acid electrolyte.²⁵ We do not expect the small Si contamination to influence the catalyst performance. The XRD patterns of the synthesized Pt_xY nanoparticles confirm the alloy formation and prove that the annealing time affects the Pt_xY phases formed. We argue that the differences in phase formation with annealing time can be explained by our thermodynamic considerations, as we predicted that the Pt₃Y phase takes a longer time to form in comparison to the Pt₂Y phase. From XRD data, no metallic Pt was observed, meaning that it all reacted with the YCl₃ precursor at 800 °C.

We hypothesize that the lower specific and mass activity obtained for Pt_xY catalysts is mainly caused by two factors: the nature of the Pt_xY phase and the nanoparticle sizes. The nature of the Pt_xY phase strongly affects the kinetic activity toward oxygen reduction. Indeed, Pt₃Y is the most active Pt_xY phase, reaching 9.4 mA/cm²_{Pt} at 0.9 V_{RHE} and outperforming Pt₂Y by a factor of 1.6,³ as previously reported. As reported in earlier studies from our laboratory,²⁰ the presence of the rare-earth metal brings about a decrease in the nearest-neighbor difference

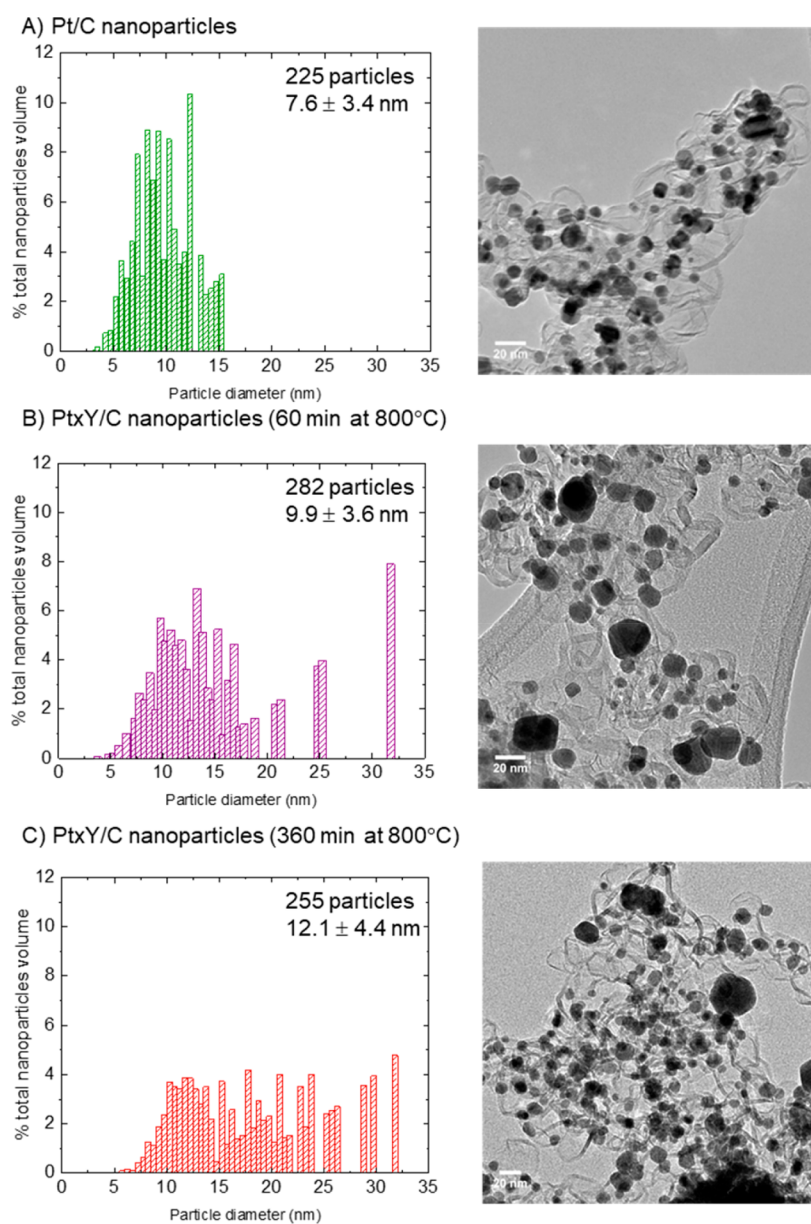


Figure 7. Particle size distributions and representative TEM micrographs for (A) the as-received Pt/C, (B) the 30 min annealed @ 800 °C Pt_xY/C and (C) the 360 min annealed @ 800 °C Pt_xY/C.

in the core of the catalyst; this strain is translated to the Pt overlayer as a compressive surface strain, increasing the oxygen reduction activity. It was also reported that Pt₂Y, whose activity similar to that of Pt corrodes after only a few cycles in 0.1 M HClO₄, ends up with catalytic activity similar to that of Pt. The size study made for Pt_xY showed that the kinetic activity and particle size are closely linked and that maximum performance is expected for particles 8–9 nm in diameter.²⁵ Indeed, the highest mass and specific activity reported for this system is of 3.1 A/mg_{Pt} and 13.5 mA/cm²_{Pt}, respectively, at 0.9 V_{RHE}. In our work, we demonstrated that ~80% and ~92% of the Pt_xY particles obtained from 60 and 360 min annealing, respectively, have particle diameters greater than 10 nm. This considerable proportion of nanoparticles with larger diameter contributes to significantly lower activity measured and explains why only 0.43 A/mg_{Pt} and 2.0 mA/cm²_{Pt} were measured at 0.9 V_{RHE}. The remaining volume having particle sizes between 2 and 9 nm

have mass activities that varies between one similar to a 6-fold improvement in comparison to Pt.

CONCLUSIONS

In conclusion, the thermodynamics of the reaction conditions of Pt and rare-earth/lanthanide chloride precursors under an H₂ atmosphere at high temperature helped us establish the conditions for alloy formation. The synthesis procedure was applied to Pt–Y catalysts because of the lower annealing temperature required and the already established high activity for oxygen electroreduction. XRD and XPS patterns showed the clear formation of Pt–Y alloy phases and demonstrated the effect of the annealing time on the phase formation, which also correlates with the thermodynamic calculations. The particle size distribution determined using TEM images showed a relatively large distribution caused by the inhomogeneous size of Pt/C nanoparticles used for the synthesis and annealing at 800 °C that favors sintering. The electrochemical testing for the

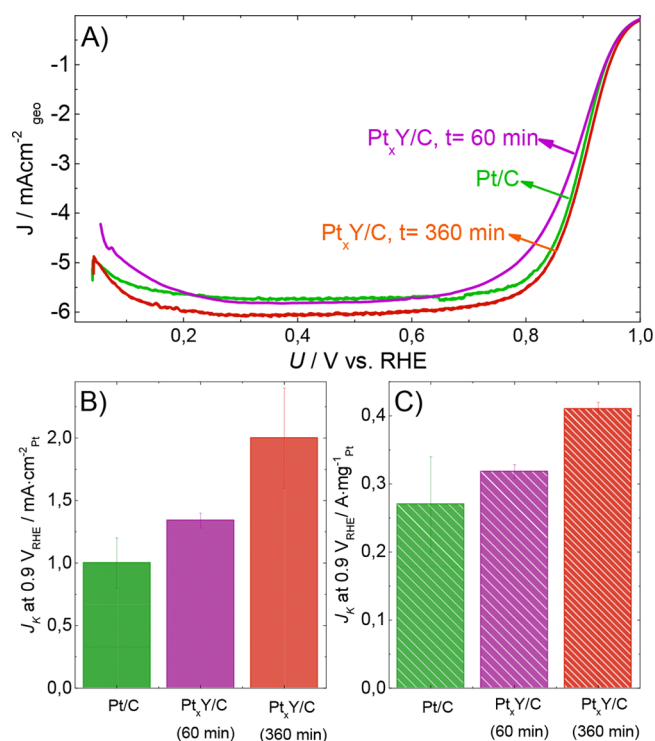


Figure 8. (A) RRDE polarization curves at 1600 rpm and 50 mV s⁻¹ for the ORR on Pt/C (green curve), Pt_xY/C (60 min at 800 °C) (purple curve), and Pt_xY/C (360 min at 800 °C) (red curve) nanoparticle catalysts in O₂-saturated 0.1 M HClO₄. Kinetic current density normalized by (B) specific surface area and (C) mass of Pt at 0.9 V_{RHE} for Pt/C and Pt_xY/C annealed for 30 and 360 min at 800 °C, on the basis of data from (A).

oxygen reduction reaction shows for the first time, for catalysts synthesized on a gram scale, improved catalytic activity. The lower mass activity of the thermally synthesized nanoparticles in comparison with the mass-selected Pt_xY can be explained by an average particle size that is too large and the nature of the Pt_xY crystalline phase. The method used for the synthesis of Pt–Y nanoparticles can easily be extended to other rare-earth and lanthanide metals on the basis of the thermodynamic data, and a clear experimental procedure has been presented. Even though we consider the synthesis of electrochemically active Pt–Y alloy a considerable achievement, the activity should be further improved and the stability tested. Decreasing the nanoparticle size distribution, favoring Pt₃Y alloy phase formation, and testing the catalyst under experimental conditions closer to fuel cell operating conditions, i.e. at higher current densities^{50–52} or in a membrane electrode assembly, are part of the ongoing experiments for extended catalyst applications.

ASSOCIATED CONTENT

Supporting Information

The Supporting Information is available free of charge on the ACS Publications website at DOI: 10.1021/acscatal.7b03972.

Further details on the thermodynamic calculations of the alloy formation, XRD of the catalysts annealed at various temperatures used to determine the annealing temperature, comparison of the ORR activity to that of commercial Pt/C catalyst, and Tafel plots (PDF)

AUTHOR INFORMATION

Corresponding Author

*E-mail for I.C.: ibchork@fysik.dtu.dk.

ORCID

Claudie Roy: 0000-0002-7254-7238

Ifan E. L. Stephens: 0000-0003-2157-492X

Ib Chorkendorff: 0000-0003-2738-0325

Notes

The authors declare no competing financial interest.

ACKNOWLEDGMENTS

This work was supported by a research grant (9455) from VILLUM FONDEN. We also acknowledge UPCAT under the project no. 2015-1-12315. The authors thank Jakob Kibsgaard for drawing the schematic of the setup presented in Figure 2.

REFERENCES

- (1) Gasteiger, H. A.; Garche, J. *Handbook of Heterogeneous Catalysis*; Ertl, G., Knözinger, H., Eds.; Wiley-VCH: Weinheim, Germany, 2008.
- (2) Reitz, W. *Materials and Manufacturing Processes*; Taylor and Francis: Oxford, U.K., 2007; Vol. 22.
- (3) Stephens, I. E. L.; Bondarenko, A. S.; Bech, L.; Chorkendorff, I. *ChemCatChem* **2012**, *4*, 341–349.
- (4) Stephens, I. E. L.; Bondarenko, A. S.; Grønberg, U.; Rossmeisl, J.; Chorkendorff, I. *Energy Environ. Sci.* **2012**, *5*, 6744.
- (5) Hong, W. T.; Risch, M.; Stoerzinger, K. A.; Grimaud, A.; Suntivich, J.; Shao-Horn, Y. *Energy Environ. Sci.* **2015**, *8*, 1404–1427.
- (6) Rossmeisl, J.; Karlberg, G. S.; Jaramillo, T.; Nørskov, J. K. *Faraday Discuss.* **2009**, *140*, 337–346.
- (7) Tripković, V.; Skúlason, E.; Siahrostami, S.; Nørskov, J. K.; Rossmeisl, J. *Electrochim. Acta* **2010**, *55*, 7975–7981.
- (8) Han, B.; Carlton, C. E.; Kongkanand, A.; Kukreja, R. S.; Theobald, B. R.; Gan, L.; O'Malley, R.; Strasser, P.; Wagner, F. T.; Shao-Horn, Y. *Energy Environ. Sci.* **2015**, *8*, 258–266.
- (9) Cui, C.; Gan, L.; Heggen, M.; Rudi, S.; Strasser, P. *Nat. Mater.* **2013**, *12*, 765–771.
- (10) Chen, C.; Kang, Y.; Huo, Z.; Zhu, Z.; Huang, W.; Xin, H. L.; Snyder, J. D.; Li, D.; Herron, J. A.; Mavrikakis, M.; Chi, M.; More, K. L.; Li, Y.; Markovic, N. M.; Somorjai, G. A.; Yang, P.; Stamenkovic, V. R. *Science* **2014**, *343*, 1339–1343.
- (11) Yoshida, T.; Kojima, K. *Electrochem. Soc. Interface* **2015**, *24*, 45–49.
- (12) Chen, S.; Gasteiger, H. A.; Hayakawa, K.; Tada, T.; Shao-Horn, Y. *J. Electrochem. Soc.* **2010**, *157*, A82.
- (13) Maillard, F.; Dubau, L.; Durst, J.; Chatenet, M.; André, J.; Rossinot, E. *Electrochem. Commun.* **2010**, *12*, 1161–1164.
- (14) Dubau, L.; Lopez-Haro, M.; Castanheira, L.; Durst, J.; Chatenet, M.; Bayle-Guillemaud, P.; Guétaz, L.; Caqué, N.; Rossinot, E.; Maillard, F. *Appl. Catal., B* **2013**, *142–143*, 801–808.
- (15) Mayrhofer, K. J. J.; Hartl, K.; Juhart, V.; Arenz, M. *J. Am. Chem. Soc.* **2009**, *131*, 16348–16349.
- (16) Huang, X.; Zhao, Z.; Cao, L.; Chen, Y.; Zhu, E.; Lin, Z.; Li, M.; Yan, A.; Zettl, A.; Wang, Y. M.; Duan, X.; Mueller, T.; Huang, Y. *Science* **2015**, *348*, 1230–1234.
- (17) Baldizzone, C.; Mezzavilla, S.; Carvalho, H. W. P.; Meier, J. C.; Schuppert, A. K.; Heggen, M.; Galeano, C.; Grunwaldt, J. D.; Schüth, F.; Mayrhofer, K. J. J. *Angew. Chem., Int. Ed.* **2014**, *53*, 14250–14254.
- (18) Greeley, J.; Stephens, I. E. L.; Bondarenko, A. S.; Johansson, T. P.; Hansen, H. A.; Jaramillo, T. F.; Rossmeisl, J.; Chorkendorff, I.; Nørskov, J. K. *Nat. Chem.* **2009**, *1*, 552–556.
- (19) Malacrida, P.; Escudero-Escribano, M.; Verdager-Casadevall, A.; Stephens, I. E. L.; Chorkendorff, I. *J. Mater. Chem. A* **2014**, *2*, 4234.
- (20) Escudero-Escribano, M.; Malacrida, P.; Hansen, M. H.; Vej-Hansen, U. G.; Velazquez-Palenzuela, A.; Tripkovic, V.; Schiøtz, J.; Rossmeisl, J.; Stephens, I. E. L.; Chorkendorff, I. *Science* **2016**, *352*, 73–76.

- (21) Escudero-Escribano, M.; Verdaguier-Casadevall, A.; Malacrida, P.; Grønberg, U.; Knudsen, B. P.; Jepsen, A. K.; Rossmel, J.; Stephens, I. E. L.; Chorkendorff, I. *J. Am. Chem. Soc.* **2012**, *134*, 16476–16479.
- (22) Ulrikkeholm, E. T.; Pedersen, A. F.; Vej-Hansen, U. G.; Escudero-Escribano, M.; Stephens, I. E. L.; Friebel, D.; Mehta, A.; Schiøtz, J.; Feidenhansl, R. K.; Nilsson, A.; Chorkendorff, I. *Surf. Sci.* **2016**, *652*, 114–122.
- (23) Johansson, T. P.; Ulrikkeholm, E. T.; Hernandez-Fernandez, P.; Escudero-Escribano, M.; Malacrida, P.; Stephens, I. E. L.; Chorkendorff, I. *Phys. Chem. Chem. Phys.* **2014**, *16*, 13718–13725.
- (24) Velázquez-Palenzuela, A.; Masini, F.; Pedersen, A. F.; Escudero-Escribano, M.; Deiana, D.; Malacrida, P.; Hansen, T. W.; Friebel, D.; Nilsson, A.; Stephens, I. E. L.; Chorkendorff, I. *J. Catal.* **2015**, *328*, 297–307.
- (25) Hernandez-Fernandez, P.; Masini, F.; McCarthy, D. N.; Streb, C. E.; Friebel, D.; Deiana, D.; Malacrida, P.; Nierhoff, A.; Bodin, A.; Wise, A. M.; Nielsen, J. H.; Hansen, T. W.; Nilsson, A.; Stephens, I. E. L.; Chorkendorff, I. *Nat. Chem.* **2014**, *6*, 732–738.
- (26) Lide, D. R. *CRC Handbook of Chemistry and Physics*; CRC Press: Boca Raton, FL, 2005.
- (27) Tsuji, M.; Uto, K.; Nagami, T.; Muto, A.; Fukushima, H.; Hayashi, J. *ChemCatChem* **2017**, *9*, 962–970.
- (28) Cui, R.; Mei, L.; Han, G.; Chen, J.; Zhang, G.; Quan, Y. *Sci. Rep.* **2017**, *7*, 41826.
- (29) Brandiele, R.; Durante, C.; Grządka, E.; Rizzi, G. A.; Zheng, J.; Badocco, D.; Centomo, P.; Pastore, P.; Granozzi, G.; Gennaro, A. *J. Mater. Chem. A* **2016**, *4*, 12232–12240.
- (30) Han, S. B.; Kwak, D. H.; Lee, Y. W.; Kim, S. J.; Lee, J. Y.; Lee, S.; Kwon, H. J.; Park, K. W. *Int. J. Electrochem. Sci.* **2016**, *11*, 3803–3814.
- (31) Yoo, S. J.; Lee, K.-S.; Hwang, S. J.; Cho, Y.-H.; Kim, S.-K.; Yun, J. W.; Sung, Y.-E.; Lim, T.-H. *Int. J. Hydrogen Energy* **2012**, *37*, 9758–9765.
- (32) Jeon, M. K.; McGinn, P. J. *J. Power Sources* **2011**, *196*, 1127–1131.
- (33) Hyun, K.; Lee, J. H.; Yoon, C. W.; Kwon, Y. *Int. J. Electrochem. Sci.* **2013**, *8*, 11752–11767.
- (34) Kanady, J. S.; Leidinger, P.; Haas, A.; Titlbach, S.; Schunk, S.; Schierle-Arndt, K.; Crumlin, E. J.; Wu, C. H.; Alivisatos, A. P. *J. Am. Chem. Soc.* **2017**, *139*, 5672–5675.
- (35) Yan, C.; Wagner, M. J. *Nano Lett.* **2013**, *13*, 2611–2614.
- (36) Lux, K. W.; Cairns, E. J. *J. Electrochem. Soc.* **2006**, *153*, A1139.
- (37) Kleykamp, H. *J. Nucl. Mater.* **1993**, *201*, 193–217.
- (38) Hellwig, L. *Thermodynamische Untersuchungen an den Systemen Yttrium-Platin und Neptunium-Platin durch EMK-Messungen mit galvanischen Festkörperketten*, Kernforschungszentrum Karlsruhe, Dissertation, KfK 2687, 1978.
- (39) Erdmann, B. *Darstellung von Actiniden-Lanthaniden-Edelmetall (Pt, Pd, Ir, Rh)-Legierungsphasen durch gekoppelte Reduktion*, Kernforschungszentrum Karlsruhe, Dissertation, KfK 1444, 1971.
- (40) Erdmann, B.; Keller, C. *J. Solid State Chem.* **1973**, *7*, 40–48.
- (41) Mayrhofer, K. J. J.; Strmcnik, D.; Blizanac, B. B.; Stamenkovic, V.; Arenz, M.; Markovic, N. M. *Electrochim. Acta* **2008**, *53*, 3181–3188.
- (42) Pedersen, C. M.; Escudero-Escribano, M.; Velázquez-Palenzuela, A.; Christensen, L. H.; Chorkendorff, I.; Stephens, I. E. L. *Electrochim. Acta* **2015**, *179*, 647–657.
- (43) Stamenković, V.; Schmidt, T. J.; Ross, P. N.; Marković, N. M. *J. Electroanal. Chem.* **2003**, *554–555*, 191–199.
- (44) Garsany, Y.; Baturina, O. a.; Swider-Lyons, K. E.; Kocha, S. S. *Anal. Chem.* **2010**, *82*, 6321–6328.
- (45) Čolić, V.; Tymoczko, J.; Maljusch, A.; Ganassin, A.; Schuhmann, W.; Bandarenka, A. S. *ChemElectroChem* **2015**, *2*, 143–149.
- (46) Binninger, T.; Fabbri, E.; Kotz, R.; Schmidt, T. J. *J. Electrochem. Soc.* **2014**, *161*, H121–H128.
- (47) Maillard, F.; Savinova, E. R.; Stimming, U. *J. Electroanal. Chem.* **2007**, *599*, 221–232.
- (48) Velázquez-Palenzuela, A.; Masini, F.; Pedersen, A. F.; Escudero-Escribano, M.; Deiana, D.; Malacrida, P.; Hansen, T. W.; Friebel, D.; Nilsson, A.; Stephens, I. E. L.; Chorkendorff, I. *J. Catal.* **2015**, *328*, 297–307.
- (49) Perez-Alonso, F. J.; McCarthy, D. N.; Nierhoff, A.; Hernandez, P.; Streb, C.; Stephens, I. E. L.; Nielsen, J. H.; Chorkendorff, I. *Angew. Chem., Int. Ed.* **2012**, *51*, 4641–4643.
- (50) Kongkanand, A.; Mathias, M. F. *J. Phys. Chem. Lett.* **2016**, *7*, 1127–1137.
- (51) Zalitis, C. M.; Kramer, D.; Kucernak, A. R. *Phys. Chem. Chem. Phys.* **2013**, *15*, 4329.
- (52) Stephens, I. E. L.; Rossmel, J.; Chorkendorff, I. *Science* **2016**, *354*, 1378–1379.

Paper II

Trends in activity and dissolution on RuO₂ under oxygen evolution conditions: particles versus well-defined extended

Trends in activity and dissolution on RuO₂ under oxygen evolution conditions: particles versus well-defined extended surfaces

Roy, Claudie ^a; Rao, Reshma R;^b Stoerzinger, Kelsey A.^c; Hwang, Jonathan ^c;
Rossmeisl, J.;^d Chorkendorff, Ib; Shao-Horn, Yang ^{b,c}; Stephens, Ifan E.L. ^{a,e};

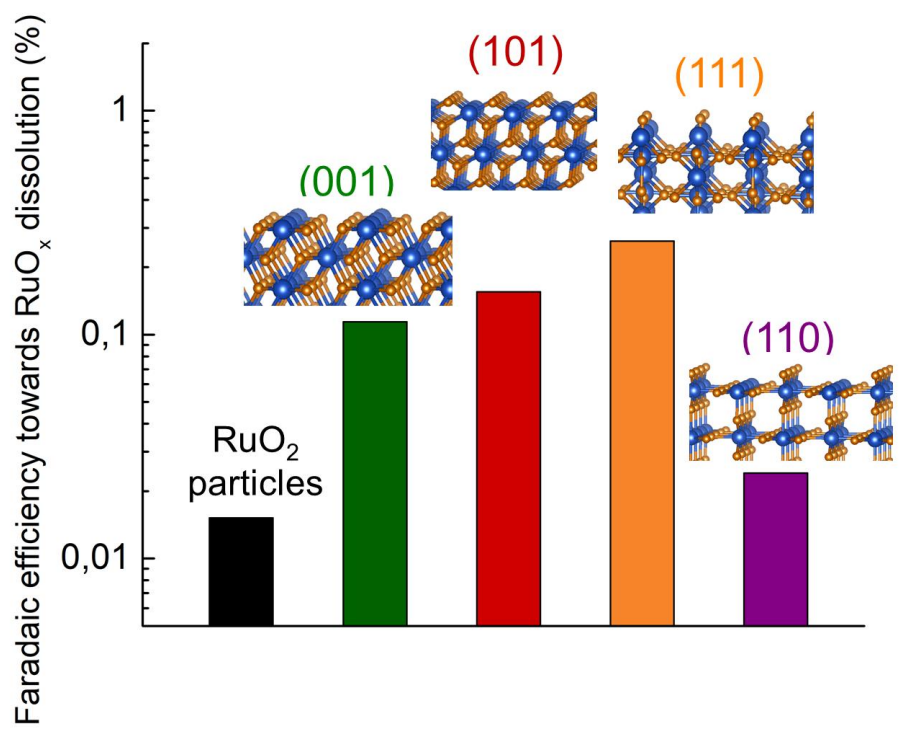
^a Surface Physics and Catalysis , Department of Physics, Technical University of Denmark, DK-2800 Kgs. Lyngby, Denmark

^b Department of Mechanical Engineering, Massachusetts Institute of Technology, Cambridge, Massachusetts 02139, United States

^c Department of Materials Science and Engineering, Massachusetts Institute of Technology, Cambridge, Massachusetts 02139, United States

^dDepartment of Chemistry, University of Copenhagen, Copenhagen, Denmark

^eDepartment of Materials, Imperial College London, London, United Kingdom



Abstract

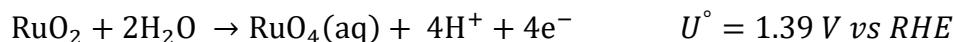
Rutile RuO₂ catalysts are the most active pure metal oxides for oxygen evolution; however, they are also unstable towards dissolution. Herein, we study the catalytic activity and stability of oriented thin films of RuO₂ with the (111), (101) and (001) orientations, in comparison to a (110) single crystal and commercial nanoparticles. These surfaces were all tested in aqueous solutions 0.05 M H₂SO₄. The initial catalyst activity ranked as follows: (001) > (101) > (111) ≈ (110). We complemented our activity data with inductively coupled plasma mass spectroscopy (ICP-MS), to measure Ru dissolution products occurring in parallel to oxygen evolution. In contrast to earlier reports, we find that, under our experimental conditions, there is no correlation between the activity and stability.

Introduction

Hydrogen production provides a means of storing electricity generated from wind and solar energy¹⁻³ in the form of chemical bonds. Hydrogen-based fuel cells can power vehicles and stationary devices; hydrogen could replace carbon or CO to reduce global CO₂ emissions from chemical and manufacturing processes. Polymer electrolyte membrane (PEM) electrolyzers can synthesize hydrogen near room temperature with rapid start up and shut down,³ ideally suited towards coupling with renewables. While hydrogen evolution, the cathode reaction occurring in a PEM electrolyzer, has minimal energy losses^{4,5}, the anodic reaction, i.e. oxygen evolution, is kinetically sluggish and limits the efficiency^{6,7}.



The combination of an acidic environment and very positive (oxidizing) potentials sets severe constraints on the choice of catalysts for PEM electrolyser anodes. Only oxides based on Ir^{8,9} show reasonable activity and stability, even though they still corrode at low, yet appreciable rate¹⁰⁻¹³. Oxides based on Ru are more active but less stable than those based on Ir^{12,14-17}. RuO₂ corrodes via the following reaction¹⁸:



Mixed oxides of Ru and Ir exhibit a better compromise between activity and stability, forming the basis for the dimensionally stabilised anode, used extensively in the chloro-alkali industry^{16,19,20}.

Several reports have shown that oxygen evolution on RuO₂ is always associated with some degree of dissolution^{12,18,21-24}. However, the Faradaic selectivity to RuO₂ corrosion varies over many orders of magnitude, depending on the pretreatment: ~0.01% in the case of sputter deposited thin films in 0.05 M H₂SO₄¹³ while it reaches values as high as ~15% for metallic Ru⁹, also in 0.05 M H₂SO₄, and ~10% for oriented SrRuO₃ in 0.1 M KOH²² (Figure 1). Figure 1 shows that RuO₂ obtained by thermal annealing^{11,13,25-27} present, on average, 2-3 orders of magnitude lower corrosion rates than metallic Ru^{9,11,18,21,26,27}, perovskite oxides containing Ru^{22,28}, hydrated RuO₂²⁶ or plasma-treated RuO₂²⁵. Furthermore, there is no clear distinction between the dissolution rates reported in acid versus alkaline electrolytes.

Over three decades ago, Kötz et al. proposed that RuO₂ dissolution and oxygen evolution share a common reaction pathway and the same intermediates²⁹. To the best of our knowledge, all studies on Ru-based oxides, thus far, have indeed suggested a correlation between dissolution rates and activity.^{9,11,18,22,29,30} Markovic¹² and co-workers have gone so far to argue that dissolution and oxygen evolution activity are *universally* correlated on *all* noble metal surfaces. Schmidt and co-workers³¹ used a thermodynamic argument to explain this correlation; suggesting that O₂ evolution degrades the catalyst by discharging oxide anions.

Vukovic *et al.* electrodeposited Ru electrode. Type A electrode: as prepared electrode, Type B electrode: electrochemical activation of type A. Ru dissolution measured in 0.5 M H₂SO₄ using RRDE. [g] Kim *et al.* measured Ru dissolution from SrRuO₃ in 0.1 M KOH held at potentials from 1.2 to 1.6 V_{RHE} for 60 seconds each using ICP. [h] Paoli *et al.* for Ru dissolution from plasma treated and thermally annealed RuO₂ nanoparticles in 0.05 M H₂SO₄ using RRDE [i] Frydendal *et al.* for Ru dissolution from thermally prepared sputter deposited thin films in 0.05 M H₂SO₄ using ICP and EQCM at a constant potential of 1.8 V_{RHE}. [This work] Further information can be found in Supplementary Information

Earlier DFT-based studies suggest that the reaction proceeds through a series of proton-coupled electron transfers, via the intermediates *OH, *O and *OOH (where * indicates an adsorbed species)^{32,33}. The calculations suggest that RuO₂ has the highest activity of pure oxides because it has the most optimal compromise in binding between these different intermediates. They also indicate that the active site on the RuO₂ surface is a coordinately unsaturated site (CUS), located on terraces.

DFT simulations also suggest that undercoordinated sites, such as steps or kinks, are more likely to corrode than terrace sites, both on noble metal surfaces³⁴, and oxides^{35,36}. Removing a terrace site requires the scission of more bonds than an undercoordinated site. Notably, recent DFT calculations by Dickens and Nørskov suggested that such undercoordinated sites are also the most catalytically active sites³⁷, in contrast to the aforementioned earlier studies^{8,38,39}.

However, our own experiments support the notion that the terrace-bound CUS sites are the active sites, as opposed to undercoordinated sites. Our in-operando surface X-ray diffraction measurements detected adsorbed *OO species on the

CUS sites under oxygen evolution conditions; presumably these constitute the precursor to gas phase O_2 molecules⁴⁰. Moreover, on oriented RuO_2 thin films in 0.1 M KOH, the oxygen evolution activity scales with the number of CUS sites on a bulk-terminated surface⁴¹.

Summarising the above, there is significant controversy in the literature over the extent to which oxygen evolution is intrinsically related to dissolution. This question is of critical importance, as effective strategies to stabilise the catalysts require that activity and stability be decoupled from each other^{16,35,36}.

In the current study, we probe the oxygen evolution activity of numerous different RuO_2 catalysts in 0.05 M H_2SO_4 ; these include (i) thin films oriented in the (100), (001), (101), and (111) directions (previously tested in 0.1 M KOH^{8,38,39}) (ii) single crystalline $RuO_2(110)$ ^{41,42} and (iii) commercial RuO_2 particles. We have quantified the amount of RuO_2 being dissolved in parallel to oxygen evolution, using inductively coupled plasma mass spectrometry (ICP-MS). In particular, we aim to address the following questions: (a) how does the OER activity compare between RuO_2 well-defined surfaces and particles, (b) is the corrosion of RuO_2 structure sensitive under oxygen evolution conditions? and (c) to what extent are activity and dissolution correlated on RuO_2 surfaces?

Results

We first established the catalytic activity of the different RuO₂ surfaces investigated in this study, namely the (101), (111) and (001) oriented thin films and the (110) single crystal. Schematics of the bulk terminated surfaces are shown in Figure 2a. The mean value of the current density at 1.6V_{RHE}, taken from the first CV recorded, ranks as follows: (111) thin film < (110) single crystal < particles < (101) thin film < (001) thin film (Figure S1). In a rutile structure, Ru can form bonds with a total of 6 atoms. The Ru_{CUS} at the (110) and (101) facets is linked by 5 Ru-O bonds to the rest of the structure, providing one surface site for the OER. However, the Ru_{CUS} at the (001) and (111) facet forms only 4 Ru-O bonds, providing 2 empty surface sites. Consistent with our earlier reports in 0.1 M KOH^{8,38,39}, Figure 2b shows that the initial activity in 0.05 M H₂SO₄ scales with the proportion of CUS Ru-O bonds.

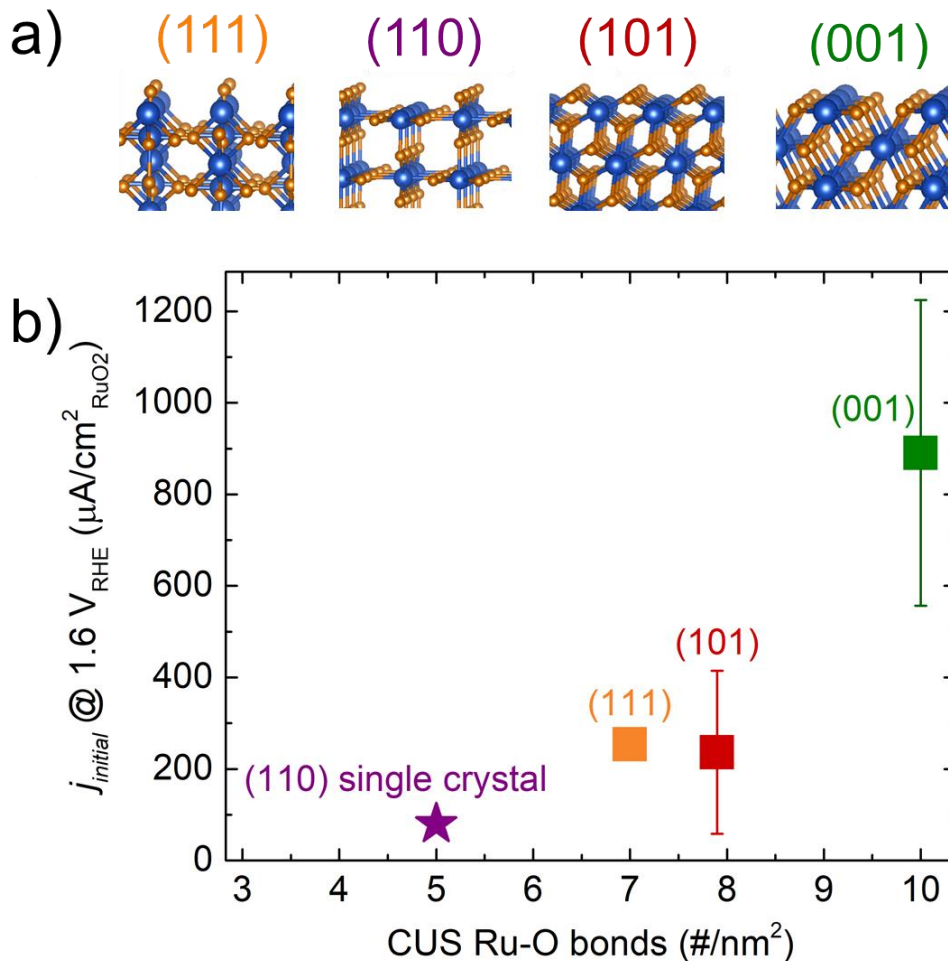


Figure 2. a) Schematics of the (111), (110), (101) and (001) surface and b) average current density measured the first cyclic voltammogram in 0.05 M H₂SO₄ over 2 hours for the (001), (111) and (101) oriented thin films and (110) single crystal, as a function of the number of CUS Ru-O bonds per nm².

Corrosion measurements on preferentially oriented thin films and RuO₂ particles were performed at 1.6 V_{RHE} for 2h. Stability test from 1.46 to 1.7 V_{RHE} using the RuO₂ particles and at 1.7 V_{RHE} for the well-defined surfaces are also available in Figure S2-3 and Figure S4, respectively. In order to evaluate the behavior of the samples for longer periods of time, the oriented thin films that were first subjected

to the stability test at 1.6 V_{RHE} were subjected to a second test, using the same experimental protocol (e.g. cycling etc, followed by the potentiostatic stability test, see Experimental). Additionally, a (110) single crystal was measured in the same experimental conditions and compared to the oriented thin films. Figure 3a and c show the OER currents measured for the first and second stability test at 1.6 V_{RHE} . The insets, respectively, show the amount of Ru dissolved during each experiment.

The first stability test shows a decay in the total current for the (001), (101) and (111) thin films over the 2 hours. On these films, any differences in total current densities between the different orientations is diminished by the end of the test. Conversely, the activity of the (110) single crystal at the end of the stability test is higher than the initial activity: this increase occurs during the first ~40 minutes, before reaching a steady state. The amount of Ru dissolved into the electrolyte increases in the following order: (110) single crystal < (111) thin film < (101) thin film < (001) thin film. The Faradaic efficiency towards RuO_x dissolution, relative to the total current density, is less than ~0.3% for the (111) surface, ~ 0.2% for the (101) surface and ~ 0.1% for the (001) surface. The (110) single crystal and the particles have the lowest Faradaic efficiency towards corrosion, at ~ 0.02% and ~ 0.01%, respectively (Figure1). We assume that the remainder of the current is consumed by O_2 evolution.

The second stability test at 1.6 V_{RHE} (Figure 3c and d) reveals striking differences from the first (Figure 3a and b). In the second test, all surfaces exhibit an initial current density significantly higher than for the first test after 2h. On the other hand, the dissolution rates are much lower than the first test. For example, on the (001)

film, 5 times less Ru dissolves into solution than during the first test. While the average current densities on the (001) thin film and (110) single crystal are similar, the corrosion rates are quite distinct. Moreover, the (110) single crystal shows much higher activity during the second stability test; however, its corrosion rate is similar to the first test.

Figure 3e and f show the activity show the amount of Ru dissolved as a function of activity the first and second stability test. In the first test at 1.6 V_{RHE} , there is a positive correlation between activity and dissolution rates amongst the thin film samples. However, the particles and the single crystal show much lower values for the average activity than the films, and intermediate dissolution rates. The (110) single crystal and the RuO_2 particles have very similar average catalytic activity during the first stability test, at around $45 \mu A/cm^2$. This observation is consistent with the transmission electron microscopy and X-ray diffraction analyses, which suggest the nanoparticles have a preferential orientation along the (110) planes (see Figure S5).

The second stability test reveals a totally different trend. While in the first test, there was a clear correlation between activity and stability amongst the thin films, there was no such correlation in the second test. The RuO_2 (110) single crystal surface showed the highest activity and stability (lowest amount of dissolved Ru). The activity of the oriented thin films remain somewhat similar during the second test, while the amount of Ru dissolved is significantly lower. The activity of the (110) single crystal and the RuO_2 particles increased while the total Ru dissolution decreased.

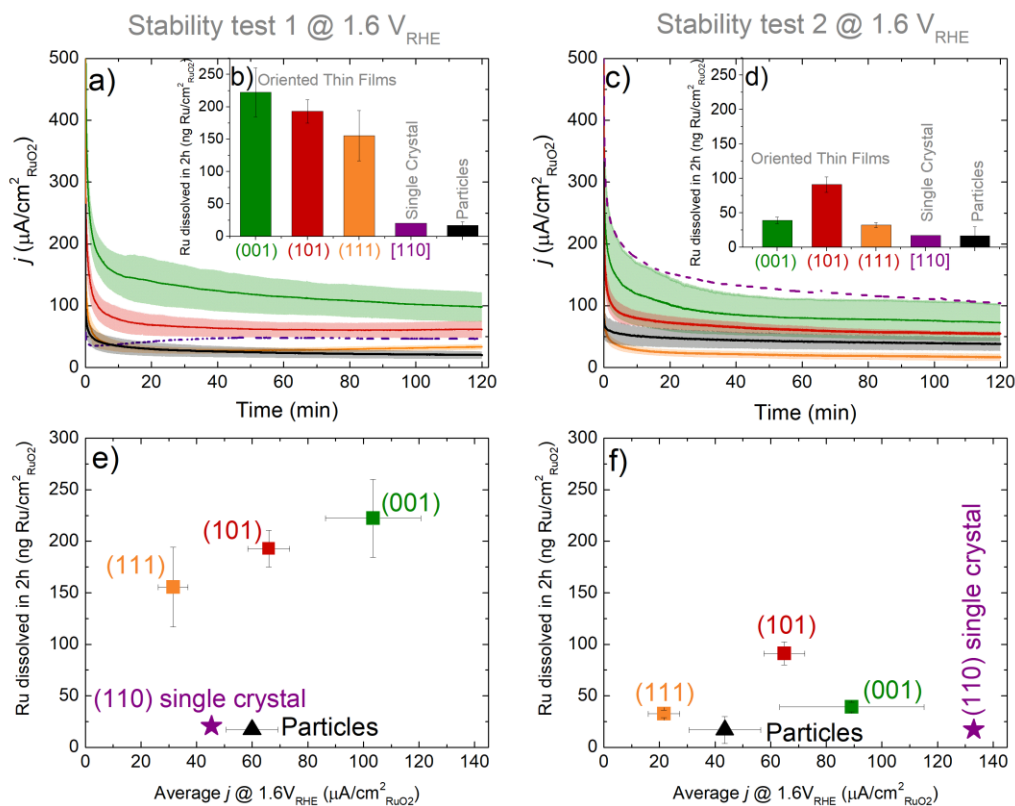


Figure 3. Two-hour potentiostatic measurements at 1.6 V_{RHE} in 0.05 M H₂SO₄ a) First stability and c) second stability test for the RuO₂ particles, and (111), (101), (110) and (001) surfaces. The insets (b,d) show the amount of Ru dissolved for each sample measured for their respective stability test. e) and f) Evaluation of the activity-stability relationship through the analysis of the average current at 1.6 V_{RHE} obtained from the stability tests as function of the amount of Ru dissolved for e) the first and f) second stability test at 1.6 V_{RHE}, respectively. The squares represented the (001), (101), (111) oriented thin films, the star the (110) single crystal and triangles the commercial RuO₂ particles.

Discussion

The fact that we always observe some degree of corrosion of RuO₂ particles and the well-defined thin films (Figure 3) is consistent with earlier reports in the literature^{11,12,18,22}. On average, the current corresponding to Ru dissolution is \leq 0.3% of the total OER current; we thus approximate the oxygen evolution current density to be equal to the total current density. This low Faradaic selectivity to corrosion is comparable to the values obtained from heat treated RuO₂ nanoparticles²⁵ or sputter deposited RuO₂¹³ under similar experimental conditions. The dissolution of RuO₂ translates into an increase in surface roughness, corroborated by the enhanced capacitance value, following the stability test (Figure S6-8). We calculate that the amount of Ru dissolved at 1.6 V_{RHE} over the duration of the 2 hour stability test ranges between 1.5 to 2.5 ML, depending on the surface orientation. Consequently, by the end of the first stability test, the surface termination may differ appreciably from the pristine surface. However, while Ru dissolution most probably modifies the surface termination, it only represents up to ~4% of the total amount of Ru in the 25 nm thin film.

In this work, we also note that the potentiostatic measurements suggest a loss in catalytic activity over time, implying that the freshly exposed surface, formed as a result of dissolution has a distinct RuO₂ termination to the as-prepared surface (Figures S6-8).

The decrease in activity during the chronoamperometry measurements can also be related to bubble formation. The static electrode configuration increases the

amount of bubbles at the surface of the catalysts, blocking more active sites than when using a rotating disk electrode setup. This phenomenon is evident when comparing the current density at the end of the 2 hours of the first stability test 1.6 V (Figure S9), relative to the current density at the beginning of the second stability test (Figure S9); bubbles were removed between tests.

We consider that our measurements underestimate the intrinsic dissolution rates of RuO₂ particles: the addition of Nafion to the ink preparation may result in lower mobility and higher local concentrations of Ru cations in solution, stabilising the surface.

Using the Ru dissolution rates and the current measured at constant potential, we aimed to establish a relationship between the oxygen evolution activity of RuO₂ and its stability. However, our finding contrasts strongly with other reports of Ru-based catalysts both tested in alkaline^{11,22} and acid^{11,12,38,43}, which show a consistent correlation between Ru dissolution rates and activity. The currents and RuO₂ dissolution rates from the first potentiostatic measurements at 1.6 V_{RHE} (Figure 3) decrease in the order (001) > (101) > (111). However, for the second test, there is no correlation between activity and stability. Our observations show that the corrosion rates are intrinsically dependent on the surface structure. When comparing the first stability test at 1.6V_{RHE} to the second one (Figure 3), it seems that the sites responsible from the OER activity and stability are decoupled; the change in RuO₂ dissolution rates between first and second stability tests are not matched by changes in activity. During the first stability test, the (001) surface has the most active and most unstable surface: the lower corrosion rate, but similar

oxygen evolution activity, during the second test, suggests that the sites most prone to corrosion have dissolved away, while the active sites for O₂ evolution remain.

Our results support the notion that the density of surface defects, such as undercoordinated sites, play a major role in controlling the stability of surface atoms^{3,11,34-36}. We suggest that (001) thin films contain the highest initial amount of surface defects, followed by the (101), (111) and (110). We hypothesize that the amount of defects on the as-received particles and single crystal is significantly lower than on the oriented thin film, explaining the much lower corrosion rate during the first corrosion test. In a similar manner, the RuO₂ particles and (110) single crystal have a similar initial activity but different initial corrosion rates. Our results show that RuO_x corrosion is generally much more pronounced during the first stability test. We conjecture that the amount of defects decreases over time before reaching a more stable state. Indeed, during the second stability test, with the exception of the (101) surface, there is little difference between the corrosion rates of the various surfaces.

Conclusions

The aim of this work was to investigate the possible relationship between activity and stability obtained from RuO₂ particles, preferentially oriented RuO₂ surfaces and a single crystal. The correlation between the activity and CUS Ru-O bonds reported in this study corroborates the previous results in base³⁸. We therefore propose that the active site for oxygen evolution in 0.05 M H₂SO₄ to be the Ru_{CUS} site.

We performed potentiostatic measurements of RuO₂ electrodes, coupled with ICP-MS to probe RuO₂ dissolution. On the basis of our results, we propose that surface structure not only has an important role in controlling activity, but also corrosion. From the first stability test at 1.6 V_{RHE}, it appears that corrosion of RuO₂ is structure sensitive. However, the active sites responsible for the oxygen evolution seem to be decoupled from the Ru sites that corrode the fastest. *In other words, activity and stability do not appear to be correlated on RuO₂ surfaces.* Based on the assumption that undercoordinated sites are responsible for dissolution, we conjecture that they are not the active sites for oxygen evolution under our experimental conditions. More detailed investigations of the surface structure are needed to elucidate the changes induced by the electrochemical environment^{41,44,45}.

The evidence we provide herein, suggesting that oxygen evolution and dissolution occur from different sites, has profound implications on future catalyst design. Such understanding corroborates our earlier work on the role of surface Ir in stabilising RuO_x¹⁶ and surface Ti on MnO_x³⁶, without compromising activity. Such

work points to ample opportunities for engendering further improvements to the stability of oxygen evolution catalysts under acidic conditions.

Experimental section:

Rutile RuO₂ films of the (100), (001), (101), and (111) orientations were grown by pulsed laser deposition (PLD), as reported previously^{8,38,39} and the experimental details are available in SI. The nanoparticles were purchased commercially (Sigma-Aldrich, 99.9% trace metal base). The (100) film was grown on a (001)-oriented SrTiO₃ substrate and the (001), (101) and (111) films were grown on (001), (101) and (111) oriented TiO₂ substrates. For the (110) orientation, a single crystal electrode was used, which was prepared by oxidative evaporation/redeposition of RuO₂ powders as described in reference^{42,46}. The particle-based film electrodes were prepared by ultrasonic dispersing RuO₂ powder (99.9% trace metal basis, Sigma-Aldrich) into tetrahydrofuran (≥99.9%, Sigma-Aldrich). A small amount of alkaline Nafion solution (3.3 % wt) was added to the ink to improve the adhesion to the fluorine doped tin oxide substrate. The ink was drop-casted and the film was dried over night.

All electrochemical measurements were conducted in a homemade three-compartment glass cell. The potentiostat used was a Bio-logic, WMP-2. A gold mesh was used as counter electrode, while an Hg/HgSO₄ electrode was used as reference electrode, calibrated to the reversible hydrogen electrode (RHE) in the same electrolyte. All measurements are reported vs RHE, as denoted by V_{RHE} . A

magnetic stirrer was used to prevent bubbles formation at the surface of the electrode as much as possible. The working electrode and counter electrode compartments were separated by a Nafion 117 membrane. The Ohmic drop measured using electrochemical impedance spectroscopy typically ranged from 50-60 Ω for the RuO₂ powder, 100-200 Ω for the oriented RuO_x thin films and ca. 40 Ω for the (110) single crystal. The Ohmic drop compensation was performed by online Ohmic drop correction, where 85% correction was applied. 0.05 M H₂SO₄ was prepared from ultrapure water (Milli-Q, 18 M Ω -cm) with sulfuric acid (99.999%, Sigma-Aldrich).

The activity of the RuO₂ particles was first evaluated by using cyclic voltammetry (CV) at 10 mV/s between 1 to 1.7 V_{RHE}. The OER activity measured from CV at 10 mV/s is comparable to that measured from galvanostatic measurements^{8,38,39}. Thus, we used CV to quantify OER activity in this study. A single stability test was then conducted at a given potential for 2 hours. The activity was again evaluated using one CV at 10 mV/s between 1 and 1.7 V_{RHE}.

The activity and stability of the oriented thin films and single crystal were evaluated in a similar manner. First, the activity was recorded using CVs at 10 mV/s between 1 and 1.6 V_{RHE}. A stability test was then performed at a constant potential of 1.6V_{RHE} for 2 hours. Finally, CVs at 10 mV/s between 1 and 1.6 V_{RHE} were recorded. For the CVs, the O₂ evolution activity was measured by averaging the current at any given *IR* corrected potential over the forward and backward scans.

With the exception of the (110) single crystal, 3 independent samples were tested for each measurement. The currents were normalised to the microscopic surface area of the catalyst, which was obtained from BET measurements for the nanoparticles and the geometric area for the oriented thin films and (110) single crystal. The BET measurements were performed using a Quantachrome ChemBET Pulsar from a single-point BET analysis performed after 12h outgassing at 150 °C. The surface area measurement were performed by measuring N₂ adsorption/desorption.

Because of the small geometric area of the oriented thin films and (110) single crystal, i.e. typically between 0.05 to 0.1 cm², and the relatively large volume of the electrolyte in the working compartment (10 mL), we were unable to accurately measure the Ru concentration for stability tests below 1.6 V_{RHE}. On the other hand, in the case of the oriented thin films, we found that if we subjected them to potentials positive of 1.7 V_{RHE}, we obtained poor reproducibility, accompanied by visible signs of delamination from the underlying substrate. Presumably, these conditions led to the exposure of the backing substrates, constituting SrTiO₃ and TiO₂, and their consequent corrosion. Such substrate effects are undesirable⁴⁷.

Although we tested the (100) oriented films, the high instability of these samples prevented us from measuring an accurate corrosion rate. For this reason, we only provide the initial activity herein (Figure S1a). Finally, for all samples the capacitance was measured using cyclic voltammetry at 100 mVs⁻¹ between 0.55 and 0.75 V_{RHE}, before and after the stability measurements.

The electrolyte was sampled three times for each sample: (i) prior to the immersion of the electrode, to ensure that the cell was not contaminated (ii) following the immersion and after recording the initial CV, to provide a baseline for the subsequent stability test (iii) after the stability test. Typically there was no difference between samples *i* and *ii*. The concentration of Ru was detected using inductively coupled plasma mass spectrometry (ICP-MS, Fischer Scientific, model iCAP-QC ICP-M) and quantified using a calibration curve (Figure S10). The amount of Ru measured was then normalized by the electrochemical surface area (ECSA) of the electrode. For all experiments, the concentration lied between 0.6 and 9.7 ppb. However, for the samples involving the particulate Ru, in around 10% of experiments, the signal intensity corresponded to a concentration 2-3 orders of magnitude higher than this value. We attributed this phenomenon to the presence of solid Ru nanoparticles being sampled by the instrument. The reliable quantification of Ru concentration using ICP-MS is only possible for dissolved species. Presumably, the particles had detached from the electrode as a result of corrosion or bubble evolution. We performed 2-3 samples of each electrolyte involving particulate Ru; we eliminated the samples with anomalously high values from our analysis.

Author Information and notes

Acknowledgements

We thank Binghong Han for TEM characterization of RuO₂ nanoparticles. We also thank Hoydoo You from the Argonne National Laboratory for providing us the (110) single crystal. C.R. gratefully acknowledges the Ministry of Higher Education and Science and Otto Mønsted's Fond for awarding her the visiting researcher grant. I.E.L.S. gratefully acknowledges the Department of Mechanical Engineering at MIT for the Peabody Visiting Associate Professorship. This work was supported by a research grant (9455) from VILLUM FONDEN. We also acknowledge UPCAT under the project no. 2015-1-12315 from energinet.dk. The film growth and structural characterization at ORNL were supported by the U.S. Department of Energy, Office of Science, Basic Energy Sciences, Materials Sciences and Engineering Division. This work is supported in part by the Skoltech-MIT Center for Electrochemical Energy and the Cooperative Agreement between the Masdar Institute, Abu Dhabi, UAE, and MIT (02/MI/MIT/CP/11/07633/GEN/G/ 00).

References

- (1) Montoya, J. H.; Seitz, L. C.; Chakthranont, P.; Vojvodic, A.; Jaramillo, T. F.; Nørskov, J. K. Materials for Solar Fuels and Chemicals. *Nat. Mater.* **2017**, *16* (1), 70–81.
- (2) Carmo, M.; Fritz, D. L.; Mergel, J.; Stolten, D. A comprehensive review on PEM water electrolysis. *Int. J. Hydrogen Energy* **2013**, *38* (12), 4901–4934.
- (3) Stamenkovic, V. R.; Strmcnik, D.; Lopes, P. P.; Markovic, N. M. Energy and fuels from electrochemical interfaces. *Nat. Mater.* **2016**, *16* (1), 57–69.
- (4) Durst, J.; Siebel, A.; Simon, C.; Hasché, F.; Herranz, J.; Gasteiger, H. A. New insights into the electrochemical hydrogen oxidation and evolution reaction mechanism. *Energy Environ. Sci.* **2014**, *7* (7), 2255–2260.
- (5) Zalitis, C. M.; Sharman, J.; Wright, E.; Kucernak, A. R. *Electrochimica Acta* Properties of the hydrogen oxidation reaction on Pt / C catalysts at optimised high mass transport conditions and its relevance to the anode reaction in PEFCs and cathode reactions in electrolyzers. *Electrochim. Acta* **2015**, *176*, 763–776.
- (6) Hong, W. T.; Risch, M.; Stoerzinger, K. A.; Grimaud, A.; Suntivich, J.; Shao-Horn, Y. Toward the rational design of non-precious transition metal oxides for oxygen electrocatalysis. *Energy Environ. Sci.* **2015**, *8* (5), 1404–1427 DOI: 10.1039/C4EE03869J.
- (7) Seh, Z. W.; Kibsgaard, J.; Dickens, C. F.; Chorkendorff, I.; Nørskov, J. K.;

- Jaramillo, T. F. Combining theory and experiment in electrocatalysis: Insights into materials design. *Science* **2017**, 355 (6321), eaad4998.
- (8) Stoerzinger, K. A.; Qiao, L.; Biegalski, M. D.; Shao-Horn, Y. Orientation-dependent oxygen evolution activities of rutile IrO₂ and RuO₂. *J. Phys. Chem. Lett.* **2014**, 5 (10), 1636–1641.
- (9) Paoli, E. A.; Masini, F.; Frydendal, R.; Deiana, D.; Schlaup, C.; Malizia, M.; Hansen, T. W.; Horch, S.; Stephens, I. E. L.; Chorkendorff, I. Oxygen evolution on well-characterized mass-selected Ru and RuO₂ nanoparticles. *Chem. Sci.* **2015**, 6 (1), 190–196.
- (10) Kasian, O.; Grote, J.-P.; Geiger, S.; Cherevko, S.; Mayrhofer, K. J. J. The common Intermediates of Oxygen Evolution and Dissolution Reactions during Water Electrolysis on Iridium. *Angew. Chemie Int. Ed.* **2017**.
- (11) Cherevko, S.; Geiger, S.; Kasian, O.; Kulyk, N.; Grote, J. P.; Savan, A.; Shrestha, B. R.; Merzlikin, S.; Breitbach, B.; Ludwig, A.; et al. Oxygen and hydrogen evolution reactions on Ru, RuO₂, Ir, and IrO₂ thin film electrodes in acidic and alkaline electrolytes: A comparative study on activity and stability. *Catal. Today* **2016**, 262, 170–180.
- (12) Danilovic, N.; Subbaraman, R.; Chang, K. C.; Chang, S. H.; Kang, Y. J.; Snyder, J.; Paulikas, A. P.; Strmcnik, D.; Kim, Y. T.; Myers, D.; et al. Activity-stability trends for the oxygen evolution reaction on monometallic oxides in acidic environments. *J. Phys. Chem. Lett.* **2014**, 5 (14), 2474–2478.

- (13) Frydendal, R.; Paoli, E. A.; Knudsen, B. P.; Wickman, B.; Malacrida, P.; Stephens, I. E. L.; Chorkendorff, I. Benchmarking the Stability of Oxygen Evolution Reaction Catalysts: The Importance of Monitoring Mass Losses. *ChemElectroChem* **2014**, *1* (12), 2075–2081.
- (14) Kötz, R.; Stucki, S. Stabilization of RuO₂ by IrO₂ for anodic oxygen evolution in acid media. *Electrochem. Acta* **1986**, *31* (10), 1311–1316.
- (15) Cherevko, S.; Reier, T.; Zeradjanin, A. R.; Pawolek, Z.; Strasser, P.; Mayrhofer, K. J. J. Stability of nanostructured iridium oxide electrocatalysts during oxygen evolution reaction in acidic environment. *Electrochem. commun.* **2014**, *48*, 81–85.
- (16) Escudero-Escribano, M.; Pedersen, A. F.; Paoli, E. A.; Frydendal, R.; Friebel, D.; Malacrida, P.; Rossmeisl, J.; Stephens, I. E. L.; Chorkendorff, I. The Importance of Surface IrO_x in Stabilizing RuO₂ for Oxygen Evolution. *J. Phys. Chem. B* **2018**, *122* (2), 947–955.
- (17) Danilovic, N.; Subbaraman, R.; Chang, K. C.; Chang, S. H.; Kang, Y.; Snyder, J.; Paulikas, A. P.; Strmcnik, D.; Kim, Y. T.; Myers, D.; et al. Using surface segregation to design stable Ru-Ir oxides for the oxygen evolution reaction in acidic environments. *Angew. Chemie - Int. Ed.* **2014**, *53* (51), 14016–14021.
- (18) Vukovic, M. Rotating Ring-Disc Electrode Study of the Enhanced Oxygen Evolution on an Activated Ruthenium Electrode. *J. Chem. Soc., Faraday Trans* **1990**, *86* (22), 3743–3746.

- (19) Beer, H. B. The Invention and Industrial Development of Metal Anodes 1. **1980**.
- (20) Trasatti, S. Electrocatalysis: understanding the success of DSA®. *Electrochim. Acta* **2000**, 45 (15–16), 2377–2385.
- (21) Chang, S. H.; Connell, J. G.; Danilovic, N.; Subbaraman, R.; Chang, K.-C.; Stamenkovic, V. R.; Markovic, N. M. Activity-stability relationship in the surface electrochemistry of the oxygen evolution reaction. *Faraday Discuss.* **2014**, 176 (0), 125–133.
- (22) Chang, S. H.; Danilovic, N.; Chang, K.-C.; Subbaraman, R.; Paulikas, A. P.; Fong, D. D.; Highland, M. J.; Baldo, P. M.; Stamenkovic, V. R.; Freeland, J. W.; et al. Functional links between stability and reactivity of strontium ruthenate single crystals during oxygen evolution. *Nat. Commun.* **2014**, 5 (4191), 1–9.
- (23) Lopes, P. P.; Strmcnik, D.; Tripkovic, D.; Connell, J. G.; Stamenkovic, V.; Markovic, N. M. Relationships between Atomic Level Surface Structure and Stability/Activity of Platinum Surface Atoms in Aqueous Environments. *ACS Catal.* **2016**, 6 (4), 2536–2544.
- (24) Cherevko, S.; Zeradjanin, A. R.; Topalov, A. a.; Kulyk, N.; Katsounaros, I.; Mayrhofer, K. J. J. Dissolution of noble metals during oxygen evolution in acidic media. *ChemCatChem* **2014**, 6 (8), 2219–2223.
- (25) Paoli, E. A.; Masini, F.; Frydendal, R.; Deiana, D.; Malacrida, P.; Hansen,

- T. W.; Chorkendorff, I.; Stephens, I. E. L. Fine-tuning the activity of oxygen evolution catalysts: The effect of oxidation pre-treatment on size-selected Ru nanoparticles. *Catal. Today* **2016**, *262*, 57–64.
- (26) Tamura, H.; Iwakura, C. Metal oxide anodes for oxygen evolution. *Int. J. Hydrogen Energy* **1982**, *7* (11), 857–865.
- (27) Hodnik, N.; Jovanovič, P.; Pavlišič, A.; Jozinović, B.; Zorko, M.; Bele, M.; Šelih, V. S.; Šala, M.; Hočevar, S.; Gaberšček, M. New insights into corrosion of ruthenium and ruthenium oxide nanoparticles in acidic media. *J. Phys. Chem. C* **2015**, *119* (18), 10140–10147.
- (28) Kim, B. J.; Abbott, D. F.; Cheng, X.; Fabbri, E.; Nachttegaal, M.; Bozza, F.; Castelli, I. E.; Lebedev, D.; Schäublin, R.; Copéret, C.; et al. Unraveling Thermodynamics, Stability, and Oxygen Evolution Activity of Strontium Ruthenium Perovskite Oxide. *ACS Catal.* **2017**, *7* (5), 3245–3256.
- (29) Kötz, R.; Stucki, S.; Scherson, D.; Kolb, D. M. In-situ identification of RuO₄ as the corrosion product during oxygen evolution on ruthenium in acid media. *J. Electroanal. Chem.* **1984**, *172* (1–2), 211–219.
- (30) Reier, T.; Nong, H. N.; Teschner, D.; Schlögl, R.; Strasser, P. Electrocatalytic Oxygen Evolution Reaction in Acidic Environments - Reaction Mechanisms and Catalysts. *Adv. Energy Mater.* **2017**, *7* (1).
- (31) Binniger, T.; Mohamed, R.; Waltar, K.; Fabbri, E.; Levecque, P.; Kötz, R.; Schmidt, T. J. Thermodynamic explanation of the universal correlation

- between oxygen evolution activity and corrosion of oxide catalysts. *Sci. Rep.* **2015**, 5 (1), 12167.
- (32) Rossmeisl, J.; Qu, Z. W.; Zhu, H.; Kroes, G. J.; Nørskov, J. K. Electrolysis of water on oxide surfaces. *J. Electroanal. Chem.* **2007**, 607 (1–2), 83–89.
- (33) Man, I. C.; Su, H. Y.; Calle-Vallejo, F.; Hansen, H. A.; Martínez, J. I.; Inoglu, N. G.; Kitchin, J.; Jaramillo, T. F.; Nørskov, J. K.; Rossmeisl, J. Universality in Oxygen Evolution Electrocatalysis on Oxide Surfaces. *ChemCatChem* **2011**, 3 (7), 1159–1165.
- (34) Jinnouchi, R.; Toyoda, E.; Hatanaka, T.; Morimoto, Y. First principles calculations on site-dependent dissolution potentials of supported and unsupported Pt particles. *J. Phys. Chem. C* **2010**, 114 (41), 17557–17568.
- (35) Man, I. Theoretical study of Photo-Catalytic oxygen evolution, Technical University of Denmark, 2011.
- (36) Frydendal, R.; Paoli, E. A.; Chorkendorff, I.; Rossmeisl, J.; Stephens, I. E. L. Toward an Active and Stable Catalyst for Oxygen Evolution in Acidic Media: Ti-Stabilized MnO₂. *Adv. Energy Mater.* **2015**, 5 (22).
- (37) Dickens, C. F. A Theoretical Investigation into the Role of Surface Defects for Oxygen Evolution on RuO₂. **2017**.
- (38) Stoerzinger, K. A.; Diaz-Morales, O.; Kolb, M.; Rao, R. R.; Frydendal, R.; Qiao, L.; Wang, X. R.; Halck, N. B.; Rossmeisl, J.; Hansen, H. A.; et al. Orientation-Dependent Oxygen Evolution on RuO₂ without Lattice

- Exchange. *ACS Energy Lett.* **2017**, 2 (4), 876–881.
- (39) Stoerzinger, K. A.; Rao, R. R.; Wang, X. R.; Hong, W. T.; Rouleau, C. M.; Shao-Horn, Y. The Role of Ru Redox in pH-Dependent Oxygen Evolution on Rutile Ruthenium Dioxide Surfaces. *Chem* **2017**, 2 (5), 668–675.
- (40) Pedersen, A. F.; Escudero-Escribano, M.; Sebok, B.; Bodin, A.; Paoli, E. A.; Frydendal, R.; Friebel, D.; Stephens, I. E. L.; Rossmeisl, J.; Chorkendorff, I.; et al. Operando XAS Study of the Surface Oxidation State on a Monolayer IrO_x on RuO_x and Ru Oxide Based Nanoparticles for Oxygen Evolution in Acidic Media. *J. Phys. Chem. B* **2017**, acs.jpcc.7b06982.
- (41) Rao, R. R.; Kolb, M. J.; Halck, N. B.; Pedersen, A. F.; Mehta, A.; You, H.; Stoerzinger, K. A.; Feng, Z.; Hansen, H. A.; Zhou, H.; et al. Towards identifying the active sites on RuO₂ (110) in catalyzing oxygen evolution. *Energy Environ. Sci.* **2017**, 0–13.
- (42) Lister, T. E.; Chu, Y.; Cullen, W.; You, H.; Yonco, R. M.; Mitchell, J. F.; Nagy, Z. Electrochemical and X-ray scattering study of well defined RuO₂ single crystal surfaces. *J. Electroanal. Chem.* **2002**, 524–525, 201–218.
- (43) Frydendal, R.; Busch, M.; Halck, N. B.; Paoli, E. A.; Krtil, P.; Chorkendorff, I.; Rossmeisl, J. Enhancing activity for the oxygen evolution reaction: The beneficial interaction of gold with manganese and cobalt oxides. *ChemCatChem* **2015**, 7 (1), 149–154 DOI: 10.1002/cctc.201402756.

- (44) Hussain, H.; Tocci, G.; Woolcot, T.; Torrelles, X.; Pang, C. L.; Humphrey, D. S.; Yim, C. M.; Grinter, D. C.; Cabailh, G.; Bikondoa, O.; et al. Structure of a model TiO₂ photocatalytic interface. *Nat. Mater.* **2016**, *16* (4), 461–466.
- (45) Li, T.; Kasian, O.; Cherevko, S.; Zhang, S.; Geiger, S.; Scheu, C.; Felfer, P.; Raabe, D.; Gault, B.; Mayrhofer, K. J. J. Atomic-scale insights into surface species of electrocatalysts in three dimensions. *Nat. Catal.* **2018**, *1* (April), 300–305.
- (46) Lister, T. E.; Tolmachev, Y. V.; Chu, Y.; Cullen, W. G.; You, H.; Yonco, R.; Nagy, Z. Cathodic activation of RuO₂ single crystal surfaces for hydrogen-evolution reaction. *J. Electroanal. Chem.* **2003**, *554–555* (1), 71–76 DOI: 10.1016/S0022-0728(03)00048-2.
- (47) Geiger, S.; Kasian, O.; Mingers, A. M.; Nicley, S. S.; Haenen, K.; Mayrhofer, K. J. J.; Cherevko, S. Catalyst Stability Benchmarking for the Oxygen Evolution Reaction: The Importance of Backing Electrode Material and Dissolution in Accelerated Aging Studies. *ChemSusChem* **2017**, *10* (21), 4140–4143.

Paper III

**Impact of Size and Lattice Oxygen on Water
Oxidation on NiFeO_xH_y**

Impact of Size and Lattice Oxygen on Water Oxidation on NiFeO_xH_y

C. Roy,^{1§} B. Sebök,^{1§} S. B. Scott,^{1§} E. M. Fiordaliso,² J. E. Sørensen,¹ A. Bodin,¹ D. B. Trimarco,¹ C. D. Damsgaard,² P.C.K. Vesborg,¹ O. Hansen,³ I.E.L. Stephens,^{1,4} J. Kibsgaard,¹ and I. Chorkendorff¹

¹: SurfCat, Department of Physics, Technical University of Denmark, Fysikvej 311, DK-2800 Kgs. Lyngby

²: Center for Electron Nanoscopy, Technical University of Denmark, Fysikvej 307 and 314, DK-2800 Kgs. Lyngby

³: Department of Micro- and Nanotechnology, Technical University of Denmark, Ørstedes Plads B.344, DK-2800 Kgs. Lyngby

⁴: Department of Materials, Imperial College London, Royal School of Mines Exhibition Road, London, SW7 2AZ – UK

§ These authors contributed equally to this work

Correspondence to: Prof. Ib Chorkendorff (ibchork@fysik.dtu.dk)

Abstract

Ni(Fe)O_xH_y are the most active catalysts for oxygen evolution in base. For this reason, they are used widely in alkaline electrolyzers. Several open questions remain regarding the reason for their exceptionally high catalytic activity. In this model study, we measure activity trends of mass-selected NiFe nanoparticles for oxygen evolution in 1 M KOH. We complement our activity measurements with electrochemistry-mass spectrometry, taken in operando, and transmission electron microscopy and low energy ion scattering spectroscopy, taken ex situ. Using isotope labelling experiments, we discover that bulk lattice oxygen does not participate in the reaction. Consequently, we attribute the high activity exclusively to surface processes. On this basis, we conclusively determine that the turnover frequency is 6.2 s⁻¹ at an overpotential of 0.3 V, which is, to the best of our knowledge, the highest reported for oxygen evolution in alkaline solution.

Introduction

Renewable energy technologies, such as wind turbines and solar panels, hold the potential to satisfy rising global energy demand while mitigating CO₂ emissions^{1,2}. Because of the intermittent nature of wind and solar energy, energy storage is one of the most critical challenges limiting their widespread implementation. One possibility is to store the energy in chemical bonds³. Thus far, one of the most promising means of converting electricity to fuels is water electrolysis where H₂ and O₂ gasses are formed⁴. Their recombination to provide electrical energy has only water as by-product, making it a clean process.

The hydrogen evolution reaction (HER), which takes place on the cathode side during water electrolysis, is possible at minimal energy losses^{5,6}. However, the slow reaction kinetics of the anodic reaction, the oxygen evolution reaction (OER) involving the transfer of 4 electrons and 4 protons, limits the efficiency of electrolyzers⁷. No electrode material approaches the equilibrium potential of 1.23 V on the reversible hydrogen electrode scale (V_{RHE})⁸⁻¹⁰, corresponding to the minimum energy needed for the reaction. Consequently, the widespread use of electrolyzers is contingent on improvements to the OER kinetics.

While Ni(Fe)O_xH_y mixed electrodes were already used in the 19th century in alkaline electrolyzers¹¹, the origin of the activity is still under intense debate^{12,13}. Pure NiO_xH_y is a very inactive catalyst, but the activity drastically increases when Fe intercalates into the structure¹²⁻¹⁶. The optimal activity is achieved for compositions between 10% and 50% Fe¹³. There are two main hypotheses regarding the role of Fe: (i) Ni is the active site and Fe affects its valency, making it more active^{17,18}; or (ii) Fe itself is the active site^{19,20}.

Some studies have indicated that the bulk, and not just the outer surface, of the catalyst is active. For example, Boettcher and co-workers reported a linear increase of the OER current as a function of catalyst loading up to ~450 monolayer equivalents²¹. The notion of bulk activity was supported by a recent theoretical study by Vojvodic and co-workers²², where they found similar thermodynamics for the OER intermediates in the bulk of the material as the (001) surface. On the other hand, Hu and co-workers showed that the apparent turnover frequency of NiFeO_x decreases at high loading,²³ either suggesting that thick samples are not as active or that the OER becomes readily transport limited.

Authors comparing the reduction wave during cyclic voltammetry of electrodeposited NiFeO_xH_y electrodes at ~1.3-1.4 V_{RHE} , attributed to Ni^{3+,4+}/Ni²⁺, with gravimetric analysis have concluded that nearly every nickel atom in the film contributes 1 e⁻ to the reduction wave^{21,24}. This indicates that every atom is electrochemically accessible, motivating the hypothesis that oxygen evolution occurs between the layered nanosheets of the layered double hydride structure of the catalyst, blurring the distinction between surface and bulk¹⁴. Both the possibility of such interlayer activity and the fact that NiFeO_xH_y films resulting from the electrodeposition techniques typically employed are highly porous complicate the

determination of the intrinsic activity, a critical step towards designing more efficient OER catalysts¹³. Determining the intrinsic activity therefore requires a model system with a known, well-defined surface area¹⁴.

Isotope-labeling studies using ¹⁸O and in operando mass spectrometry are a powerful tool to distinguish surface from bulk catalysis²⁵. Most of the catalysts probed using this method have revealed at least some degree of lattice oxygen involvement, including Au²⁶, IrO₂/Ti²⁷, Co₃O₄ spinel²⁸, Ru-based catalysts^{25,29,30} and perovskite materials with high metal-oxygen bond covalency³¹. Others, including oriented thin films of rutile RuO₂²⁹ and perovskites with low metal-oxygen bond covalency³¹, have not. Shao-Horn and co-workers observed that lattice exchange occurs with materials that have a catalytic activity that is pH dependent, indicating non-concerted proton-electron transfers in the OER mechanism³¹. Based on that argument, Ni(Fe)O_xH_y, which shows higher catalytic activity in stronger alkaline electrolyte, should also show participation of lattice oxygen³². However, to the best of our knowledge, no studies have probed Ni(Fe)O_xH_y using isotopically labeled water, even though they comprise the catalyst-of-choice for industrial water electrolysis.

Such isotope studies consist of preparing NiFe catalyst with one oxygen isotope (¹⁶O or ¹⁸O) or isotopic ratio, and then monitoring the O₂ products during oxygen evolution in an electrolyte having a different isotopic ratio using a mass spectrometer (¹⁶O₂ at m/z=32, ¹⁶O¹⁸O at m/z=34, and/or ¹⁸O₂ at m/z=36). If the O₂ evolved during OER has the same isotopic composition as the electrolyte, this is strong evidence that the oxygen atoms come directly from water molecules oxidized at the surface, and not from evolution of lattice oxygen. If the O₂ evolved during OER does not represent the isotopic composition of the electrode, this could represent either lattice exchange or evolution of low-mobility intercalated water molecules in-between the layered nanosheets.

Drawing a conclusion on participation of lattice oxygen requires high sensitivity and thorough characterization: (i) to ensure that the isotopic oxygen is included into the NiFe catalyst, and (ii) to correctly identify whether it is evolved during the OER, and iii) to quantify accurately that amount. To satisfy these requirements, we used a novel microchip-based electrochemistry-mass spectrometry technology that has uniquely high sensitivity. For example, it can detect of 0.05 monolayer equivalents of H₂ desorbing from a flat Pt surface with a signal-to-noise ratio of ~20.³³ We complement the in operando mass spectrometry experiments with post-characterization by low-energy ion scattering (LEIS), a surface sensitive technique, enabling the differentiation of ¹⁶O and ¹⁸O at the surface of the NiFe catalyst.

In the present study, we prepared size-selected NiFe particles using a magnetron nanoparticle source (Figure 1a). This physical synthesis method yields homogenous, monodisperse and chemically pure metallic particles, with a well-defined size and loading, ideal for fundamental studies^{34,35}. We compare the nanoparticles to NiFeO_xH_y

electrodeposited thin films. We test the catalytic activity using a rotating disk electrode assembly in 1.0 M KOH, where the particles oxidize in operando. We complement these experiments with X-ray photoelectron spectroscopy (XPS), high-resolution transmission electron microscopy (HRTEM) and scanning electron microscopy (SEM), and perform the isotope studies described above. As we will show, the nanoparticle samples function as a model system with a well-defined and tunable active catalytic surface area, which is the combined surface area of the approximately spherical nanoparticles.

Together, the nanoparticle model system, extensive characterization, and isotope studies enable us to answer two fundamental questions: (i) What is the intrinsic activity of the active sites on a well-defined surface of NiFeO_xH_y , and (ii) does lattice oxygen participate in the reaction?

Results

Figure 1b shows the size distribution of the as-prepared nanoparticles. The size distribution was determined by TEM as shown in Figure S1 (Supporting Information). As presented in Figure 1b, all nanoparticles have a regular and spherical shape regardless of their mass. The average particle diameters are 3.9 ± 0.5 nm, 5.4 ± 0.5 nm, 6.7 ± 0.6 nm, and 8.4 ± 0.5 nm, respectively, for the four selected masses, as shown in Figure 1c. A small population of larger particles with double the intended mass, resulting from doubly charged nanoparticles passing the mass filter can be seen, especially in case of the 8.4 nm particles.

The as-deposited 6.7 nm nanoparticles were characterized with the surface sensitive methods, LEIS and XPS, as shown in Figure 2a and b (green curve), respectively. The LEIS spectra show clear Ni and Fe peaks, which cannot be differentiated due to the small difference between their atomic masses. The nanoparticles were also characterized after electrochemical testing (blue curves), showing additional features identified as K, O and C most probably from residual KOH electrolyte, nanoparticle oxidation, and air exposure. For a detailed understanding of the catalyst composition and oxidation state, the nanoparticles were further probed using XPS. XPS spectra (Figure 2b) reveal metallic Ni and Fe. XPS analysis after electrochemical treatment shows that oxide and hydroxide states are formed for both Ni and Fe. More precisely, NiO and $\text{Ni}(\text{OH})_2$, and FeOOH and Fe_2O_3 , are identified from the Ni and Fe 2p peaks, respectively. The composition determined based on the XPS spectra shows similar Fe content before electrochemical testing to the target for the deposition, namely 25%, and an Fe content of $\sim 15\%$ after electrochemical testing for all nanoparticle sizes (Figure S2).

One challenge with nanoparticle catalysts is that they often coalesce under reaction conditions^{36–38}. In addition, the conditions under which OER electrodes operate can cause metal dissolution^{39,40}. As a first step to evaluate the stability and resistance towards corrosion and sintering, SEM images were acquired before and after OER at identical

locations to directly visualize any change in particle size or positions⁴¹. From the example images shown in Figure 2c taken before and after testing the activity, it can be seen that the 5.4 nm NiFe particles do not coalesce or dissolve during the 2 h potentiostatic measurement at 1.6 V_{RHE}. Most of the nanoparticles can be directly found in both images. To further probe the stability, a chronoamperometric measurement was performed at 1.6 V_{RHE}. As presented in Figure 3, the OER current was stable over 41 days (~1000 h). This result further confirms the stability of NiFe catalyst previously reported by stable chronoamperometric measurement at 10 mA/cm² over 24h^{42,43}.

To gain insight into the morphology and composition at the atomic level, we acquired identical location HRTEM images of particles deposited on graphene covered Au TEM grids both before and after two cyclic voltammetry cycles (CVs) at 10 mV/s up to 1.5 V_{RHE}. The electrochemical treatment was mild to avoid the corrosion of the carbon grid at more anodic potentials. Before OER, the NiFe nanoparticles show polycrystalline structure. An example image in Figure 4a shows a single particle in which the Ni₃Fe phase can be identified⁴⁴. Figure 4b and 4c show HRTEM images of the same nanoparticles before and after being electrochemically tested, respectively. We found that after electrochemical testing, the nanoparticles maintain their shape and their polycrystalline nature, as indicated by the non-uniform orientation of lattice fringes, and by the contrast difference caused by diffraction. We used EDX along with focused electron beam to map the dispersion of Ni and Fe in the particles using cross sectional line scans. The comparison of the Ni and Fe concentration before and after electrochemical testing shows that some of the Fe leaches out after OER (Figure S3).

Representative CVs of samples from each of the four nanoparticle size groups, taken after 2 hours at 1.6 V vs RHE, are plotted in Figure 5a showing a clear difference in activity for the different particle sizes. The smallest particles, i.e. 3.9 nm and 5.4 nm, provide the highest current normalized to the deposited metal mass. A significant OER current is observed starting from $U = \sim 1.5$ V_{RHE} (overpotential of $\eta = 270$ mV). Using what is typically attributed to Ni²⁺ to Ni^{3+/4+} redox couple¹³, we showed that the integral of the Ni reduction peak scales better with the calculated surface area than the total loading (Figure S4). Less than one electron is transferred per Ni atom in the larger nanoparticles. Figure 5b shows the average mass activity on deposited metal basis at $\eta = 270, 300$ and 370 mV as a function of particle size. The activity was taken from the current recorded at a scan rate of 10 mV/s. No obvious difference in trend is observed when comparing the mass activity as a function of size for different overpotentials.

To determine the intrinsic activity, we convert the activity to turnover frequency (TOF), i.e. the number of O₂ molecules produced per active site per unit time, using three estimates for the number of active sites. TOF_{bulk} assumes that all deposited Ni and Fe atoms are active, TOF_{redox} assumes one active site per electron transferred in the Ni reduction peak of the cyclic voltammogram, and TOF_{surface}, assumes that only the surface metal atoms of the nanoparticles are active sites (details of the calculations can be found in the supplementary

information). We also include the $\text{TOF}_{\text{redox}}$ calculated for $\text{NiFeO}_x\text{Hythin}$ films, for which the activity was measured by the same procedure as the nanoparticles (Figure S5).

The TOFs thus calculated show different trends with particle size. TOF_{bulk} is highest for the smaller particles, i.e. 5.4 nm and 3.9 nm, and lower for the larger particles. $\text{TOF}_{\text{redox}}$ and $\text{TOF}_{\text{surface}}$ do not show any obvious trends, though $\text{TOF}_{\text{redox}}$ has a larger scatter. Calculated surface area is thus a better predictor of activity than is the Ni redox feature or the total loading for the nanoparticle samples.

The $\text{TOF}_{\text{surface}}$ and TOF_{bulk} of the 5.4 nm NiFe nanoparticles were compared to state-of-the-art non-noble metal catalysts for the OER in alkaline media (Figure 6b). The reaction rate of 5.4 nm NiFe particles at 1.53 V_{RHE} ($\eta = 300\text{mV}$) of $6.2 \pm 1.6 \text{ s}^{-1}$ (TOF_{surf}) and $1.2 \pm 0.3 \text{ s}^{-1}$ (TOF_{bulk}) are among the highest reported for non-noble metal catalysts in alkaline electrolyte^{16,24,42,45–48}.

To provide further insight on which TOF represents the true intrinsic activity, we used three complimentary isotope labeling procedures, all on samples with 6.7 nm particles, referred to below as procedure *a*, *b*, and *c*, and illustrated schematically in Figure 7. Because of the natural oxidation of NiFe particles when exposed to air, we oxidized the catalyst in H_2^{16}O and performed OER in ^{18}O -based electrolyte (procedure *a*). We also oxidized the NiFe particles in H_2^{18}O (procedure *b*) and $^{18}\text{O}_2$ atmosphere (procedure *c*) to study the possible differences between hydroxide and oxide compounds.

In procedure *a*, ^{16}O is incorporated into the NiFe nanoparticles through cycling in 0.1 M KOH made from ultrapure water, and the oxygen evolution process takes place in 0.1 M KOH made from ^{18}O water (~97% ^{18}O). Due to the natural abundance of ^{16}O , this has the advantage that the nanoparticles can easily be prepared with 99.8% ^{16}O . On the other hand, the lower purity of ^{18}O -labeled water limits the sensitivity towards isotope exchange of the subsequent EC-MS measurement. In procedures *b* and *c*, ^{18}O is incorporated in the NiFe structure either by cycling in ^{18}O -labelled 0.1 M KOH electrolyte or by heating at 450 °C in the vacuum chamber in the presence of $^{18}\text{O}_2$ gas, respectively. This allows for greater sensitivity towards lattice exchange, but adds some uncertainty to the initial isotopic composition of the catalyst.

In procedure *a*, the sample of deposited particles were cycled in 0.1 M KOH made from ultrapure water until a stable CV was obtained, i.e. 20 cycles 0.5 -1.5 V_{RHE} . At this point we assumed that the catalyst is in the fully oxygenated active form, nominally $\text{M}(\text{}^{16}\text{OH})_2$ where $\text{M}=\text{Ni}_x\text{Fe}_{1-x}$. The electrode is then transferred at open-circuit voltage to a stagnant thin-layer cell filled with ^{18}O -labeled 0.1 M KOH for measurement by EC-MS. The first cycle up to 1.55 V_{RHE} and back to 0.5 V_{RHE} , is shown in Figure 8a, with the potential and current plotted in the bottom panel, and calibrated $m/z=34$ ($^{16}\text{O}^{18}\text{O}$) mass spectrometer signal plotted (red trace) in the top panel against a shared time axis. Coplotted with the measured $^{16}\text{O}^{18}\text{O}$ signal is the $^{16}\text{O}^{18}\text{O}$ signal expected due to oxidation of the electrolyte, which contains only ~97% ^{18}O (green dotted trace). The expected $^{16}\text{O}^{18}\text{O}$ signal is the measured $^{18}\text{O}_2$ ($m/z=34$) signal

multiplied by the steady-state $^{16}\text{O}^{18}\text{O}/^{18}\text{O}_2$ ratio. This ratio, as well as the calibration, were determined in operando by steady-state oxygen evolution (Figure S6). The measured and expected $^{16}\text{O}^{18}\text{O}$ coincide, indicating that all of the signal at $m/z=34$ can be explained by oxidation of the electrolyte.

To illustrate the sensitivity, we have included in Figure 8a the expected excess $m/z=34$ signal if 1% of the total ^{16}O contained by the catalyst, equivalent to approximately 10% of a monolayer, were released as $^{16}\text{O}^{18}\text{O}$. 1% of the total oxygen released 45 seconds corresponds to 0.2% of a ML per second, which is significantly above the detection limit. In comparison, the oxygen production rate in this experiment is calculated to be 19% ML per second. This proves that if even 1% of the OER activity were due to lattice oxygen evolution, it would be detectable.

The results of procedures *b* and *c* (Figure S7a-d) show similar results but because of high natural abundance of ^{16}O (99.8%) the sensitivity towards isotope exchange at $m/z=34$ and 36 is much higher. To determine whether the result is general, we also performed the isotope experiment (following procedure *a*) on a NiFe oxyhydroxide thin film, and again observed no lattice exchange (Figure S7e). Additionally, to prove that our setup is indeed sensitive enough to detect lattice exchange when it does take place, we performed the same experiment on IrO_2/Ti in acid, as described in Reference ²⁷, and reproduce their result of > 1 ML isotope exchange. This “positive” result is directly compared with the “negative” results for NiFeO_xH_y in Figure S8.

In procedure *a*, following EC-MS, the sample was rinsed in H_2^{18}O before being transferred back to vacuum for LEIS. The LEIS spectrum after OER, i.e. the purple line in Figure 8b, shows extra peaks when compared to the initial LEIS spectrum (black line) that we attribute to ^{16}O , ^{18}O , impurity Na and Mg salt deposits from the H_2^{18}O rinsing, and residual K from the electrolyte. The sample was then Ar-sputtered for 30 minutes before another LEIS spectrum was taken. This spectrum (blue line) shows an increased $^{16}\text{O}/^{18}\text{O}$ ratio, compared to the initial one. We therefore attribute the ^{18}O peak to residual K^{18}OH and/or other hydroxide salts on the surface of the sample and the ^{16}O peak to ^{16}O remaining in the catalyst. After both procedures *b* and *c*, the $^{18}\text{O}/^{16}\text{O}$ ratio in LEIS after OER, rinsing with ultrapure water, and sputtering, is approximately 1:1, with little to no K or other impurities, as shown in Figure S7. In both cases there is a clear ^{18}O signal even before sputtering, indicating that this isotope is present at the surface of the catalyst. The post-sputtering 1:1 ratio presumably reflects the nominal $\text{M}(^{18}\text{OH})(^{16}\text{OH})$ formula resulting from the experimental procedures as illustrated in Figure 7b and c. Because the natural abundance of ^{18}O is so low (0.2%), the presence of ^{18}O on the LEIS spectra in procedures *b* and *c* implies that it was incorporated during the catalyst preparation before OER, and not during transfer through air from EC-MS to LEIS.

Discussion

The results obtained from the identical location SEM (Figure 2c), in addition to the stable current over 1,000 hours (Figure 3) suggest the NiFeO_xH_y particles are stable against corrosion. The activity dependence on particle size is similar at 270, 300 and 370 mV overpotential (Figure 5); this observation suggests a kinetically controlled current. If lattice oxygen was participating in the reaction, we could anticipate that diffusion of reactants or products within the particles might play a role for the largest nanoparticles and at high current densities. This observation is also only valid if the diffusion of the reactants and products were sufficiently slow. However, we do not observe any sign of such effects. Furthermore, the activity of the particles normalized to surface area, i.e. the turnover frequency per surface metal atom (TOF_{surface}), does not change with particle size (Figure 6a). In contrast, the activity of the particles normalized to total mass, which is proportional to the turnover frequency per metal atom (TOF_{bulk}), decreases with increasing particle size. Differing Fe content cannot explain the observed trends (Figure S2b).

Finally, in-operando mass spectrometry and LEIS measurements for isotope experiments using three different approaches all indicate that oxygen is retained in the catalyst during OER, both in the bulk and, to at least some degree, on the surface of the catalyst as well. The significance of this result is two-fold: First, it provides strong evidence against activity below the outer surface, as this would involve lattice oxidation and/or oxidation of low-mobility intercalated water. Second, the oxygen evolution mechanism does not proceed via lattice oxygen.

Previous studies showing linear correlation between loading and activity have used porous electrodes without a well-defined outer surface²¹. Given the evidence presented here against bulk activity, we suggest that this observation can be explained by the surface area scaling linear with loading for these porous materials.

As mentioned previously, lattice exchange is material dependent. The phenomenon is observed with Co₃O₄²⁸, iridium-based catalysts²⁷ and few perovskites³¹. Besides being sensitive to the nature of the material, the lattice oxygen exchange seems to be also dependent on the structure. Indeed, in the case of oriented RuO₂ thin films, it was reported that the lattice exchange was only observed with RuO₂-based amorphous or nanocrystalline phases with undercoordinated edge-sites^{25,30}, and not with the rutile form²⁹. While we did not observe lattice exchange during OER in NiFe nanoparticles or an electrodeposited NiFe film, the results may not be generalizable to all synthesis methods. Furthermore, we cannot rule out that such phenomena could in principle occur at much higher potentials which, unfortunately, cannot yet be studied in our EC-MS setup, due to bubble formation.

The absence of participation of lattice oxygen in NiFeO_xH_y is in disagreement with the hypothesis that lattice exchange should occur with materials that have a catalytic activity that is pH-dependent on the hydrogen scale³¹, as this is the case for NiFeO_xH_y catalyst⁴⁹. In contrast, it provides evidence for a mechanism, such as that proposed by Bell and co-workers, in which the active metal site does not bind oxygen except during OER¹⁹. Finally,

based on these observations, we can conclude that that the best measure of intrinsic activity is $\text{TOF}_{\text{surface}}$, where the oxygen evolved is normalized by the surface of the particles.

Conclusion

In summary, we used well-characterized mass-selected nanoparticles of Ni and Fe as a model system to investigate their fundamental properties under oxygen evolution conditions. We provided insight into the reaction using low-energy ion scattering and the unique capabilities of the microchip-based electrochemistry-mass spectrometry setup. The particles show exceptionally high activity and stability over 1000 h at 1.6 V_{RHE}. Isotope-labeling experiments performed following three distinct approaches show that there is no participation of lattice oxygen in the oxygen evolution. This allows us to conclude that the active sites responsible for such exceptional activity are only located at the surface of the nanoparticles. With this knowledge, we can report a TOF of $6.2 \pm 1.6 \text{ s}^{-1}$ at $\eta=0.3\text{V}$ and thus set a new lower bound on the intrinsic activity achievable with NiFeO_xH_y-based OER catalysts. Further enhancements to the catalytic activity should focus on tailoring the surface, as opposed to bulk, chemistry.

Methods:

Preparation of mass-selected NiFe nanoparticles

NiFe nanoparticles were prepared using a noble gas-aggregation, magnetron sputtering nanoparticle source combined with a lateral time-of-flight mass filter (Figure 1a) capable of mass selection of the nanoparticles before deposition⁵⁰ (Nano-Beam 2011, Birmingham Instruments Ltd.) similar to the one described by Pratontep et al⁵¹. A 75 at% Ni/ 25 at% Fe sputtering target (99.95%, Kurt J. Lesker Ltd., UK) was used and the particles were deposited onto clean and smooth Au disks. The nanoparticle source is fully UHV compatible and the mass filter has a base pressure in the low 10^{-10} mbar region. The mass filter was set to be used with negatively charged particles, and to have a mass resolution of approx. $m/\Delta m=20$ to maximize the current of particles. The vast majority of the particles exiting the nanoparticle source is carrying a single charge, thus the current measured on the sample during the deposition together with the deposition time can be translated into the number of deposited particles. If not otherwise stated, the loading of the electrodes was 15% projected surface area coverage, which corresponds to a total metal mass loading of 50 - 125 ng meaning 315 – 785 ng/cm² loading in circular spots having 4.5 mm diameter depending on particle size.

Determination of particle size distributions

NiFe nanoparticles with masses of 120,000, 350,000, 950,000 and 2,000,000 amu were deposited onto Cu TEM grids covered with lacey carbon (300 mesh, Agar Scientific Ltd., UK). After deposition and transfer under atmospheric conditions, the particles were imaged in bright-field TEM mode in an FEI Tecnai T20 G² equipped with a thermionic electron source, using 200 keV acceleration voltage. The images were analyzed with ImageJ software to extract the average area of the particle projections, and a diameter was calculated assuming circular shape (Figure S1).

Electrochemical measurements

Electrochemical measurements were performed using a rotating disk electrode in a PTFE (Teflon) cell at 1,600 rpm in N₂-saturated 1.0 M KOH. A carbon rod was used as counter electrode, while a Hg/HgO electrode was used as reference electrode, which was calibrated to the reversible hydrogen electrode (RHE) in the same electrolyte saturated with 1 bar H₂ over a clean Pt mesh before each experiment. The Ohmic drop was measured by using electrochemical impedance spectroscopy over a range of 10-200,000 Hz at a AC amplitude of 10 mV. The high-frequency intercept was fitted to an equivalent circuit to obtain the Ohmic losses which typically ranged from 4 to 18 Ω . The Ohmic drop compensation was done by online Ohmic drop correction where 85% correction was applied. 1.0 M KOH was prepared from ultrapure water (Milli-Q, 18 M Ω cm) with KOH (Semiconductor grade, pellets, 99.9%).

The initial catalytic activity was measured by recording 5 cyclic voltammograms (CVs) at 10 mVs⁻¹ up to 1.6 V_{RHE} followed by a 2 hour potentiostatic measurement at 1.6 V_{RHE}. Finally, the activity was again assessed using CVs. The activity of the different samples for the oxygen evolution reaction presented in this work was taken from the last CV. For each experiment 3 independent samples were tested and the activity was averaged (see Figures S9, S10 and S11). The longer stability measurement was a static measurement at 1.6V_{RHE}, for which the NiFe particles were deposited onto a Au sheet. Because of the duration of this experiment, only 2 samples were tested. The mass activity was obtained by normalising the current with the total mass of Ni and Fe determined from the deposition current and time.

To compare the differences between lattice oxygen participation in NiFeO_xH_y nanoparticles and thin film, thin films of NiFeO_xH_y were electrodeposited. Using a three-electrode setup, a current of -0.2 mA/cm² for 5 min in an electrolyte of 0.1 M Ni(NO₃)₂·6H₂O and 5 mM FeCl₂. The composition determine by XPS indicates a mixed of 32\% Fe and 68\% Ni at the surface (See Figure S5).

Turnover frequency

To calculate the turnover frequency (TOF) we used the following formulas:

$$TOF(s^{-1}) = \frac{r_{O_2}}{\# \text{ of active sites}}$$

The rate of O₂ turnovers (r_{O_2} [s⁻¹]) was calculated from the raw current:

$$r_{O_2} = i \times \left(\frac{N_A}{zF} \right)$$

Where i (A) is the current, N_A is the Avogadro number (6.022×10^{23} O₂ molecules per mol O₂), z the number of electron involved in the evolution of 1 mol of O₂ and F (96,485 C/mol) the Faraday constant.

We determined a minimum (TOF_{min}) and a maximum (TOF_{max}) TOF based on two different assumptions on the number of active sites.

For the calculation of TOF_{min}, we assumed that all metal atoms deposited are active for OER. In order to calculate the total number of Ni and Fe metal atoms deposited on the surface ($N_{metal\ atom}^{total}$), the number of deposited particles ($N_{particles}$) were multiplied by the average number of atoms in each particle ($N_{metal}^{particle}$):

$$N_{metal\ atom}^{total} = N_{particles} \times N_{metal\ atom}^{particle}$$

$N_{particles}$ can be calculated from the deposition current ($I_{depo}[A]$), time of deposition ($t_{depo}[s]$) and the electric charge ($6.242 \cdot 10^{-18}$ electrons/C) using the following equation:

$$N_{particles} = I_{depo} \times t_{depo} \times C$$

Finally, to calculate the number of metal atoms in a particle, we used the deposited particle mass set by the mass filter ($m_{particle}[kg]$), the Avogadro constant ($N_A[mol^{-1}]$) and the average molar mass ($\overline{M_{Ni_xFe_{100-x}}}[kgmol^{-1}]$) using the composition determined from the XPS after electrochemical treatment for each sample.

$$N_{metalatom}^{particle} = \frac{N_A \times m_{particle}}{\overline{M_{Ni_xFe_{100-x}}}}$$

To calculate the TOF_{max}, the number of surface Ni and Fe atoms had to be calculated. The diameter of the nanoparticles was determined by TEM images, and use to calculate the surface area per particle ($A_{particle}$) assuming spherical shape. Finally, this area was multiplied by the total number of particles, $N_{particles}$, and the density of surface metal atoms to get the total number of surface Ni and Fe atoms. The assumed density of surface metal atoms (ρ_{atoms}) of 12.5 metal atoms per nm² is based on the metal-metal distance of 2.83 Å for NiFeO_xH_y measured *in-situ* under OER conditions¹⁹.

$$N_{surfaceatom}^{total} = N_{particles} \times \rho_{atoms} \times A_{particle}$$

X-ray Photoelectron Spectroscopy (XPS) and Low Energy Ion Scattering (LEIS) characterization:

LEIS (Figures S12-S13) and XPS spectra (Figures S14-S16) were recorded for each sample after deposition (without breaking the vacuum) and after activity testing. In order to get rid of the remaining electrolyte on the surface after the activity test, the samples were thoroughly rinsed with ultrapure water (18.2 MΩ cm) before loading into the UHV chamber in order to prevent the formation of a “thick” potassium layer hindering the detection of other elements.

For LEIS measurements 1 keV He⁺ ions from an Omicron ISE100 ion gun were used and the energy of the scattered ions was recorded with the same 7-channel analyser used for XPS measurement operated in constant retard ratio mode (with a retard ratio of 5). The LEIS spectra presented are normalized based on the intensity of the gold peak at approx. 925 eV.

For the XPS measurements unmonochromatized MgKα radiation from a SPECS XR50 dual filament X-ray gun was used. The electron energies were measured with an Omicron NanoSAM 7-channel energy analyser operated in constant pass energy mode. A pass

energy of 50 eV was chosen to increase the signal from the low loadings of nanoparticles. For each sample, a survey scan and detailed scans of Au 4f, O 1s, Ni 2p_{3/2} and Fe 2p_{3/2} were recorded. All the spectra were charge corrected based on the Au 4f_{7/2} peak, which we assumed to correspond to metallic Au at 84 eV binding energy. A Shirley background was subtracted from the detailed spectra presented and the intensities were normalised with the Au 4f peak area.

Identical location Scanning Electron Microscopy (SEM) imaging:

Identical location SEM imaging was performed on a sample containing 5.4 nm NiFe particles on the Au electrode after deposition and transfer under atmospheric conditions and after electrochemical testing. SEM images were acquired at 5 kV using an FEI Helios EBS3 microscope equipped with a field emission gun and a through-the-lens detector for high resolution imaging.

Identical location Transmission Electron Microscopy (TEM) imaging and Energy Dispersive Spectroscopy (EDX) line scans:

Identical location HRTEM images were recorded at 80 kV electron energy, using a FEI Titan E-Cell 80-300 ST TEM with a monochromated electron source and post objective aberration correction. For the identical location TEM studies particles were deposited on Au coated Cu TEM grids with suspended monolayer graphene layers (Quantifoil, Germany). After imaging, the grids were mounted to an RDE setup and subjected to 2 CVs at 10mVs⁻¹ between 1 and 1.5 V_{RHE} in 1 M KOH. After the electrochemical oxidation the particles were transferred back to the TEM and imaged a second time. EDX line scans were recorded using an Oxford silicon drift detector on random particles before and after electrochemical oxidation.

Electrochemical Mass Spectrometry (EC-MS) experiments:

In order to investigate oxygen exchange between the NiFe particles and the electrolyte, isotopically labeled electrolyte (with ¹⁸O) and electrochemical mass spectrometry were used. The EC-MS setup is based on a microfabricated membrane coated with a fluorinated polymer and a well defined capillary and it is described elsewhere³³. Below the membrane, a small cavity is pressurized with He carrier gas and together with the capillary forces the electrolyte is kept out of the chip. The cavity is connected to a vacuum chamber equipped with a quadrupole mass spectrometer (Pfeiffer Vacuum QMA 125) through a well-defined microfabricated capillary limiting the flow of molecules to a level what can be handled by a single turbomolecular pump. For the experiments a self-designed stagnant layer electrochemical cell was used where the electrolyte thickness was 100 μm which, together with the design of the vacuum chamber and microchip, gives a time response below 1 s. Details of the experimental method and setup used can be found elsewhere³³. All

experiments were performed using 0.1 M KOH electrolyte either made with ultrapure water (natural isotope distribution) or ^{18}O enriched water (97.2% H_2^{18}O , 1.3% H_2^{17}O , 1.5% H_2^{16}O , Medical Isotopes). The mass spectrometer signals were calibrated internally for each experiment, as was steady-state ratio of $m/z=34$ to $m/z=36$ for procedure a. The raw data for these calibrations are shown (for procedure a) in Figure S6.

Data availability:

The data that support the plots within this paper and other findings of this study are available from the corresponding author upon reasonable request.

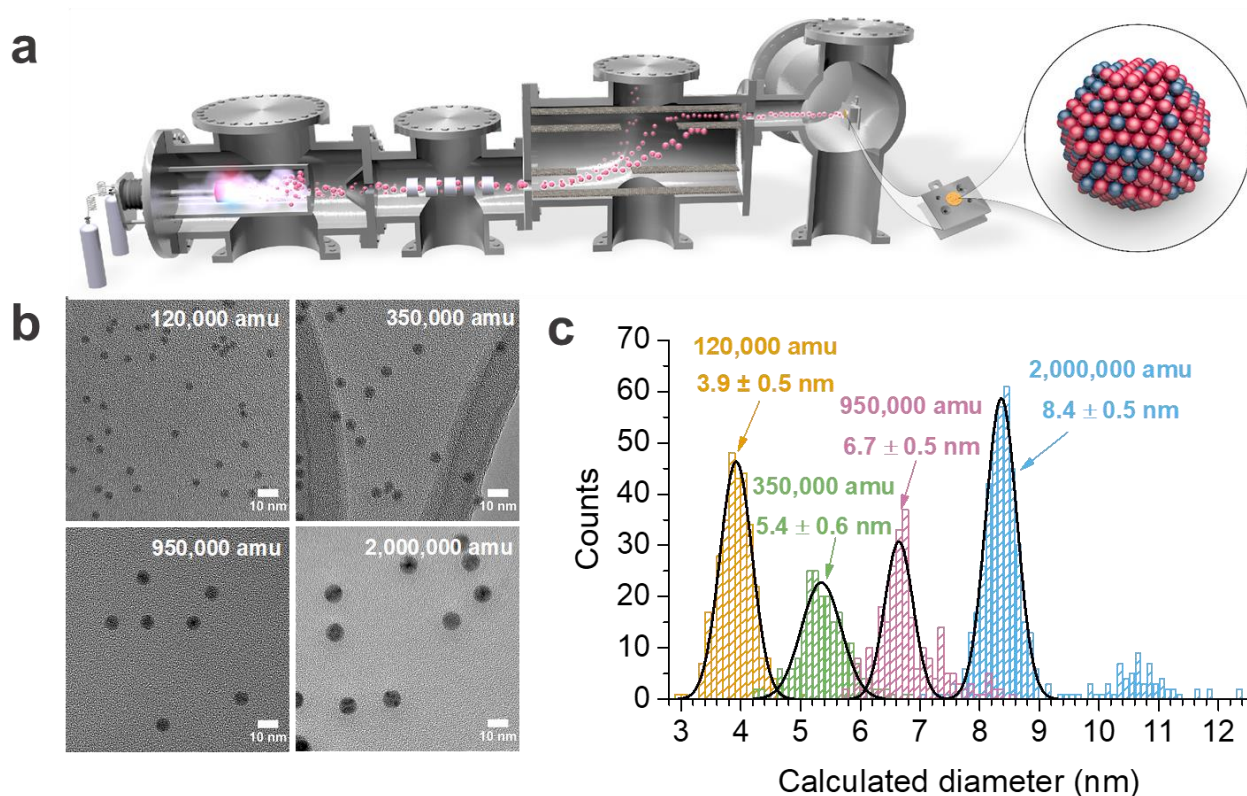


Figure 1: Deposition of mass-selected nanoparticles. (a) DC magnetron sputtering, gas aggregation mass-selected nanoparticle source with lateral time-of-flight mass filter. Mass selected NiFe nanoparticles were deposited on polycrystalline gold disks for activity measurements. (b) Transmission Electron Microscopy (TEM) images of 4 different masses of NiFe nanoparticles, and (c) size distributions determined using the diameter measured on the TEM images showing the average size and 2σ for each mass deposited.

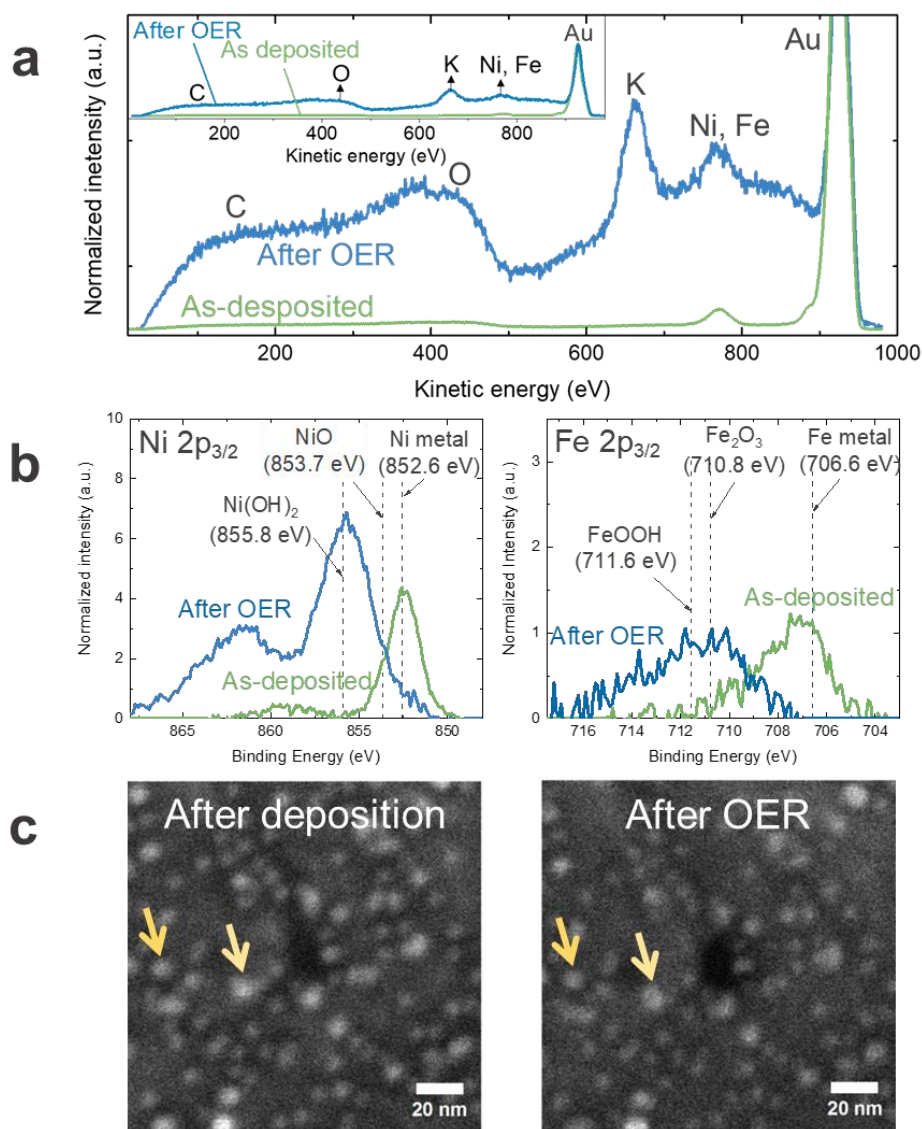


Figure 2: Ex situ characterization of the deposited 6.7 nm NiFe particles. (a) Low energy ion scattering (LEIS) spectra, (b) X-ray photoelectron spectroscopy (XPS) spectra, and (c) scanning electron microscopy (SEM) of nanoparticles as deposited (green traces, left SEM image) and after electrochemical testing (blue traces, right SEM image). The LEIS spectra were normalized to the height of the Au peak. The XPS spectra, shown for the Ni $2p_{3/2}$ and Fe $2p_{3/2}$ regions, were charge corrected and normalized with the Au 4f peak area after the subtraction of a Shirley-background. The reference XPS binding energies were taken from References^{52–54}. The SEM images are taken at identical location to evaluate the resistance against sintering and corrosion.

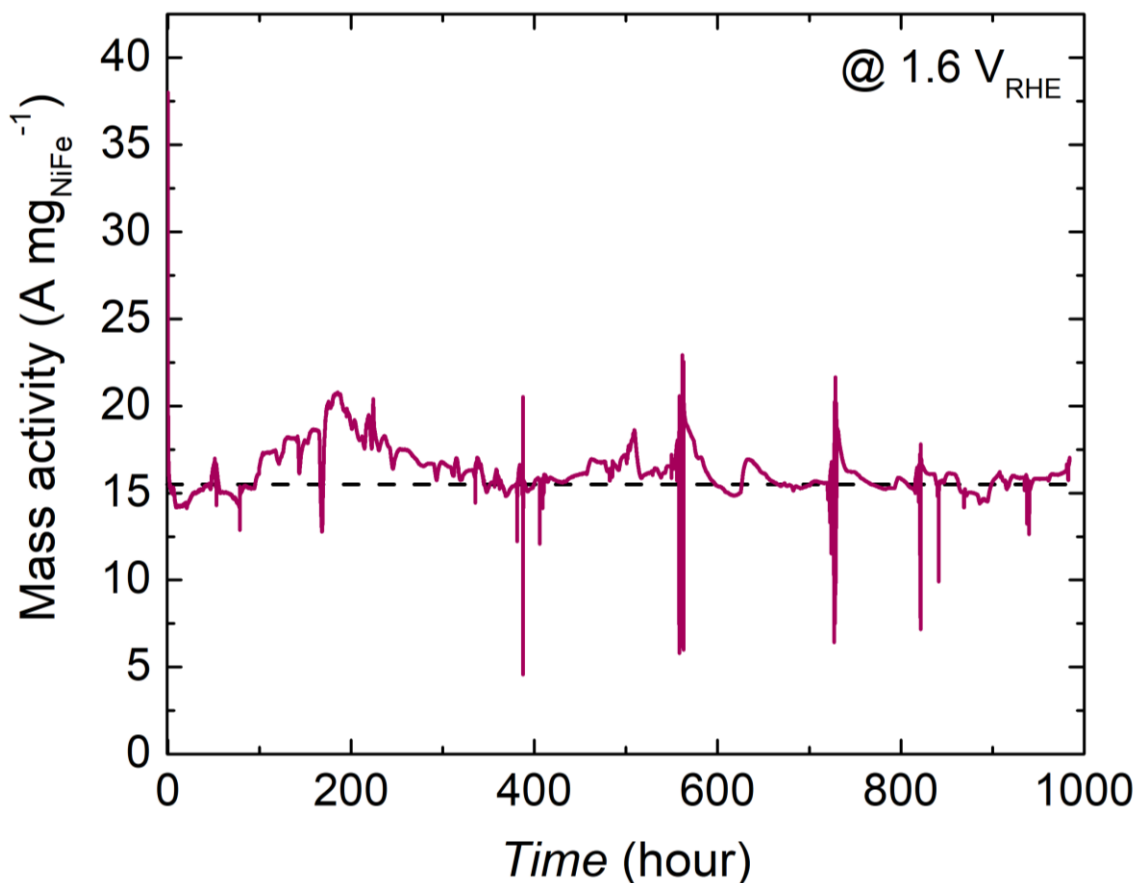


Figure 3: Stability of NiFe nanoparticles at 1.6V_{RHE} in 1 M KOH. The figure shows the mass activity of ~100 ng 6.7 nm NiFe nanoparticles at 1.6 V_{RHE}, iR corr., in 1 M KOH. Note that the label on the x-axis shows the time of the measurement in days. The dashed line is a guide to the eye.

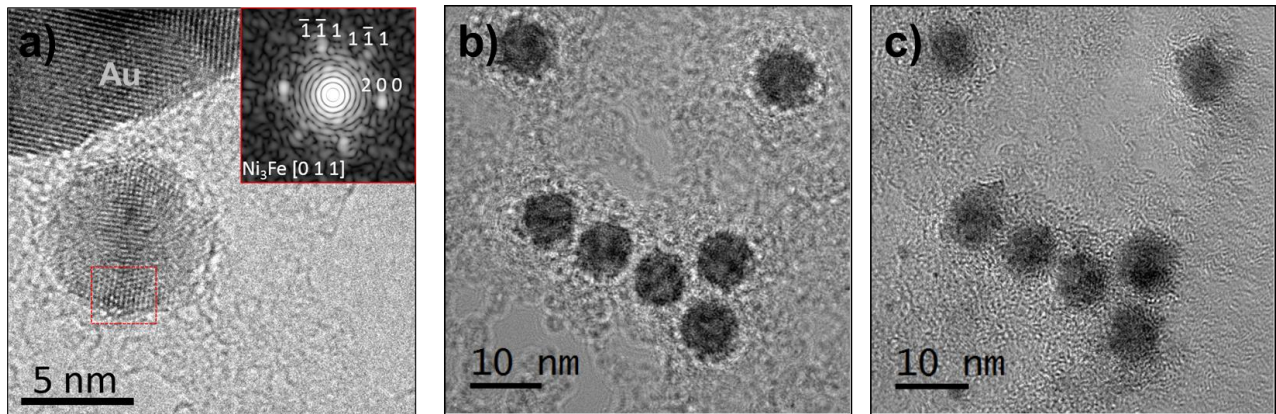


Figure 4: High-resolution TEM (HRTEM) investigation of the particles. High resolution TEM images of 6.7 nm (950k amu) NiFe nanoparticles deposited on Au TEM grids. (a) HRTEM image of a nanoparticle with Fourier transform of the highlighted area showing Ni_3Fe phase. (b) and (c) show identical location HRTEM images of nanoparticles before (b) and after electrochemical oxidation (c).

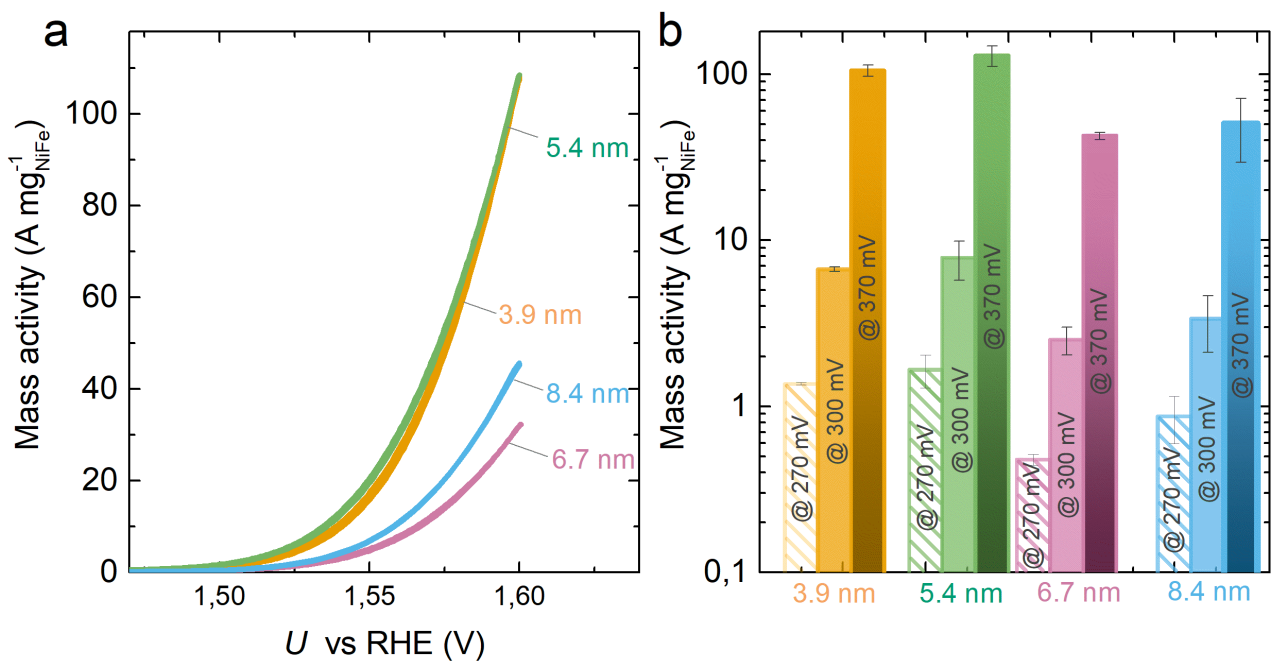


Figure 5: Catalytic activity of the NiFe nanoparticles. (a) Cyclic voltammetry at 10 mV/s of representative NiFeO_xH_y nanoparticle samples for each nanoparticle size. The current is normalized to the total metal mass loading. (b) Mass-normalized activities at $\eta = 270, 300$ and 370 mV. The average mass activity and standard deviation come from three independent samples. All activity measurements were done on Au substrates in N₂-saturated 1 M KOH at 1,600 rpm. The metal mass was determined from the nanoparticle deposition current.

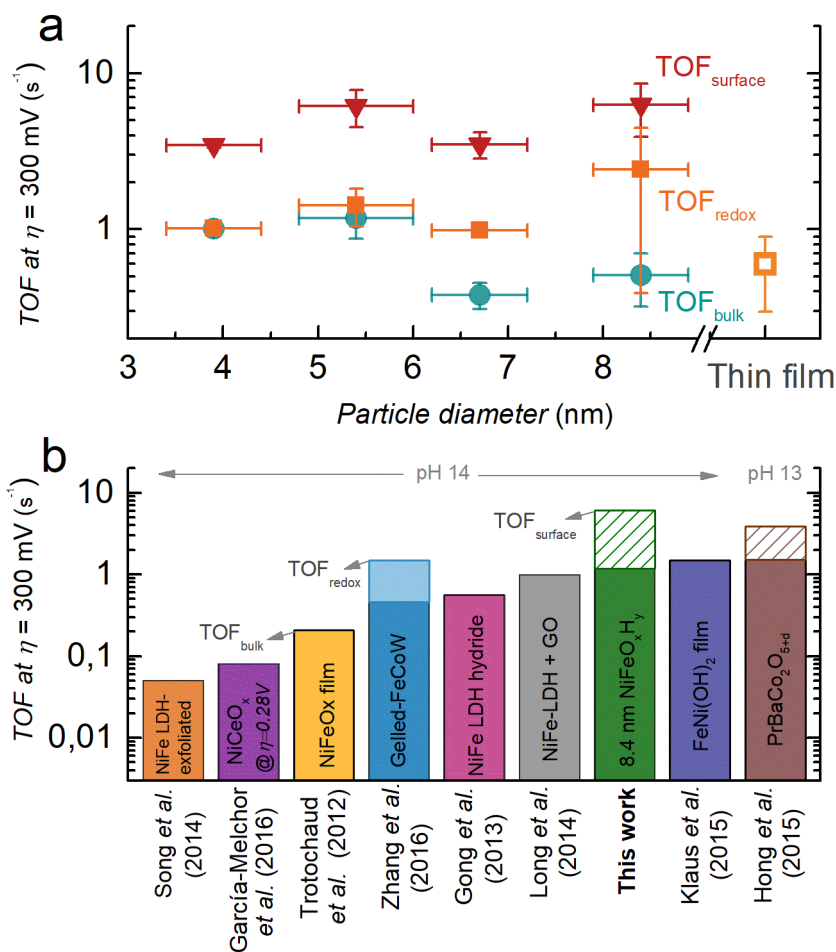


Figure 6: Turnover frequency as a function of size, and comparison to state-of-the-art non-noble metal catalysts. (a) Turnover frequency calculated from the total metal mass (TOF_{bulk}), the Ni redox peak (TOF_{redox}), and the estimated surface atoms (TOF_{surface}), of the NiFe nanoparticles at $\eta=300$ mV measured in N₂-saturated 1.0 M KOH at 10mV/s as function of particle size. The Ni redox peak was used to measure the TOF of the NiFe thin film. (b) TOF of state-of-the-art non-noble OER catalysts in alkaline. From ref. ⁴⁷ for NiFe LDH-Exfoliated; from ⁴² for NiCeO_x; from ²⁴ for NiFeOx film; from ⁵⁵ for Gelled-FeCoW; from ⁴⁶ for NiFe LDH hydride; from ⁴⁸ for NiFe-LDH + GO; from ¹⁶ for FeNi(OH)₂ film and from ⁵⁶ for PrBaCo₂O_{5+d}. When possible both minimum (bulk) and maximum (surface or redox) TOF were estimated. The TOF_{redox} of Gelled-FeCoW was calculated using the Co redox peak, and the TOF_{surf} for PrBaCo₂O_{5+d} was calculated based on surface area from N₂ physisorption (BET).

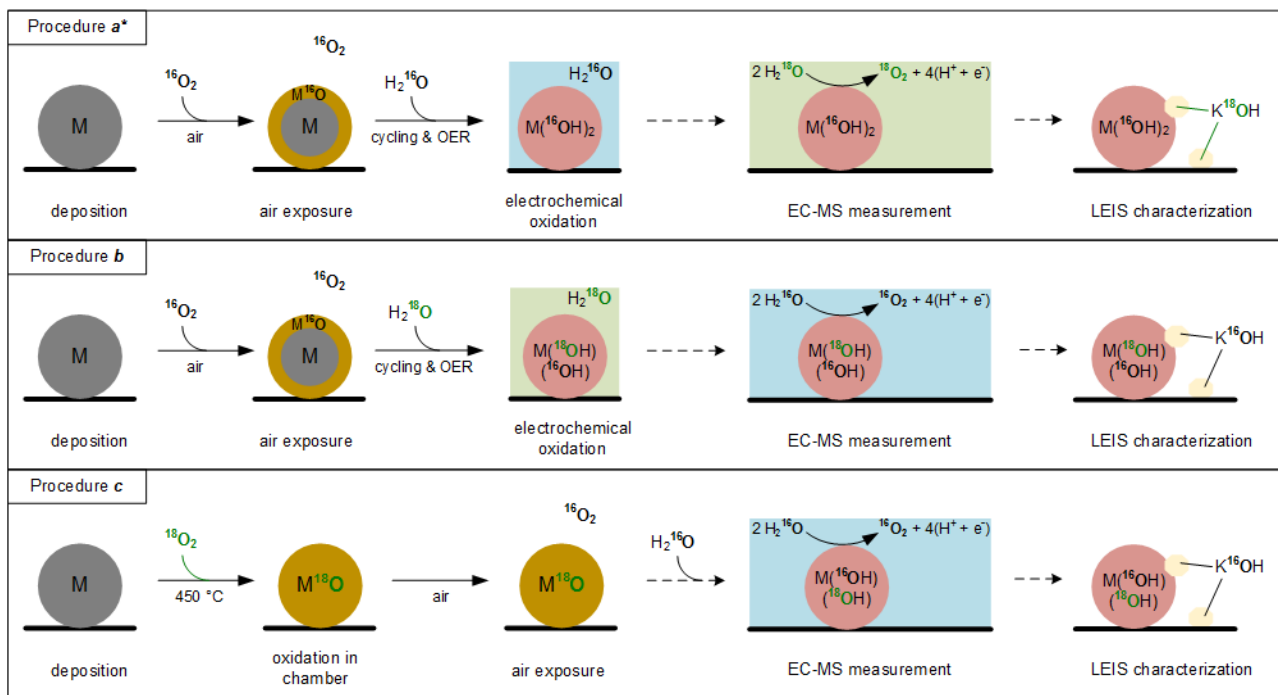


Figure 7: Isotope labelling experimental procedures. Schematic representation of the isotopic labelling experiments. Procedure *a* uses H_2^{16}O to oxidized the nanoparticles and H_2^{18}O for the oxygen evolution, while the opposite is done for Procedure *b*. Procedure *c* uses $^{18}\text{O}_2$ gas to oxidize NiFe and the oxygen evolution is performed in ^{16}O water. In the representation, M refers to Ni and Fe metal atoms. *The main text focuses on procedure *a*.

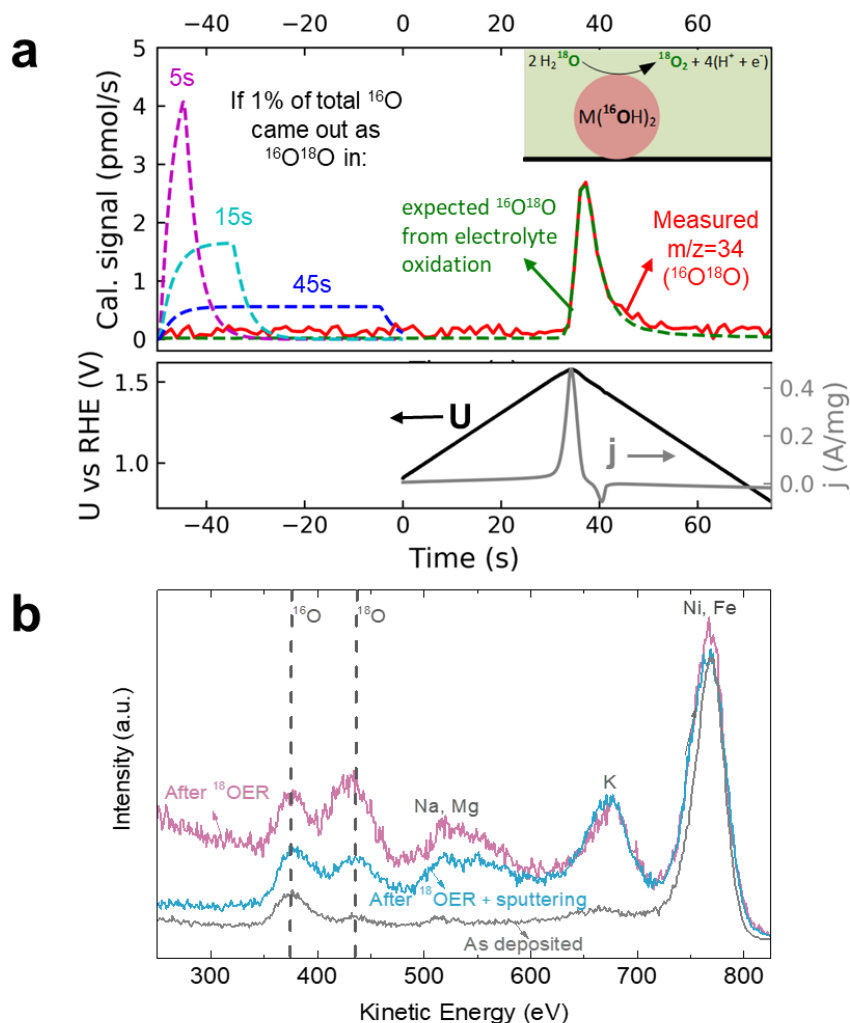


Figure 8: EC-MS and LEIS results from isotope labelling experiment using procedure a. a) First electrochemical potential cycle in H_2^{18}O electrolyte after sample preparation with ^{16}O . The bottom panel shows the potential (black, left axis) and current (gray, right axis). The top panel shows calibrated mass spectrometer signal of $^{16}\text{O}^{18}\text{O}$ ($m/z=34$) (red) detected during oxygen evolution in 0.1 M KOH made with H_2^{18}O (top panel). The $^{16}\text{O}^{18}\text{O}$ signal expected without lattice exchange due to the composition of the electrolyte, which is a constant fraction of the $^{18}\text{O}_2$ ($m/z=36$) signal, is co-plotted (dashed green). The top panel also shows simulations of the $m/z=34$ signal if 1% of the total ^{16}O contained by the oxidized catalyst came out as $^{18}\text{O}^{16}\text{O}$ in 5s (magenta), 15s (cyan) or 45s (blue). b) The low-energy ion scattering spectra of the sample as deposited (grey), after EC-MS experiment (purple) and after sputtering (blue).

ACKNOWLEDGEMENTS

This work was supported by a research grant (9455) from VILLUM FONDEN. We also acknowledge UPCAT under the project no. 2015-1-12315.

AUTHOR CONTRIBUTIONS

I.E.L.S., J.K. and I.C. conceived the experiments. C.R. participated in the conception of the experiments, performed the electrochemical measurements. B.S. participated in the conception of the experiments, prepared the nanoparticles, performed the UHV experiments, S.B.S. performed and helped in the design of the EC-MS experiments. D.B.T., P.C.V. and O.H. designed and helped with the interpretation of the EC-MS experiments. E.M.F. and C.D.D. performed the microscopy characterization. J.E.S and A.B. contributed to the LEIS measurements. C.R., B.S., and S.B.S. co-wrote the manuscript. All authors discussed the results and commented on the manuscript.

REFERENCES

1. Lewis, N. S. & Nocera, D. G. Powering the planet: Chemical challenges in solar energy utilization. *Proc. Natl. Acad. Sci.* **103**, 15729–15735 (2006).
2. Debe, M. K. Electrocatalyst approaches and challenges for automotive fuel cells. *Nature* **486**, 43–51 (2012).
3. Montoya, J. H. *et al.* Materials for Solar Fuels and Chemicals. *Nat. Mater.* **16**, 70–81 (2017).
4. Hong, W. T. *et al.* Toward the rational design of non-precious transition metal oxides for oxygen electrocatalysis. *Energy Environ. Sci.* **8**, 1404–1427 (2015).
5. Durst, J. *et al.* New insights into the electrochemical hydrogen oxidation and evolution reaction mechanism. *Energy Environ. Sci.* **7**, 2255–2260 (2014).
6. Stamenkovic, V. R., Strmcnik, D., Lopes, P. P. & Markovic, N. M. Energy and fuels from electrochemical interfaces. *Nat. Mater.* **16**, 57–69 (2016).
7. Greeley, J. & Markovic, N. M. The road from animal electricity to green energy: combining experiment and theory in electrocatalysis. *Energy Environ. Sci.* **5**, 9246 (2012).
8. Cifrain, M., Kordesch, K., Vielstich, W., Lamm, A. & Gasteiger, H. Hydrogen/oxygen (Air) fuel cells with alkaline electrolytes. *Fuel* **1**, 267–280 (2003).
9. Jang, B. W. *et al.* Fuels of the future. *Energy Environ. Sci.* **3**, 253 (2010).
10. Seh, Z. W. *et al.* Combining theory and experiment in electrocatalysis: Insights into materials design. *Science* **355**, eaad4998 (2017).
11. *The production of hydrogen and oxygen through the electrolysis of water. Scientific American Supplement No. 819 XXXII*, (1891).
12. Trotochaud, L., Young, S. L., Ranney, J. K. & Boettcher, S. W. Nickel-Iron oxyhydroxide oxygen-evolution electrocatalysts: The role of intentional and incidental iron incorporation. *J. Am. Chem. Soc.* **136**, 6744–6753 (2014).
13. Dionigi, F. & Strasser, P. NiFe-Based (Oxy)hydroxide Catalysts for Oxygen Evolution Reaction in Non-Acidic Electrolytes. *Adv. Energy Mater.* **6**, 1600621 (2016).
14. Burke, M. S., Enman, L. J., Batchellor, A. S., Zou, S. & Boettcher, S. W. Oxygen Evolution Reaction Electrocatalysis on Transition Metal Oxides and (Oxy)hydroxides: Activity Trends and Design Principles. *Chem. Mater.* **27**, 7549–7558 (2015).
15. Enman, L. J., Burke, M. S., Batchellor, A. S. & Boettcher, S. W. Effects of Intentionally Incorporated Metal Cations on the Oxygen Evolution Electrocatalytic Activity of Nickel (Oxy)hydroxide in Alkaline Media. *ACS Catal.* **6**, 2416–2423 (2016).
16. Klaus, S., Cai, Y., Louie, M. W., Trotochaud, L. & Bell, A. T. Effects of Fe electrolyte impurities on Ni(OH)₂/NiOOH structure and oxygen evolution activity. *J. Phys. Chem. C* **119**, 7243–7254 (2015).
17. Li, N. *et al.* Influence of iron doping on tetravalent nickel content in catalytic oxygen evolving films. *Proc. Natl. Acad. Sci.* **114**, 1486–1491 (2017).
18. Görlin, M. *et al.* Oxygen evolution reaction dynamics, faradaic charge efficiency, and the active metal redox states of Ni-Fe oxide water splitting electrocatalysts. *J. Am. Chem. Soc.* **138**, 5603–5614 (2016).
19. Friebel, D. *et al.* Identification of highly active Fe sites in (Ni,Fe)OOH for electrocatalytic water splitting. *J. Am. Chem. Soc.* **137**, 1305–1313 (2015).

20. Stevens, M. B., Trang, C. D. M., Enman, L. J., Deng, J. & Boettcher, S. W. Reactive Fe-Sites in Ni/Fe (Oxy)hydroxide Are Responsible for Exceptional Oxygen Electrocatalysis Activity. *J. Am. Chem. Soc.* **33**, 11361–11364 (2017).
21. Batchellor, A. S. & Boettcher, S. W. Pulse-Electrodeposited Ni-Fe (Oxy)hydroxide Oxygen Evolution Electrocatalysts with High Geometric and Intrinsic Activities at Large Mass Loadings. *ACS Catal.* **5**, 6680–6689 (2015).
22. Doyle, A. D., Bajdich, M. & Vojvodic, A. Theoretical Insights to Bulk Activity Towards Oxygen Evolution in Oxyhydroxides. *Catal. Letters* **147**, 1533–1539 (2017).
23. Morales-Guio, C. G., Liardet, L. & Hu, X. Oxidatively Electrodeposited Thin-Film Transition Metal (Oxy)hydroxides as Oxygen Evolution Catalysts. *J. Am. Chem. Soc.* **138**, 8946–8957 (2016).
24. Trotochaud, L., Ranney, J. K., Williams, K. N. & Boettcher, S. W. Solution-cast metal oxide thin film electrocatalysts for oxygen evolution. *J. Am. Chem. Soc.* **134**, 17253–17261 (2012).
25. Wohlfahrt-Mehrens, M. & Heitbaum, J. Oxygen evolution on Ru and RuO₂ electrodes studied using isotope labelling and on-line mass spectrometry. *J. Electroanal. Chem. Interfacial Electrochem.* **237**, 251–260 (1987).
26. Diaz-Morales, O., Calle-Vallejo, F., de Munck, C. & Koper, M. T. M. Electrochemical water splitting by gold: evidence for an oxide decomposition mechanism. *Chem. Sci.* **4**, 2334 (2013).
27. Fierro, S., Nagel, T., Baltruschat, H. & Comninellis, C. Investigation of the oxygen evolution reaction on Ti/IrO₂ electrodes using isotope labelling and on-line mass spectrometry. *Electrochem. commun.* **9**, 1969–1974 (2007).
28. Amin, H. M. A. & Baltruschat, H. How many surface atoms in Co₃O₄ take part in oxygen evolution? Isotope labeling together with differential electrochemical mass spectrometry. *Phys. Chem. Chem. Phys.* **19**, 25527–25536 (2017).
29. Stoerzinger, K. A. *et al.* Orientation-Dependent Oxygen Evolution on RuO₂ without Lattice Exchange. *ACS Energy Lett.* **2**, 876–881 (2017).
30. Macounova, K., Makarova, M. & Krtil, P. Oxygen evolution on nanocrystalline RuO₂ and Ru_{0.9}Ni_{0.1}O_{2-δ} electrodes - DEMS approach to reaction mechanism determination. *Electrochem. commun.* **11**, 1865–1868 (2009).
31. Grimaud, A. *et al.* Activating lattice oxygen redox reactions in metal oxides to catalyse oxygen evolution. *Nat. Chem.* **9**, 457–465 (2017).
32. Lu, X. & Zhao, C. Electrodeposition of hierarchically structured three-dimensional nickel–iron electrodes for efficient oxygen evolution at high current densities. *Nat. Commun.* **6**, 1–7 (2015).
33. Trimarco, D. B. *et al.* Enabling real-time detection of electrochemical desorption phenomena with sub-monolayer sensitivity. *Electrochim. Acta* (2018).
34. Paoli, E. A. *et al.* Oxygen evolution on well-characterized mass-selected Ru and RuO₂ nanoparticles. *Chem. Sci.* **6**, 190–196 (2015).
35. Li, Z. Y. *et al.* Three-dimensional atomic-scale structure of size-selected gold nanoclusters. *Nature* **451**, 46–48 (2008).
36. Ferreira, P. J. *et al.* Instability of Pt/C Electrocatalysts in Proton Exchange Membrane Fuel Cells. *J. Electrochem. Soc.* **152**, A2256 (2005).
37. Meier, J. C. *et al.* Design criteria for stable Pt/C fuel cell catalysts. *Beilstein J. Nanotechnol.* **5**, 44–67 (2014).
38. Fiordaliso, E. M., Dahl, S. & Chorkendorff, I. Strong metal support interaction of Pt and Ru nanoparticles deposited on HOPG probed by the H-D exchange reaction. *J.*

- Phys. Chem. C* **116**, 5773–5780 (2012).
39. Binninger, T. *et al.* Thermodynamic explanation of the universal correlation between oxygen evolution activity and corrosion of oxide catalysts. *Sci. Rep.* **5**, 12167 (2015).
 40. Spöri, C. *et al.* The Stability Challenges of Oxygen Evolving Electrocatalysts: Towards a Common Fundamental Understanding and Mitigation of Catalyst Degradation. *Angew. Chemie - Int. Ed.* **56**, 5994–6021 (2017).
 41. Hartl, K., Hanzlik, M. & Arenz, M. IL-TEM investigations on the degradation mechanism of Pt/C electrocatalysts with different carbon supports. *Energy Environ. Sci.* **4**, 234–238 (2011).
 42. Ng, J. W. D. *et al.* Gold-supported cerium-doped NiOx catalysts for water oxidation. *Nat. Energy* **1**, 16053 (2016).
 43. Xu, X., Song, F. & Hu, X. A nickel iron diselenide-derived efficient oxygen-evolution catalyst. *Nat. Commun.* **7**, 1–7 (2016).
 44. Silva, H. *et al.* Synthesis and characterization of Fe-Ni/ χ -Al₂O₃ egg-shell catalyst for H₂ generation by ammonia decomposition. *Appl. Catal. A Gen.* **505**, 548–556 (2015).
 45. Zhang, B. *et al.* Homogeneously dispersed , multimetal oxygen-evolving catalysts. *Science* **352**, 333 (2016).
 46. Gong, M. *et al.* An advanced Ni-Fe layered double hydroxide electrocatalyst for water oxidation. *J. Am. Chem. Soc.* **135**, 8452–8455 (2013).
 47. Song, F. & Hu, X. Exfoliation of layered double hydroxides for enhanced oxygen evolution catalysis. *Nat. Commun.* **5**, 1–9 (2014).
 48. Long, X. *et al.* A strongly coupled graphene and FeNi double hydroxide hybrid as an excellent electrocatalyst for the oxygen evolution reaction. *Angew. Chemie - Int. Ed.* **53**, 7584–7588 (2014).
 49. Lu, X. & Zhao, C. Electrodeposition of hierarchically structured densities. *Nat. Commun.* **6**, 1–7 (2015).
 50. Von Issendorff, B. & Palmer, R. E. A new high transmission infinite range mass selector for cluster and nanoparticle beams. *Rev. Sci. Instrum.* **70**, 4497–4501 (1999).
 51. Pratontep, S., Carroll, S. J., Xirouchaki, C., Streun, M. & Palmer, R. E. Size-selected cluster beam source based on radio frequency magnetron plasma sputtering and gas condensation. *Rev. Sci. Instrum.* **76**, (2005).
 52. Biesinger, M. C., Lau, L. W. M., Gerson, A. R. & Smart, R. S. C. The role of the Auger parameter in XPS studies of nickel metal, halides and oxides. *Phys. Chem. Chem. Phys.* **14**, 2434 (2012).
 53. Biesinger, M. C. *et al.* Resolving surface chemical states in XPS analysis of first row transition metals, oxides and hydroxides: Cr, Mn, Fe, Co and Ni. *Appl. Surf. Sci.* **257**, 2717–2730 (2011).
 54. Grosvenor, A. P., Biesinger, M. C., Smart, R. S. C. & McIntyre, N. S. New interpretations of XPS spectra of nickel metal and oxides. *Surf. Sci.* **600**, 1771–1779 (2006).
 55. Zhang, B. *et al.* Homogeneously dispersed multimetal oxygen-evolving catalysts. *Science* **352**, 333–337 (2016).
 56. Hong, W. T. *et al.* Toward the rational design of non-precious transition metal oxides for oxygen electrocatalysis. *Energy Environ. Sci.* **8**, 1404–1427 (2015).



